# Dissertation

*submitted to the*

Combined Faculty of Mathematics, Engineering and Natural Sciences
of Heidelberg University, Germany

*for the degree of*

Doctor of Natural Sciences

*Put forward by*

Friederike Juliane Ihssen

*born in:* Hamburg, Germany
Oral examination: July 5th, 2023

# Resolving the QCD phase structure

Referees: Prof. Dr. Jan M. Pawlowski
Prof. Dr. Manfred Salmhofer

**Resolving the QCD phase structure**

This thesis discusses the quantitative description of the phase structure of Quantum Chromodynamics (QCD). We find that, in strongly correlated theories such as QCD, even a qualitative investigation of the phase structure can require highly quantitative methods. Hence, the development of a method with systematic error control is essential. In the present work, we use functional renormalisation group (fRG) method to this aim. This work focusses on three ideas: Firstly, we identify quantitatively dominating and sub-leading scattering-processes in our approximations. This allows a formulation of low energy effective theories of the four-quark interaction, as well as the description of gluon condensation. For the former, we present results for meson and quark masses. The latter provides an estimate of the Yang-Mills mass gap. Secondly, we further develop the use of highly precise numerical methods from fluid-dynamics in the fRG. In particular we use Discontinuous Galerkin methods, which are able to capture shock-development. Shock-waves are found to play a big role in a possible creation-mechanism of first-order phase transitions. Lastly, we focus on general RG-transformations (gRGt). For example, they allow a real time formulation of fRG flows and hence give access to spectral functions. Furthermore, we use them to formulate complex RG-flows, which enables us to locate Lee-Yang singularities in the complex plane and extrapolate the position of (real) phase transitions. Finally, we also use gRGts to formulate significant qualitative improvements of current fRG approximation schemes by means of dynamical field transformations.

**Zur Bestimmung der QCD Phasenstruktur**

Diese Arbeit befasst sich mit der quantitativen Beschreibung der Phasenstruktur der Quanten Chromodynamik (QCD). Es stellt sich heraus, dass in einer stark korrelierten Theorie, wie der QCD, sehr präzise Methoden bereits für eine qualitative Erfassung der Phasenstruktur notwendig sein können. Die Entwicklung einer solchen Methode mit systematischer Fehlererfassung ist daher essenziell. Wir nutzen hierfür Methoden der funktionalen Renormierungsgruppe (fRG) und verfolgen drei Ansätze in dieser Arbeit: Die Erfassung/Identifizierung quantitativ dominierender Streuprozesse und solcher, die Korrekturen darstellen. Dies geschieht im Kontext von effektiven Niedrigenergie-Theorien zu vier-Quark Streuprozessen und der Entstehung von Gluon-Kondensaten. Es werden quantitative Ergebnisse für Meson- und Quarkmassen sowie die Yang-Mills Massenlücke präsentiert. Weiterhin entwickeln wir die Verwendung von Methoden aus der Fluid-Dynamik beim Lösen der fRG Gleichungen weiter. Hier verwenden wir insbesondere Diskontinuierliche Galerkin Methoden, welche es erlauben die Entstehung von Schockwellen zu erfassen. Besonders im Entstehungsmechanismus von Phasenübergängen erster Ordnung können diese eine wichtige Rolle spielen. Zuletzt fokussieren wir uns auf verallgemeinerte RG-Transformationen. Diese ermöglichen zum Beispiel eine Realzeitformulierung der fRG mit Zugriff auf Spektralfunktionen oder die Formulierung komplexer RG-Flüsse. Letztere werden zur Bestimmung von Lee-Yang Singularitäten und den damit einhergehenden Phasenübergängen sowie kritischer Punkte genutzt. Verallgemeinerte RG-Transformationen bieten auch die Möglichkeit qualitativer Verbesserungen der verwendeten Näherungen durch dynamische Felddefinitionen.

This thesis was solely written by the author. It is, however, result of a joint effort in a research collaboration. As such, this thesis includes work from collaborators who contributed to different projects. These projects make up a large part of the thesis and are published or available as preprints. The corresponding publications are,

- *Shocks and quark-meson scatterings at large density* [1]
  with Eduardo Grossi, Jan M. Pawlowski and Nicolas Wink,
  Published in PhysRev D. 104 016028 (2021)

- *Gluon condensates and effective gluon mass* [2]
  with Jan Horak, Joannis Papavassiliou, Jan M. Pawlowski, Axel Weber and Christof Wetterich
  Published in SciPostPhys 13.2.042 (2022)

- *Renormalised spectral flows* [3]
  with Jens Braun, Yong-rui Chen, Wei-jie Fu, Andreas Geißel, Jan Horak, Chuang Huang, Jan M. Pawlowski, Manuel Reichert, Fabian Rennecke, Yang-yang Tan, Sebastian Töpfel, Jonas Wessely and Nicolas Wink
  e-print available from 2206.10232 [hep-th] (2022)

- *Functional flows for complex effective actions* [4]
  with Jan M. Pawlowski
  e-print available from 2207.10057 [hep-ph] (2022)

- *Local Discontinuous Galerkin for the Functional Renormalisation Group* [5]
  with Jan M. Pawlowski, Franz R. Sattler and Nicolas Wink
  e-print available from 2207.12266 [hep-ph] (2022)

- *Numerical RG-time integration of the effective potential: Analysis and Benchmark* [6]
  with Franz R. Sattler and Nicolas Wink
  e-print available from 2302.04736 [hep-th] (2023)

- *Scalar spectral functions from the spectral fRG* [7]
  with Jan Horak, Jan M. Pawlowski, Jonas Wessely and Nicolas Wink
  e-print available from 2303.16719 [hep-th] (2023)

Furthermore, this manuscript contains preliminary work in collaboration with,

- *Preliminary: Flowing fields and optimal RG-flows* [8]
  with Jan M. Pawlowski

- *Preliminary: Towards quantitative precision in functional QCD* [9]
  with Jan M. Pawlowski, Franz R. Sattler and Nicolas Wink

- *Preliminary: Local Discontinuous Galerkin for higher quark-mesonic scattering orders* [10]
  with Jan M. Pawlowski, Franz R. Sattler and Nicolas Wink

- *Preliminary: Towards the chiral phase structure at large densities* [11]
  with Wladimir Krinitsin and Jan M. Pawlowski

Text and figures from these publications are not marked as such. Sections based on published work reference the corresponding publication.

On the authors contribution: All computations in [1] were performed by the author and a large portion of the main text was drafted by the author. This publication was the first to use the *dune-FRGDG* module, which was developed by the author under the supervision of the coauthors. The module was further developed in [5], in close collaboration with F. R. Sattler. It was used by the author and collaborators as a basis in subsequent publications and preprints [4, 8–11]. A GitHub repository of the simplified dune-FRGDG module is provided in [12]. The author performed all computations in [5] and contributed largely to the manuscript.
The author contributed all numerical computations, as well as a large part of the manuscripts to [4, 8, 9].
All computations of the effective potential in [2] were performed by the author. The author contributed largely to the computational details and the results section of the manuscript.
[3] was published within the fQCD collaboration [13]. The author contributed to discussions and parts/revisions of the manuscript.
The manuscripts [7, 10, 11] are the results of Master projects of students, which were co-supervised by the author.
The author made minor contributions to the manuscript [6] and discussions therein, as such it is only featured in the appendix.
Figures were plotted using Mathematica [14], Python [15] and Julia [16].

# Contents

# CHAPTER 1

# Introduction

"What is matter made of?" - Particle physics answers this question with an effective description by the Standard Model. It comprises three of the four known fundamental forces, strong, weak and electromagnetic, and uses them to describe the interaction of elementary particles. The answer to our initial question is an interplay of all the above: three generations of fermionic matter particles, the quarks and leptons, and their interactions in terms of bosonic force carriers. So instead, we ask a more nuanced question in this thesis: "How, and under which conditions, is nuclear matter created?"

Heavy-ion collision experiments, such as RHIC, LHC and STAR to name a few, provide numerous amounts of data on the state of nuclear matter at high temperatures $T$ and high baryon chemical potential $\mu_B$. An interpretation and understanding of these experimental results is provided by the theory of Quantum Chromodynamics (QCD), which describes the interactions of quarks and the carriers of the strong force, the gluons [17–26]. QCD has a rich phase structure, which contains the known states of hadronic matter at low temperatures and densities and transitions to a quark-gluon-plasma (QGP) with increasing temperatures. Possible (color-)superconducting states, which might be found in neutron stars, have been predicted at high densities [27]. The phase transition between hadronic states and the QGP is linked to two phenomena: color confinement and chiral symmetry breaking. Together they determine a phase transition line, which starts as a smooth crossover at high temperatures and results in the conjectured critical endpoint (CEP) with increasing density, after which a first order phase transition occurs, see the sketch in Figure 1.1.

Many theoretical, ab initio results for QCD have been obtained from lattice calculations and allow to map out the crossover region. However, this Monte-Carlo based method begins to suffer from the sign problem at finite density, and extrapolated results are no longer reliable for $\mu_B/T \gtrsim 2-3$ [28–37]. To date, the lattice has only been able to exclude the location of the CEP up to this bound [38]. The sparseness of theoretical results at high densities is added to by the lack of experimental data in this regime, caused by limited detector efficiency in identifying signatures of phase transitions [39]. The relevance of the CEP arises from its critical long-range correlations. For example, particle number correlations in heavy-ion experiments are promising observables for example, see [40].

Due to their non-perturbative nature and lack of a sign problem, functional methods, such as

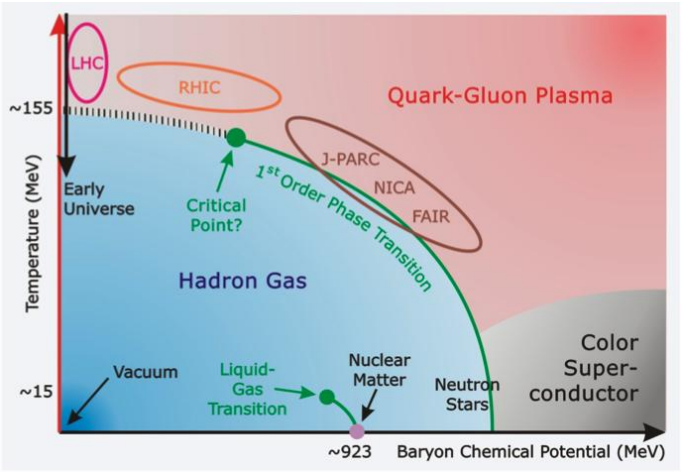


Figure 1.1.: A sketch of the QCD phase structure. Figure taken from [41].

the functional renormalisation group (fRG) [42–51] or Dyson-Schwinger equations [19,52–57] have added significantly to the prediction of the CEP location and reach as far as $\mu_B/T \lesssim 6$. The fRG, which is inherently a method suited for physics of different scales, is our tool of choice to investigate the phase structure of QCD: a theory defined by asymptotic freedom, strong non-perturbative dynamics at low energies and competing order effects. In this work, we make use of the flexibility of the fRG, which allows to systematically include (and exclude) degrees of freedom from a given theory to pave the way for a quantitative computation of the QCD phase diagram at high densities. We focus on three different ways to qualitatively and quantitatively improve the current state-of-the-art results.

In principle, the fRG has a one-loop structure which accounts for all quantum effects. In practice however, one has to chose a truncated ansatz to compute the complex field and momentum dependencies. Here, we can benefit from the modularity of the fRG, where we can systematically add (and remove) degrees of freedom (DoF) to test their quantitative relevance to physical observables. This allows e.g. for a systematic inclusion of four-quark scattering processes and the construction of low energy effective theories (LEFT) of QCD [58–60]. We investigate LEFTs to study the process of spontaneous chiral symmetry breaking caused by the formation of fermionic bound states, in the present context the mesons, across the phase structure. The inclusion of higher mesonic scattering orders allows the prediction of the QCD phase boundary in the area $\mu_B/T \lesssim 6$, beyond this ratio the LEFT needs to include the formation of e.g. diquark condensates and vector mesons to remain quantitatively accurate [61–64]. The phase structure is obtained from an order parameter potential, which tracks the formation of symmetry breaking condensates [1,10], see Figure 8.9 for an example in the quark-meson model. We also apply this procedure to a fRG study of confinement, where we consider the condensation process of gluons and give a prediction of the gluon mass gap [2]. The corresponding order parameter potential is shown in Figure 4.1.

An elaborated numerical approach is vital to the quantitative control of the order parameter potential, especially in the vicinity of the CEP and first order regimes. Here, the strong dynamics of the RG-flow have the potential to create shocks and discontinuities, which affect the phase boundary already on a qualitative level and may hint at a hidden mechanism for first order phase transitions [1,65], see Figure 8.7. Hence, our second technical advance within this work is the computation of fully field dependent order parameter potentials using Discontinuous

Galerkin (DG) methods, which are able to accurately track shock development and propagation. In light of highly dynamic, higher dimensional potentials with multiple condensates or the inclusion of more elaborate momentum dependencies to our truncation, we also focus on computational improvements of the numerical evaluation of RG-flows, such as runtime speed ups and the application of different DG schemes.

Thirdly, we investigate possible improvements or extensions of the flow equations. This is done by investigating general RG-transformations, first proposed by Wegner [66], which go beyond the standard formulation in terms of the Wetterich or Polchinski flows [67, 68]. These novel technical developments are tested using the O(N) model. Together with the previously outlined numerical advances, these developments can also be applied in broader context ranging from condensed matter systems at the smallest momentum scales over Standard model and Beyond Standard Model physics and QCD at high energy scales, to statistical physics and quantum gravity. We consider an adaption of generalised RG-flows to complex sources, allowing to identify the Lee-Yang singularities in the complex plane and thereby extrapolating a real phase transition, see Figure 6.10a. A future application would be an extrapolation of the CEP in QCD. Furthermore, we use RG-flows which expand the flow about its ground state by using a RG-adapted reparametrisation of dynamical, flowing fields. Lastly, we also turn our focus toward real-time applications of the fRG using the CS-flow to compute spectral functions.

This thesis addresses the above points of improvement. Since they are tightly interwoven in applications, the thesis is structured as follows: we start with methodological developments, which we later on apply to QCD. We begin with a short introduction to QCD in Chapter 2 and its low energy effective theories. Next, we introduce the functional renormalisation group in Chapter 3, where we also emphasise general RG-reparametrisations of the flow. With these two ingredients we turn our focus to the computation of a gluon condensate in Chapter 4, which is directly linked to confinement, the corresponding publication is [2]. In Chapter 5 we give a brief introduction to Discontinuous Methods and show results for an order potential of a simple O(N) model. The chapter corresponds to [5], refers also to [6], and gives insight to the numerical developments which can be openly accessed on GitHub [12]. We proceed with an investigation of complex functional flows for the Wilsonian and 1PI effective actions, and the construction of an RG-adapted flow in Chapter 6. These flows are applied to an O(N) model, which allows to locate (complex) Lee-Yang singularities and their corresponding phase transition on the real axis. This chapter is based on [4]. It is followed by two more applications of general RG reparametrisations to the O(N) model in Chapter 7, which we hope to use for QCD calculations in the future. The content of this chapter is based on [8] and [7]. We provide a compilation of results on the quark-meson model and its phase structure in Chapter 8, compare [1, 10, 11]. Finally, a full QCD computation is presented in Chapter 9, see also [9]. We close with a summary and outlook in Chapter 10.

# CHAPTER 2

# Quantum Chromodynamics

The experimental discovery of a many different hadronic particle species in the 1950s suggested a missing ingredient to the understanding of fundamental particles. In fact, sorting these particles into groups according to their quantum numbers, such as charge or isospin, suggested an underlying pattern: the existence of three smaller particles inside the hadrons, the quarks. Quarks are, to our current understanding, the fundamental, fermionic building blocks of hadronic matter.

The understanding of quark interactions was furthered by the discoveries of the $\Omega^-$ hyperion and the $\Delta^{++}$ baryon. It suggested an additional quantum number in the description of quarks, such that the Pauli exclusion principle is satisfied for the quarks within the hadrons. This additional quantum number $N_c = 3$ is called color charge and arises from the local $SU(3)$ gauge symmetry of quarks and anti-quarks. Their interactions are carried by an octet of vector gauge bosons, the gluons. This picture is further complemented by different species of quarks (u,d,s,c,b,t), which are called flavors.

In the following, we introduce the basic concepts and our notation for a quantum field theory of quarks and anti-quarks with an $SU(N)$ symmetry in Section 2.1. Next, we point out two mechanisms underlying the (known) phase structure of Quantum Chromodynamics (QCD) in Section 2.2: confinement and chiral symmetry breaking. We close in Section 2.3 by giving an overview of the current state-of-the-art computations of the QCD phase structure, as well as an introduction to low energy effective models, such as the quark-meson model.

## 2.1. Fundamentals of gauge theories

Quantum Chromodynamics captures the invariance of quark color charge under local $SU(N_c)$ gauge transformations. In such a theory, the fermionic (quark) fields $\psi$ are invariant under local transformations,

$$\psi(x) \to V(x)\psi(x), \quad \text{with} \quad V(x) = \exp\left(\mathrm{i}\alpha^a(x)t^a\right), \tag{2.1}$$

where $t^a$ are the $N_c^2 - 1$ hermitian *generators* of the $SU(N_c)$ symmetry group and $\alpha^a$ are some arbitrary functions of the spacetime coordinate $x$. The fermionic fields $\psi$ are given in the *fundamental representation* of $SU(N_c)$, which is a complex $N_c$-dimensional vector.

The generators $t^a$ form a basis for any infinitesimal group element/transformation of $SU(N_c)$,

$$V(x) \to 1 + \mathrm{i}\alpha^a(x)t^a + \mathcal{O}(\alpha^2)\,, \tag{2.2}$$

which is possible for any *Lie group*. In explicit calculations we use $t^a = \frac{\lambda^a}{2}$, where $\lambda^a$ are the Gell-Mann matrices for $SU(3)$ and $t^a = \frac{\sigma^a}{2}$, with the Pauli matrices $\sigma^a$ in $SU(2)$. Since the generators form a basis, we can write their commutator as a linear combination,

$$[t^a, t^b] = \mathrm{i}f^{abc}t^c\,, \tag{2.3}$$

where the sum-convention over indices is implied. The $f^{abc}$ are called *structure constants*. The structure constants and commutation operation completely define the vector space spanned by the generators, which forms a *Lie Algebra* $su(N_c)$. In the present work, we chose the normalisation of the structure constants as

$$\mathrm{tr}_f\left(t^a t^b\right) = \frac{1}{2}\delta^{ab}\,, \tag{2.4}$$

in the fundamental representation, with the indices $a, b = 1, \ldots, N_c^2 - 1$.

### 2.1.1. Gauge symmetry

All derivations in the present section are performed in Euclidean spacetime. For the construction of a gauge invariant theory of quarks, we need a derivative that transforms covariantly under gauge transformations $V(x)$. Hence the concept of a partial derivative $\partial_\mu$ is extended to the *covariant derivative*,

$$D_\mu = \partial_\mu - \mathrm{i}g_s A_\mu\,, \quad \text{with} \quad A_\mu = A_\mu^a(x)t^a\,. \tag{2.5}$$

The coupling $g_s$ to the gauge field is introduced as a simple rescaling for later convenience. $A_\mu$ is an algebra valued field that arises as a consequence of the local symmetry and is called *comparator*. The covariance $D_\mu(A) \to D_\mu(A^V) = V D_\mu V^\dagger$ of the derivative is now ensured by the transformation of the comparator,

$$A_\mu^a(x)t^a \to V(x)\left(A_\mu^a(x)t^a + \frac{\mathrm{i}}{g}\partial_\mu\right)V(x)^\dagger\,. \tag{2.6}$$

Hence, the gauge field effectively removes contributions that arise from gauge group transformations in the difference quotient of the fermionic field and $D\psi$ transforms the same as (2.1).

The gauge field $A_\mu$ is a gauge boson and is called gluon in case of $SU(3)$. It is a virtual particle and the force carriers of the strong interaction. As such, it is part of the algebra and is commonly indicated in the *adjoint representation*, which is given by $(t^c_{\mathrm{ad}})^{ab} = if^{abc}$.

The gauge invariant Euclidean classical action for the fermions is now simply obtained by replacing the plain derivative with the covariant one

$$S_{\mathrm{D}}[\psi, \bar{\psi}, A] = \int_x \bar{\psi}(\not{D} + m_q)\psi\,, \tag{2.7}$$

where the integral is performed over $d$ spacetime dimensions $\int_x = \int d^d x$.

The description is completed by adding a kinetic term for the gluons, which also needs to be gauge invariant. A natural candidate is the commutator of the covariant derivative, which defines the field-strength tensor,

$$F_{\mu\nu} := F^a_{\mu\nu} t^a = \frac{\mathrm{i}}{g_s}[D_\mu, D_\nu], \quad \text{with} \quad F^a_{\mu\nu} = \partial_\mu A^a_\nu - \partial_\nu A^a_\mu + g_s f^{abc} A^b_\mu A^c_\nu . \tag{2.8}$$

Equation (2.8) clarifies the difference between Abelian and non-Abelian gauge theories: In an Abelian symmetry group, the structure constants are all vanishing and the gauge field cannot interact with itself, such as for example in quantum electrodynamics. However, if the structure constants are non vanishing, we have a non-Abelian theory, and the theory allows for self-interactions of the gauge field. This becomes manifest in the last term, which gives rise to three and four gluon interaction vertices in the classical (Euclidean) action (2.9). Hence, in the case of a non-Abelian gauge theory, one can also leave out the quarks and consider the pure interactions of the gauge field, Yang-Mills theory,

$$S_{\mathrm{YM}}[A] = \frac{1}{4}\int_x F^a_{\mu\nu} F^a_{\mu\nu} = \frac{1}{2}\int_x \mathrm{tr}_f F^2_{\mu\nu} . \tag{2.9}$$

This is particularly interesting, since key features of $SU(2)$ and $SU(3)$ Yang-Mills theory are asymptotic freedom and confinement, whose qualitative effects translate to QCD. We briefly outline both features in Section 2.1.3 and Section 2.2.1. Moreover we investigate gluon condensation and its connection to confinement in Chapter 4, see also the related publication [2].

### 2.1.2. Quantisation and gauge fixing

After having established the basic ingredients of the classical action of a gauge theory in the previous section, we proceed with its quantisation. Unlike the fermionic quark field, we face immediate problems in the quantisation of virtual particles, due to double counting created by the gauge symmetry. We illustrate this by a consideration of the naive path integral of Yang-Mills theory,

$$\int \mathrm{d}A \exp\left(-S_{\mathrm{YM}}[A]\right) , \tag{2.10}$$

where integration over all configurations of the gauge field $A$ are is implied. Due to gauge invariance, many of these configurations are degenerate and introduce a redundancy to the counted degrees of freedom in the path integral. More precisely, every configuration belonging to a gauge orbit $\{A^V\}$, where $V$ is a transformation of the symmetry group, see (2.1), is physically equivalent and should only be counted once in the path integral. This means, that the Hilbert space $\mathscr{A}$ of all field configurations $A$ is too big and not physical. This is also reflected in the fact, that the naive two-point function is not invertible, since the canonically quantised conjugate momentum of $A_0$ is simply

$$\Pi^0 = \frac{\partial \mathscr{L}_{\mathrm{YM}}}{\partial \dot{A}_0} = 0 . \tag{2.11}$$

This redundancy can be removed by singling out an element of the gauge orbit $\{A^V\}$, which is achieved by introducing a gauge fixing condition $\mathscr{F}[A] = 0$. This gauge fixing condition might

suffer from the Gribov-ambiguity. That is, it might not be satisfied by any element of the gauge orbit, or it might be fulfilled by multiple elements, the Gribov copies. In this case, the problem is fixed by singling out a specific region [69], but we restrict ourselves to the assumption of a unique solution for now. The aim is now to reformulate the path integral from a simple integral over configurations in $\mathscr{A}$ to an integral over the physical space and an integral over all gauge transformations.

The integration over gauge transformations $V(x) = \exp(\mathrm{i}\alpha^a(x)t^a)$ and the gauge fixing condition are introduced to the path integral by insertion of a 1, following the procedure of Faddeev and Popov,

$$1 = \int \mathrm{d}\alpha(x)\delta(\mathscr{F}[A^\alpha])\det\left(\frac{\delta\mathscr{F}[A^\alpha]}{\delta\alpha}\right) \tag{2.12}$$

where,

$$(A^\alpha)^a_\mu t^a = \exp(\mathrm{i}\alpha^a t^a)\left[A^b_\mu t^b + \frac{\mathrm{i}\partial_\mu}{g_s}\right]\exp(-\mathrm{i}\alpha^c t^c)\,, \tag{2.13}$$

is the gauge field transformed by (2.6) using the definition of a gauge transformation in (2.1). Throughout this work, we mostly use variants of the generalised Lorentz gauge,

$$(\mathscr{F}[A])^a = \partial_\mu A^a_\mu - \omega^a(x)\,. \tag{2.14}$$

where $\omega^a$ is a Gaussian weight centered around 0, with some width $\xi$. This covariant gauge is convenient, since it does not single out a single spacetime direction. As long as the gauge fixing condition $\mathscr{F}[A]$ is linear, the functional derivative $\frac{\delta\mathscr{F}[A^\alpha]}{\delta\alpha}$ is independent of $\alpha$. We will make use of this property in the following.

Inserting (2.12) into the path integral (2.10) and performing the integration over gauge transformations $\alpha$ yields,

$$\int \mathrm{d}A\exp(-S_{\mathrm{YM}}[A]) = N(\xi)\int \mathrm{d}A_{\mathrm{gf}}\det\left(\frac{\delta\mathscr{F}[A^\alpha]}{\delta\alpha}\right)\exp\left(-S_{\mathrm{YM}}[A] - \frac{1}{2\xi}\int_x(\partial_\mu A^a_\mu)^2\right), \tag{2.15}$$

where we now integrate over the physically inequivalent configurations with the gauge fixed measure $\mathrm{d}A_{\mathrm{gf}}$. We remain with some normalisation factor $N(\xi)$ which stems from the Gaussian weighting. This factor drops out when considering general local and gauge invariant observables $\mathscr{O}$ since,

$$\langle\mathscr{O}\rangle = \frac{\int \mathrm{d}A\,\mathscr{O}[A]\exp(-S_{\mathrm{YM}}[A])}{\int \mathrm{d}A\exp(-S_{\mathrm{YM}}[A])} = \frac{\int \mathrm{d}A_{\mathrm{gf}}\det\left(\frac{\delta\mathscr{F}[A^\alpha]}{\delta\alpha}\right)\mathscr{O}[A]\exp\left(-S_{\mathrm{YM}}[A] - \frac{1}{2\xi}\int_x(\partial_\mu A^a_\mu)^2\right)}{\int \mathrm{d}A_{\mathrm{gf}}\det\left(\frac{\delta\mathscr{F}[A^\alpha]}{\delta\alpha}\right)\exp\left(-S_{\mathrm{YM}}[A] - \frac{1}{2\xi}\int_x(\partial_\mu A^a_\mu)^2\right)}\,. \tag{2.16}$$

The gauge fixing procedure also cures the inversion problem in the propagator and the vanishing covariant momentum alluded to in (2.11), since it effectively adds a $\frac{1}{2\xi}\int_x(\partial_\mu A^a_\mu)^2$ term to the classical action.

It remains to investigate the determinant in (2.15). Using the expression in (2.14) and the transformation (2.13) the derivative can be evaluated to,

$$\frac{\delta(\mathscr{F}[A^\alpha])^a}{\delta\alpha^b} = \frac{1}{g_s}\partial_\mu D^{ab}_\mu\,. \tag{2.17}$$

From this equation we can see that in a non-Abelian gauge theory, the Fadeev-Popov determinant introduces an interaction of the virtual particle. For an easier interpretation in terms of Feynman rules, this determinant is commonly represented as a functional integral over two artificial Grassman valued fields $c^a$ and $\bar{c}^a$ in the adjoint representation,

$$\det\left(\frac{1}{g_s}\partial_\mu D_\mu\right) = \int \mathrm{d}c\mathrm{d}\bar{c}\,\exp\left(-\int_x \bar{c}^a \partial_\mu D_\mu^{ab} c^b\right). \tag{2.18}$$

The coupling factor is usually absorbed into the ghost and anti-ghost fields $c$ and $\bar{c}$. The ghosts should be seen as a tool which fits nicely into the field formalism. Most importantly, as Grassman-valued Lorentz scalars, they do not agree with the spin-statistics theorem and should not be considered as particles, hence the name "ghosts".

From (2.18) we can infer the last contribution to the gauge fixed action of Yang-Mills theory, the ghost action,

$$S_{\mathrm{gh}}[A,c,\bar{c}] = \int_x \bar{c}^a \partial_\mu D_\mu^{ab} c^b\,. \tag{2.19}$$

We close the discussion of the quantisation and gauge fixing of Yang-Mills theory by addressing the manifestation of gauge invariance in the gauge fixed action. For a sensible quantisation of Yang-Mills theory a gauge fixing was introduced, which enables one to define covariant momenta and a propagator for the gauge field. In the process of gauge fixing, the gauge invariance is broken explicitly. However, we still require gauge invariance of physical observables which are computed from a gauge fixed action. To achieve this, the $n$-point correlation functions need to fulfil the *Slavnov-Taylor identities* (STIs) in non-Abelian gauge theories [70, 71]. The STIs follow by requiring that the effects from carrying out an arbitrary gauge transformation vanish from the path integral. While these relations encode all information of the gauge symmetry, the evaluation of the STIs requires the computation of expectation values and is no longer algebraic on a quantum level. In terms of the action, the remainders of gauge invariance in the gauge fixed theory are found in BRST-symmetry [72, 73]. The underlying transformation of BRST-symmetry is a combined transformation of the gauge field $A$, the gauge fixing and the ghosts $c, \bar{c}$ and gives a precise relation between the ghosts, anti-ghosts and the unphysical polarisation states of the virtual particles (gluons). It is a continuous symmetry and is thus, by Noether's theorem, linked to a conserved BRST-charge $Q$. The conservation of $Q$ is then used to construct the physical Hilbert space, similarly to the physical photon polarisations obtained from the Gupta-Bleuler formalism in QED.

A rigorous proof of the existence of Yang-Mills theory remains one of the unsolved Millennium problems to this day [74]. To our current knowledge there is no proof following the axioms put forward in [75] or [76, 77] of the existence of Yang Mills theory on a four dimensional Euclidean spacetime and its mass gap, which we comment on in Section 2.2.1.

The gauge fixed QCD action consists of the classical actions for the quarks (2.7) and gluons (2.9), as well as the ghost action (2.19) and the gauge fixing term yielding,

$$S_{\mathrm{QCD}} = \int_x \left\{\bar{\psi}(\not{D} + m_q)\psi + \frac{1}{4}F^a_{\mu\nu}F^a_{\mu\nu} + \bar{c}^a\partial_\mu D^{ab}_\mu c^b + \frac{1}{2\xi}(\partial_\mu A^a_\mu)^2\right\}. \tag{2.20}$$

The fermionic part of the action implies summation over all $N_c = 3$ colors, as well as $N_f = 6$ flavors which are given by the different quark species up, down, strange, charm, beauty and top (u,d,s,c,b,t). The quark mass $m_q$ term changes for different species. This is important, since the

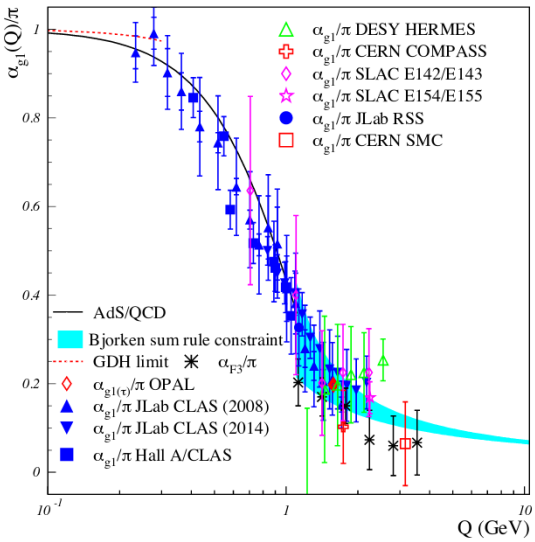


Figure 2.1.: Running coupling $\alpha_s$ of QCD as a function of scattering momentum transfer $Q$. The figure was taken from [79] and is using experimental data from [80–86].

heavy quark flavors (c,b,t) do not contribute to the dynamics in the infrared. Most applications in the low energy sector of QCD therefore omit the heavy quark flavors ($m_q > 1$ GeV) and focus the three lighter quarks. The current quark masses of the up and down quark are very small $m_u = 1.8 - 2.8$ MeV and $m_d = 4.3 - 5.2$ MeV even in comparison to the next lightest quark, the strange quark with $m_s = 92 - 104\,\text{MeV}$ [78]. Therefore, model computations often use a $N_f = 2$ symmetric model considering up and down quarks or a $N_f = 2+1$ computation which adds the strange quark [51]. We discuss low energy effective theories of QCD in Section 2.3, after having discussed some more general aspects of the theory.

### 2.1.3. Asymptotic freedom

At quantum level, the scale invariance of a classical theory is broken by the appearance of a renormalisation scale $\mu$ in the couplings. The renormalisation scale is fixed by the renormalisation conditions, which are in principle arbitrary, but are usually physically motivated and allow to directly interpret the results. The scale dependence of QCD shows in the running gluonic coupling $\alpha_s$, which is depicted as a function of scattering momentum transfer in Figure 2.1. As we can see from the figure, this effect is accessible both theoretically and from experiment.

Since the renormalisation scale $\mu$ is not a physical quantity in itself, the renormalised connected correlation functions $G_n(x_1,\dots,x_n) = \langle \Phi_i(x_1)\dots\Phi_j(x_n)\rangle|_{\text{conn.}}$, where the $\Phi_i$ are components of the superfield $\Phi = (A_\mu, \bar{c}, c, \bar{q}, q)$, cannot depend on it. Still, the $G_n$ depend on renormalised masses and couplings, which in turn depend on the renormalisation scale $\mu$. Hence, all these $\mu$ dependencies must cancel out in the correlation functions. This necessity is captured by the *Callan-Symanzik* or *renormalisation group equation*,

$$\left(\mu\partial_\mu + \beta^{(\mu)}_{\lambda_i}\partial_{\lambda_i} + n_j\gamma^{(\mu)}_{\Phi_j}\right)G_n = 0\,. \tag{2.21}$$

where we sum over all couplings and masses $\lambda_i$, as well as (super)-fields $n = (n_1,\dots)$. The $\beta$-functions are given by, $\beta^{(\mu)}_{\lambda_i} = \mu\partial_\mu\lambda_i$ as well as the rescaling of the fields $\gamma^{(\mu)}_{\Phi_j} = \frac{\mu}{2}\partial_\mu \log Z_{\Phi_j}$.

From the Callan-Symanzik equation (2.21), one can compute the $\beta$-function perturbatively to a given loop order by inserting the corresponding expressions for given $G_n$.

The one-loop $\beta$-function of the gauge coupling for a $SU(N_c)$ gauge theory with $N_f$ quark flavors follows as,

$$\mu\partial_\mu\alpha_s = (2N_f - 11N_c)\frac{\alpha_s^2}{6\pi}, \tag{2.22}$$

where the renormalisation scale was identified with the energy scale $\mu$. In the case of QCD at high energies $\mu$, the running is negative, since $N_c = 3$ and $N_f = 6$. This implies, that the (positive) gauge coupling decreases with increasing energies, and that $\alpha_s \to 0$ for $\mu \to \infty$. This effectively shuts off all interactions and the quarks and gluons become free particles in the ultraviolet, which is called *asymptotic freedom*. On the contrary, the gauge coupling increases with decreasing energy scale $\mu$. Once $\alpha_s > 1$ perturbation theory no longer works and we enter a strongly correlated, non-perturbative regime requiring non-perturbative methods which are expanded on in Chapter 3.

We can conclude from this discussion, that QCD behaves vastly different across different energy scales, making for a rich phase structure across finite temperatures and particle densities.

## 2.2. Phases of QCD

For an investigation of QCD phases, and later the phase structure, we take a look at the symmetries of the QCD action (2.20): Firstly, we have the $SU(N_c)$ gauge symmetry and secondly we have an additional, approximate symmetry of the fermions, called *chiral symmetry*. This symmetry arises in the limit of massless light quarks, the *chiral limit*, where QCD displays a global $U(N_f)_L \times U(N_f)_R$ flavor symmetry. Even though *chiral symmetry* is not realised in nature, due to the small current quark masses, it is a reasonable approximation for the two light quarks ($N_f = 2$) and for some applications also the three lightest quarks ($N_f = 3$).

The (spontaneous) breaking of $SU(N_c) \times U(N_f)_L \times U(N_f)_R$ at low temperatures and particle densities describes two interesting phenomena. Firstly, whereas high energy QCD describes a theory of free quarks and gluons, low energy QCD shows an interesting feature: all color charges seem to be confined to composite, color-neutral particles. Secondly, the process of spontaneous chiral symmetry breaking, accounts for a significant mass generation in bound states near the vacuum. Here we find that the current quark masses only account for $\approx 1\%$ of the total mass of the nucleons.

### 2.2.1. Confinement

Broadly speaking, color confinement is the phenomenon that color charged particles only appear within composite particles and do not appear as asymptotic states. To date there is still no rigorous proof of confinement or an explanation that is generally agreed upon [87]. However, there are signatures of confinement in terms of order parameters and varying confinement scenarios that we address in the following.

Let us consider pure Yang-Mills theory with static quark sources in a simplified setting. Here, we can describe the confinement effect in terms of a free energy/potential $V_{\bar{q}q}$ between a static quark and anti-quark pair as a function of their distance $r$. At large energies, where the coupling is small and the theory perturbative, a Coulomb-type potential is expected. At small energies

however, confinement is reflected in the linear potential between the quark-anti-quark pair when pulled apart, to wit

$$\lim_{r\Lambda_{\mathrm{QCD}}\to 0} V_{\bar{q}q}(r) \propto \frac{1}{r}\,, \quad \text{and} \quad \lim_{r\Lambda_{QCD}\to\infty} V_{\bar{q}q}(r) \propto \sigma r\,. \tag{2.23}$$

where $\Lambda_{\mathrm{QCD}}$ is the confinement scale and $\sigma$ the string tension. Equation (2.23) implies a constantly growing force between a separating quark pair. In fact, completely separating a quark pair would require an infinite amount of energy, which is more than simply creating a new quark-anti-quark pair from vacuum. Hence, we chose to consider a static quark-anti-quark pair, where such a process cannot take place. In the case of dynamical quarks, such as for example in collider experiments, one finds many color neutral particles instead of single colored particles as a result of so called *string breaking*. The additionally created quark-anti-quark pairs shield the color force of the original pair and lead to a levelling off of the potential $V_{\bar{q}q}(r)$ at finite $r$.

The static potential $V_{\bar{q}q}(r)$ can be computed from the Wilson line, which describes a quark-anti-quark pair in the infinite quark mass limit, that is created, separated to a distance $r$ and annihilated at some later time along a world-line $\mathscr{C}_r$. The Wilson loop is given by,

$$\left\langle \mathrm{tr}\,\mathscr{P}\exp\left\{ i\oint_{\mathscr{C}_r} dx_\mu A_\mu \right\} \right\rangle \propto \exp\left(-V_{\bar{q}q}(r)\right), \tag{2.24}$$

where $\mathscr{P}$ is the path-ordering operator and $\oint_{\mathscr{C}_r}$ denotes the integration along the world-line $\mathscr{C}_r$. The main idea behind (2.24) is the construction of a *parallel transporter* of gauge transformations, which allows to define gauge invariant correlation functions of fermionic fields. At finite temperature, this idea can be transferred to an integration over two loops in the periodic imaginary time direction, for more details on the finite temperature formalism see Appendix B.1. This defines the Polyakov loop in finite temperature Yang-Mills theory,

$$L = \frac{1}{N_c}\mathrm{tr_f}\,\mathscr{P}\exp\{ig_s\oint A_0(x)\}\,, \tag{2.25}$$

where the integral $\oint$ is now over $x_0 \in [0, 1/T]$ and $T$ denotes the temperature. The expectation value of the Polyakov loop $\langle L\rangle$ is commonly used as an order parameter for quark confinement, to wit,

$$\langle L\rangle = \begin{cases} 0\,, & \text{confining phase}\,, \\ \neq 0\,, & \text{deconfining phase}\,. \end{cases} \tag{2.26}$$

Most notably, $\langle L\rangle$ is not invariant under the center symmetry $Z_{N_c}$ of the gauge group with $L \to z\,L$ and $z \in Z_{N_c}$, whereas the Yang-Mills action is. This symmetry can be restored by averaging over the symmetry group, see Appendix B.2.1. To conclude, the Polyakov loop expectation value links the confinement-deconfinement phase transition to the spontaneous breaking of center symmetry of the gauge group.

Quark confinement can linked to gluon confinement by computing the Polyakov loop potential from gauge dependent Greens functions of the gluonic (background) field [88, 89]. In this way, it can be related to the Kugo-Ojima [90] and Gribov-Zwanziger [69, 91] confinement scenarios. Since this work mostly focusses on variants of the Lorenz gauge and the Gribov-Zwanziger

scenario considers the Coulomb gauge, we refer its discussion to the above literature. Kugo and Ojima formulate a confinement criterion for the wave function renormalisation factors/dressing functions of the gauge boson in the Lorenz gauge. Using the conservation of BRST charge in physical states they found that the absence of colored particles requires the gluon propagator to develop a mass gap, that is,

$$m_{\text{gap}}^2 = p^2 Z_A^\perp(p)|_{p^2\to 0} > 0\,, \tag{2.27}$$

where $Z_A^\perp$ is the transverse part of the gluon dressing function, see (4.34). Traces of this mass gap can be found in the correlation functions in the infrared momentum region and are formulated in terms of the leading momentum behaviour of the dressing functions of the gluon and ghost, respectively,

$$Z_A^\perp(p^2\to 0) \simeq \left(p^2\right)^{\kappa_A}\,, \quad \text{and} \quad Z_c(p^2\to 0) \simeq \left(p^2\right)^{\kappa_C}\,, \tag{2.28}$$

their exact definition follow from the two-point function and we refer to (4.34) and (4.44) in Chapter 4, where investigate gluon-condensation as a potential mechanism for the creation of a mass-gap.

The exponents $\kappa_A$ and $\kappa_C$ distinguish between different infra-red solutions, consistent with renormalisation group invariance [92]. They differ by an infrared boundary condition for $Z_C(0)$. For the boundary condition $Z_C(p^2\to 0)\to 0$ there is a unique *scaling solution* [93, 94], which is characterised by the sum rule $0 = \kappa_A + 2\kappa_C + (4-d)/2$, where $d$ is the spacetime dimension. Even though the precise value of these parameters may value for specific choices of truncations and method, most functional approaches use,

$$\kappa_A \approx -1.19\,, \quad \text{and} \quad \kappa_C \approx 0.595\,, \tag{2.29}$$

see e.g. [95]. These results allow the aforementioned confinement scenarios of Kugo-Ojima and Gribov-Zwanziger.

Another set of exponents is given if we ask for finite $Z_C(0)$. Then (2.27) goes to a constant in the infrared. This solution is named *decoupling solution*, since the gluon decouples from the dynamics as would a massive particle [92, 96]. In this case, the scaling exponents are given by,

$$\kappa_A = -1\,, \quad \text{and} \quad \kappa_C = 0\,. \tag{2.30}$$

Both approaches only differ in the deep infrared and are suspected to be linked to different resolutions of circumventing the occurrence of Gribov copies [92].

### 2.2.2. Chiral symmetry (breaking)

In the process of constructing the Lorentz invariant representation of *Dirac fermions*, another possible symmetry of (massless) fermionic theories becomes apparent. This is most obvious in the *Weyl* or *chiral* representation of the *Dirac algebra*, where the four-dimensional generators of Lorentz boosts and rotations are block diagonal. This hints at the *reducibility* of the Lorentz group and the (four-dimensional representation of the) fermionic field $\psi$. In fact, $\psi$ can be understood in terms of two (two-dimensional) objects $\psi_L$ and $\psi_R$, the left-handed and right-handed *Weyl spinors* respectively,

$$\psi = \begin{pmatrix} \psi_L \\ \psi_R \end{pmatrix}. \tag{2.31}$$

At vanishing fermionic mass, the *chiral limit*, the dynamics of the left-handed and right-handed blocks decouple completely. Thus in a massless fermionic gauge theory, the left-handed and right-handed components can be rotated separately in flavor-space. In the case of $N_f$ massless fermionic flavors, the action is symmetric under left- and right-handed unitary flavor transformations $U(N_f)_L \times U(N_f)_R$. These transformations can be divided further into *vector*-symmetries, which treat left- and right handed parts equally, as well as *axial*-symmetries, which do not.

At this point, we simplify the discussion by setting $N_f = 2$, which we use throughout this work. The $N_f = 2$ flavor case corresponds to the two lightest quarks $u$ and $d$, which are massless in good approximation. Heavier quark flavors decouple from the dynamics at low energies.

The flavor rotation symmetry is now written in terms of vector and axial components $U(1)_V \times U(1)_A \times SU(2)_L \times SU(2)_R$. The $U(1)_A$ symmetry is broken anomalously by non-trivial topological effects of the gauge field and is phenomenologically relevant in the three flavor case to explain $\eta - \eta'$ mixing in the mesonic mass spectrum [97–99]. For the purpose of this work, we drop this symmetry. The $U(1)_V$ symmetry is linked to baryon number conservation and can spontaneously be broken and finally the remaining $SU(2)_L \times SU(2)_R$ symmetry is called *chiral symmetry*.

At high temperatures and/or particle densities chiral symmetry is approximately realised and only hampered by the small current quark masses. Near the vacuum, however, chiral symmetry is spontaneously broken by the formation of a quark-antiquark condensate,

$$\langle \bar{q} q \rangle = \langle \bar{q}_L q_R + \bar{q}_R q_L \rangle \,, \tag{2.32}$$

in which the mixing of handedness becomes apparent. In the process of spontaneous symmetry breaking the $SU(2)_L \times SU(2)_R$ is broken to a remaining $SU(2)_V$ symmetry called isospin. The Goldstone bosons of this process form an isospin triplet and are given by the pions $(\pi^+, \pi^0, \pi^-)$. Since the original chiral symmetry is only approximate, due to the small current quark mass, the physical scenario predicts pseudo-Goldstone bosons with massive pions. Before discussing low energy effective models for chiral symmetry breaking in Section 2.3, we close with a remark on the $N_f = 3$ case, which also takes the strange quark into account. Here, the flavor symmetry is spontaneously broken, such that only the $SU(3)_V$ symmetry remains. The Goldstone bosons form an octet of mesons with spin 0, comprising the three pions, as well as the Kaons $(K^0, K^+, K^-, \bar{K}^0)$ and $\eta$ mesons. Additionally to the quark-anti-quark condensate, spontaneous chiral symmetry breaking also comprises the formation of baryons, where the $U(1)_V$ symmetry is broken additionally.

## 2.3. Low energy effective theories of QCD

*This subsection is based in parts on [1].*

Within functional QCD low energy effective theories (LEFT) of bound states emerge naturally from the momentum scale flow of the theory at momentum or cutoff scales $k \lesssim 1\,\text{GeV}$, [42, 44, 45, 48, 51, 59, 102, 103]. In this regime, the gluonic degrees of freedom decouple from the dynamics due to the gluonic mass gap in QCD, for a detailed discussion see [48, 51, 104].

We have seen in Figure 2.1, that the strong coupling $\alpha_s$ increases towards lower energy scales. This increase of $\alpha_s$ translates into two gluon exchange diagrams generating effective four-quark interaction channels as $\Gamma^{(4)}_{\bar{q}q\bar{q}q,k} \propto \alpha^2_{k,s}$. In general, all possible interaction channels, which are

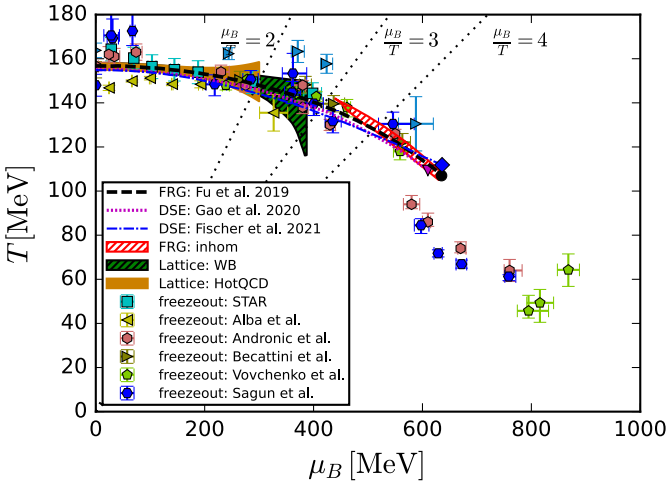


Figure 2.2.: QCD phase structure computed from functional methods, with a range of validity $\mu_B/T(\mu_B) \lesssim 4$ of the low energy description in terms of quark-meson interactions. The figure is taken from [51], with additional data from [100, 101].

allowed by the $SU(N_c) \times U(1)_V \times SU(2)_L \times SU(2)_R$ symmetry, are generated. The interaction strength of particular channels can diverge at some place in the phase diagram, hinting at a condensation process and the formation of a bound state. These bound states introduce new dynamic degrees of freedom, which can be captured by bosonising the four-quark channel using a Hubbard-Stratonivich transformation [105, 106], for a discussion of the emergent LEFT see [103].

In the following, we discuss the validity and emergence of LEFTs in the context of the QCD phase structure Section 2.3.1, and introduce the basic formalism for the most important one: the quark-meson model in Section 2.3.2.

### 2.3.1. Emergent LEFTs and their range of validity

The key ingredient for the emergence of LEFTs is the scale-dependent four-quark scattering, whose dynamics at large momentum scales is driven by a box diagram with a two-gluon exchange between quark currents. This box-diagram is represented using a (Fierz-)complete basis of tensor structures of the allowed $SU(N_c) \times U(1)_V \times SU(2)_L \times SU(2)_R$ symmetry. For the discussion of its low-momentum behaviour we restrict ourselves to the momentum-independent tensor structures, that is 10 tensor structures in $N_f = 2$ flavor QCD and 28 (32) tensor structures in $N_f = 3$ flavor QCD, the relevant cases for the discussion of the phase structure of QCD. It has been shown in [44, 48] that in the vacuum the scalar-pseudoscalar channel is dominating the dynamics by far, both above and below the chiral symmetry breaking scale of $k \approx 500\,\text{MeV}$: switching of all other channels leads to negligible effects for most physical observables. Moreover, in [64] is has been shown for $N_f = 2$-flavor QCD in the chiral limit, that qualitatively this dominance persists up to large densities or chemical potentials, $\mu_B/T_c(0) \approx 6$, where $T_c(\mu_B)$ is the chiral crossover or phase transition temperature at a given baryon chemical potential $\mu_B$. This highly interesting first dominance study in QCD is based on qualitative approximations, and a conservative error estimate leads us to $\mu_B/T_c(0) \lesssim 4-8$ for the (total) dominance regime of the scalar-pseudoscalar channel.

This supports the computations in [51], where the phase structure of 2- and 2+1-flavor QCD was computed within a one-channel approximation (scalar-pseudoscalar) to the Fierz-complete tensor structure for $\mu_B/T(\mu_B) \lesssim 4$, see Figure 2.2. Then, dynamical hadronisation takes into account multi-scattering events of the resonant channels (multi-scatterings of pions and the scalar $\sigma$-mode) that are relevant for the critical dynamics in a regime with second or first order transitions, which is the model we introduce in Section 2.3.2. In summary we estimate the reliability regime of the present approximations in functional QCD (see also respective considerations in DSEs ( [19, 56, 100]) to be

$$\mu_B/T(\mu_B) \lesssim 4\,. \tag{2.33}$$

The critical end point (CEP) computed both within the most recent fRG-computations, $\mu_B/T(\mu_B) = 5.59$ from [51] and DSE, $\mu_B/T(\mu_B) = 5.54$ from [100], for the physical case of 2+1-flavor QCD agree well, which sustains the respective reliability of these estimates. Still it is not within the regime of quantitative reliability of the current approximation.

Consequently, (2.33) entails that for a quantitatively sound prediction of the CEP the current approximation to the full first principle QCD-flow has to be improved systematically in two directions for chemical potentials $\mu_B/T(\mu_B) \gtrsim 4$: Firstly, we need to include at least the dominant tensor structure at large densities, the color-superconducting (csc) - or diquark-channel. This extension will be considered elsewhere. Secondly, the self-consistent computation of the order parameter potential set-up in [25] is required. This is done in the present work within a recently developed numerical approach that also allows the inclusion of the formation and propagation of shocks [65].

### 2.3.2. The quark-meson model

The quark-meson model is a Nambu–Jona-Lasinio (NJL)-type model, describing an effective theory of quark and meson interactions constructed from fermions with chiral symmetry. A similar example of an effective theory is used to describe the formation of Cooper pairs from electrons in the BCS theory of superconductivity. In the following, we briefly recapitulate the fRG-approach to the (Polyakov-enhanced) quark-meson model (QM model). The inclusion of the dynamical mesons as low energy effective degrees of freedom has to be seen as an efficient and convenient book-keeping device for the respective resonant interaction channels. In particular, this substitutes the rather tedious inclusion of the resonant parts of the higher-order scattering processes of quarks. Still, if used on a quantitative level, even for large UV-cutoff scales its effective action does not reduce to a simple local classical actions. For more details and in particular its quantitative properties as an emergent low energy theory in QCD we refer to [44, 45, 48, 51]. Validity checks, benchmarks and bounds in comparison to QCD have been provided in [103].

The key ingredient to the QM model is the scalar-pseudo scalar four-quark channel, which is given by

$$\mathscr{L}^{(S-P)}_{(q\bar{q})^2} = -\frac{\lambda^{(S-P)}}{2} Z_q^2 [(\bar{q}\tau^0 q)^2 - (\bar{q}\gamma_5 \boldsymbol{\tau} q)^2]\,, \tag{2.34}$$

where $\tau^0 = \mathbb{1}/\sqrt{2N_f}$ and $\boldsymbol{\tau}$ are the normalized generators of flavor $U_f(1)$ and $SU_f(N_f)$ in the fundamental representation, respectively. $\lambda^{(S-P)}$ is coupling of the $(S-P)$ channel and $Z_q$ the quark wave function renormalisation. During the formation of bound states $\lambda^{(S-P)}$ diverges. This resonance is directly connected to the formation of mesons, as dynamical

degrees of freedom, which can be captured in an auxiliary field $\phi \propto \bar{q}\tau q$. The auxiliary field $\phi$ is introduced to the action via an exact transformation of the fermionic generating functional, a Hubbard-Stratonivic transformation,

$$\int \mathscr{D}\phi \exp\left\{-\int_x \left[\frac{1}{2}m^2\phi^2 + h\bar{q}(\tau\cdot\phi)q\right]\right\} = \int \mathscr{D}\phi \exp\left\{-\int_x \left[\frac{1}{2}\left(m\phi + \frac{h}{m}\bar{q}\tau q\right)^2 - \frac{h^2}{2m^2}(\bar{q}\tau q)^2\right]\right\} = \mathscr{N}\exp\left\{\int_x \left[\frac{h^2}{2m^2}(\bar{q}\tau q)^2\right]\right\}, \tag{2.35}$$

where $\mathscr{N}$ is the remaining Gaussian integral, which is just a number and drops in the normalisation. By identifying $\lambda^{(S-P)} = \frac{h^2}{m^2}$, we find that the $(S-P)$ channel can be rewritten as a mass term and coupling to the gluons of the auxiliary field. By varying $\phi$ in the first term in (2.35), we find that on a classical level $\phi = \frac{h}{m^2}\bar{q}\tau q$, which manifests the structure of $\phi$ as a quark bilinear.

For a representation of $\phi$ in the $N_f = 2$ case, we make use of the equivalence of $SU(2)_L \times SU(2)_R \cong SO(4)$ to implement chiral symmetry in the mesonic fields. The simplest representation of the meson fields is thus the $O(4)$-vector,

$$\phi = (\sigma, \boldsymbol{\pi})^t, \tag{2.36}$$

where $\sigma$ corresponds to the scalar sigma meson and $\boldsymbol{\pi}$ to the pseudo-scalar pions. The pions form an isospin triplet and correspond to the $SU(2)_V \cong SO(3)$ symmetry, which is not broken. A convenient order parameter for chiral symmetry breaking is thus given by the expectation value of the sigma meson $\langle\sigma\rangle$.

The chiral phase transition of the QM model, and by extension two flavor QCD, therefore lies in the O(4) universality class. Moreover, the dynamics that drive chiral symmetry breaking are determined by the mesonic field $\phi$, whereas the fermions only contribute via the fermionic determinant. This explains also our interest in $O(N)$ models in general: not only are they a good testing ground for our methods, but they also provide information about the critical behaviour of the theory.

We continue by defining the chiral invariant $\rho$, which is given by,

$$\rho = \frac{1}{2}\phi^2 = \frac{1}{2}(\boldsymbol{\pi}^2 + \sigma^2). \tag{2.37}$$

All interactions are indicated in terms of $\rho$ which ensures the chiral symmetry of the ansatz. Finally, the UV action of the two flavor Quark-Meson model at finite temperature $T$ and quark density $\mu_q = \mu_B/3$ is given by

$$S_{\text{UV}}[q,\bar{q},\phi] = \int_x \left\{\bar{q}\left[\partial\!\!\!/ + h_\sigma(\tau_0\sigma + \boldsymbol{\tau}\boldsymbol{\pi}) - \gamma_0\mu_q\right]q + \frac{1}{2}\left(\partial_\mu\phi\right)^2 + V_{\text{UV}}(\rho) - c_\sigma\sigma\right\}, \tag{2.38a}$$

and the spatial integration at finite temperature reads

$$\int_x = \int_0^{1/T} dt \int d^3x\,, \qquad \int_p = T\sum_{n\in\mathbb{Z}}\int \frac{d^3p}{(2\pi)^3}\,. \tag{2.38b}$$

We have also introduced the corresponding momentum integration, $\int_p$, for a detailed derivation of the finite temperature and density formalism see Appendix B.1. The classical potential $V_{\text{UV}}(\rho)$ includes the mesonic mass term and a $\phi^4$ interaction,

$$V_{\text{UV}}(\rho) = m_\phi^2\,\rho + \frac{1}{2}\lambda_\phi\,\rho^2\,, \tag{2.38c}$$

where the $\phi^4$ term already introduces local higher order quark scatterings. We have also introduced an explicit symmetry breaking term $c_\sigma$, which is linked to a finite quark mass $m_q$ at the level of the UV action. This mass exists in QCD, see (2.20), where we have small current quark masses for the up and down quarks. The term $\int_x \bar{q} m_q q$ can be removed by a redefinition of the field

$$\sigma \to \sigma - \frac{m_q}{h}\,. \tag{2.39}$$

which results in the linear term with

$$c_\sigma = m_\phi^2 \frac{m_q}{h}\,. \tag{2.40}$$

This term turns the pions from formerly massless Goldstone-bosons into pseudo-Goldstone bosons and accounts for a small pion mass.

In its most general form, this ansatz for the quantum effective action comprises $\rho$ and momentum dependent wave function renormalisations $Z_q$ and $Z_\phi$, as well as a $\rho$-dependent effective potential $V(\rho)$ and Yukawa coupling $h(\rho)$. Since the full field and momentum dependence of this ansatz is very extensive, we will use various approximations and discuss their validity in the following chapters.

# CHAPTER 3

# The functional renormalisation group

In the previous chapter we discussed the classical action of Quantum Chromodynamics. In particular, we found that, like most quantum field theories, QCD behaves vastly different at differing energy scales, recall Figure 2.1. The scale dependence of masses and couplings arises from self-interactions: For example in quantum electrodynamics an electron adds to its effective mass by emitting and reabsorbing a photon. Similarly, the bare quark masses and couplings change with energy scale and the theory needs to be *renormalised*.

Depending on the strength of interaction, we can differentiate between perturbative and non-perturbative regimes: if the couplings strength $\alpha_s \ll 1$, a perturbative expansion in the coupling will converge and we can renormalise by introducing the appropriate counter terms. However, this is not the case for QCD, where $\alpha_s > 1$ at low energies and we reach a non-perturbative regime below $\approx 1\,\text{GeV}$. The most prominent approach to compute observables in strongly correlated, non-perturbative systems is the lattice [107–109]. Lattice QCD simulations yield quantitative ab initio results in the vicinity of the finite temperature axis, but face the sign problem at higher baryon densities [110]. For a discussion of the QCD phase diagram using lattice methods see [111] and for recent developments see e.g. [32–35, 37, 112–114].

Functional methods stand in contrast with and in addition to the lattice. The sign problem does not affect functional methods and computations reach up to arbitrarily high densities. However, to reduce the amount of complexity in order to solve the functional equations, one needs to chose an approximation/truncation. On one side, this enables us to test which vertices or dependences are negligible, since they can be readily switched off. On the downside, one always computes in an approximation and might obtain apparent convergence whilst neglecting important effects. We expand on systematic expansion schemes and error estimates in Section 3.2.2. Thus within functional QCD, we aim at reliably reproducing lattice results at low densities, see Figure 2.2, whilst making new predictions in the high density regime where the critical endpoint is located. For recent works within with Dyson-Schwinger equations (DSE) see e.g. [19, 26, 53, 55, 56, 100, 115]. For recent results within the functional renormalisation group (fRG) see e.g. [50, 51, 64, 104, 116–120].

In the following, we introduce our functional method of choice, the functional renormalisation group (fRG). The fRG uses renormalisation group transformations to establish a link between different scales of a theory, usually those are momentum scales. The change with the so called

RG-scale is then tracked in a differential formulation, which we expand on in Section 3.2, after introducing the functional formulation in Section 3.1. We close this chapter with a discussion of RG-flows in terms of general RG reparametrisations in Section 3.3, which we use to expand the functional flow to a complex setting in Chapter 6 or for a dynamical field definition in Chapter 7. The fRG can also be used in a real time setting in form of the Callan-Symanzik flow, whose derivation we outline in Section 3.4. In summary, the fRG is a convenient tool to track QCD observables from high energies, where we have an essentially free theory, to a strongly correlated regime!

## 3.1. Generating functionals

*This section is based in parts on [4] and [3].*

Following the previous section, we use an Euclidean field theory approach with imaginary time. In an attempt to keep this derivation as general as possible we use the super-field formalism with the (super) field $\Phi = (\Phi_1, ...\Phi_n)$ containing all fields. For example, in an $O(N)$ theory we have $\Phi = (\phi_1, ..., \phi_N)$. In QCD, the super field is given by, e.g., $\Phi = (A_\mu, c, \bar{c}, q, \bar{q})$ with gluons $A_\mu$, ghosts $c, \bar{c}$, and quarks $q, \bar{q}$. Accordingly, all other quantities are given in terms of vectors and matrices corresponding to the indices of the super field.

The starting point of our analysis is the path integral or partition function of the theory, $Z[J]$, with the current $J = (J_1, ..., J_n)$ and the fundamental quantum fields $\varphi = (\varphi_1, \dots, \varphi_n)$. All correlation functions in a Euclidean field theory can be obtained from this generating functional. It is defined by its derivatives,

$$\langle \varphi_{i_1}(x_1) \dots \varphi_{i_n}(x_n) \rangle_J = \frac{1}{Z[J]} \frac{\delta^n Z[J]}{\delta J_{i_1}(x_1) \dots \delta J_{i_n}(x_n)}, \tag{3.1}$$

which are the full normalised correlation functions including their disconnected parts. Additionally, it also has a (formal) path integral representation,

$$Z[J] = \frac{1}{\mathcal{N}} \int [d\varphi']_{\text{ren}} \exp\left( -S[\varphi'] + \int_x J \cdot \varphi' \right), \tag{3.2}$$

where $S$ is the classical action, $\int_x = \int d^d x$ implies integration over $d$ Euclidean space-time dimensions and $\mathcal{N}$ a normalisation factor that drops out in the computation of correlation functions, see (3.1). $[d\varphi']_{\text{ren}}$ the renormalised field measure. In principle this explicit form of the generating functional is not needed for the formalism. The key assumption is that the path integral exists and its functional derivatives are finite. However, the formulation using the generating functional will be quite helpful in illustrating the transition between classical and quantum regimes by means of the flow equation in the following.

While the generating functional $Z[J]$ in (3.2) generates the full correlation functions (3.1) including their disconnected parts, its logarithm,

$$W[J] = \log Z[J], \tag{3.3}$$

generates the full connected correlation functions,

$$\langle \varphi_{i_1}(x_1) \dots \varphi_{i_n}(x_n) \rangle_J^{(c)} = \frac{\delta^n W[J]}{\delta J_{i_1}(x_1) \dots \delta J_{i_n}(x_n)}, \tag{3.4}$$

for a given background current $J$. Here, the superscript refers to the connectedness.

Equation (3.4) includes the external propagators. They can be amputated by using a current $J = S^{(2)}\varphi$, that is proportional to the classical dispersion,

$$S^{(2)}[\varphi_0] = \frac{\delta^2 S}{\delta \varphi^2}[\varphi_0], \tag{3.5}$$

At some (background) field configuration $\varphi_0$ This leads us to,

$$S_{\text{eff}}[\phi] = -W[J = S^{(2)}\phi], \tag{3.6}$$

which defines the Wilsonian effective action and is the generating functional of amputated connected correlation functions. In (3.6) we have suppressed the background $\varphi_0$. For scalar theories it is typically chosen to be the vanishing background, $\varphi_0 = 0$. Derivatives w.r.t. $\phi$ lead to (3.4), where each field is multiplied by $S^{(2)}$, thus removing the classical external propagators. Moreover, the external current $J$ is now expressed in terms of a background mean field $\phi$.

Finally, one-particle irreducible (1PI) correlation functions are generated by the Legendre transform of the Schwinger functional, the effective action $\Gamma[\Phi]$,

$$\begin{aligned}\Gamma[\Phi] &= \sup_J \left[ \int_x J \cdot \Phi - W[J] \right] \\ &= -\ln\left[ \int [d\varphi']_{\text{ren}} \exp\left( -S[\Phi + \varphi'] + \int_x \varphi' \frac{\delta \Gamma[\Phi]}{\delta \Phi(x)} \right) \right].\end{aligned} \tag{3.7}$$

where $\Phi = \langle \varphi \rangle$ is now the mean (super-)field. With this transformation, the degree of redundancy on the correlation functions is decreased by removing those, that can be cut into correlation functions of the same order. This includes for example successive repetitions of the same diagram. The 1PI connected correlation functions read,

$$\langle \varphi(x_1) \dots \varphi(x_n) \rangle_\Phi^{(\text{1PI})} = \Gamma^{(n)}[\Phi]. \tag{3.8}$$

All generating functionals, (3.2), (3.3), (3.7), carry the full information about the theory under investigation with a decreasing degree of redundancy. Importantly, their functional flow equations, which we derive in Section 3.2, constitute different general diffusion equations with different properties. This proves advantageous in various applications, since for example, the effective action is convex by its definition as a Legendre transformation which can create numerical problems if violated.

By taking a functional derivative with respect to one of the fields $\Phi_i$ of (3.32) we obtain the one-point function,

$$\frac{\delta \Gamma[\Phi]}{\delta \Phi_i(x)} = J_i(x)|_{J = J_{\text{sup}}}. \tag{3.9}$$

At vanishing background $J = 0$, (3.9) gives the quantum equations of motion (EOM) in analogy to the classical equations of motion $\frac{\delta S[\Phi]}{\delta \Phi_i(x)} = 0$.

We note further, that the propagator is given by the full connected two-point correlation function, which is also the inverse of the 1PI two-point function $\Gamma^{(2)}$,

$$G = W^{(2)} = \frac{1}{\Gamma^{(2)}}, \tag{3.10}$$

which can be understood as a series expansion of the 1PI two-point correlator.

## 3.2. The 1PI flow equation and expansion schemes

We derive the flow of the 1PI generating functional, the Wetterich flow, in Section 3.2.1. The 1PI formulation is used as an example, since it carries the smallest degree of redundancy and is closely connected to the classical action. Consequently, it is most commonly used in applications. We will focus on more general formulations of the RG equations and their benefits in later sections. We close this section by discussing expansion schemes and systematic errors of the functional equations and their applicability to QCD in Section 3.2.2.

### 3.2.1. The functional renormalisation group equation

We have already seen the main idea behind the *renormalisation group* in the *renormalisation group equation* (2.21), which expresses the scale dependence on a scale $\mu$ of a given quantum theory through a differential equation. This is a consequence of the group property: as $\mu$ varies, the theory is given by a self similar replica of itself and can be inferred from another (previous) scale $\tilde{\mu}$. A conceptual understanding of this property was provided in the 'block spin' renormalisation group by Kardanoff in 1966 [121]. Here the change of scale $\mu$ corresponds to a grouping of lattice spins into blocks. In this way, an RG transformation (step) allows to transform a 2D lattice of spins into a coarse grained version of itself with $2 \times 2$ spin tiles, called block-spins. After enough RG steps, the system is coarse grained enough to have reached a size on which we can observe, for example predict the overall magnetisation of the solid. For most computational applications, a formulation in terms of momentum is preferred and we will also use this approach in this work. The idea was first introduced by Wilson in [122] and consists of solving the theory via a 'coarse graining' of momentum shells. In QCD this means that we start from a free theory at high energies $\gg 1\,\mathrm{GeV}$ and use the RG to step towards the low energy regime, where we have a strongly correlated, non-perturbative system. The functional renormalisation group provides a differential equation, which allows to interpolate between the classical action of this free theory $S$ at a high momentum scale $\Lambda_{UV}$ and the full quantum effective action $\Gamma$. Quantum effects are successively included by considering the differential change in momentum scale $k + \delta k \to k$ until $k = 0$ is reached. The aim is now to define the interpolating $\Gamma_k$, where $k \in [0, \Lambda_{UV}]$, which gives the effective action for a quantum system at intermediate energy scales $k$. $\Gamma_k$ then acts as the classical action for all energy scales lower than $k$.

The suppression of lower momentum modes is implemented via an infrared cutoff term, which acts as an artificial mass term and is added to the classical action,

$$\Delta S_k[\varphi] = \frac{1}{2} \int_x \varphi R_k \varphi \,, \tag{3.11}$$

where the matrix $R_k$ is the so called regulator term. The suppression of quantum fluctuations can be seen from the (formal) path integral,

$$Z[J] = \frac{1}{\mathcal{N}} \int [d\varphi']_{\mathrm{ren}} \exp\left( -\Delta S_k[\varphi'] - S[\varphi'] + \int J \cdot \varphi' \right), \tag{3.12}$$

which turns into a Gaussian in the limit $R_k \to \infty$, effectively dropping all quantum fluctuations. The specific form of regulator is usually chosen to fit the momentum contribution of the two-point-function and varies with the model. Generally, the regulator needs to fulfil two conditions to ensure that it does not change the physics of the theory at hand,

- The introduction of an infrared regularisation, which ensures the suppression of lower momenta during the interpolation,

$$\lim_{\frac{p^2}{k^2}\to 0} \frac{R_k(p^2)}{k^2} > 0\,. \tag{3.13a}$$

- The physical limit for vanishing cutoff $k$ or UV momentum scales $p$, where the regulator needs to vanish,

$$\lim_{\frac{k^2}{p^2}\to 0} \frac{R_k(p^2)}{k^2} = 0\,. \tag{3.13b}$$

Subtleties of regulator optimisation are discussed in Section 3.2.3.

The average effective action $\Gamma_k$ at scale $k$ is defined via a Legendre transformation, analogously to (3.7). We introduce a slight modification and define $\Gamma_k + \Delta S_k$ as the Legendre transformed of $W_k$. Thereby, the known cutoff term is removed from the functional

$$\begin{aligned}\Gamma_k[\Phi] &= \sup_J \left( \int_x J\cdot\Phi - W_k[J]\right) - \Delta S_k[\Phi] \\ &= -\ln\left( \int [d\varphi']_{\text{ren}} \exp\left[ -S[\Phi+\varphi'] - \Delta S_k[\varphi'] + \int_x \varphi' \frac{\delta\Gamma_k[\Phi]}{\delta\Phi(x)}\right]\right).\end{aligned} \tag{3.14}$$

The flow of $\Gamma_k$ is obtained by taking a derivative with respect to the dimensionless RG-scale (the RG-time) $t = \ln(k/\Lambda)$. This *exact renormalisation group equation* of the 1PI effective action is called the Wetterich equation [67],

$$\partial_t \Gamma_k[\Phi] = \frac{1}{2}\mathrm{Tr}\left[\left(\frac{1}{\Gamma_k^{(2)}[\Phi] + R_k}\right)\partial_t R_k\right] = \frac{1}{2}\mathrm{Tr}\big[(G_k)\partial_t R_k\big], \tag{3.15}$$

where $G_k$ is the regularised propagator. The trace implies integration over momentum and summation over color, flavor, Dirac indices and fields and manifests the one-loop exactness of the Wetterich equation. By convention, the RG-time is usually defined to flow from 0 to $-\infty$, but since we use a lot of methods from hydrodynamics this convention changes throughout this work. A more detailed and general derivation of this equation is discussed in Section 3.3.

We close by pointing out some features of the Wetterich equation: This equation is exact and non perturbative. In theory, all quantum effects are contained in the full solution but might not be contained in the model or approximation used, more details are given in Section 3.2.2. Unlike the full propagator for physical fields $\Gamma^{(2)}$, the interpolating $\Gamma_k^{(2)}$ can be negative at finite RG-scales, which causes $\Gamma_k$ to lose its convexity during the RG-scale integration. In these cases the eigenvalues of $\Gamma_k^{(2)} + R_k$ are still positive. Since the regulator was constructed such that it vanishes at vanishing cutoff, the flow works to restore the convexity of $\Gamma_k$ with each RG step.

### 3.2.2. Systematic expansions and error estimates

*This section is based on [8].*

The fRG flow for the effective action $\Gamma[\Phi]$ of a given theory, has a simple one-loop form in terms of the full field- and momentum dependent propagator. The flows of its $n$th moments, the one-particle irreducible correlation functions, are derived from this master equation by taking $n$ field derivatives of the flow of $\Gamma[\Phi]$,

$$\Gamma^{(n)}_{\Phi^{i_1}\dots\Phi^{i_n}}[\Phi](p_1,\dots,p_n) = \frac{\delta^n\Gamma[\Phi]}{\delta\Phi_{i_1}(p_1)\cdots\delta\Phi_{i_n}(p_n)}\,. \tag{3.16}$$

This leads us to a coupled infinite hierarchy of flows for these moments or correlation functions, that typically only admits analytical or numerical solutions within a given order of a systematic expansion scheme of the full system at hand.

One of these systematic expansion schemes is the vertex expansion. Here the effective action is expanded in terms of its moments, while keeping the full momentum dependences of these moments,

$$\Gamma_k[\Phi] = \sum_{n=0}^{\infty}\frac{1}{n!}\int_{x_1,\dots,x_n}\Gamma^{(n)}_{\Phi^{i_1}\dots\Phi^{i_n}}[\bar\Phi](p_1,\dots,p_n)\Big[\Phi^{i_1}(p_1)-\bar\Phi^{i_1}(p_1)\Big]\dots\Big[\Phi^{i_n}(p_n)-\bar\Phi^{i_n}(p_n)\Big]\,. \tag{3.17}$$

A complimentary systematic scheme is the derivative expansion, where all moments are taken into account, but the momentum dependence of $\Gamma_k[\Phi]-S[\Phi]$ is expanded in powers of momenta. Evidently, these schemes can be combined in a systematic way, leading to mixed schemes.

All expansion schemes have in common, that the respective expansion of the effective action is linked to an expansion of the theory or its Hilbert space around a state that captures the essential features of the full ground state. This is most evident within the derivative expansion where the zeroth order takes into account point like interactions to all orders without any momentum dependences in form of the effective potential. Then, higher orders include momentum dependences in powers of $p^2/m^2_{\rm gap}$ of the theory. Evidently, such a scheme fails (or shows a rather slow convergence) in the presence of intricate momentum dependences of scattering processes. One such example are complicated Fermi surfaces in interacting theories.

In turn, the vertex expansion is an expansion in the full moments of the theory, starting with the momentum-dependent (inverse) propagator, the full covariance of the theory. Its implicit expansion parameter is the phase space suppression of higher order interactions for local interactions, and the one loop form of the Wetterich flow gives an easy access to the respective error control. While it is amiable towards intricate momentum dependences of vertices, the convergence of this scheme is slowed down in the presence of long range resonant interactions or large couplings. This can be treated in terms of emergent dynamical effective fields that are introduced for resonant interaction channels within the flow equation. For four-field interactions such as four-quark scatterings in QCD this has been developed in [123]. It is tantamount to a flowing self-consistent Hubbard-Stratonovich transformation and are simple to implement due to the underlying Gaußian nature of the field transformation.

### Systematic expansions in QCD

For an explanation of the tasks at hand we concentrate on QCD at finite temperature and density, which features the most advanced computations within mixtures of the two systematic expansion schemes discussed above: In QCD, mixtures of the vertex and derivative expansion with emergent dynamical fields for resonant channels of the four-quark interactions have been applied. In most cases the scalar-pseudoscalar channel has been dynamically hadronised,

leading to emergent pions and $\sigma$ mesonic fields, see Section 2.3 and the literature [44, 45, 48, 51, 102, 124]. For an additional dynamical hadronisation of the vector channel, leading to emergent vector mesons, see [59]. The complete structure of emergent hadrons has been discussed in [60]. Augmented with a full effective potential for the respective mesonic fields, which includes the point-like scattering of the emergent mesonic fields for small momenta, this is a rather efficient description of QCD at high and low energies as well as at finite temperature and density or baryon-chemical potential.

The study of QCD within the systematic vertex expansion with full momentum dependences has been initiated by studying quenched [44] and unquenched [48] vacuum QCD including dynamical hadronisation. Dedicated studies in Yang-Mills theory at finite and vanishing temperature, as well as in three dimensions in [47, 49, 125], are concentrating on the confinement aspects and its systematic. The respective results have also been used in a mixed scheme application to the full phase structure of QCD in [126] and the magnetic equation of state in [117]. Its systematic improvement in terms of higher vertices with full momentum dependences is work in progress in the fQCD collaboration [13], aiming at apparent convergence of the scheme.

This leaves us with an equally important remaining task, which we focus on in this thesis: one has to control multi-scattering effects of fundamental and emergent degrees of freedom. In particular QCD at high density with potentially competing order effects, first order regimes and mixed phases is highly challenging. There, the very efficient vertex expansion scheme with dynamical hadronisation has to be augmented with elaborate numerical methods to resolve a (multi-dimensional) effective potential, as well as the complicated momentum structure of scattering processes in a dense medium. An important recent technical advance has been the introduction and adaptation of state-of-the art numerical methods for the solution of general diffusion equations for the computation of the RG-flow of effective potentials [65], which we discuss in Chapter 5.

We conclude our brief discussion of systematic expansions and their convergence in QCD with the remark, that the respective structural results and arguments straightforwardly carry over to general theories.

### 3.2.3. Regulators and optimisation criteria

*This section is based on [11].*

In principle, the flow equation (3.15) is exact for any regulator that implements the infrared suppression of lower momentum modes and the ultraviolet renormalisation. The full flow should not depend on the regulator any more. However, in most cases concrete evaluations are, with very few exceptions, subject to approximations of the full effective action. If a vertex structure is omitted in an approximation, the regulators effect on that vertex is also missing and hence any back-coupling of it to the overall flow. In this way, regulator effects may accumulate for $k \to 0$ and do not cancel out like they should. Therefore, it is important to chose the an optimised regulator for a specific approximation. A possible optimisation criterion for operators in a given truncation is the minimal length of the RG trajectory, compare [127, 128]. Here, the optimal regulator $R_{\rm opt}$ fulfils

$$\|p^2(G[\Phi,R_{\rm opt}]-G[\Phi,0])\| = \min_{R\in R(\Lambda)} \|p^2(G[\Phi,R]-G[\Phi,0])\|\,, \tag{3.18}$$

where $p$ is the momentum, the regulators $R$ are taken at the UV scale $\Lambda$ of the theory and $G[\Phi,R]$ is the field dependent propagator. The prefactor $p^2$ is chosen to accommodate for

a dimensionless quantity and access to massless modes at $k = 0$. Equation (3.18) defines a semblance of length of the RG-flow for a monotonous propagator. The norm $\|\cdot\|$ is given by the Sobolev norm for an operator $\psi$

$$\|\psi\|^2 = \sum_{|\alpha|\leq n} \frac{n!}{(n-|\alpha|)!\alpha_1!\dots\alpha_d!} \left\| \frac{\partial^{|\alpha|}\psi(p)}{\partial p^{\alpha_1}\dots\partial p^{\alpha_d}} \right\|_{L_2}^2 , \tag{3.19}$$

where $\alpha \in \mathbb{N}^d$, $|\alpha| = \sum_i \alpha_i$ and $n \in \mathbb{N}$ is the highest order momentum dependency in the truncation scheme. The $L_2$ operator norm is hence taken over the momentum derivatives of the propagator in (3.18).

The optimisation (3.18) takes the contributions of higher momentum derivatives into account. In contrast, the zeroth order derivative expansion which we will use frequently throughout this work, only takes the classical momentum dependence into account. Hence, the derivatives in (3.19) do not contribute and we can find an optimal, non-analytic regulator [127, 129, 130]. However, for truncations beyond LPA the non-analytic structure of the flat regulator shows in the higher momentum derivatives. By comparison, a smooth regulator function gives a much smaller contribution in the momentum derivatives and is hence the more optimised choice in a momentum dependent truncation.

## 3.3. General functional flows

*This section is based on [4].*

Previously, we have introduced the fRG via the Wetterich flow (3.15), since it is the most commonly used master equation in QCD applications. In this section, we take a step back and consider a formulation in terms of general RG transformations, put forward by Wegner in [131]. Wegner's flow expresses the invariance of fixed points and critical behaviour under a large set of general differential reparametrisations and RG transformations. In the context of this work, we use them to optimise our approximation scheme, to simplifying our numerical expressions and in a real time setting, see Chapter 6 and Chapter 7. Furthermore we encounter them in the context of dynamical hadronisation in Chapter 9.

For the sake of simplicity, we only consider scalar fields $\phi = (\phi_1, \dots, \phi_n)$ in the following. All applications of these concepts are considering scalar $O(N)$ theories. In terms of the Wilsonian effective action $S_{\text{eff}}[\phi]$ in (3.6), Wegner's flow reads

$$\partial_t P[\phi] + \frac{\delta}{\delta\phi(x)}\Big(\Psi[\phi]P[\phi]\Big) = 0\,, \qquad P[\phi] = e^{-S_{\text{eff}}[\phi]}\,. \tag{3.20}$$

The RG-time $t$ is the logarithm of the cutoff scale $k$,

$$t = \log k/\Lambda\,, \tag{3.21}$$

with some reference scale $\Lambda$. The cutoff scale can be both an infrared (IR) or ultraviolet (UV) cutoff scale or simply the (geodesic) parameter of a general reparametrisation [127]. In the present work we consider an infrared cutoff scale $k$ for explicit applications. This means that quantum fluctuations with $p^2 \lesssim k^2$ are suppressed below this cutoff scale and fluctuations with $p^2 \gtrsim k^2$ are integrated out (or in).

The exponential $P[\phi]$ in (3.20) is nothing but the path integral measure. General reparametrisations induced by (3.20) leave the path integral unchanged, which is easily seen by integrating

(3.20) over all fields: the integral of the right hand side vanishes as the integrand is a total derivative. The RG kernel $\Psi[\phi]$ is typically chosen as

$$\Psi[\phi] = \frac{1}{2}\mathscr{C}[\phi]\frac{\delta S_{\text{eff}}[\phi]}{\delta\phi} + \gamma_\phi \phi\,, \tag{3.22}$$

with the boundary condition that $\Psi$ vanishes at $k = 0$ if $k$ is an infrared cutoff scale.

The second term on the right hand side of (3.22) with a field-independent $\gamma_\phi$ entails a rescaling of the field $\phi$, and has been introduced for convenience. Moreover, a field-dependent $\gamma_\phi$ can be considered as a driving term. Both, field-independent and field-dependent anomalous dimensions are commonly not considered in (3.22).

In turn, for $k \to \infty$ the kernel (3.22) should suppress all fluctuations, leading to a simple initial condition. These two requirements are more easily seen in terms of the flow for $S_{\text{eff}}$, for which Wegner's flow reads

$$\left(\partial_t + \int \phi\,\gamma_{\text{eff}}\frac{\delta}{\delta\phi}\right) S_{\text{eff}}[\phi] = \frac{1}{2}\,\text{Tr}\,\mathscr{C}[\phi]\Big[S^{(2)}_{\text{eff}}[\phi] - (S^{(1)}_{\text{eff}}[\phi])^2\Big], \tag{3.23a}$$

where the field-independent term $\text{Tr}\,\gamma_\phi$ was dropped and

$$\gamma_{\text{eff}}[\phi] = \gamma_\phi - \frac{1}{2}\frac{\delta\mathscr{C}[\phi]}{\delta\phi}\,. \tag{3.23b}$$

In (3.23a) we have also used the common notation

$$S^{(n)}_{\text{eff}}[\phi] = \frac{\delta^n S_{\text{eff}}[\phi]}{\delta\phi^n}\,. \tag{3.24}$$

The right-hand side in (3.23a) is the trace of the RG kernel $\mathscr{C}[\phi]$ contracted with the connected two-point function of the theory. The left-hand side contains the scale derivative of the Wilson effective action and a generalised anomalous dimension term. We note that we may also recast the $(S^{(1)}_{\text{eff}}[\phi])^2$ term as part of the generalised anomalous dimension by shifting $\phi\,\gamma_{\text{eff}} \to \phi\,\gamma_{\text{eff}} + 1/2 S^{(1)}_{\text{eff}}[\phi]$ in the first line.

Standard Wilsonian RG transformations are obtained for a field-independent kernel $\mathscr{C}$ with $\delta\mathscr{C}/\delta\phi = 0$, while field-dependent kernels introduce a reparametrisation of the theory. For more details and applications, in particular to gauge theories, see [132, 133], for a respective review see [134].

### 3.3.1. Standard flow for the Wilsonian effective action

Now we briefly describe how the standard Polchinski-type flow [68] for the Wilsonian effective action is derived from (3.20). Its derivation from the path integral is described in Appendix B.5.1. In short, we add an infrared cutoff function to the classical action of the theory, analogously to Section 3.2. Note, that in [68] an ultraviolet regulator was considered, but the structure of the flow is identical. Then, the RG kernel is given by

$$\mathscr{C}[\phi_0] = -G^{(0)}_k[\phi_0]\,\partial_t R_k\,G^{(0)}_k[\phi_0], \tag{3.25}$$

where the propagator $G^{(0)}_k$ is the classical propagator of the theory, including the regulator correction,

$$G^{(0)}_k[\phi_0] = \frac{1}{S^{(2)}_k} = \frac{1}{S^{(2)}[\phi_0] + R_k}\,. \tag{3.26}$$

In the path integral this kernel is derived with the current

$$J = \left(G_k^{(0)}\right)^{-1}[\phi_0]\,\phi\,, \tag{3.27}$$

in the Schwinger functional $W[J] = \log Z[J]$, see (B.69) in Appendix B.5.1. Accordingly the anomalous dimension follows as

$$\gamma_\phi = -\left(\partial_t S_k^{(2)}\right) G_k^{(0)}\,. \tag{3.28}$$

When inserting the kernel and the anomalous dimension in the general flow (3.23), the right-hand side line is simply the trace of $-1/2\,\partial_t R_k\, G_k[\phi]$ with the full propagator

$$G_k[\phi](x,y) = \langle\varphi(x)\varphi(y)\rangle - \phi(x)\phi(y)\,, \tag{3.29}$$

with the mean field $\phi = \langle\varphi\rangle$, for more details we refer to Appendix B.5.1. In most applications one separates the full two-point function from the Wilsonian effective action,

$$S_{\text{eff},k}[\phi] = S_{\text{int},k}[\phi,\phi_0] - \frac{1}{2}\int_x \phi\, S_k^{(2)}[\phi_0]\,\phi\,. \tag{3.30a}$$

This split eliminates the trivial running of $S^{(2)}[\phi_0]$ from the flow and makes numerical computations more convenient. Inserting the split (3.30a) and the kernel (3.25) into the Polchinski flow (3.23a) leads to the flow of the interaction part $S_{\text{int},k}[\phi]$

$$\partial_t S_{\text{int},k}[\phi] = \frac{1}{2}\text{Tr}\,\partial_t G_k^{(0)}\left[S_{\text{int},k}^{(2)}[\phi] - \left(S_{\text{int},k}^{(1)}[\phi]\right)^2\right], \tag{3.30b}$$

where we have dropped the $\phi$-independent term $1/2\,G_k^{(0)}\,\partial_t S_k^{(2)}$ on the right hand side, see also (B.75). The standard Polchinski equation is given by (3.30) with an ultraviolet regulator. We emphasise again, that the use of either UV or IR regulators makes no structural difference, while it does conceptually and practically.

Finally, it can easily be shown that for infrared cutoff kernels such as the Polchinski kernel (3.25), the decay properties (3.13) of the infrared regulator ensure a finite UV effective action as the initial condition. The flow of the UV relevant vertices is then governed by RG consistency, [61, 127, 128].

### 3.3.2. General functional flows for the effective action

The 1PI analogue of Wegner's flow equation (3.20) for the Wilsonian effective action or effective Hamiltonians was derived in [127]. There, the starting point was the partition function with a source $\int J_\phi\,\hat\phi[\varphi]$ with the fundamental field $\varphi$, as well as a cutoff term for the composite field

$$S[\varphi] \to S[\varphi] + \frac{1}{2}\int \hat\phi[\varphi] R_k \hat\phi[\varphi]\,, \tag{3.31}$$

for the composite field $\hat\phi$, and possibly also cutoff terms for the fundamental fields. Then the Legendre transform is taken with respect to all the currents, including $J_\phi$,

$$\Gamma_k[\phi] = \sup_{J_\phi}\left(\int J_\phi\,\phi - \log Z_k[J_\phi]\right) - \frac{1}{2}\int \phi\, R_k\,\phi\,, \tag{3.32}$$

where we suppressed the potential Legendre transform w.r.t. the original field $\varphi$ for the sake of simplicity. For example, this general setup includes two-particle irreducible (2PI) actions (for $\phi(x,y)=\varphi(x)\varphi(y)$), and nPI actions, or density functionals (for $\phi(x)=\varphi(x)\varphi(x)$), see [127]. The general flow equation for such a 1PI effective action $\Gamma_k[\phi]$ with $\phi=\langle\hat{\phi}\rangle$ reads

$$\left(\partial_t+\int_x\dot{\phi}\frac{\delta}{\delta\phi}\right)\Gamma_k[\phi]=\frac{1}{2}\operatorname{Tr}G_k[\phi]\left(\partial_t+2\frac{\delta\dot{\phi}}{\delta\phi}\right)R_k\,, \tag{3.33a}$$

where $G_k$ is now the full propagator of the composite field $\phi$,

$$G_k[\phi](x,y)=\langle\hat{\phi}(x)\hat{\phi}(y)\rangle-\phi(x)\phi(y)\,, \tag{3.33b}$$

that is related to the inverse of the two-point function

$$G_k[\phi]=\frac{1}{\Gamma^{(2)}[\phi]+R_k}\,. \tag{3.33c}$$

The differential change $\dot{\phi}[\phi]$, is related to the expectation value of the differential variable transformation of the integration field $\hat{\phi}$ with

$$\dot{\phi}[\phi]=\langle\partial_t\hat{\phi}_k\rangle[\phi]\,. \tag{3.33d}$$

Equation (3.33d) defines the change of the composite field basis with the RG-flow. We emphasise that $\phi$ itself does not depend on the RG-scale $k$, as it is the field/variable of the effective action. The change of the implicit dependence of the effective field $\hat{\phi}$ on the fundamental field $\varphi$ with the scale is *defined* via a given function $\dot{\phi}[\phi]$, for more details see [127], or a discussion of the special role of field zero modes and respective modifications see [51].

We remark that a variant of (3.33) has been derived in [135], based on (3.32) without regulators for the composite fields. Then the flow equation is simply the rotation of the standard flow equation in terms of the propagators of the composite fields, and hence the Jacobian of the transformation is accompanying all propagators. It can be seen as a special case of (3.33).

Wegner's flow equation for the Wilson effective action (3.23) and the general 1PI flow (3.33) are connected via the relation

$$\Psi=\dot{\phi}\,, \tag{3.34}$$

with an additional RG kernel $\Psi$. This can readily be checked with a Legendre transform, see also [136].

### Standard flow for the 1PI effective action

We can reduce the general flow (3.33) to the standard flow equation of the 1PI effective action by using $\dot{\phi}=0$. This choice entails that $\phi=\langle\varphi\rangle$ is the mean value of the fundamental field. Inserting this choice in (3.33) leads us to the Wetterich equation (3.15),

$$\partial_t\Gamma_k[\phi]=\frac{1}{2}\operatorname{Tr}G_k[\phi]\,\partial_t R_k \tag{3.35}$$

see also [137, 138].

In summary, Wegner's flow (3.20) for the Wilson effective action (3.23) and its 1PI analogue (3.33) constitute the general functional flow framework that accommodates an adaptive setup of functional flows: the kernel $\mathscr{C}$ or the transformation field $\phi$ can be adapted to the structure of the theory at hand.

### 3.3.3. Applications of general functional flows: Flowing fields

*This section is based on [8].*

In the following we discuss two qualitatively different examples of how flowing fields $\dot{\phi} \neq 0$ (recall (3.33)) can be used for an RG-adapted expansion scheme. In this context it is convenient to distinguish three different construction principles behind the choice of flowing fields:

(i) Firstly, we can use flowing fields to adapt the field basis $\phi$ to the phase (symmetric or broken) the theory is in, at a given cutoff scale $k$. This application of [127] has been put forward in [139] in an O(N)-theory, and is called Goldstonisation. Naturally, this optimises a given expansion scheme.

(ii) Flowing fields can be used to enforce the expansion of the effective action about the full two-point function or covariance of the theory. This powerful idea has been put forward in [140], for a recent application to complex effective actions see [4], which is included in Chapter 6. This choice is also enforced by full functional optimisation as put forward in [127], and is also obtained within the implementation of optimal transport [141], applied to the Wegner flow [131].

(iii) On the other hand, we can use flowing fields for simplifying the effective action, which is at the root of the essential RG put forward in [136]. There, these simplifications are classified in terms of essential and inessential couplings [131]. An explicit application to an O(N) theory was put forward in [8], and is featured in Section 7.1. This application also implicitly enforces *(ii)*.

In all these cases, a reparametrisation with *flowing* fields allows us to expand the theory, or rather its effective action, about a dynamically adjusted expansion point that is as close as possible to the scale-dependent ground state of the theory. Note also, that a generic use of flowing fields, that aims at optimal expansions, is almost inevitably a mixture of *(i)*-*(iii)*.

The differential flow $\dot{\phi}$ in (3.33) is now at our disposal: For example, we may choose and explicit field transformation in the class *(i)*, as put forward in [139, 142]. Alternatively we may enforce the class *(ii)* or *(iii)* with constraints on the flow, e.g. that of the two-point function or a specific momentum channel of a four-point function. Structurally, this is given by

$$\dot{\phi}_k(\phi, k) \qquad \longrightarrow \qquad \partial_t \Gamma_k^{(n)}[\phi](p) \equiv 0\,, \tag{3.36}$$

for a specific $n$ and $\phi \in \mathscr{I}_\phi$, $p \in \mathscr{I}_p$ take values in some intervals or sets $\mathscr{I}_\phi$ and $\mathscr{I}_p$ respectively. Equation (3.36) entails the differential form of the transformation from the microscopic fundamental fields to emergent effective fields. So far, it has been considered for $n = 2$ in the context of functional optimisation in [127] and [92] with $p > k$, in [140] for keeping the covariance of the theory fixed, and in [136, 143] (for $p = 0$) in the context of essential fRG flows. For $n = 4$ is has been used in QCD for dynamical hadronisation of momentum channels of the four-quark scattering vertex, for an application within this work see Chapter 9 or [51, 144]. Moreover, it has been used for dynamical composite dimers in applications to ultracold gases in [145]. We proceed by illustrating this general framework by discussing two examples in the low-energy sector of QCD.

For the remainder of this section, we distinguish two different sets of fields (in a slight abuse of notation). Firstly, we have the untransformed field $\varphi$, which is directly linked to the mean value of the fundamental field $\langle\varphi\rangle$ with $\dot{\phi} = 0$ from (3.31), and accordingly $\rho_\varphi = \varphi^2/2$ as

defined below in (3.37). Secondly, we consider the flowing field $\phi$ with the corresponding invariant $\rho = \phi^2/2$. In this notation we have $\varphi = \phi$, if $\dot{\phi} = 0$ as stated in the derivation of (3.35).

### Flowing fields at work in QCD

We recall the combined expansion scheme for QCD, which was described in Section 3.2.2. There momentum dependence of scatterings is taken into account within the vertex expansion. This expansion has been shown to converge rapidly, if all the resonant channels are treated within dynamical hadronisation: the phase space suppression is very effective and in the absence of a small parameter this is called apparent convergence. In turn, multi-scattering events get important in the presence of close massless modes. Prominent examples in QCD are the pion in the chiral limit or the $\sigma$ and density modes close a potential critical end point. The slowing down of the convergence in the chiral limit has been studied in [117]: while for physical pion masses, $m_\pi \approx 140\,\text{MeV}$ a Taylor expansion of the meson potential $V_{\text{eff}}(\rho_\varphi)$ with

$$\rho_\varphi = \frac{1}{2}\left(\sigma^2 + \boldsymbol{\pi}^2\right), \quad \text{and} \quad \varphi^T = (\sigma, \pi_1, \pi_2, \pi_3), \tag{3.37}$$

converges rapidly within 5 - 7 orders of $\rho_\varphi$, see also [44, 45, 48, 51], far more orders are required for pion masses $m_\pi \lesssim 1\,\text{MeV}$, where also critical scaling sets in. The critical part of QCD in this regime is the mesonic sector, which is simply described by a (non-local) O(4)-model after integrating out all other degrees of freedom. This was already outlined in Section 2.3.2, where we also introduced the effective mesonic potential $V_{\text{eff}}(\rho_\varphi)$.

The pivotal correlation function in these regimes is the full two-point function $\Gamma^{(2)}[\varphi_c](p)$ for constant backgrounds $\varphi_c$. Space-time or rather momentum-dependent backgrounds are covered by the higher order correlation functions $\Gamma^{(n)}[\varphi_c](p_1, ..., p_n)$. In the vertex expansion their importance drops rapidly due to phase space suppression. Moreover, evaluated on the constant solution of the equations of motion $\varphi_{\text{EoM}}$ with

$$\left.\frac{\delta\Gamma[\varphi]}{\delta\varphi}\right|_{\varphi=\varphi_{\text{EoM}}} = 0\,, \tag{3.38}$$

the two point function $\Gamma^{(2)}[\varphi_{\text{EoM}}](p)$ in the mixed expansion converges rapidly towards that of the ground state of the theory, the optimal expansion point.

The full two point function for constant fields is obtained by taking the second $\pi_i$-derivative at vanishing $\boldsymbol{\pi} = \mathbf{0}$. It reads

$$\Gamma^{(2)}_{\pi_1\pi_1}[\varphi](p) = Z_\varphi(\rho_\varphi, p)\left[p^2 + m^2_\varphi(\rho_\varphi)\right], \tag{3.39}$$

with the pole mass $m_\varphi(\rho_\varphi)$ defined by the on-shell condition $\Gamma^{(2)}_{\pi_1\pi_1}[\varphi](p^2 = -m_\varphi(\rho_\varphi)) = 0$. The wave function $Z_\varphi(\rho_\varphi, p)$ is the coefficient of the operator $(\partial_\mu\varphi)^2$ in the effective action and the evaluation of the derivatives at $\boldsymbol{\pi} = \mathbf{0}$ eliminates terms proportional to $\varphi$-derivatives of $Z_\varphi$ and $m^2_\varphi(\rho_\varphi)$.

Equation (3.39) leaves us with the particular task of determining the field- and momentum-dependent wave function $Z_\varphi(\rho_\varphi, p)$. Importantly, if the latter is non-trivial, this hints at the field $\varphi$ not being the physical field that leads to a simple description of the ground state and hence the theory. Moreover, its resolution is then a non-trivial numerical task. This suggests to

dynamically change the field with the momentum scale such that the dispersion (3.39) takes a simple classical form, $\varphi \to \phi(p,\varphi)$, leading to the dispersion

$$\Gamma^{(2)}_{\phi_i\phi_j}[\phi](p) = \left[p^2 + m^2_\phi(\rho)\right]\delta^{ij}\,, \tag{3.40}$$

or variants of it. This transformation can be included in terms of an fRG flow, where the transformation $\varphi \to \phi(\varphi,p)$ can be implemented and monitored successively as a function of the infrared cutoff scale $k$ with $\varphi \to \phi_k(\varphi,p)$. However, instead of using $\varphi \to \phi_k(\varphi,p)$, one is using the successive field transformation from the RG-adapted field basis $\phi$ at a given scale $k$ to the RG-adapted field basis at the scale $k-\Delta k$, encoded in the flow $\dot\phi_k(\phi,p)$. Here, the argument of $\dot\phi$ is the flowing field $\phi$ at the scale $k$.

We emphasise that within this transformation the fields $\phi$ are the mean fields in the effective action and carry no $k$-dependence. Their relation to the fundamental fields is solely carried by the $k$-dependent function $\dot\phi_k(\phi,p)$.

- As a first example for *(iii)*, we now choose an RG-adapted field basis with $Z_\phi = 1$ for all cutoff scales,

$$\dot\phi_k(\phi,k) \qquad \longrightarrow \qquad Z_{\phi,k}(\phi,p) \equiv 1\,, \tag{3.41}$$

  for all $k$, see [136]. Equation (3.41) entails the differential form of the transformation from the microscopic fundamental fields to emergent effective fields with a classical dispersion. A momentum independent implementation of (3.41) is given in Section 7.1.

- A second example is an application of *(i)* to scalar O(N) theories, which can be found in [139]. Here the reparametrisation of the theory in terms of flowing fields has been used to flow the fundamental fields $\varphi^T = (\varphi_1,...,\varphi_N)$ in a Cartesian basis into polar coordinates

$$\phi^T = (\rho,\boldsymbol{\theta}), \quad \varphi = \sqrt{2\rho}\, e^{\mathrm{i}\theta^a t^a} \begin{pmatrix} 1 \\ 0 \\ \vdots \\ 0 \end{pmatrix}, \tag{3.42}$$

  Here, the $t^a$ with $a = 1,...,N-1$ are the generators of the quotient O(N)/O(N-1), and the subgroup O(N-1) leaves the vacuum vector $(1,0,...,0)$ invariant.

The field $\rho = \varphi^2/2$ in (3.42) is the radial field, and the phase fields $\theta^a$ are the Goldstone fields. In the broken phase, the basis (3.42) is advantageous, because the phase fields describe the Goldstone fields or rather their fluctuations for all values of the field, while in the Cartesian basis this only holds true at the expansion point $\varphi^T = (\varphi_1 = \sigma, \mathbf{0})$. In turn, the polar basis has a parametrisation singularity for $\rho \to 0$ and hence in the symmetric phase the Cartesian basis is more natural. Accordingly, it is suggestive to define a basis that interpolates between the Cartesian basis in the symmetric phase (or small field values $\rho$) and the polar basis in the broken phase (or large field values of $\rho$). This is linked to an expansion scheme of the theory about the ground state of the theory, and has been called Goldstonisation in [139]. Notably, in the large N limit, the flow equation of the effective potential only depends on the Goldstone wave function $Z_\theta$. The compatibility of the results within the interpolating flowing fields with that in the standard Cartesian basis has been explicitly shown in [139]. The setup, notation and results have been also used in [142] for an application to the thermodynamics of a Bose gases.

There are many more applications including non-relativistic theories in and out of equilibrium, e.g. [146], where a formulation in phase fields is better adapted to the physics phenomena at play, as one is setting up an expansion in the (dynamical) physical degrees of freedom.

The two examples are complimentary: while defining flowing fields that are adapted to the different phases of the theory, the formulation in [139, 142] does not aim for a classical dispersion. On the contrary, in the large $N$ limit the whole effective potential is generated from the field-dependent wave function $Z_\pi(\rho, p)$ of the Goldstone modes.

A more recent and intriguing application, directly aiming at (3.40), has been put forward in terms of the essential renormalisation group [136, 143] for critical scaling in scalar models and quantum gravity. In particular, the choice (3.41) has been suggested in [136] and used in the three-dimensional O(1) model for a refined analysis of the Wilson-Fischer fixed point. In terms of the essential renormalisation group put forward in [136] the wave function $Z_\phi$ is an inessential coupling that can be absorbed in a redefinition of the field. As discussed above in the context of the O(N) application in [139], in the large N limit the essential effective potential originates from the inessential wave function alone. This interesting structure and potential simplifications ask for a more detailed analysis.

All these applications as well as that in [139, 142] are guided by the search for the optimal expansion and parametrisation of the theory about and in terms of the ground state, see also [140]. This expansion about the full propagator, or covariance of the theory, is also is at the core of the RG-adapted expansion of the Wilson effective action and the 1PI effective action put forward in [4] for fRG flows for complex actions. The respective functional optimisation setting is discussed in [127], and is related but not identical to a distinction of essential and inessential couplings. For a recent perspective of such a functional optimisation in terms of optimal transport [141].

The above considerations and in particular the relation of optimal expansions to that about the ground state or full covariance of the theory also emphasise the importance of physical constraints for this general reparametrisation setup. For instance, instead of the form (3.40) of the reparametrised kinetic operator or covariance obtained from $Z_\phi \equiv 1$ but unchanged mass function (in terms of the new field variable $\phi$), we may have chosen (3.40) with $m^2_\phi(\rho) = 0$ or any other mass function $m^2_\phi(\rho) \geq 0$. While such transformations exist and seemingly remove a relevant or marginal parameters (in $d \geq 2$) from the theory, they encode the expansion of a theory with pole mass $m^2_\phi(\rho)$ about theories with the pole mass $m^2_\phi(\rho) = 0$ or any other choice. Within the present Euclidean setting this is a smooth transformation. However, while possible, it is certainly not optimal and functional optimisation in [127] for the full two-point function shows this manifestly. Moreover, in the real-time or Minkowski version of the O(N) model, the respective transformation maps the spectrum of a given theory to a different one. Such a transformation necessarily moves pole and cut positions of correlation functions and has to be taken with a grain of salt. In any case it is hardly optimal. This concludes our brief discussion of general reparametrisations and flowing fields.

## 3.4. Real time fRG

*This section is taken from [3].*

In this section, we turn our focus toward real-time applications of the fRG. These are required for the investigation of timelike phenomena, ranging from scattering processes, the formation and spectrum of bound states to the time evolution of quantum systems close and far from

equilibrium. For real-time applications of the fRG in a broad variety of research fields, see, e.g., [147–167].

We begin by discussing the issue of finding a Lorentz invariant, causality preserving cutoff function for fRG flows in Section 3.4.1. Such a cutoff comes at the prize of the built in finiteness of the method, hence we present a novel *finite renormalised* fRG approach in Section 3.4.2. The renormalisation is transported along with the flow and hence is called *flowing renormalisation*. One of its advantages is its manifest finiteness, also for regulators or regularisation schemes that do not directly implement a UV decay in the loops of the flow equation. This allows for its application to general non-perturbative truncation schemes.

In particular, this novel fRG setup can be used to derive a spectral fRG approach in real time, the *spectral fRG*, which we consider in Section 7.2. Our approach is based on the spectral representation of correlation functions, and is manifestly finite as well as Lorentz (or Galilei/Schrödinger) invariant. It builds on the novel functional spectral approach setup [168, 169] which has already been used in [166].

### 3.4.1. Infrared regularisation and symmetries

To apply the functional flow equation (3.35) in a real-time setting, we first need to discuss some properties of the flow linked to the choice of regulator.

Firstly, we saw in (3.13) that the regulator implements an IR regularisation through an, in general momentum-dependent, mass term that effectively suppresses quantum fluctuations of field modes with momenta $p^2 \lesssim k^2$. The second property of the regulator is a suppression of modes with $p^2 \gtrsim k^2$ in the momentum-loop integrals, rendering the flow and all its field derivatives UV finite.

In addition to these conditions, which guarantee the finiteness of fRG flows, we might want to impose additional, physically motivated conditions onto the regulators. For relativistic theories it is desirable that the regulators do not spoil Lorentz/Poincaré invariance. Furthermore, for studies of real-time properties, i.e. in Minkowski space, causality should also not be violated. The latter is directly related to the existence of a spectral representation for the propagator of $\phi$.

To maintain Lorentz invariance, the regulator should be a function of the four-momentum squared, $R_k^\phi(p^2)$. However, as discussed, e.g., in [149], such regulators might spoil causality through unphysical poles or cuts in the complex frequency plane. Typically, such regulators either do not admit a spectral representation or generate fictitious mass poles that only disappear in the vanishing cutoff limit, for a discussion of the latter see [149, 152, 156].

A further common choice are regulators that only depend on the spatial momenta, $R_k^\phi(\vec{p}^{\,2})$. Clearly, these regulators do not lead to additional poles in the complex frequency plane, but merely modify the dispersion of the fields. Thus, they admit a spectral representations at the cost of violating Lorentz invariance. If the system is in a medium, explicit Lorentz symmetry breaking might seem innocuous, as it is broken anyway. While this has been confirmed in specific examples [156, 170], it is *a priori* unclear in general. Especially when considering limiting cases of a phase diagram such as $T \to 0$, the question becomes much more intricate than the comparisons in the aforementioned works.

Hence, effectively we either violate (or at least complicate) causality, or we violate Lorentz invariance. All known examples of regulators rely on the regularisation conditions in (3.13). However, by relaxing at least one of these conditions, there is a natural choice for a regulator

which preserves both causality and Lorentz invariance,

$$R^{\phi}_{k,\mathrm{CS}} = Z_\phi\, k^2\,, \qquad r_{\mathrm{CS}}(x) = 1\,, \tag{3.43}$$

which we refer to as the Callan-Symanzik (CS) regulator. It implements IR regularisation through an explicit mass $\Delta m^2_\phi = Z_\phi\, k^2$. In this case the flow equation (3.35) has been derived in [171]. To our knowledge, it is indeed the first occurrence of such a closed (and one loop) exact functional equation for the effective action. The insertion of the CS regulator in (3.35) leads us to the (inhomogeneous) functional CS equation. However, it violates the second condition in (3.13). The CS regulator only lowers the UV degree of divergence by two, for example, quadratically divergent diagrams such as the tadpole diagram in the two point function of the $\phi^4$ theory in $d = 4$ leads to logarithmically divergent tadpole diagrams in the CS equation. In short, at each $k$ in the flow, all loop momenta contribute. To render the flow finite, an additional UV regularisation is required in general.

The structural similarity of the Wetterich equation (3.35) with regulators obeying (3.13) and the flow with the CS regulator (3.43) is misleading. While the former equation implements a Wilson-type momentum-shell integration in a fixed underlying quantum field theory, the CS flow constitutes a flow in the space of theories. To be specific, the need for additional UV regularisation at different cutoff scales $k$ implies that we have different theories which require a different renormalisation. Hence, the flow must be re-renormalised; only specifying the initial effective action $\Gamma_{k_{\mathrm{init}}}$ does not necessarily lead to a finite renormalised solution of the flow equation. This renormalisation is typically done with an RG transformation, leading to finite renormalised loops as well as the $\beta$-function and anomalous dimension terms in (3.44). This can be achieved instead by the introduction of explicit counter terms to the flow, supplemented with renormalisation conditions which are fixed at a, in general $k$-dependent, renormalisation scale $\mu$, as has been done in [3].

### 3.4.2. Functional flows with flowing renormalisation

In this section we discuss the finiteness of infrared flows and the finiteness of the ultraviolet limit of the effective action. Both properties are related to the UV renormalisation that is implicitly or explicitly implemented in the flow equation. This leads us to the concept of flowing renormalisation.

#### RG consistency and UV scaling

The underlying RG invariance of the theory at $k = 0$ implies that the full effective action $\Gamma = \Gamma_{k=0}$ obeys the homogeneous renormalisation group equation [127], see also (2.21). This entails the invariance of the underlying quantum field theory under self-similarity transformations of the theory. In the presence of *RG-adapted* regulators the scale invariance, $\mu \frac{d\Gamma[\Phi]}{d\mu} = 0$, of the theory is maintained [3, 127]. As a consequence we obtain the general flow equation that comprises the change of a cutoff scale, here $k$, as well as an accompanying general RG transformation. These general reparametrisations (self-similarity transformations) also involve non-linear field transformations, $\Phi_i \to \phi_i[\Phi]$, which we have seen in Section 3.3.

Thus a flow equation with reparametrisations at each flow step can be derived [127],

$$\left(s\partial_s + \beta^{(s)}_{\lambda_i}\partial_{\lambda_i} + \int_x \gamma^{(s)}_{\Phi_j}\Phi_j \frac{\delta}{\delta\Phi_j}\right)\Gamma_k[\Phi] = \frac{1}{2}\mathrm{Tr}\, G_k[\Phi]\,(\partial_t + 2\gamma_\Phi)R^\Phi_k\,, \tag{3.44}$$

where we consider $k(s)$ and $\mu(s)$ with

$$s\partial_s = \mu\partial_\mu + \partial_t\,. \tag{3.45}$$

The $\beta$-functions $\beta^{(s)}$ and anomalous dimensions $\gamma^{(s)}$ then encode the full $s$-scaling of a combined cutoff ($k$-) and RG ($\mu$-) flow, including a reparametrisation of the theory,

$$\gamma^{(s)}_\Phi \Phi = s\frac{d\Phi}{ds}\,, \qquad \beta^{(s)}_\lambda = s\frac{d\lambda}{ds}\,. \tag{3.46}$$

Furthermore $\gamma^{(s)}_\Phi = \gamma^{(\mu)}_\Phi + \gamma_\Phi$, and $\gamma_\Phi = -\frac{1}{2}\partial_t \log Z_\Phi$ occurs due to the standard linear reparametrisations of the fields. Equation (3.44) including the field-dependent generalisation $\gamma_\Phi$ is the general fRG setup for the effective action, see Section 3.3.

For regulators with the second property (UV decay), general reparametrisations encoded in the anomalous dimensions and $\beta$-functions may facilitate the computations or implement functional optimisation schemes. It is simply a convenience for infrared flows with finite flow equations, but is a necessity in the absence of ultraviolet finite loops, as is the case for the CS regulator, (3.43). Then, the rescalings implement the required UV renormalisation via multiplicative renormalisation. While this is a formally correct procedure, the implementation of multiplicative renormalisation within non-perturbative truncation schemes is intricate. This intricacy is present for all diagrammatic methods such as DSEs or 2PI methods, a detailed discussion is provided in [172].

### Functional RG with flowing renormalisation

The generalised flow equation (3.44) can be used with an infrared regulator and an additional ultraviolet one to derive a flow equation which also incorporates an explicit UV renormalisation in a manifestly finite approach. This is implemented in terms of a generalised BPHZ scheme with the subtraction of a flowing counter term action. In contradistinction to multiplicative schemes this leads to finite loop diagrams by subtraction. Such a construction has the benefit of a simple and robust numerical implementation.

The *flowing* (UV) renormalisation of the flow is introduced by tracking a UV scale $\Lambda = \Lambda(k)$ alongside with the infrared flow and subsequently taking the limit $\Lambda \to \infty$. This novel flow equation, with flowing renormalisation, is derived in [3] and reads,

$$\partial_t \Gamma_k[\phi] = \frac{1}{2}\mathrm{Tr}\, G_\phi[\phi]\,\partial_t R^\phi - \partial_t S_{\rm ct}[\phi]\,. \tag{3.47}$$

Here, the flow of the counter term action (3.48) accounts for the flow of the renormalisation conditions, as well as the finiteness of the flow itself for infrared regulators $R^\phi$ such as the CS regulator. The counter term action is given by,

$$\partial_t S_{\rm ct}[\phi] := -\lim_{\Lambda\to\infty}\left(\frac{1}{2}\mathrm{Tr}\, G^\phi_{k,\Lambda}\,\mathscr{D}_k\,\partial_{t_\Lambda} R^\phi_{k,\Lambda}\right), \tag{3.48}$$

where the factor $\mathscr{D}_k$ is a relative measure of RG steps in the $k$- and $\Lambda$-direction,

$$\mathscr{D}_k = \partial_t \log\Lambda(k)\,, \tag{3.49}$$

where $t_\Lambda = \log(\Lambda/k_{\rm ref})$, with a reference scale $k_{\rm ref}$. $R^\phi_{k,\Lambda}$ is the UV-regulator term as a function of the UV-scale $\Lambda$. We recover the infrared regulator for $\lim_{\Lambda\to\infty} R^\phi_{k,\Lambda} = R^\phi$.

In the case of UV-finite regulators $R^\phi$ the flow (3.48) reduces to the standard momentum-flow, since $\lim_{\Lambda\to\infty}\left(\partial_{t_\Lambda} R^\phi_{k,\Lambda}\right) = 0$. In general however, this naive limit can only be taken for infrared momentum cutoffs that decay sufficiently fast in the ultraviolet. Most importantly, we can identify the terms $\propto \mathscr{D}_k$ as UV-cutoff flows that can be used for a flowing renormalisation scheme.

The derivation, put forward in [3], holds true for general infrared regulators. For our specific real time applications we consider regulators $R^\phi_{k,\Lambda}$ with

$$R^\phi_{k,\Lambda}(p) = Z_\phi\, k^2\, r(x_\Lambda)\,, \qquad x_\Lambda = \frac{\vec{p}^{\,2}}{\Lambda^2}\,, \tag{3.50}$$

where we have used a spatial momentum regulator in order to retain causality in a simple manner, as discussed in the previous section. For $\Lambda\to\infty$ we require

$$\lim_{\Lambda\to\infty} R^\phi_{k,\Lambda} = Z_\phi\, k^2\,, \tag{3.51}$$

to recover the CS regulator. Equation (3.51) defines a set of possible shape functions $r(x)$

The counter term action depends on a finite set of renormalisation parameters and removes all terms with positive powers $\Lambda^n$ as well as logarithms $\log\Lambda/k_{\rm ref}$ from the flow. This renders the infinite UV cutoff limit finite,

$$\lim_{\Lambda\to\infty}\left|\partial_t\Gamma_{k,\Lambda}[\phi]\right| < \infty\,. \tag{3.52}$$

Accordingly, the amount of renormalisation parameters is equivalent to the number of UV relevant and marginal directions. Moreover, in the limit $\Lambda\to\infty$ the counter term action takes a local form for approximations with local vertices that reduce to the classical ones for large momenta. It can be augmented with general reparametrisations of the theory, leading to a generalisation of (3.44). We defer this to [3].

This general setup also allows us to monitor and change the renormalisation conditions within the infrared flow. This generalises the standard fRG setup, in which the (UV) renormalisation and the respective renormalisation conditions are implicit in the choice of the finite initial action.

### Finite CS flows and flowing renormalisation conditions

In Section 7.2 we use this flow to set up spectral functional flows with the finite CS flows derived from (3.47). For the CS flow the general equation reduces to

$$\partial_t\Gamma_k[\phi] = \mathrm{Tr}\, G_\phi[\phi]\, k^2 - \partial_t S_{\rm ct}[\phi]\,, \tag{3.53}$$

where a CS regulator in a manifestly UV finite setting is assumed and the finite limit $\Lambda\to\infty$ can be safely taken. As for the general equation (3.47) the novelty of (3.53) is not its finiteness per se. Indeed, already the original functional CS equation as derived in [171] can be shown to be finite order by order in perturbation theory. However, (3.53) is manifestly finite in *general* perturbative and non-perturbative truncation schemes with a manifestly finite effective action. Moreover, the present setup allows for a direct computation of the flow of the counter term action, only dependent on a set of renormalisation parameters which are in one-to-one correspondence to the coefficients of the UV marginal and relevant operators.

The general flow (3.47) and its finite CS limit (3.53) seemingly imply that we are left with the task of computing the non-trivial scaling factor $\mathscr{D}_k$ as well as the $\Lambda$-trajectory at each RG step. This would exact a heavy price for the finiteness (3.52). It is therefore noteworthy that we do not have to compute $\partial_t S_{\mathrm{ct}}[\phi]$ from the flow of $\Lambda(k)$, since we can fix it completely by choosing a set of renormalisation conditions. Then, the subtraction $\partial_t S_{\mathrm{ct}}[\phi]$ is determined such that the flow of these conditions vanishes. This choice is practically implemented by subtracting the $t$-flow of the correlation functions $\Gamma_k^{(n)}(p^2 = \mu^2)$, that is the renormalisation condition from the full $t$-flow. This renders the functional $t$-flow finite (if one also subtracts the zero point function) and guarantees the RG conditions to hold.

# CHAPTER 4

## Gluon condensation and mass gap

*This chapter is based on [2], text and figures are taken from the publication. We begin by investigating the gluon mass gap, which is linked to gluon confinement via the Kugo-Ojima confinement criterion, see Section 2.2.1. The publication studies mechanisms for the creation of a gluon condensate and makes a prediction for the gluon mass gap.*

Yang-Mills theory exhibits a mass gap, in spite of the fact that the fundamental degrees of freedom are massless at the level of the classical action. While perturbation theory is based on massless gluons, non-perturbative quantum fluctuations lead to exponentially decaying correlation functions for gauge invariant observables, which are characteristic of massive excitations. The lightest excitations are glueballs [173, 174], and the lightest glueball mass sets the mass gap or confinement scale. This dynamical emergence of a mass gap in the gauge sector of QCD has been established by numerous lattice studies, see e.g. [175–179], and continuum studies, see e.g. [180–188].

In a gauge fixed version of QCD the effects of the mass gap manifest themselves through the appearance of distinctive patterns in the infrared momentum region of correlation functions. Most of the related investigations have been performed in Landau gauge QCD. In particular the infrared behaviour of the gluon propagator in Landau gauge has been explored within large-volume lattice simulations [189–197] and non-perturbative functional methods, such as Dyson-Schwinger equations (DSEs) [92, 198–201] and the functional renormalisation group (fRG) [95, 104, 202, 203]. In combination, these investigations have led to a coherent picture: with exception of the deep infrared regime far below the confinement scale $\Lambda_{\rm QCD}$, the results obtained for the gluon propagator in the non-perturbative domain are in excellent agreement. In particular, they are found to be well compatible with a description in terms of an effective gluon mass. Put differently, they show the dynamical emergence of a mass gap in the gluon propagator, as well as in higher order correlation functions.

The precise relation between the gluon mass in gauge fixed QCD and the physical mass gap in Yang-Mills theory is still an open question. Nonetheless, in covariant gauges a mass gap in the gluon propagator is required for quark confinement to occur. This has been established through the study of the Polyakov loop expectation value in [88, 89].

This situation asks for the identification and investigation of potential mechanisms which are

able to create an effective gluon mass term. Commonly, gauge boson masses are generated by the formation of condensates, even in the absence of fundamental scalar fields. The textbook implementation of such a scenario is realised within the theory of superconductivity. There, the massive photon associated with the Meissner effect is linked to the condensation of the Cooper pairs, see e.g. [204, 205], and references therein. In pure Yang-Mills theory, a potential connection between the effective gluon mass and gluon condensates of dimension four has mostly been discussed within the operator product expansion (OPE) [96, 206, 207]. It has been argued in [208] that a non-perturbative condensate of composite color octets in QCD leads to a simple description of gluon masses by the Higgs mechanism. In this scenario, the massive gluons can be identified with the lowest mass vector mesons, with a rather successful phenomenology [209, 210].

The chapter is a first fRG study of a potential dynamical emergence of the effective mass in the gauge fixed gluon propagator in QCD color condensates. This condensate is computed from the Euclidean effective potential of a constant field strength $F_{\mu\nu}$ as in [211], with precision ghost and gluon propagators obtained within the fRG [47]. We find minima and saddle points for finite non-zero $F_{\mu\nu}$. The minimum value of $F_{\mu\nu}$ is related to an effective gluon mass, and the final color blind result is obtained from an average over color directions. Our computation of the effective gluon mass agrees very well with lattice results and results obtained from alternative dynamical scenarios within the error bars, despite the qualitative nature of the computation. The present study serves as a promising starting point for a systematic exploration of the connection between gluon condensates and gluon mass gap.

## 4.1. Gluon condensates

Gluon condensation can be described by non-vanishing expectation values of composite operators, such as the field strength squared, $F_{\mu\nu}F_{\mu\nu}$, being a scalar under Lorentz transformations. In terms of the free energy or effective action of QCD, this entails that quantum effects would trigger a non-trivial potential in these condensates, with the possibility of capturing also the dynamics of the respective interaction channel. In this context, the classical action of Yang-Mills theory, as introduced in (2.9), is the first (trivial) term of such a non-trivial potential.

### 4.1.1. Color condensates

Color condensates [208, 212–214] could render the gluons massive through a dynamical realisation of the Higgs mechanism. Note that, strictly speaking, a local gauge symmetry cannot be broken spontaneously. Nonetheless, as is well-known from the description of the electroweak sector of the Standard Model, the language of spontaneous symmetry breaking in a fixed gauge can be particularly useful, and will be employed in what follows.

Below we discuss a color condensate operator, derived from $F_{\mu\nu}$ in the case of the physical gauge group $SU(3)$. Generally, a possible condensate operator of dimension four is given by the traceless hermitian $N_c \times N_c$ matrices

$$\chi^{AB} = \left( F^{AC}_{\mu\nu} F^{CB}_{\mu\nu} - \frac{1}{N_c} F^{CD}_{\mu\nu} F^{DC}_{\mu\nu} \delta^{AB} \right), \tag{4.1}$$

where $A, B, C, D = 1, ..., N_c$ are color indices in the fundamental representation, $F^{AB}_{\mu\nu} = F^a_{\mu\nu}(t^a)^{AB}$. The subtraction of the diagonal term makes the operator traceless, $\chi^{AA} = 0$, and for $N_c = 3$ this

is an octet operator. In terms of the field strength components $F^a_{\mu\nu}$, the condensate in (4.1) reads,

$$\chi^{AB} = \frac{1}{2} F^a_{\mu\nu} F^b_{\mu\nu} \Big( \{t^a\,,\, t^b\}^{AB} - \frac{1}{N_c} \delta^{ab} \delta^{AB} \Big) , \tag{4.2}$$

We note in passing that the above operator is only present for $N_c \geq 3$. It vanishes in $SU(2)$, as the symmetric group invariant vanishes, $d^{abc} = \mathrm{tr}\, t^a \{t^b\,,\, t^c\} = 0$. This suggests already that, in a realistic condensation scenario leading to a gluon mass gap, (4.1) should be augmented with further color condensate operators.

Introducing the composite color condensate field $\chi^{AB}$, the quantum effective action $\Gamma$ will typically contain an induced kinetic term,

$$\Gamma_\chi = Z_\chi \int_x (D_\mu \chi)^{AB} (D_\mu \chi)^{BA} , \tag{4.3}$$

with a wave function renormalisation $Z_\chi$. For a non-zero expectation value $\langle \chi^{AB} \rangle$, this induces a mass term for some of the gluons,

$$m_A^2 \propto Z_\chi g_s^2 \langle \chi \rangle^2 . \tag{4.4}$$

Mass terms for all gluons in $SU(3)$ require condensates of more than one octet in different directions since at least a $U(1) \times U(1)$-subgroup remains unbroken, as for example in [208, 212–214]. This argument also applies to higher gauge groups, $N_c \geq 3$, and we have already pointed out in this context that the color condensate operator (4.2) vanishes for $N_c = 2$. Besides different mass terms, octet condensates can also induce different effective gauge couplings for different gluons, due to terms in the effective action, see e.g. [215, 216],

$$\int_x F^{AB}_{\mu\nu} \chi^{BC} F^{CA}_{\mu\nu} . \tag{4.5}$$

This closes our discussion of the color condensation in Yang-Mills theories.

### 4.1.2. Color condensates and the field strength tensor

The investigation of flow equations with dynamical composite fields such as the color condensate field discussed in the last section is well understood. It has been introduced and discussed in [51, 123, 127, 131, 136, 217–221], for applications to QCD see [42, 45, 48, 51, 59, 102] and the review [104]. However, full computations including the composite field $\chi^{AB}$ require a substantial effort, and will be considered elsewhere.

In the present work we restrict ourselves to a qualitative study, whose principal aim is to gather insights on the possible role of non-singlet condensates in the confining dynamics. This is done by building on results for the condensation of the field strength tensor within functional renormalisation group investigations in [211, 222, 223]. Such a colored expectation value of $F_{\mu\nu}$ is linked to non-vanishing expectation values of the color condensate operator $\chi$ in (4.1) as well as potential non-vanishing expectation values of further color condensate operators. Hence, $\langle F_{\mu\nu} \rangle$ can be used to describe the dynamical emergence of the effective gluon mass via color condensates, for details see Section 4.1.3.

We emphasise that a description in terms of $F_{\mu\nu}$ and its expectation value makes it difficult to include the full dynamics of the color condensate sector as well as the condensation pattern,

as this requires the computation of the dynamics of higher order terms in $F_{\mu\nu}$ and covariant derivatives. We also note that such an expansion about $\langle F_{\mu\nu}\rangle$ works naturally for observables or more generally, expectation values of gauge invariant operators. There, singling out a color direction is simply a means of computation. In turn, for gauge-variant expressions the expansion about a non-trivial configuration mixes with the gauge fixing, and it is difficult to undo the color selection quantitatively. This can be done with an additional color averaging $\langle\cdot\rangle_{\text{av}}$, which can be implemented systematically. As this concerns the understanding and underlying structure of our work, we further explain this with two simple examples. While important, it is not in our main line of reasoning and hence is deferred to Appendix B.2.1.

In any case, while such an averaging is to date always implied in lattice simulations of gauge fixed correlation functions as well as in most computations in functional QCD using an expansion about $\langle F_{\mu\nu}\rangle = 0$, it is difficult to implement quantitatively in an expansion about a colored background. It is this current lack of a quantitatively reliable averaging step that makes the current investigation qualitative and it constitutes our largest source for the systematic error.

In the present work, we compute the respective gauge invariant effective potential $\mathscr{W}_{\text{eff}}(F_{\mu\nu})$ for constant field strength $F_{\mu\nu}$ from the effective action $\Gamma[A]$,

$$\mathscr{W}_{\text{eff}}(F_{\mu\nu}) = \frac{1}{\mathscr{V}}\Gamma_k[A(F_{\mu\nu})]\,, \tag{4.6}$$

with the space time volume $\mathscr{V}$. Specifically, we choose gauge fields with the following constant self-dual field strengths:

The components $F_{\mu\nu} = 0$ for $\mu\nu \neq 01, 10, 23, 32$ vanish, and we have

$$F_{01} = F_{23} = \frac{F^a}{2g_s}t^a\,, \quad F^a_{01} = \frac{F^a}{2g_s}\,, \quad F^a = Fn^a\,, \tag{4.7a}$$

with a constant vector $n^a$ with $n^a n^a = 1$. The field strength (4.7a) can be generated from the gauge fields

$$A^a_\mu = -\frac{1}{2}F^a_{\mu\nu}x_\nu\,. \tag{4.7b}$$

Evidently, the configuration is self-dual,

$$F_{\mu\nu} = \tilde{F}_{\mu\nu}\,, \quad \text{with} \quad \tilde{F}_{\mu\nu} = \frac{1}{2}\epsilon_{\mu\nu\rho\sigma}F_{\rho\sigma}\,, \tag{4.7c}$$

and is covariantly constant, $[D_\rho\,, F_{\mu\nu}] = 0$.

The classical action and the classical potential $\mathscr{W}_{\text{cl}}$ as well as the color condensate (4.1) is obtained from the field strength squared, which reads for the configuration (4.7),

$$F_{\mu\nu}F_{\mu\nu} = \frac{F^2}{g_s^2}(n^a t^a)^2\,, \qquad F^a_{\mu\nu}F^a_{\mu\nu} = \frac{1}{g_s^2}F^2\,. \tag{4.8}$$

For example, for the configuration (4.7) with (4.8), the classical potential reduces to

$$\mathscr{W}_{\text{cl}}(F^a) = \frac{1}{2}\,\text{tr}_{\text{f}}F^aF^b\,t^at^b = \frac{1}{4g_s^2}F^2\,, \tag{4.9}$$

where $\text{tr}_{\text{f}}$ stands for the group trace in the fundamental representation. From now on we only consider configurations of the type (4.7), and hence $\mathscr{W}_{\text{eff}}$ will be written as a function of $Fn^a$,

that is $\mathscr{W}_{\text{eff}}(F^a)$ instead of $\mathscr{W}_{\text{eff}}(F_{\mu\nu})$. The factor $1/g_s^2$ in (4.8) reflects the RG-scaling of the field strength, and has been introduced for convenience. Moreover, as both the gauge fields and the field strength in (4.7b) point in direction $n^a$ of the algebra, they can be rotated into the Cartan subalgebra without loss of generality.

Below, we briefly discuss $SU(2)$ and $SU(3)$ gauge groups, the former case as the simplest example, the latter case for its physical relevance:

In the $SU(2)$ gauge group, the Cartan subalgebra is generated by $t^3 = \sigma^3/2$ and the self-dual field strength (4.7) is given by

$$F_{01} = F_{23} = \frac{F}{2g_s}\, t^3 . \tag{4.10}$$

We have already discussed above that in $SU(2)$ the symmetric group invariant $d^{abc}$ vanishes, and hence $\chi^{AB}_{SU(2)} = 0$, implying $(F_{\mu\nu}F_{\mu\nu})^{AB} = 1/2 F^a_{\mu\nu}F^a_{\mu\nu}\delta^{AB}$ for all configurations. For (4.10) we find

$$(F_{\mu\nu}F_{\mu\nu})^{AB} = \frac{F^2}{2g_s^2}\delta^{AB} . \tag{4.11}$$

The explicit computation in this work is done for the physical gauge group $SU(3)$ with the Cartan generators $t^3, t^8$. These are related to the Gell-Mann matrices by $t^a = \lambda^a/2$, the respective vector $n$ has the components $n^a = 0$ for $a \neq 3, 8$. A self-dual field strength (4.7) is given by

$$F_{01} = F_{23} = \frac{F}{2g_s}\left(n^3 t^3 + n^8 t^8\right). \tag{4.12}$$

The octet condensate operator (4.1) for the configuration (4.12) reads

$$\chi^{AB} = \frac{F^2}{2g_s^2}\Big[n^a n^b \left\{t^a\,,\, t^b\right\}^{AB} - \frac{1}{3}\delta^{AB}\Big] = \frac{F^2}{2g_s^2}\delta^{AB}\left[\delta^{A1}\nu_+ + \delta^{A2}\nu_- + \delta^{A3}\nu_3\right], \tag{4.13}$$

where

$$\nu_\pm = \frac{1}{2}\left(\frac{n^8}{\sqrt{3}} \pm n^3\right)^2 - \frac{1}{3}, \qquad \nu_3 = \frac{2}{3}(n^8)^2 - \frac{1}{3}. \tag{4.14}$$

where the trace(less) condition, $\chi^{AA} = 0$, translates into $\nu_+ + \nu_- + \nu_3 = 0$ with $(n^3)^2 + (n^8)^2 = 1$.

Non-vanishing octet condensate expectation values are in one to one correspondence to non-trivial expectation values of its corresponding gauge-invariant eigenvalues. Hence, a non-trivial expectation value of the field strength triggers one for the octet condensate $\chi^{AB}$ and other color condensate operators. Therefore, in Section 4.3, we compute the effective potential for covariantly constant field strength or rather $\mathscr{W}_{\text{eff}}[Fn^a]$ for the field strength amplitude $Fn^a$ defined in (4.7a), and the constant algebra element $n^a t^a$ is rotated into the Cartan subalgebra. The respective effective potential is shown in Figure 4.1 for the physical $SU(3)$ case with the two Cartan components $F_{01}n^3$ and $F_{01}n^8$. The absolute minima are related by Weyl reflections.

Our explicit computation of the effective gluon mass is based on an expansion about the minimum $\langle F\rangle(n^a)$ in the three-direction with $n^a = \delta^{a3}$. In $SU(2)$ this is the Cartan direction,

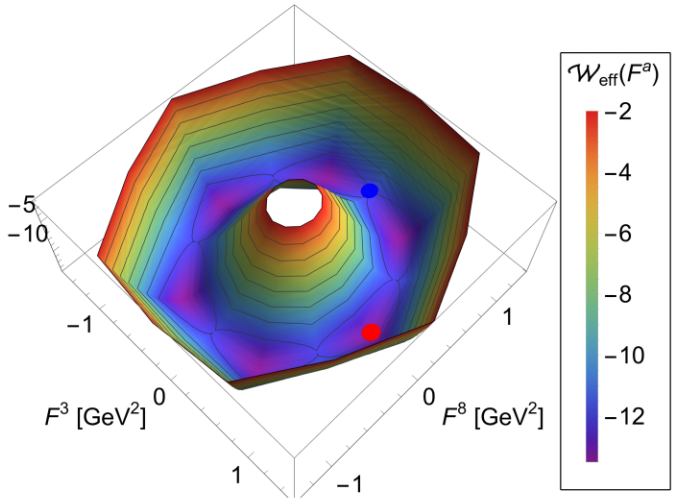


Figure 4.1.: Effective potential $\mathcal{W}_{\text{eff}}(F^a)$ in the plane spanned by the Cartan subalgebras. The position of the non-trivial global minimum is highlighted in red.

and in $SU(3)$ one of the absolute minima points in the three-direction, see Figure 4.1. Then, the expansion about the minimum reads

$$F^a_{01} = F^a_{23} = \frac{\langle F \rangle}{2g_s}\delta^{a3} + \mathcal{O}(a)\,, \tag{4.15}$$

for both gauge groups, where $a_\mu$ is the gauge field, that carries the fluctuations about the field strength expectation value. Note that the gauge field, that generates (4.16) also points in the Cartan direction. We find with (4.7b),

$$A^a_\mu = \frac{\langle F \rangle}{4g_s}\Big(x_0\delta_{\mu 1} - x_1\delta_{\mu 0} + x_2\delta_{\mu 3} - x_3\delta_{\mu 2}\Big) + a_\mu\,. \tag{4.16}$$

The fluctuation field $a_\mu$ that carries the dynamics of the gauge field, leading to the $\mathcal{O}(a)$-terms in (4.15). Within this setting we shall derive our estimates for the effective gluon mass as well as discussing constraints and bounds for this mass.

### 4.1.3. Condensates and the gluon mass gap

It is left to discuss the emergence of an effective gluon mass term in the presence of gluon condensates via the expectation value $\langle F^a_{\mu\nu}\rangle \propto t^3$ in (4.15), or any other algebra direction. This expectation value is computed from the effective potential $\mathcal{W}(F^a)$ discussed in 4.1.2.

Expanding the effective potential in terms of the gauge field $a_\mu$ leads to contributions of the effective potential to the $n$-point functions of the gauge field, including the two-point function. However, no contribution to the mass operator in the $a$-direction, $A^a_\mu A^a_\mu$, is generated. In particular no mass contribution in the Cartan $a = 3$ direction is induced, as is readily shown for $SU(2)$. In the following, we will concentrate on the latter contribution and obtain the color blind mass by a color average discussed in Appendix B.2.1.

While the effective potential does not contribute to the effective mass term, the latter receives contributions from other terms in the full, gauge invariant quantum effective action $\Gamma[A]$. Such an action can be defined within the background field approach, which will be detailed in

Section 4.2. For the time being we simply assume its existence and consider the higher order term

$$\Gamma_F[A] = \frac{Z_F}{4}\int_x (D_\mu F_{\nu\rho})^a (D_\mu F_{\nu\rho})^a \,, \tag{4.17}$$

where $Z_F$ is the wave function renormalisation of the condensate term. Equation (4.17) is the lowest order term that generates an effective gluon mass term within an expansion about the condensate $\langle F\rangle$. An obvious generalisation of (4.17) is provided by

$$\frac{1}{4}\int_x (D_\mu F_{\sigma\rho})^b Z_F{}^{ab}_{\rho\sigma\alpha\beta} (F_{\mu\nu})(D^b_\mu F_{\alpha\beta})^a \,, \tag{4.18}$$

with $Z_F{}^{ab}_{\rho\sigma\alpha\beta}(0) = Z_F \delta_{\sigma\alpha}\delta_{\rho\beta}\delta^{ab}$. In the following we will use the approximation

$$Z_F{}^{ab}_{\rho\sigma\alpha\beta}(\langle F_{\mu\nu}\rangle) \approx Z_F{}^{ab}_{\rho\sigma\alpha\beta}(0) \,, \tag{4.19}$$

hence only considering the term (4.17).

Equation (4.17) leads to an effective gluon mass, but does not contribute to (covariantly constant) solutions of the equations of motions as its first field derivative vanishes for covariantly constant field strengths. The relevant contribution to the effective gluon mass term is obtained by expanding (4.17) in powers of the gauge field, while treating the field strength within the expansion (4.15). To that end we conveniently recast (4.17) into the form

$$\Gamma_F[A] = -\frac{Z_F}{2}\int_x F^{CB}_{\nu\rho}(D^2)^{BA} F^{AC}_{\nu\rho} \,, \tag{4.20}$$

where the factor $1/2$ in (4.17) is now carried by the trace in the fundamental representation. The $\mathcal{O}(A^2)$ term is given by

$$\Gamma_F[A] = \frac{Z_F}{2}\, g_s^2 \int_x (F_{\nu\rho}F_{\nu\rho})^{AB} (A_\mu A_\mu)^{BA} + \cdots \,, \tag{4.21}$$

and we expand $(F_{\nu\rho}F_{\nu\rho})^{AB}$ about the field strength expectation value (4.15). This implies a non-vanishing condensate expectation value for (4.1) as well as non-vanishing values for other color condensate operators. The expansion about (4.15) leads us to

$$(F_{\nu\rho}F_{\nu\rho})^{AB} = \frac{1}{g_s^2}\langle F\rangle^2 [(n^a t^a)^2]^{AB} + \mathcal{O}(A) \,. \tag{4.22}$$

We drop the higher order terms in (4.22) and insert it in (4.21), to wit,

$$\Gamma_F[A] \simeq \frac{Z_F}{2}\langle F\rangle^2 \int_x \mathrm{tr}_{\mathrm{f}}(t^3)^2 A_\mu^2 + \cdots \,, \tag{4.23}$$

Now we evaluate (4.23) for the configurations (4.7), which leads to our final expression for the effective gluon mass triggered by an expectation value of the field strength proportional to $t^3$.

We first discuss the simple example of an $SU(2)$ gauge group. There, the configuration (4.15) leads to an $F_{\mu\nu}^2$ that is proportional to the identity tensor $\mathbb{1}$ in the algebra, as $4(t^3)^2 = \mathbb{1}$. Indeed,

as discussed below (4.10), general field strength tensors lead to diagonal $F^2_{\mu\nu}$. In summary, in $SU(2)$, a field strength condensate in the $t^3$-direction leads to

$$\Gamma_F[A] \simeq \frac{1}{2} m_3^2 \int_x A^a_\mu A^a_\mu + \cdots , \quad m_3^2 = \frac{Z_F}{8} \langle F \rangle^2 , \tag{4.24}$$

with a uniform mass for all gluons. The subscript $_3$ indicates that, while uniform, the mass is generated by $\langle F^a_{\mu\nu} \rangle \propto \delta^{a3}$. Importantly, (4.24) entails that a color condensate leads to gluons with an effective mass. However, the current procedure with an expansion about a non-vanishing field strength does not allow to directly infer the full effective gluon mass obtained in a color blind computation from $m_3^2$ in (4.24). At this state we only can offer estimates, whose derivation is deferred to the end of the present section.

Before we come to these estimates, we proceed with the $SU(3)$ example. There, we also use the Cartan-valued configuration (4.15) (with $n^8 = 0$), as one of the absolute minima in the full effective potential $\mathscr{W}_{\text{eff}}$ points in this direction, see Figure 4.1. In contradistinction to $SU(2)$, the square $4(t^3)^2$ is not the identity matrix in the algebra, but a projection onto the first two colors,

$$(t^3)^2 = \frac{1}{4} \delta^{AB} \left( \delta^{A1} + \delta^{A2} \right) . \tag{4.25}$$

As expected, the expansion about a minimum of the field strength, tantamount to one about the octet condensate (4.1), breaks color, and indeed, the gluon with the third color is massless if only considering contributions from $\Gamma_F$. Hence, while the present expansion shows, that the gluons acquire an effective mass term $\propto \delta^{ab}$, the relation of its *necessarily color blind* strength $m_A^2$ to the color-sensitive masses derived here is not straightforward.

Therefore, in the present work we simply deduce self-consistency constraints for the effective mass $m_A^2$ starting with the gluon mass $m_3^2$, inferred from a field strength in the $t^3$ direction. To begin with, color symmetry can be restored by averaging over global color rotations as always implied in lattice simulations as well as in most computations in functional QCD. After this averaging, all masses are identical and non-vanishing. A color average of (4.23) leads us to

$$\Gamma_{A^2}[A] = \frac{Z_F}{2} f_{\text{av}}(N_c) \langle F \rangle^2 \int_x A^a_\mu A^a_\mu , \tag{4.26}$$

with $f_{\text{av}}(N_c)$ encodes the color average of the factor $(t^3)^2$ in (4.23),

$$f_{\text{av}}(N_c) = \langle (t^3)^2 \rangle_{\text{av}} . \tag{4.27}$$

The color average in (4.27) necessarily leads to a color insensitive sum over all generators squared in the fundamental representation, which is simply the second Casimir $C_2(N_c) = (N_c^2 - 1)/(2N_c)$ in the fundamental representation times the identity matrix. Moreover, there is an undetermined prefactor $c_{\text{av}}(N_c)$, which leads us to

$$\left\langle (t^3)^2 \right\rangle_{\text{av}} = c_{\text{av}}(N_c) \sum_{a=1}^{N_c^2-1} (t^a)^2 = c_{\text{av}}(N_c) C_2(N_c) \mathbb{1} . \tag{4.28}$$

In the present work we will only provide constraints for $c_{\text{av}}(N_c)$ and hence for $f_{\text{av}}(N_c)$ in (4.27). For example, a 'natural' bound for the averaging factor is unity, $c_{\text{av}}(N_c) \leq 1$.

In summary we arrive at

$$m_A^2 = \frac{Z_F}{2} f_{\text{av}}(N_c) \langle F \rangle^2 , \tag{4.29}$$

In B.2.2 we will show, that self-consistency of the averaging in the large $N_c$ limit entails that in this limit $f_{\text{av}}(N_c) \propto N_c$. Indeed, this limit holds true for $N_c$-independent $c_{\text{av}}$. In particular this includes the case, where we saturate the 'natural' bound $c_{\text{av}} = 1$, leading to

$$f_{\text{av}} = (N_c^2 - 1)/(2N_c) . \tag{4.30}$$

For this saturation $f_{\text{av}}$ we obtain

$$m_A^2 = \frac{Z_F}{4} \frac{N_c^2 - 1}{N_c} \langle F \rangle^2 , \tag{4.31}$$

Equation (4.31) will eventually yield our value of the gluon mass. In Section 4.2, we present the formalism employed for working with the constant field strength configurations in (4.8). The computation of the minimum position $F^a = \langle F \rangle n^a$ is detailed in Section 4.3, and an estimate of the wave function of the condensate together with the result for the mass gap is presented in Section 4.4.

## 4.2. Background field approach

The condensate $\langle F \rangle$ for the field strength configuration of (4.12) is given by the minimum of an effective potential $\mathscr{W}_{\text{eff}}(F\, n^a)$, derived from a gauge invariant effective action $\Gamma[A]$, see (4.6). Such an action is defined in the background field approach [224], building on a linear decomposition of the full gauge field $A_\mu$ into a fluctuating and background field. This linear split is given by $A_\mu = \bar{A}_\mu + a_\mu$, where $a_\mu$ denotes the fluctuation field and $\bar{A}_\mu$ the background field. On the quantum level, this relation has to be augmented with the respective wave function renormalisations $Z_{\bar{A}} = Z_{g_s}^{-2}$ for the background field $\bar{A}_\mu$ and $Z_a$ for the fluctuation field $a_\mu$, as the two fields carry different RG scalings: As indicated above, the background field scales inversely to the strong coupling, while the fluctuation field carries the RG-scaling of the gauge field in the underlying gauge without background field. The gauge fixing condition involves the background field,

$$\bar{D}_\mu a_\mu = 0 , \tag{4.32}$$

with the background covariant derivative $\bar{D} = D(\bar{A})$, see (2.5). Note, that (4.32) is invariant under background gauge transformations,

$$a \to a + i[\omega, a] , \qquad \bar{A} \to \bar{A} + \frac{1}{g_s} \bar{D}\omega , \tag{4.33}$$

implying a standard gauge transformation for the full gauge field: $A_\mu \to A_\mu + (1/g_s) D\omega$. Consequently, the full gauge-fixed classical action is invariant under (4.33), and so is the full effective action $\Gamma[\bar{A}, a]$. Moreover, the single-field background effective action $\Gamma[A] := \Gamma[A, 0]$ is gauge invariant and can be expanded in gauge invariant operators. For this reason, it also allows for a more direct access to observables. In what follows we use the potential condensate background (4.7).

### 4.2.1. The background effective action and condensates

The gauge invariance of the background effective action allows us to embed the momentum-dependent kinetic terms and vertices in an expansion about a vanishing gauge field in full gauge invariant terms that reduce to the original ones for $A_\mu \to 0$. An important example is given by the (transverse) kinetic term of the gauge field, see e.g. [88, 89, 211],

$$\Gamma[A] \propto \frac{1}{2}\int_p A^a_\mu(p)\, Z_A(p^2)\, p^2\, \Pi^\perp_{\mu\nu}(p) A^a_\nu(-p)\,, \tag{4.34}$$

with the abbreviation $\int_p = \int d^4p/(2\pi)^4$, and the transverse and longitudinal projection operators

$$\Pi^\perp_{\mu\nu}(p) = \delta_{\mu\nu} - \frac{p_\mu p_\nu}{p^2}\,, \qquad \Pi^\parallel_{\mu\nu}(p) = \frac{p_\mu p_\nu}{p^2}\,. \tag{4.35}$$

The kinetic operator $Z_A(p^2)p^2$ is identified as the $A_\mu \to 0$ limit of the second field derivative of a gauge invariant term in the effective action $\Gamma[A]$. This leads us straightforwardly to the parametrisation

$$\Gamma[A] = \frac{1}{2}\int \mathrm{tr} F_{\mu\nu} f_{A,\mu\nu\rho\sigma}(D) F_{\rho\sigma} + \cdots\,, \tag{4.36a}$$

with the split

$$\begin{aligned} f_{A,\mu\nu\rho\sigma}(D) = &\frac{1}{2} Z_A(\Delta_s)(\delta_{\mu\rho}\delta_{\nu\sigma} - \delta_{\mu\sigma}\delta_{\nu\rho}) \\ &+ F_{\gamma\delta} f_{A,\gamma\delta\mu\nu\rho\sigma}(D)\,. \end{aligned} \tag{4.36b}$$

In (4.36b), we have introduced the spin-$s$ Laplacians

$$\Delta_0 = -D^2\,, \qquad \Delta_{1,\mu\nu} = \mathscr{D}_{T,\mu\nu} = -D^2\delta_{\mu\nu} + 2ig_s F_{\mu\nu}\,, \tag{4.36c}$$

see also (B.20). Equation (4.36b) represents the most general parametrisation for a covariant function coupled to two field strengths. Since $f_{A,\gamma\delta\mu\nu\rho\sigma}$ is a function of the Laplacian $D$, higher order terms in the field strength tensor are contained in the second term of (4.36b). For $A_\mu = 0$, all these decompositions reduce to their the momentum-dependent versions. In particular, the kinetic term (4.34) is obtained from (4.36b) by taking two gauge field derivatives at $A = 0$.

A further relevant example is the sum of the classical action and the term $\Gamma_F$ in (4.17) that generates the effective gluon mass. This combination is obtained with

$$Z_A(-D^2) = Z_A - Z_F D^2\,, \quad f_{A,\gamma\delta\mu\nu\rho\sigma} = 0\,. \tag{4.37}$$

Here, $Z_A$ is the constant background wave function renormalisation multiplying the classical action, which also entails $Z_A = Z_{g_s}^{-2}$.

The example given in (4.37) is central for two reasons: Firstly, it demonstrates how the condensate studied in this work emerges from the general, gauge-invariant form of the effective action (4.36a), which is defined in the next section within the background field formalism. Secondly, it establishes a link between the wave function renormalisation of the condensate and the kinetic operator of the gluon field $Z_A(\Delta_s)$. More explicitly, due to the generality of the split (4.36b), (4.37) entails that the wave function renormalisation of the condensate (4.17) is

simply given by the $D^2$-coefficient of the dressing function of the gluon propagator. In the limit of vanishing background, this simply corresponds to the $p^4$-term in the gluon propagator.

Note that the use of different $\Delta_s$ in the split (4.36b) leads to different forms for $f_{\mu_1\cdots\mu_6}$, thus modifying the parametrisation of the kinetic term. Still, the different field modes carry different spin, and the use of the respective Laplacians makes the split in (4.36b) to be the most natural. Typically, higher order terms within this split are suppressed in the effective action. For example, the second derivative of the classical Yang-Mills action is given by $\Delta_1 = \mathscr{D}_T$, multiplied by a covariant transverse projection operator. For covariantly constant fields with $[D, F] = 0$, we get

$$\frac{\delta^2}{\delta A_\rho \delta A_\sigma}\frac{1}{2}\int_x \mathrm{tr} F_{\mu\nu}^2 = \mathscr{D}_{T,\rho\gamma}\,\Pi^\perp_{\gamma\sigma}(D)\,, \tag{4.38}$$

where the trace is taken in the fundamental representation. Above, we introduced the covariant transverse and longitudinal projections,

$$\Pi^\perp_{\mu\nu}(D) = \delta_{\mu\nu} - \Pi^\parallel_{\mu\nu}(D)\,, \quad \Pi^\parallel_{\mu\nu}(D) = D_\mu \frac{1}{D^2} D_\nu\,. \tag{4.39}$$

Equation (4.39) defines a decomposition in a covariantly transverse subspace with $D_\mu \Pi^\perp(D) = 0$. It is complete, $\Pi^\perp(D) + \Pi^\parallel(D) = \mathbb{1}$, and trivially orthogonal. Finally, the operators have the projection property $(\Pi^\perp(D))^2 = \Pi^\perp(D)$ and $(\Pi^\parallel(D))^2 = \Pi^\parallel(D)$.

### 4.2.2. Gluon and ghost two-point functions

When supplemented by a wave function renormalisation $Z_A(\mathscr{D}_T)$, (4.38) provides a very good approximation of the full two-point function of the background gluon. This suggests the split in (4.36b) with the spin one Laplacian $\Delta_1 = \mathscr{D}_T$ for the transverse two-point function, and with the second term being subleading,

$$\Gamma^{(2,0)}_{AA,\mu\nu}[A,0] = Z_A(\mathscr{D}_T)\,\mathscr{D}_{T,\mu\sigma}\,\Pi^\perp_{\sigma\nu}(D) + F_{\gamma\delta}\,\Delta f_{A,\gamma\delta\mu\sigma}(D)\,\Pi^\perp_{\sigma\nu}(D)\,, \tag{4.40}$$

where $\Delta f_{A,\gamma\delta\mu\nu}$ is a combination of derivatives of $f_{A,\mu\nu\rho\sigma}$ fully contracted with powers of the field strength, see (4.36b), and $\bar{A} = A$. The transversality of (4.40) follows from the gauge invariance of the background effective action, as does its covariance. In (4.40) we have used the notation

$$\Gamma^{(n,m)}_{\bar{A}^n\phi_{i_1}\cdots\phi_{i_m}}[\bar{A},\phi] = \frac{\Gamma[\bar{A},\phi]}{\delta\bar{A}^n\delta\phi^m}\,, \qquad \phi = (a,c,\bar{c})\,, \tag{4.41}$$

with $\phi$ denoting the ghost and gluon fluctuation field. We shall use the split (4.36b) leading to (4.40) and similar natural splits for the covariant versions of the momentum dependent two-point functions, thus going from the Landau gauge to the Landau-DeWitt gauge.

In particular one finds, that a similar line of arguments holds true for the kinetic operator $Z_a(p^2)p^2$ of the fluctuation field $a_\mu$,

$$\Gamma^{(0,2)}_{aa,\mu\nu}[0,0] = Z_a(p^2)\,p^2\Pi^\perp_{\mu\nu}(p) + \frac{1}{\xi}p^2\Pi^\parallel_{\mu\nu}(p)\,, \tag{4.42}$$

where (4.35) was employed, and a diagonal form in the algebra, $\mathbb{1}^{ab} = \delta^{ab}$, is implied. Background gauge invariance entails that $\Gamma^{(0,2)}[A,0]$ is a covariant operator under the background gauge transformations (4.32). In consequence, the transverse part of $\Gamma^{(0,2)}_{aa}[A,0]$ can be

parametrised by the generic form of a background gauge covariant function already employed in (4.36b), i.e.,

$$\Gamma^{(0,2)}_{aa,\mu\nu}[A,0] = Z_a(\mathscr{D}_T)\,\mathscr{D}_{T,\mu\sigma}\,\Pi^{\perp}_{\sigma\nu}(D) - \frac{1}{\xi}D^2\,\Pi^{\parallel}_{\mu\nu}(D) + F_{\gamma\delta}\,\Delta f_{a,\gamma\delta\mu\sigma}(D)\,\Pi^{\perp}_{\sigma\nu}(D)\,. \tag{4.43}$$

In (4.43) we have used the spin-1 Laplacian $\Delta_1 = \mathscr{D}_T$ defined in (4.36c) in the wave function renormalisation $Z_a$, since the transverse fluctuating gluon is a spin-1 field. For two-flavour QCD, the validity of such covariant expansions has been confirmed explicitly for the quark-gluon vertex, whose non-classical tensor structure can be related to higher order gauge-invariant terms $\bar{q}\not{D}^n q$ [48].

Finally, in the case of the ghost two-point function we parametrise

$$\Gamma^{(0,2)}_{c\bar{c}}[A,0] = -D^2 Z_c(-D^2) + F_{\mu\nu}\,\Delta f_{c,\mu\nu}(D)\,, \tag{4.44}$$

where the use of the spin zero Laplacian in (4.44) is suggested by the ghost being a spin zero field. For $A_\mu = 0$, the ghost two point function in (4.44) reduces to that in standard covariant gauges.

The infrared behaviour of $Z_a(p)$ in the Landau gauge is an extensively studied subject, both on the lattice as well as with functional approaches, see e.g. [92, 104, 197, 198, 200, 201]. In particular, two types of solutions have emerged:

(*i*) The *scaling* solution [90] has an infrared vanishing gluon propagator and a scaling infrared behaviour,

$$Z_{a,\mathrm{IR}} \propto (-D^2)^{-2\kappa}\,, \qquad Z_{c,\mathrm{IR}} \propto (-D^2)^{\kappa}\,. \tag{4.45}$$

with $\kappa \approx 0.6$. In (4.45) we have dropped terms proportional to the field strength. Note that in this IR solution the ghost is infrared divergent. For the present computations we shall use the fRG results from [47] within a quantitatively reliable approximation, for respective DSE results see [225].

(*ii*) An entire family of *decoupling* or *massive* solutions [96], where the gluon propagator and the ghost dressing function saturate at finite non-vanishing values at the origin, in agreement with the IR behaviour found in large-volume lattice simulations. Specifically, we have

$$Z_{a,\mathrm{IR}} \propto \frac{1 + c_a D^2 \log\left(\frac{-D^2}{\Lambda^2_{\mathrm{QCD}}}\right)}{-D^2}\,, \qquad Z_{c,\mathrm{IR}} \propto c_c\,. \tag{4.46}$$

Note that the fluctuating propagator can be mapped to the background one by means of an exact identity, characteristic of the Batalin-Vilkoviski formalism, which involves a special two-point function, see e.g. [200, 226].

We emphasise that both types of solutions agree quantitatively for momenta $p^2 \gtrsim \Lambda^2_{\mathrm{QCD}}$, with $\Lambda_{\mathrm{QCD}}$ related to the infrared mass gap. As a result, the deviations induced to phenomenological observables by the use of either type are quantitatively minimal, see e.g. [48, 227]. In fact, in the present work we will cover all potential solutions listed above, and show that their IR differences are immaterial to the central question of dynamical condensate formation.

Both types of solutions, (4.45) and (4.46), are infrared irregular, and do not admit a Taylor expansion about $-D^2 = 0$. Instead, we can expand the wave function renormalisations about

the infrared asymptotics. Making use of the relation between the condensate and gluon wave function renormalisation established in (4.37), we arrive at

$$Z_{a/A}(-D^2) = Z_{a/A,\mathrm{IR}}(-D^2) + (-D^2)\, Z_{a/A,F} + \mathcal{O}(D^4)\,, \tag{4.47}$$

for both $Z_a$ and $Z_A$ with $Z_{a/A,\mathrm{IR}}$ defined in (4.45) and (4.46), and $Z_{a/A,F}$ is the wave function $Z_F$ for fluctuation field and background field respectively. The first term $Z_{a/A,\mathrm{IR}}$ carries the irregular infrared asymptotic behaviour, and $Z_{a/A,F}$ is the (uniquely defined) constant prefactor of the linear term in $-D^2$. The expansion (4.47) makes explicit that scaling and decoupling solutions only differ in the IR leading term $Z_{a/A,\mathrm{IR}}$, while coinciding in the expansion in powers of $-D^2$. This in particular entails that the overlap between gluon propagator and the condensate (4.17) is independent of the leading IR behaviour of the respective solution, scaling or decoupling.

We are ultimately interested in the physical mass gap $m_{\mathrm{gap}}$ of the fluctuation field $a_\mu$ resulting from the condensate term (4.17) in the full field $A = \bar{A} + a$. The derivation of the fluctuation field mass gap works analogously to that of (4.29) in Section 4.1.3 leads to a contribution $\Gamma_{\mathrm{gap}}$ in the effective action with

$$\Gamma_{\mathrm{gap}} = \frac{1}{2} m_{\mathrm{gap}}^2 \int_x a_\mu^b a_\mu^b\,, \tag{4.48}$$

where the effective gluon mass of the fluctuation gluon $a_\mu$ is given by

$$m_{\mathrm{gap}}^2 = \frac{Z_{\mathrm{cond}}}{2} f_{\mathrm{av}}(N_c) \langle F \rangle^2\,. \tag{4.49}$$

with $Z_{\mathrm{cond}} = Z_{a,F}$ and the averaging factor $f_{\mathrm{av}}(N_c)$ introduced in (4.26) and discussed there. In particular we have $Z_F = Z_{A,F} \neq Z_{\mathrm{cond}}$. The wavfunction $Z_F$ is used in (4.29) for the mass term in a gauge invariant effective action, and in the present approach this is the background field effective action. The difference between the wave functions is the ratio of the respective wave functions of the background and fluctuation gluons.

In (4.37) we observed that the wave function renormalisation $Z_{\mathrm{cond}}$ of the condensate studied here generally appears in the dressing function of the respective gluon propagator, cf. (4.47). This connection will be utilised in Section 4.1.3 to determine $Z_{\mathrm{cond}}$ from the input gluon propagators [47] employed in the computation of the background effective potential $\mathscr{W}_{\mathrm{eff}}(F^a)$. Supplemented with the non-trivial effective potential minimum $\langle F \rangle$, this procedure eventually lead to our heuristic estimate of the gluon mass gap in Landau gauge Yang-Mills theory.

## 4.3. Background effective potential

Now we compute the value of the field strength condensate $\langle F_{\mu\nu} \rangle$ discussed in Section 4.1.2. For this purpose, we update the fRG computation done in [211] to a self-consistent one with fRG precision gluon and ghost propagators from [47]. In Section 4.3.1 we briefly review the approach, and in Section 4.3.3 we report on the results for the condensate.

### 4.3.1. Flow of the background effective potential

For the full computation we resort to the functional renormalisation group approach, for QCD-related reviews see [104, 127, 202, 203, 228, 229]. In this approach, an infrared regulator $R_k(p)$ is added to the classical dispersion. In the infrared, that is $p/k \to 0$, the regulator endows all

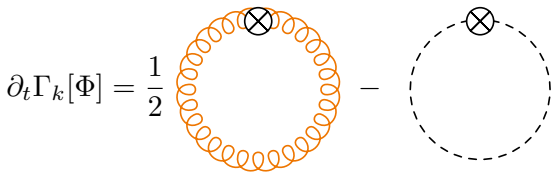

Figure 4.2.: Depicition of the flow equation for the effective action, (4.50). Spiralling orange lines depict the full field-dependent gluon propagator $\langle AA\rangle_c = G_{aa}[\bar{A},\phi]$, dashed back lines depicted the full field-dependent ghost propagator $\langle c\bar{c}\rangle_c = G_{c\bar{c}}[\bar{A},\phi]$, where the subscript stands for connected part. The circled cross stands for the regulator insertions $\partial_t R_a$ (gluon loop) and $\partial_t R_c$ (ghost loop).

fields with a mass, typically proportional to the cutoff scale $k$. In addition, the regulator $R_k(p)$ vanishes rapidly as $p/k \to \infty$, and the ultraviolet physics is not modified. The change of the scale dependent effective action, $\Gamma_k$, under a variation of the cutoff scale $k$ is described by the flow equation. In the background field approach it reads

$$\partial_t \Gamma_k[\bar{A},\phi] = \frac{1}{2}\operatorname{Tr} R_a[\bar{A}]\, G_{aa}[\bar{A},\phi] - \operatorname{Tr} R_c[\bar{A}]\, G_{c\bar{c}}[\bar{A},\phi], \tag{4.50}$$

where $t = \log k/\Lambda$ is the (negative) RG-time, and $G_A, G_c$ are the fluctuation propagators of gluon and ghost respectively,

$$G_{\phi_1\phi_2}[\bar{A},\phi] = \left[\frac{1}{\Gamma_k^{(0,2)}[\bar{A},\phi] + R_k[\bar{A}]}\right]_{\phi_1\phi_2}. \tag{4.51}$$

The traces in (4.50) sum over momenta, Lorentz and gauge group indices, details can be found in Appendix B.2.4. The regulator function $R_k = (R_a, R_c)$ transforms covariantly under background gauge transformations, which preserve the background gauge invariance of the effective action. The current work utilises the propagator data from [47], which requires the use of the same regulators for our computation of the background effective potential. For details on the regulators see Appendix B.2.3.

For the derivation of the (background) field strength condensate we solve the equation of motion stemming from the effective potential $\mathscr{W}_{\rm eff}(F^a$ of covariantly constant field strength defined in (4.6). In the fRG approach it is obtained from its scale-dependent analogue,

$$\mathscr{W}_k(F^a) = \frac{1}{\mathscr{V}}\Gamma_k[A(F^a),0], \tag{4.52a}$$

with the full effective potential being defined at vanishing cutoff scale $k = 0$,

$$\mathscr{W}_{\rm eff}(F^a) = \mathscr{W}_{k=0}(F^a). \tag{4.52b}$$

The effective potential $\mathscr{W}_k$ is obtained by integrating the flow equation of the background effective action $\partial_t\Gamma_k[A(F),0]$, derived from (4.50) from the initial ultraviolet scale $k_{\rm UV}$ to the running cutoff scale $k$. The only input in this flow are the two-point functions $\Gamma_{aa}^{(0,2)}[A(F),0]$ and $\Gamma_{c\bar{c}}^{(0,2)}[A(F),0]$, which we can infer from Landau gauge results. This is the background

Landau-deWitt gauge with $\bar{A} = 0$. For vanishing background the two-point functions only depend on momenta, $\Gamma_k^{(0,2)}(p)$. We use the results from [47], with

$$\Gamma^{(0,2)}_{aa,k}(p) = p^2\, Z_{a,k}(p^2)\Pi^{\perp}(p) + p^2\left[\frac{1}{\xi} + Z^{\parallel}_{a,k}(p^2)\right]\Pi^{\parallel}(p)\,,$$
$$\Gamma^{(0,2)}_{c\bar{c}}(p) = p^2\, Z_{c,k}(p^2)\,, \tag{4.53}$$

with the transverse and longitudinal projection operators introduced in (4.35). In (4.53), $\mathbb{1}^{ab} = \delta^{ab}$ is implied in both two-point functions. The longitudinal dressing $Z^{\parallel}_{a,k}$ signals the breaking of BRST invariance due to the presence of the regulators, and vanishes in the limit $k \to 0$. There, the gluon two-point function in (4.53) reduces to that of (4.42). Moreover it is absent in the gluon propagator for the Landau gauge, $\xi \to 0$,

Now we switch on the background field and use the decomposition (4.43) for the transverse gluon two-point function. Moreover, we drop the second line proportional to $\Delta f_a$ comprising higher order terms. They are associated with non-classical tensor structures and can be shown to be small in the perturbative and semi-perturbative regimes. In the Landau-DeWitt gauge, only the gauge-fixing survives in the longitudinal propagator and we can drop the cutoff contribution $Z^{\parallel}_{a,k}$. For the ghost we use (4.44), where we drop the second term proportional to $\Delta f_c$. This leads us to

$$\Gamma^{(0,2)}_{aa,k}(p) \simeq \mathscr{D}_T\, Z_{a,k}(\mathscr{D}_T)\Pi^{\perp}(-D) - \frac{1}{\xi} D_\mu D_\nu\,,$$
$$\Gamma^{(0,2)}_{c\bar{c}}(p) \simeq -D^2\, Z_{c,k}(-D^2)\,, \tag{4.54}$$

valid for covariantly constant field strength with $[D, F] = 0$. For these configurations, the transverse projection operator commutes with functions of the Laplacians $\Delta_0$ and $\Delta_1$.

### 4.3.2. RG-consistent initial condition

The flow equation (4.52a) of the effective potential $\mathscr{W}_k(F^a)$ is readily obtained by inserting the approximations of (4.54) into the flow (4.50). The flow is evaluated for the generic condensate background (4.7). The details can be found in Appendix B.2.3. Finally, the effective potential $\mathscr{W}_{\text{eff}}(F^a)$ of Yang-Mills theory is obtained from the integrated flow. We arrive at

$$\mathscr{W}_k(F^a) = \mathscr{W}_{k_{\text{UV}}}(F^a) + \int_{k_{\text{UV}}}^{k} \frac{\mathrm{d}k'}{k'}\, \partial_{t'} \mathscr{W}_{k'}(F^a)\,, \tag{4.55}$$

where $\mathscr{W}_{k_{\text{UV}}}$ is well approximated by the classical potential (4.9) for a large initial cutoff scale $k_{\text{UV}}$. Perturbation theory is valid for these scales, and the background field effective action $\Gamma_{k_{\text{UV}}}[A]$ reduces to the classical Yang-Mills action of (2.9), augmented with a wave function renormalisation $Z_{A,k_{\text{UV}}}$. All other terms are suppressed by inverse powers of $k_{\text{UV}}$. This amounts to

$$\mathscr{W}_{k_{\text{UV}}}(F^a) = \frac{Z_{A,k_{\text{UV}}}}{4\, g_s^2} F^2 = \frac{F^2}{16\pi\alpha_s(k_{\text{UV}})}\,, \tag{4.56}$$

where

$$\alpha_s(k) = \frac{1}{4\pi}\frac{g_s^2}{Z_A(k)}\,, \quad \text{with} \quad Z_A(k_{\text{UV}}) = 1\,, \tag{4.57}$$

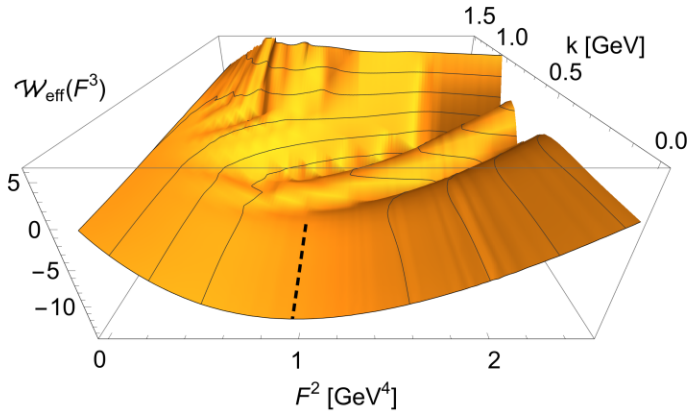


Figure 4.3.: Effective Potential as a function of $F^2$ with a field strength pointing in the $t^3$-direction: $(n^3, n^8) = (1, 0)$, and the cutoff scale $k$. The dashed line singles out the absolute minimum of $W(F)$, see (4.59). The substructure of the potential at cutoff scale $k \gtrsim 0.5\,\text{GeV}$ is related to the regulator used, see Appendix C.1.1. It leaves no trace in the potential for $k \to 0$.

and $g_s^2$ is the running coupling at the initial scale $k_{\text{UV}}$.

The onset of this asymptotic UV regime for cutoff scales $k \gtrsim k_{\text{on}}$ depends on the chosen regulator or rather its shape. Roughly speaking, the sharper the regulator drops of in momenta at about the cutoff scale, the larger is the onset scale $k_{\text{on}}$. For the ghost and gluon regulators underlying the computation of the propagators in [47], (B.17), we choose an initial scale $k_{\text{UV}} = 20\,\text{GeV}$. This is safely in the asymptotic UV regime of the regulators (B.17), as is also explicitly discussed in Appendix C.1.1. In summary, the computation is initialised at

$$\alpha_s(k_{\text{UV}}) = 0.184 \quad \text{with} \quad k_{\text{UV}} = 20\,\text{GeV}\,, \tag{4.58}$$

and the running coupling data are also taken from [47], which ensures the self-consistency of the computation.

In (4.57) we have used that the background wave function renormalisation $Z_A$ satisfies $Z_A^{-1} = Z_{g_s}^2$, a consequence of background gauge invariance. Moreover, RG-consistency, see e.g. [61, 127], enforces (4.57): the flow of the initial effective action with an infinitesimal change of the initial cutoff scale is given by the flow equation. Phrased in terms of the effective potential in (4.55), this is the simple requirement that $\mathcal{W}_k$ and in particular $\mathcal{W}_{\text{eff}} = \mathcal{W}_k$ is independent of $k_{\text{UV}}$. Then, differentiation of (4.55) with respect to $k_{\text{UV}}$ readily leads to (4.56). More details are deferred to Appendix C.1.1.

### 4.3.3. Results

The above derivation allows the numerical computation of the scale dependent effective potential $\mathcal{W}_k(F^a)$ by performing the integration in (4.55) up to the respective RG-scale $k$. The result is shown in Figure 4.3, which shows the $k$-dependent effective potential as a function of $F^2$, with a field strength pointing in the $t^3$-direction: $(n^3, n^8) = (1, 0)$. The condensate $\langle F \rangle$ is given by the solution of the equation of motion (EoM) for the effective potential $\mathcal{W}_{\text{eff}}(F^a)$, given by

$$\left.\frac{\partial \mathcal{W}_{\text{eff}}(F^a)}{\partial F}\right|_{F=\langle F\rangle} = 0\,, \tag{4.59}$$

for the generic field strengths of (4.12). The emergence of a non-trivial minimum is clearly visible in the non-perturbative regime $\lesssim 1$ GeV, and its position indicated with the black dashed line in Figure 4.3.

The gauge invariant information of the field strength $F_{\mu\nu}$ is stored in its eigenvalues, which do not change under (unitary) gauge transformations. In the present case, only the $F_{01} = F_{23}$ components and their anti-symmetric counterparts are non-vanishing, and they are proportional to a combination of the Cartan generators, see (4.12). The traces in the flow equation are in the adjoint representation, and the six non-vanishing eigenvalues of $n^3 t^3 + n^8 t^8$ are given by

$$\tau_{\pm}^{(1)} = \pm n^3\,, \qquad \tau_{\pm}^{(2)} = \pm\Big(\frac{1}{2}n^3 + \frac{\sqrt{3}}{2}n^8\Big), \qquad \tau_{\pm}^{(3)} = \pm\Big(\frac{1}{2}n^3 - \frac{\sqrt{3}}{2}n^8\Big), \tag{4.60}$$

for more details see e.g. [230, 231]. The global, degenerate minima in Figure 4.1 are located in the direction of the eigenvectors. The underlying Weyl symmetry maps the different minima into each other, and is seen in Figure 4.1.

From (4.59) we determine the expectation values or rather saddle point position of the condensate in both directions. We find that the expectation value in $n^3$-direction is a global minimum, while in the $n^8$-direction the EoM singles out a saddle point. Both points are indicated by the red and blue dots respectively in Figure 4.1. We determine the value of the minimum by interpolation,

$$\langle F\rangle^2_{\lambda_3} = 0.98(11)\,\mathrm{GeV}^4\,, \tag{4.61}$$

where the error is obtained by a variation of 2% in the initial coupling $\alpha_s$. More details on the RG-consistency of this procedure are provided in Appendix C.1.1. Equation (4.61) is the result of an $SU(3)$ computation without the $N_c$ rescaling.

As discussed below (4.12), the minimum in (4.61) is composed by the condensates of both $F^2$ and $F\tilde{F}$. In that sense, the value quoted in (4.61) should be interpreted as an upper estimate for the colorless condensate $\langle F^2\rangle$. The present first-principle Yang-Mills result (4.61) corroborates the phenomenological estimates, i.e. $\langle F^2\rangle = 0.854(16)\,\mathrm{GeV}^4$ [232], as already remarked in [211]. Indeed, the normalisation procedure used here is similar to that in the phenomenological computation. In contrast, both (4.61) and the phenomenological estimates disagree with the lattice estimate $\langle F^2\rangle = 3.0(3)\,\mathrm{GeV}^4$ [233]. The latter value is extracted from $\langle G^2\rangle = 0.077(7)$ in [233], and applying $\langle F^2\rangle = 4\pi^2\langle G^2\rangle$. In this context we remark that the total normalisation may differ, even though all procedures provide RG-invariant results: for example, one may multiply the respective result by the RG-invariant ratio of couplings at different momenta, $\alpha_s(p_1^2)/\alpha_s(p_2^2)$, resulting in a global factor. This amounts to mapping the factor $\alpha_s$ from one momentum scale to another. While we lack a comprehensive interpretation, we simply point out that the lattice definition involves $\alpha_s$ at a low momentum scale, conversely to the present procedure, and that used in phenomenological applications.

For comparison we also provide the saddle point value,

$$\langle F\rangle^2_{\lambda_8} = 0.85(11)\,\mathrm{GeV}^4\,, \tag{4.62}$$

which may be used for a further error estimate of the relation between octet and colorless condensates, as the octet condensate should be averaged over all color directions.

## 4.4. Gluon mass gap

The aim of this section is to use (4.49) and (4.61) for an estimate of the mass gap. Evidently, to accomplish this, the determination of the wave function renormalisation $Z_{\mathrm{cond}}$ is required.

Inspecting the condensate generating kinetic term, see (4.17), one finds that its analogue for the fluctuating gluon also contains contributions of the type

$$\frac{Z_{\text{cond}}}{2}\int_x a^a_\mu(\partial^2)^2\Pi^\perp_{\mu\nu}(\partial)a^a_\nu+\dots\,. \tag{4.63}$$

Hence, the kinetic term for the field strength not only gives rise to the condensate, but also overlaps with the gluon propagator. More specifically, as can be read off (4.63), the $p^4$-term of the fluctuation gluon two-point function carries the wave function renormalisation $Z_{\text{cond}}$ as a prefactor, as made explicit in (4.47).

Note that by means of (4.36a) and (4.37), the $p^4$-term must be solely given by (4.63), as $Z_A$ implicitly defined in (4.36b) encodes the full gluon propagator dressing function, see (4.34). In terms of an operator product expansion, $Z_{\text{cond}}$ can be extracted by determining the $p^4$-coefficient in the origin of the inverse input gluon propagator data from [47], used in the calculation of the condensate effective potential in Section 4.3. Utilising the knowledge of the analytic structure in IR for scaling and decoupling scenarios, the $p^4$-coefficient is extracted via a fit. These fits are given by

$$Z_{\text{fit}}(p^2)=Z_{\text{as}}(p^2)+Z_{p^2}+Z_{\text{cond}}\,p^2\,, \tag{4.64}$$

where only the infrared asymptotes $Z_{\text{as}}(p^2)$ distinguish different solutions. A detailed discussion of the fitting procedure is provided in Appendix C.1.2, and the respective fits $Z^{(\text{scal})}_{\text{fit}}$ and $Z^{(\text{scal})}_{\text{fit}}$ in comparison to the propagator data from [47] are depicted in Figure 4.4.

Equation (4.64) makes it apparent that scaling and decoupling solutions differ only in the infrared, where the $p^4$ term is subleading. Hence, determining $Z_{\text{cond}}$ from both data sets separately amounts to two different ways of determining the same quantity. Therefore, we combine both input propagators to determine the value of $Z_{\text{cond}}$. In doing so, we arrive at the value for the wave function renormalisation

$$Z_{\text{cond}}=0.162(7)\,\text{GeV}^{-2}\,. \tag{4.65}$$

Now we us the wave function renormalisation from (4.65), the condensate value $\langle F^2$ (4.30) as well as the saturation bound (4.30) for the averaging factor $f_{\text{av}}$ in the relation for the effective gluon mass (4.49). This leads us to

$$m_{\text{gap}}=0.325(20)\,\text{GeV}\,. \tag{4.66}$$

Equation (4.66) is the main result of the present work and provides an estimate for the effective gluon mass in the Landau gauge. The relatively large uncertainty in (4.66) originates predominantly from the error for $Z_{\text{cond}}$ in (4.65). In particular, it does not include a systematic error estimate, and is solely rooted in the small amount of data points for the gluon propagator of [47] in the deep IR.

A large source for the systematic error is the current lack of a quantitative color average as discussed in detail in Appendix B.2.1. Moreover, the field strength condensate (4.61) also receives contributions from the topological condensate $\langle F\tilde{F}\rangle$, see the discussion there and below (4.12). Accordingly, we simply note that inserting the literature value from phenomenological $\langle F^2\rangle$ estimates [232] reduces the value in (4.66) to $m_{\text{gap}}=0.304(25)\,\text{GeV}$. The same value is obtained by the use of the saddle point value (4.62), which we use as an error estimate.

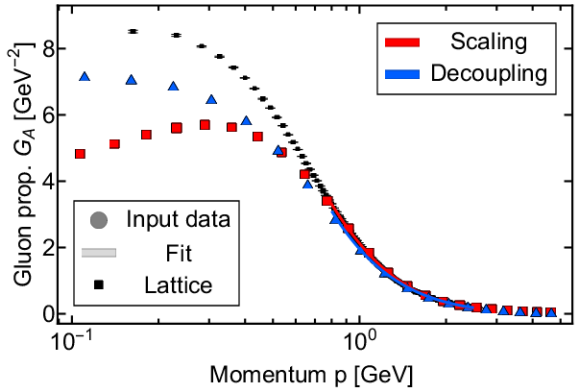


Figure 4.4.: Gluon propagators from [47] in the scaling (red) and decoupling (blue) scenario. Colored markers show the data. Solid lines show the respective fits from which the wave function renormalisation $Z_{\text{cond}}$ (cf. (4.63)) is computed, plotted over the fit interval. The fit Ansätze are given in (C.7), see also Appendix C.1.2 for details of the fitting procedure. The lattice data are that from [234] and [192, 194].

We can compare our result for the gluon mass gap (4.66) to that of the lattice data [234] shown in Figure 4.4, given by the value of the inverse lattice propagator in the origin. From the data point with smallest momentum we extract

$$m_{\text{gap}}^{(\text{lattice})} = 0.3427(8)\,\text{GeV}\,. \tag{4.67}$$

which agrees with our estimate (4.66) within the error bars.

A further direct test of the present results is provided by the comparison with the effective gluon mass in (C.16) obtained via the Schwinger mechanism with $m_{\text{gap}} = 0.320(35)\,\text{GeV}$. This is an alternative approach for the dynamical emergence of a gluon mass gap in the Landau gauge, for details see Appendix C.1.3. The results compare very well, which is to be expected as our propagator with the gluon mass gap agrees well with the lattice results, as does the propagator obtained with the Schwinger mechanism.

We emphasise again, that the investigation put forward here makes use of a colorless condensate and the *key assumption* of its direct relation to the color octet condensate, as discussed in Section 4.1.1. Therefore, our study should be understood as a qualitative one, proposing a possible mechanism for mass generation that yields a mass gap estimate with the right order of magnitude. In fact, the non-trivial compatibility of the present results for the effective gluon mass with that obtained from lattice propagators corroborates the aforementioned key assumption.

We close this section with the remark that, while the effective gluon mass or rather the gluon mass gap in the Landau or Landau-DeWitt gauge is a gauge variant quantity, its size is directly related to physical scales such as the string tension and the confinement-deconfinement temperature, see [88, 89]. Still, its value varies with the gauge as does its precise relation to the physical scales and mechanisms. Consequently, the numerical estimates of its value are rather disparate, ranging from a few hundred MeV up to 1 GeV, depending on the details of the approach and the definition employed, see e.g. [79, 96, 180, 196, 235–245]. Nonetheless, all these determinations convey information about the same gauge-invariant physical information, namely the Yang-Mills mass gap.

## 4.5. Summary and outlook

In the present work we have explored the dynamical emergence of a mass gap in the Yang-Mills correlation functions via the formation of color condensates, in the physical case with the $SU(3)$ gauge group one of these condensates is the octet condensate, see (4.1). Such a condensate may be triggered by a Higgs-type mechanism in low energy QCD, similar and potentially related to dynamical chiral symmetry breaking in QCD with the pion as pseudo-Goldstone bosons.

In the current work we have carried out a qualitative analysis within the fRG approach to QCD by computing the minimum $\langle F \rangle$ of the effective potential $W(F^a)$ in the three direction of the Cartan sub group. This non-vanishing field strength is related to non-vanishing color condensates as discussed in Section 4.1.2. We have computed the effective potential $\mathscr{W}(F^a)$ for covariantly constant field strength which develops a non-trivial minimum if quantum fluctuations are successively taken into account with the fRG flow, see Figure 4.1. The condensate value (4.61) is in good agreement with phenomenological estimates, but both disagree with lattice results. As discussed in Section 4.3.3, this latter discrepancy may be due to a difference in the normalisations employed.

The relation between the condensate and the effective mass gap is given by (4.49). We emphasise that the mass gap (4.49) triggered by the condensate depends on the RG-condition and naturally has the RG-properties of a mass function: while the condensate itself is independent of the RG-condition, the condensate wave function is not and carries the RG-properties of the inverse gluon propagator. Consequently, the mass gap derived from (4.49) has the RG scaling of the inverse gluon propagator, as it should. Accordingly, for a comparison of the results for the mass gap obtained here with that in the literature the potentially different RG-schemes and conditions have to be taken into account. Most fRG-computations including the present one are done in MOM$^2$, for a detailed discussion see [227].

These considerations result in our estimate of the gluon mass gap, $m_{\text{gap}} = 322(34)\,\text{MeV}$, which compares very well to the lattice estimate $m_{\text{gap}}^{(\text{lattice})} = 0.3427(8)\,\text{MeV}$ from [192, 194, 234] obtained after matching the momentum scales and the renormalisation point. We have also compared our result for the mass gap with that obtained with the longitudinal Schwinger mechanism within the framework of the pinch technique [200], see Appendix C.1.3 and the very recent analysis see [246]. This analysis leads to $m_{\text{gap}}^{(\text{Schwinger})} = 320(35)\,\text{MeV}$ which is in excellent agreement with our estimate.

In summary, the findings of the present work suggest that the gluon condensation as a mechanism for mass generation works well, and the key assumption in the present work, the direct relation between colorless and octet condensate holds. Beyond improving the systematic error of the numerical estimate, on theoretical grounds it would be desirable to establish a deeper connection between the Schwinger mechanism and the condensate formation.

As an outlook, the present computation can be upgraded with the dynamical inclusion of the composite octet condensate operator, discussed in Section 4.1.1. Then, the octet condensate is taken into account as an effective low energy degree of freedom, which resolves the underlying assumption of the current approximation, the equivalence of octet condensate and colorless condensate. It also allows us to study the relevance of a potentially non-trivial condensate dynamics. We hope to report on respective results in the near future.

# CHAPTER 5

# Discontinuous Galerkin methods in the fRG

*This chapter is a compilation of [1], [5] and [10]. The general concept of solving RG-flows within a numerical fluid dynamics setting is introduced at the example of the O(N) model. We discuss challenges of this formulation and report on technical improvements that were made along the way.*

In this chapter we introduce the computational tools, which we use to investigate the chiral phase structure of QCD within the fRG. Whilst keeping this specific purpose in mind, we find that these tools can be used in a much more general context: charting the phase structure of theories with competing order effects, (multi-)critical endpoints and lines of first and second order as well as crossover regimes. Even a qualitative access to some of the most eminent physics of phase transitions requires a firm quantitative grip on the non-trivial dynamics in the respective regimes. To chart the location of phase boundaries as well as their nature, the task turns out to be two-fold, with both aspects being deeply interconnected on a technical level:

The first task concerns first order phase transitions, which have recently been linked to shock formation in field space [65, 247]. This implies, that the occurrence of first order phase transitions or their absence can only be reliably predicted within a numerical implementation of the fRG approach that captures the emergence and evolution of shocks.

The second task concerns competing order effects, where even small changes in the flow can have qualitative impact on the resulting ground state. Accordingly, these challenges require both the resolution of momentum dependences of higher scattering kernels and a quantitative resolution of full field dependences in the fRG.

Consequently, for an access to the phase structure of generic theories ranging from highest to lowest momentum momentum scales within a numerical fRG approach, a numerically fully reliable and versatile framework, that captures the intricacies discussed above, is required.

A common truncation scheme in this case is the derivative expansion, which was briefly introduced in Section 3.2.2 or for a review see [104] and references therein. In this truncation scheme, the effective action is expanded in gradients of the field. To leading order, the dynamics is then encoded by the effective potential, whose flow is governed by a second order PDE, which we derive as an example in Section 5.1. Hence, solving Partial Differential equations (PDE) is an important task in the context of phase transitions within the fRG.

In recent years, this task has been approached by employing a variety of numerical methods for solving increasingly complex models and approximations. For example, the application of numerical fluid dynamics to FRG equations has been thoroughly investigated in zero-dimensions [248–250].

The dynamics of spontaneous symmetry breaking and convexity restoration in dimensions $d > 2$ has been tackled by introducing Discontinuous Galerkin methods (DG) in the large-$N$ limit [65]. An application of its naive extension to higher order derivatives, the direct DG (dDG) method, to the quark meson model at finite $N$ has provided results for the phase structure at high temperatures and around the critical point [1], see also Chapter 8 in this thesis. Moreover, these investigations found the potential for the creation of shock-waves in the RG-flows, emphasizing the advantage of using inherently discontinuous numerical methods. It was also found that the dDG, and hence all derived finite element methods, without further derivative reconstruction, fail to solve the RG-flows at high densities.

At high densities, the dominance of the $\sigma$-mode at finite $N$ introduces strong non-linear diffusive effects to the flow. Such effects lie beyond the scope of dDG methods and necessitate the introduction of higher order accurate schemes. Thus, the Local Discontinuous Galerkin (LDG) methods [251] were introduced to the fRG. They properly handle the more subtle structure of the second order derivatives in these equations, leading to enhanced numerical stability. Since the implementation of these schemes becomes increasingly complex, we provide a simple application to an O(N) model, see also [5]. Furthermore, we an open source version of the code is openly accessible at https://github.com/satfra/dune-FRGDG, combined with a detailed explanation of the code. The code is written as a module for the high performance PDE framework DUNE [252].

In the following we introduce the fRG flows for a scalar O(N) model in Section 5.1. These equations are then used to explain the Discontinuous Galerkin discretisation in Section 5.2. We close this section by performing some benchmark checks in Section 5.3.

## 5.1. The O(N) model

*This section is based loosely on [5].*

In this section we derive the RG-flow of the O(N)-model in vacuum as an example for all future calculations using the O(N) model and related models. The model is a common test subject when first considering new methods due to its simplicity. Simultaneously, it has a large range of applications, ranging from condensed matter physics over cosmology to QCD, see [104] and references therein.

The O(N) model has been studied extensively within the fRG [130, 253–270], ranging from fixed points to its RG-time evolution in physical systems. Therefore, it constitutes an excellent toy-model for our purpose. Particularly, it features second order phase transitions and allows, in principle, for first-order phase transitions.

### 5.1.1. Model and flow equation

We begin the derivation by introducing an appropriate expansion scheme, the derivative expansion, see Section 3.2.2. For the O(N)-model, the average effective action reads at first

order,

$$\Gamma_k[\phi] = \int d^d x \left\{ \frac{1}{2} Z_k(\rho)(\partial_\mu \phi)^2 + V_k(\rho) - c_\sigma \sigma \right\}, \tag{5.1}$$

where $d$ is the space-time dimension and $\phi = (\sigma, \pi)^t$ is an $N$-component vector. The potential $V$ only depends on the O(N) invariant $\rho = \frac{\sigma^2+\pi^2}{2}$ and takes all momentum-independent higher scattering orders into account. This notation follows the usual applications of the O(N) model to QCD, see also Section 2.3.2. In a QCD setting, the factor $-c_\sigma \sigma$ corresponds to the explicit symmetry breaking induced by bare quark masses and decouples from the RG-flow, since it is a term linear in the field. It only enters when solving the equation of motion after performing the RG integration and can therefore be ignored in the following. To simplify even further, we restrict ourselves to the Local Potential Approximation (LPA) and set $Z_k(\rho) = 1$. Thereby our ansatz only retains the classical momentum dependency.

The RG-flow is derived from the Wetterich equation (3.15), by inserting our ansatz for the effective action (5.1). The flow is evaluated at constant fields $\phi(x) = \phi$, since momentum dependent quantum corrections are not taken into account within LPA. At constant fields, the spatial integration on the left-had side of the Wetterich equation simplifies to a volume factor,

$$\partial_t \Gamma_k[\phi] = \mathcal{V}_d \, \partial_t V(\rho), \qquad \text{with} \qquad \mathcal{V}_d = \int \mathrm{d}^d x \,, \tag{5.2}$$

whereas on the other hand

$$\frac{1}{2}\mathrm{Tr}\big[(G_k)\partial_t R_k\big] = \frac{1}{2}\int_p (2\pi)^d \delta(0)\, G_{k,i}(p)\partial_t R_k^i = \frac{1}{2}\int_p \mathcal{V}_d \, G_{i,k}(p)\partial_t R_k^i \,, \tag{5.3}$$

where $\int_p = \int \frac{\mathrm{d}^d p}{(2\pi)^d}$ and the trace sums over the field components $i \in \{1, \dots, N\}$ and integrates the momentum loop. The propagator, together with the Regulator derivative, generate a volume factor, due to their momentum structures at constant fields $G(p,q) = G(p)(2\pi)^d \delta(p+q)$ and $\partial_t R_k(p,q) = \partial_t R_k(p)\delta(p+q)$ respectively. This conveniently cancels with the left-hand side (5.2).

It remains to evaluate the momentum loop in (5.3), which generates one of the standardised loop-threshold functions. For a simple scalar (bosonic) loop with a single propagator it is a function of the mass and reads (in vacuum),

$$B_1\left(m^2\right) = \int_p \frac{\partial_t R_k(p)}{\Gamma_k^{(2)} + R_k} = \int_p \frac{\partial_t R_k(p)}{Z_k\, p^2 + R_k(p) + m^2} \,, \tag{5.4}$$

where we insert the approximation of the effective action (5.1) to obtain the propagator. The mass $m$ is generally $\rho$ dependent and follows from the truncation, see (5.6). The threshold functions are given for a specific choice of regulator $R_k(p)$. The current example we uses the flat (or Litim regulator) [129], which is given by,

$$R_k(p^2) = Z_k\, p^2\, r(p^2/k^2), \qquad \text{and} \qquad r_{\text{flat}}(y) = \left(\frac{1}{y} - 1\right)\theta(1-y). \tag{5.5}$$

where $r(y)$ is called the shape-function. The non-analytic flat regulator is a convenient (and the optimal) choice in LPA, since it results in analytic threshold functions. We have commented on the importance of the regulator-choice for specific approximations of the effective action in

Section 3.2.3. Generally, the flow equations of higher correlation functions will contain loops with multiple propagators of different field-species and regulator choices. Their definitions are given in Appendix B.7.2, usually in a finite temperature and density setting, see Appendix B.1. We use various regulators throughout this work, which are given in Appendix B.7.1.

We complete our derivation by evaluating the scalar field at the ground state $\phi_0 = (\sigma, \mathbf{0})$. With this parametrisation, the curvature masses are given by

$$\begin{aligned} m_\sigma^2 &= \partial_\rho V_k(\rho) + 2\rho\, \partial_\rho^2 V_k(\rho)\,, \\ m_\pi^2 &= \partial_\rho V_k(\rho)\,. \end{aligned} \tag{5.6}$$

Finally, the resulting flow of the effective potential follows as

$$\partial_t V_k(\rho) = -\frac{v_d k^{d+2}}{2(2\pi)^d}\left[\frac{N-1}{k^2 + \partial_\rho V_k(\rho)} + \frac{1}{k^2 + \partial_\rho V_k(\rho) + 2\rho\, \partial_\rho^2 V_k(\rho)}\right], \tag{5.7}$$

where the angular integration gives rise to the factor $v_d = \frac{2\pi^{d/2}}{\Gamma(d/2)d}$. Equation (5.7) uses the (non-standard) convention for the positive RG-time $t = \ln(\Lambda/k)$, since this chapter explicitly focusses on the parallels to numerical hydrodynamics, where time progresses positively.

### 5.1.2. A fluid dynamics perspective

With very few exceptions, fully field dependent RG-flows can only be solved numerically. To find an appropriate method, we look at (5.7) from a numerical hydrodynamics perspective in terms of convection and diffusion. This idea was first introduced in [65]. First, we observe that the right-hand side is not dependent on the potential itself, but only on its derivatives. Hence we eliminate the potential from the equation and introduce its first derivative,

$$u(\rho) = \partial_\rho V(\rho)\,, \tag{5.8}$$

as a new variable. The RG-flow of $u$ is obtained by taking an additional $\rho$-derivative of (5.7), which yields

$$\partial_t u = \partial_\rho \left[f_{N-1}(u) + f_1(u + 2\rho\,\partial_\rho u)\right], \qquad \text{with} \qquad f_i(x) = i\,\frac{A_d\, k^2}{k^2 + x}\,, \tag{5.9}$$

and $A_d = \frac{v_d k^d}{2(2\pi)^d}$. Formally, this is a second-order partial differential equation (PDE) with a highly non-linear flow. $f_{N-1}(u)$ is a purely convective term. Its effects correspond to a wave-like transportation of information, albeit non-linear in its propagation amplitude. $f_1(u + 2\rho\,\partial_\rho u)$ has a derivative contribution, which creates non-linear diffusive effects of varying strength. The convective and diffusive contributions to the flow are unbounded from below, due to having poles at $u = -k^2$ and $u + 2\rho\,\partial_\rho u = -k^2$, which is linked to the convexity restoration of the potential. For specific initial conditions, or driven systems (for example the quark-meson model), the combination of wave-propagation and convexity restoration has the potential to create very strong dynamics and shock-waves. Their numerical treatment requires the utilisation of inherently discontinuous and higher order accurate methods. A very promising candidate for such an endeavour are the Discontinuous Galerkin methods, which we briefly introduce in the following section.

## 5.2. The Discontinious Galerkin method

Discontinuous Galerkin methods (DGM) have been used for a wide range of hyperbolic, elliptic and parabolic partial differential equations, for applications see e.g. [271–273], for an introduction e.g. [274]. In a sense, they combine the main features of finite element (FEM) and finite volume methods (FVM) and thus compensate for shortcomings of both methods. These features are the *parallelisability, geometric flexibility* and *inherent discontinuity* of FVMs and the *higher order accuracy* of FEMs. For specific parameter choices DGMs can be reduced simple to FEMs or FVMs. Therefore, all converged results obtained by such methods are reproducible with DGMs. If the DGMs do not converge for a specific computation, one must question if FEMs or FVMs might only achieve apparent convergence. Examples are pseudo-spectral methods, which are applicable to FRG equations in the absence of shocks, and have been used successfully in e.g. [262, 275–278], as well as finite difference methods, which were used, with slight modifications, in [279–283].

We proceed by introducing the DG discretisation in Section 5.2.1. This is followed by a discussion of local Discontinious Galerkin methods in Section 5.2.2, which are a necessary improvement for higher order accuracy in presence of strong diffusive effects. Throughout both sections, we comment on our implementation within the open source DUNE (Distributed and Unified Numerics Environment) library [284–289]. For more extensive details on the numerical implementation see also Appendix A.

### 5.2.1. Weak formulation and discrete problem

*This subsection is based on the initial publication using the DUNE framework [1] and conveys the basic idea and advantages of DGMs.*

Let us first consider a simple conservative partial differential equation given by,

$$\partial_t u(x) = \partial_x F(u,x) + s(u,x)\,, \tag{5.10}$$

where $t$ is the time variable and $x$ the spatial coordinate. We call $F$ the (conservative) *flux* and $s$ a *source term*. This equation is solved on a computational domain $\Omega_h$, which is composed of $K$ disjoint elements, called cells, $D^k$ such that

$$\Omega \simeq \Omega_h = \bigcup_{k=1}^{K} D^k\,. \tag{5.11}$$

Making for the inherently discontinuous nature of the method. For calculations in this work, we used the Dune-grid *YaspGrid*, which is contained in the module *dune-grid* and allows for n-dimensional cubic grids and parallelised computation. In the case of a one dimensional grid, the grid-cells are simply disjoint intervals $D^k$ of possibly differing lengths. In a more general formulation the domain $\Omega_h$ would be given as an n-dimensional rectangular grid and the elements $D^k$ would be implemented as cubic grid cells.

The solution in each cell $D^k$ is approximated by a polynomial,

$$u(t,x) \simeq u_h(t,x) = \bigoplus_{k=1}^{K} u_h^k(t,x)\,. \tag{5.12}$$

Then $u_h^k(t,x)$ is the local solution in each cell and the index $h$ denotes the approximation. The local solution is approximated by a polynomial of degree $P = N_p - 1$ such that,

$$u_h^k(t,x) = \sum_{p=1}^{N_p} \hat{u}_p^k(t)\psi_p(x), \tag{5.13}$$

in each element $D^k$. The local approximation $u_h^k(t,x)$ is given by a modal expansion, where $\{\psi_p\}$ is a local polynomial basis with time dependent expansion coefficients $\hat{u}_n^k(t)$. Thus the global solution consists of $K$ local polynomial solutions of order $P$. If we set $P = 0$, we obtain a basic FVM, whereas $K = 1$ corresponds to a spectral method, a one cell FEM. An intermediate choice of both parameters $P$ and $K$ allows for the parallel computation of FEM solutions within each cell $K$, which allows a significant speed-up in large grids. The local approximation was implemented using the *dune-pdelab* module, specifically using the class *QkDGLocalFiniteElementMap*. In the one-dimensional case, basis functions $q_n$ are given by the Legendre-Polynomials up to order $N_p$. For the purpose of higher dimensional computations the basis functions are taken from the polynomial space $Q_k$ of the Legendre-Polynomials, i.e. they are given by a tensorial product of one-dimensional bases.

For the convergence of the DG method, we require that the integral over a cell $D_k$ vanishes for each component $\psi_p$ of the polynomial basis. We use a locally defined weak formulation of this requirement,

$$\int_{D^k} \left((\partial_t u_h + s_h)\psi_p + F_h \partial_x \psi_p\right) dx = -\int_{\partial D^k} \psi_p \left(f^* \hat{\boldsymbol{n}}\right) dx\,, \tag{5.14}$$

which is obtained via an integration by parts of the original equation (5.10). The right hand side of the equation is modified to contain the numerical flux $f^*$, which ensures communication across interfaces. $\hat{\boldsymbol{n}}$ is the outward pointing normal vector. We chose to use the local Lax-Friedrichs flux for $f^*$, which averages the flux on both sides of boundary and adds an additional diffusion term smoothing out jumps across the boundary:

$$f^*(u_h^+, u_h^-) = \frac{1}{2}\left(f_h(u_h^+) + f_h(u_h^-)\right) + \frac{C}{2}[[\boldsymbol{u_h}]]\,, \tag{5.15}$$

where and the indices + and - denote the outside (neighbouring) and interior element at the boundary. The brackets denote a jump across the boundary,

$$[[\boldsymbol{u}]] = \left(\hat{\boldsymbol{n}}^- u^- + \hat{\boldsymbol{n}}^+ u^+\right).$$

$C$ is the local maximal wave speed, which corresponds to the speed of the fastest propagating mode across the boundary. In one dimensions this corresponds to

$$C \geq \max_{\partial D^{\{i,i+1\}}} |\partial_u f(u)|\,. \tag{5.16}$$

The local Lax-Friedrichs flux is the most natural extension from the analytic solution of linear conservation laws to the non-linear case. It relies on the so called Roe condition, which reflects the assumption that the system is dominated by one strong wave.

This concludes the setup of a direct Discontinuous Galerkin discretisation, which was successfully applied to the large-N limit of the O(N) flow in (4.50) and showed impressive convergence properties [65]. Note, that (5.10) does not contain any second derivatives of $u$ and convergence is not necessarily maintained if $\partial_x u$ is fed back into the flow.

### 5.2.2. Local Discontinuous Galerkin

*This subsection is based on [5], where we introduce the LDG method with a code example [12].*

Originally developed for purely convective hyperbolic equations, such as (5.10), the DG method has later been adapted for PDEs which are convection-dominated but have a diffusive component.

In [1] a direct DG extension has been applied to the problem of a quark-meson model, which gets a non-linear diffusive component through the massive mode that arises when the theory exhibits spontaneous symmetry breaking. The direct extension consisted of obtaining necessary derivative terms directly from the solution. This means that the numerical approximation of the derivative is given by,

$$\partial_x u_h^k(t,x) = \sum_{p=1}^{P+1} u_p^k(t)\partial_x \psi_p(x)\,. \tag{5.17}$$

However, this direct definition of a numerical derivative is problematic. In [290] it has been shown that this formulation may yield errors of O(1) even if it is stable. In the case of [1], this method has also shown itself to be unstable in the vicinity of the first order regime of the quark-meson model.

To remedy the shortcomings of this naive extension, we will use the local Discontinuous Galerkin (LDG) method. It has become one of the most widely used extension of the DG method in this direction and is particularly suited to solve convection-diffusion equations with possibly discontinuous solutions, retaining its stability and convergence [291].

The main idea of the LDG method is to reduce a higher order operator, i.e. the flux $\partial_x F(u,\partial_x u)$, to a system of two equations of first order. We will now present a simple example of an LDG method based on the formulation in [251], which assumes a term linear in the derivative $\partial_x u$ with a diffusion coefficient $a(u) \geq 0$,

$$\partial_t u - \partial_x\big(a(u)\partial_x u\big) = 0\,. \tag{5.18}$$

We chose this formulation, because the linear diffusion term allows for an interpretation in terms of diffusive effects in fluid dynamics. With a bit of additional effort, the Wetterich RG-flows can be reduced to such a structure by taking additional derivatives of the flow equation, see Appendix B.3.1. The condition $a(u) \geq 0$ assures the smoothing effect of the diffusion. We will see examples of RG-flows with negative diffusion in Appendix C.3.3, which are inherently numerically unstable. The main idea in solving this system is a stationary equation which captures the additional derivative term by rewriting $q = \sqrt{a(u)}\,\partial_x u$,

$$\begin{aligned} \partial_t u - \partial_x\big(\sqrt{a(u)}q\big) &= 0\,, \\ q - \partial_x j(u) &= 0\,. \end{aligned} \tag{5.19}$$

Supplemented by some initial condition for $u(t=0,x)$. The system now contains an *instationary* equation for the RG-time evolution of $u$ and a *stationary* equation for $q$. The conservative flux of the stationary equation given by

$$j(s) = \int_0^u \sqrt{a(u')}\mathrm{d}u'\,, \tag{5.20}$$

which follows simply from applying the chain rule

$$\sqrt{a(u)}\partial_x u = \partial_u j(u)\partial_x u = \partial_x j(u)\,. \tag{5.21}$$

The specific mould of the equation given in (5.18) is only applicable to the O(1) model. For arbitrary N the system is extended by another equation and we refer to Appendix A, as well as the code example in Appendix A.3.2 or the respective github repository [12].

## 5.3. Computations and convergence

*This section is based on [5], all figures are taken from the publication.*

We start in Section 5.3.1, by investigating the zero dimensional case, which provides a good testing ground for new methods, as it is conceptually rather simple and suits the mould Equation (5.18). Furthermore, this limit has recently been thoroughly investigated [4, 248–250]. It provides an excellent testing ground for method development, since benchmark results can easily be obtained from a direct evaluation of the generating functional (3.2). Simply put, it is a simple variant of the O(N)-model, with $N = 1$ and $d = 0$, where $d$ is the dimension of space-time. The flow of the full O(N)-model will be solved in Section 5.3.2. Here, the system of equations is a bit more extensive, as specified in Appendix A. We benchmark results by comparing to the (analytic) O(1) case in zero dimensions and the large $N$ limit, where the system can be solved with the DG method.

### 5.3.1. Zero dimensional model

For $d = 0$ and $N = 1$ it makes sense to rewrite the equations in term of the single scalar field $\phi = \sqrt{2\rho}$. The flow (4.50) then simplifies to,

$$\partial_t V_k(\phi) = -\frac{k^2}{k^2 + \partial_\phi^2 V_k(\phi)}\,. \tag{5.22}$$

Here $k^2 + \partial_\phi^2 V_k(\phi)$ is the regularized propagator, which must be a positive quantity for the equation. In the current case, this property is conserved [292]. Furthermore, with standard initial conditions the resulting effective potential is strictly convex for $k \to 0$ even if $m^2 < 0$. This is in contrast to higher dimensions, where the resulting effective potential is still convex but not necessarily strictly convex. This is linked to the absence of spontaneous symmetry breaking in low dimensions. As a consequence, the minimum of the effective potential is $\phi_0 = 0$, while otherwise a non-zero value would be possible. Due to the convexity of effective potential, a flat region can emerge $V_{k=0}(\phi \leq \phi_0) = 0$. The absence of such a regime simplifies the numerical effort considerably. Nevertheless, discretizing the system proceeds in the same fashion, making lower dimensional systems very attractive to benchmark numerical methods in QFT.

#### A simple diffusive system

To apply the LDG method from Section 5.2.2 to the formulation in $\phi$, the equation must be reformulated such that it is a closed expression of the second derivative of the potential, which we rename $\nu(\phi) = \partial_\phi^2 V_k(\phi)$. Similarly to the procedure in [1, 65], we take two derivatives with respect to $\phi$ of the flow (5.22) to close the formulation in $\nu(\phi) = \partial_\phi^2 V_k(\phi)$. All information

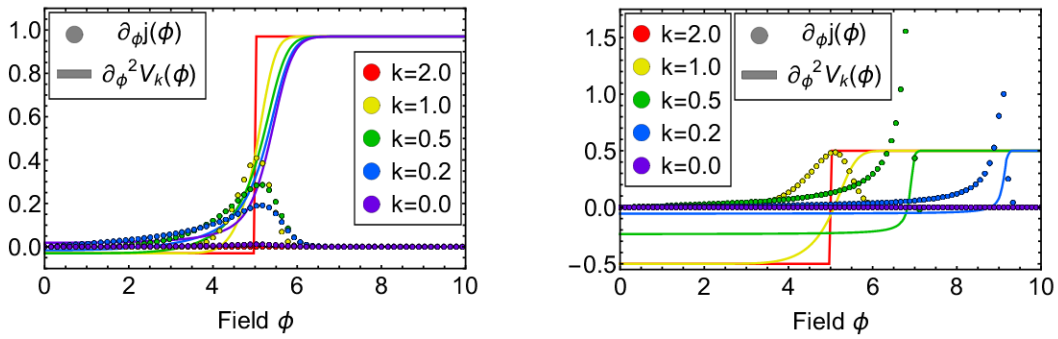


(a) Riemann Problem for $v_0 = 0$: The jump smoothes out, but does not travel. The diffusion flow vanishes, while flattening out around the jump.

(b) Riemann Problem for $v_0 = -0.5$: The jump travels with ongoing RG-time and leaves the grid. The diffusion flow vanishes eventually at $k = 0$, but travels shock-like with the jump towards higher grid values.

Figure 5.1.: RG-time evolution of the Riemann problem in $d = 0$. We plot the stationary diffusion flux $q = \partial_\phi j(\phi)$ and the second derivative of the potential $\partial_\phi^2 V_k(\phi)$, which are the numerical solutions to the system given in (5.23). Figure 5.1a shows a freezing in of the jump position, whereas Figure 5.1b shows the jump travelling to higher field values before vanishing. In both cases the sharp jump is flattened out, as expected of a diffusive system.

generated by the flow is contained within the second derivative. This can already be inferred from the fact that the fundamental object in functional formulations is the propagator and therefore the two-point function, which is by definition a (functional) derivative. Therefore, we introduce the schematic flow equation

$$\partial_t v = \partial_\phi^2 f(v) = \partial_\phi \big( \partial_v f(v)\, \partial_\phi v \big) . \tag{5.23}$$

We can now make use of the formalism given in (5.19) and indicate the (square root of the) diffusion coefficient,

$$\sqrt{a(v)} = \frac{k}{k^2 + v} . \tag{5.24}$$

By performing the (analytic) integration (5.20) we obtain the stationary flux,

$$j(v) = k \log(k^2 + v) . \tag{5.25}$$

Note, that we dropped a constant term in (5.25), which would arise from the integration boundaries in the original definition (5.20). This term does not contribute here because the flow $f(v)$ in (5.23) does not explicitly depend on $\phi$.

### The Riemann Problem

We study the behaviour of this simple diffusive system in a first order regime. This is not only a common check for how the scheme deals with jumps in the solution, but is also interesting for physical systems in critical regions. For example, it was found in [1] that the quark-meson model in the large-$N$ limit displays shock development at high densities $\mu$. With the following investigation we can now expand on how the addition of diffusion would affect these systems.

We consider initial conditions that contain a single jump in the solution. This is also known as the Riemann-problem

$$v(\phi)|_{t=0} = v_0 + \theta(\phi - 5) A , \tag{5.26}$$

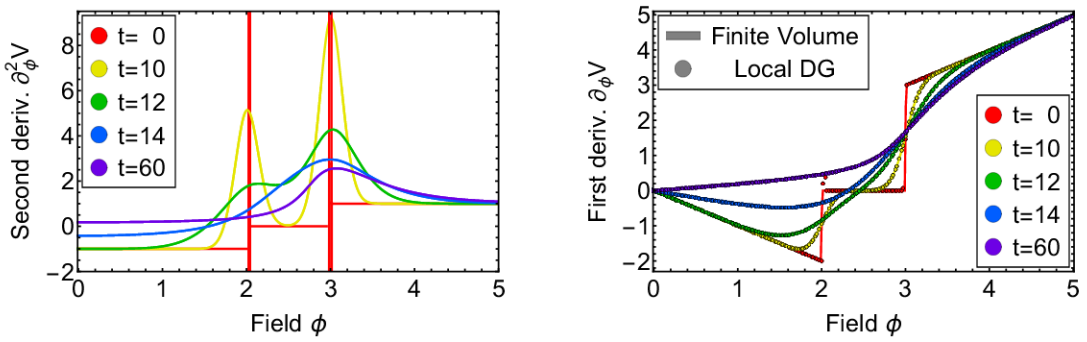


(a) Numerical solution to the flow of the initial conditions given in (5.27), in terms of the second derivative $v(\phi) = \partial_\phi^2 V(\phi)$. The singularity in the initial conditions is projected onto the polynomial basis (5.13).

(b) Comparison of the flow of the first derivative of the initial conditions given in (5.27). The LDG result is obtained by integrating the numerical solution. The finite volume result is taken from [249].

Figure 5.2.: RG-time dependence of the potential in (5.27) in terms of its derivatives.

where the jump is situated in the middle of the numerical grid $\phi \in \{0, 10\}$, $v_0$ is the initial value in the regime $\phi \leq 5$ and $|A| = 1$ the height of the jump. All computations start at an RG-scale of $\Lambda = 2$. For clarification on the implementation and the numerical intricacies see Appendix A.3.

Figure 5.1 shows that the diffusive contribution to the flux may or may not travel with the RG-time, depending on the initial value $v_0$. Figure 5.1a shows a scenario with little dynamics: The diffusion is smoothing out the jump until it vanishes with $k \to 0$. Throughout this process the diffusion-peak-position, and therefore also the position of the steepest slope in the potential derivative, are barely moving. In contrast to this, Figure 5.1b shows the dynamical case where the diffusion flux is first smoothing out the jump and subsequently pushing the original jump to higher values of the spatial coordinate $\phi$. In this dynamical scenario the diffusive flux is developing a discontinuity at intermediate RG-times, which eventually vanishes again in the limit $k \to 0$.

The result of this simple consideration is already remarkable. The jumps do not get flattened away like in usual diffusion equations. The width freezes to a finite value, demonstrating support for almost shock like structures throughout the RG-flow. In comparison to ordinary dispersive shock waves, no ringing arises in the vicinity of the jump.

### Non-Analytic 1st derivative

In the spirit of [249] (Sec. V.A: Test case I), we study a UV-potential with kinks. The initial potential is given by

$$V(\phi) = \begin{cases} -\frac{1}{2}\phi^2, & \phi \leq 2, \\ -2, & 2 < \phi \leq 2, \\ \frac{1}{2}(\phi^2 - 13), & 3 < \phi, \end{cases} \tag{5.27}$$

at an initial UV-cutoff scale $\Lambda = 10^6$. In order to match the calculation in [249] we adapt the same regulator $R_k(p) = \Lambda e^{-t}$, which modifies the flow equations only slightly. Previous studies [1, 65, 248, 249] focus on solving fRG flow equations in terms of the first potential derivative $u = \partial_\phi V$. Hence, (5.27) was designed with the Riemann problem in mind, since kinks

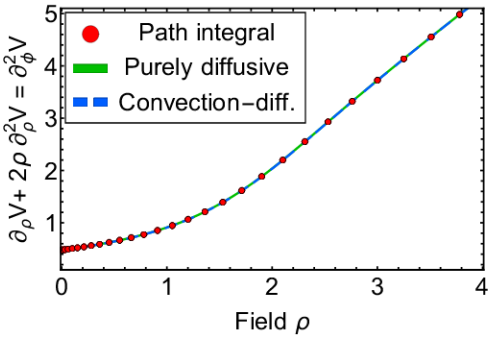


Figure 5.3.: Graphical comparison of the second derivative of the effective potential $V$ as a function of $\rho$. We compare data from a numerical evaluation of the path integral (3.2), the purely diffusive system Section 5.3.1 and the convective diffusive system Section 5.1.

in the potential translate to a discontinuity in $u$. The LDG framework is formulated in terms of the second derivative $v = \partial_\phi u$, which requires us to resolve delta-peaks at $|\phi| = 2,\ 3$. In the weak formulation (5.14) this amounts to a projection of the initial data onto the polynomial basis (5.13) at hand.

The solution to the flow is shown in Figure 5.2. The computational domain $\Omega = [-6, 6]$ is divided in $K = 101$ equally sized cells. The chosen value for $K$ ensures that the initial singularities at $\Lambda$ are not situated on cell interfaces. Within cells, we use a polynomial order of $P = 4$. This choice demonstrates nicely, how the flux-formulation of the LDG scheme is able to deal with oscillatory behaviour around discontinuities. We compare our solution to the calculation of [249], shown in Figure 5.2b, where this initial potential was first considered. The results are nicely in agreement, as expected. Figure 5.2a shows the direct numerical solution of (5.22) in terms of the second derivative $v = \partial_\phi u$. Here, oscillations appear at early RG-times due to the projection of delta-peaks on a polynomial basis.

### 5.3.2. A convection-diffusion system

In this section, we perform some benchmark checks. For this purpose we compare to the zero dimensional example from Section 5.3.1, as well as the large-$N$ limit, which has been investigated in various contexts in [1, 65, 250]. Both examples test different features of the presented scheme. The zero dimensional case, formulated in terms of the field $\phi$, is a diffusive system. Recovering the results from Section 5.3.1 therefore checks convergence of the convection-diffusion system in the diffusion dominated scenario. On the other hand, the large-$N$ limit is a purely convective system, since the second derivative term (i.e. the diffusion term) drops out in the limit $N \to \infty$. Performing computations at a very large $N$ therefore allows to check convergence features in a convection dominated scenario. However, at this point we would like to remark that the solution of the equation for $N \to \infty$ does not necessarily coincide with the solution at $N = \infty$, see [250, 293–295] for a critical discussion.

For computations we use a simple $\phi^4$ potential as initial condition, to wit

$$V_\Lambda(\phi) = m^2\rho + \frac{1}{2}\lambda\rho^2 . \tag{5.28}$$

We chose $m^2 = -0.5$, so that we recover a symmetry breaking scenario in $d > 2$, as well as $\lambda = 0.5$.

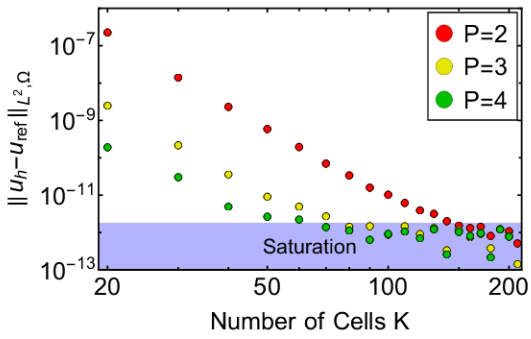


Figure 5.4.: $L^2$ error with respect to a reference computation $u_{\text{ref}}$. The reference computation is given by the solution with $K = 250$ and $P = 4$, whereas $u_h$ is the numerical solution for the O(N) computation using different polynomial orders and numbers of cells $K$.

### Comparison to the purely diffusive system

Let us preface the comparison to the purely diffusive scenario with a general discussion of the $O(1)$ case. In many applications, the O(N) model uses a formulation in the chiral invariant $\rho = \frac{\phi^2}{2}$. This choice of variable imposes the $Z_2$ symmetry of the potential and raises the question of which boundary conditions to use at $\rho \to 0$. By comparison, the formulation in Section 5.3.1 is given in terms of $\phi$. Here, the symmetry of the potential needs to be checked explicitly. For a throughout investigation of the coordinate choice see [248].
In particular for $N = 1$ the formulation in $\rho$ (5.7) is not ideal. In dimensions $d > 2$, where we have a spontaneous symmetry breaking, the flow is strongly governed by the convexity restoring property. This property requires $\frac{u+2\rho v}{k^2} > -1$ for the massive mode ($N = 1$) and additionally $\frac{u}{k^2} > -1$ for the massless modes ($N > 1$), such that the pole in the flow equation (5.7) is not reached at finite $k > 0$. This requirement demands increasingly high numerical precision as $k \to 0$ in the broken phase and presents a big challenge for all numerical schemes which attempt to resolve the effective potential in the broken phase, see e.g. [65, 260]. In the standard example of $\phi^4$ initial conditions, convexity restoration is driven by the massless modes. At $N = 1$ or for more intricate initial conditions, where $\partial_\rho u < 0$ for some $\rho$, the dynamics are governed by the massive mode such that the relation $\frac{u+2\rho v}{k^2} > -1$ has to be fulfilled. While this property is, in principle, enforced by the flow, it requires precision in two distinct expressions $u$, $v$ as opposed to one in the purely diffusive case (5.22). A prominent example for the scenarios with $d > 2$ and $\partial_\rho u < 0$ is the high density regime of the quark-meson model, or more generally, of QCD. These ingredients to the flow equations cause strong dynamics and potentially shock development [1]. Numerical intricacies connected to shock development and convexity restoration are discussed in Appendix C.2.

In this sense, a comparison to Section 5.3.1 is somewhat trivial, since it is simply an O(N) model with $N = 1$ and $d = 0$. There is no spontaneous symmetry breaking process and the result for a simple $\phi^4$ theory can also be obtained from a numerical evaluation of the path integral (3.2). Thus, the full effective potential $V_{k=0}(\rho)$ is computed in $d = 0$ by a direct numerical evaluation of $Z[J]$ with the classical action specified by the initial conditions in (5.28), following the steps of the derivation in Section 3.1. In order to capture the full result with the fRG, the computation is started at an initial cutoff scale of $\Lambda = 20$, where the numerical result of the regulator modified path integral $Z_k[J]$ corresponds to the initial conditions $V_\Lambda(\rho)$ (5.28).

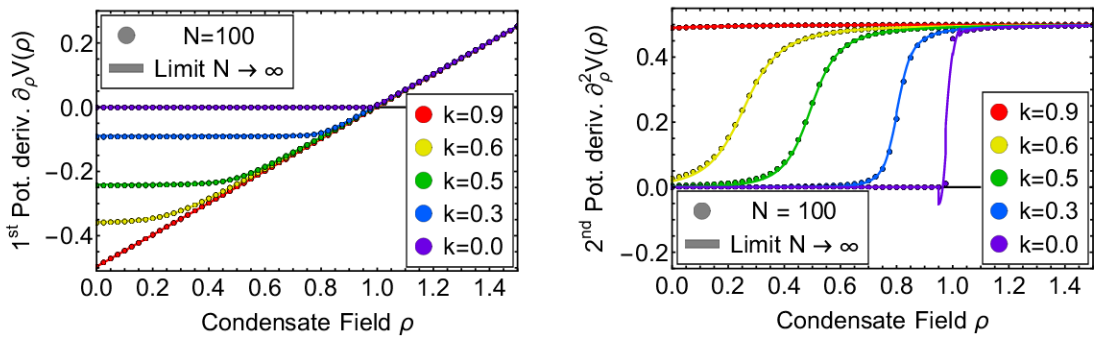


(a) Graphical comparison of the first derivative of the effective potential $u = \partial_\rho V$.

(b) Graphical comparison of the second derivative of the effective potential $v = \partial_\rho u = \partial_\rho^2 V$.

Figure 5.5.: Graphical comparison of the purely convective large-$N$ limit and the convection-diffusion system (5.7) at $N = 100$. We consider the broken symmetry phase in $d = 3$ using the initial conditions from (5.28). In the large-$N$ limit, the derivative is obtained by interpolation of the numerical data. This interpolation struggles with the resolution of the kink within the first derivative in (b).

We now perform a benchmark check between the numerical path integral result, the purely diffusive system in Section 5.3.1, and the current convection-diffusion driven system. A graphical comparison is given in Figure 5.3. To further showcase the convergence of the convective-diffusive LDG scheme we compute a reference solution $u_{\text{ref}}(\rho)$. This computation uses a grid with $K = 250$ cells and a polynomial order $N = 4$ for values of $\rho \in [0, 8]$. The integration is performed up to an RG-scale $k = 0.002$. This reference solution is compared to numerical solutions $u_h$ using varying polynomial orders $P = 2,\ 3,\ 4$ and cell numbers $K \in [20, 220]$. For the quantitative comparison we make use of the $L^2$ norm

$$\|u_h - u_{\text{ref}}\|_{L^2,\Omega} = \int_0^{3.5} \Big(u_h(\rho) - u_{\text{ref}}(\rho)\Big)^2 d\rho\,.$$

Results are given in Figure 5.4. We do not see the expected linear behaviour from [65], since the error saturates at $10^{-12}$ due to the finite floating point precision of the calculation.

### Comparison to the Large-N limit

In a second benchmark test we recover the large-$N$ limit in the broken symmetry phase. In the limit $N \to \infty$ the massive mode $m_\sigma = u + 2\rho\partial_\rho u$ drops out of the flow completely, resulting in a purely convective system. Previous work investigated the large-$N$ limit from this perspective [1, 65]. Using the initial conditions in (5.28), we compute in $d = 3$ and $N = 100$. This computation is compared to the results from [65] in Figure 5.5, which confirms that the large-$N$ limit is recovered by comparing the first potential derivative $u = \partial_\rho V$. Furthermore, the LDG scheme allows to precisely resolve the second derivative of the potential $v = \partial_\rho u = \partial_\rho^2 V$, see Figure 5.5b. The feed back of $v$ to the flow of $u$ is suppressed by a factor of $1/99$. Still, $v$ is computed separately and provided with a numerical flux which allows to get rid of numerical oscillations of the dDG method around the clearly visible jump in the limit $k \to 0$ at $\rho \approx 1.0$.

Figure 5.5 demonstrates the limitations of the dDG scheme at finite $N$. Even though dDG is able to provide higher derivative terms due to the polynomial basis (5.13), the formulation lacks a numerical flux for explicit higher derivative operators. If the solution $u$ is flat, the

missing numerical flux to the finite $N$ flow (5.7) is negligible and computations retain their convergence properties [1]. However, in case of non analyticities, the numerical flux of higher derivative operators can no longer be neglected, which becomes apparent from the oscillations around the jump in the large-$N$ computation for $k \to 0$.

## 5.4. Outlook

*This section is based on [5].*

The formulation of the LDG method presented here, which has been adapted from [251], is of course only one of many. For example, in the case of higher-dimensional systems, replacing $q - \partial_x j(u) = 0$ with $q - \partial_x u = 0$ and using an alternating flux definition may be desired for a lower performance impact and simplification of the implementation. This alternative method is based on [296] and explained in Appendix A.3. It should be noted that usually the integration in the definition of $j(s)$ can not be performed analytically and thus requires numerical integration. Hence, other LDG methods may also be desirable, e.g. methods that directly infer $\nabla \boldsymbol{w}$ by giving a numerically sensible definition of this quantity, see e.g. [296], thus making the rewriting into $u$ and $v$ we had to perform in Appendix B.3.1 superfluous. This of course has its drawbacks, as the stability of the method may become suboptimal.

Additionally, fRG flows seem to be strongly dominated by certain substructures of the equations. The regulator derivative in the equations forces all changes to be in a narrow region in momentum space. This property is translated directly to field space, with the exception of the convexity restoring regime, resulting in the convection dominated nature of the equations. One direct consequence is the large asymmetry of the diffusive flux, which lead to a breakdown of the scheme in [1]. This reflects simply the fact that the RG-flow evolves from the UV to the IR and information gets propagated along these trajectories, c.f. [65, 249] for an extensive discussion. LDG resolves this elegantly, by taking precisely this structural property of the flow into account. From a physics perspective, this is not the end of the line for potentially exploitable structures within these equation. One prominent example is the convexity restoring regime, where the solution approaches zero for a finite domain. In the present equations, its this is driven by a singularity in the analytically continued equation [292]. Computationally, this is tightly linked to time-stepping.

Not very surprisingly, for more complex and computationally intensive problems more elaborate time-stepping schemes must be considered. For example, the fRG flows in the symmetry-broken phase become stiff and explicit time stepping becomes highly inefficient. A possible remedy for this problem are implicit time-stepping schemes, see also Appendix A.2.

Most applications in the following chapters make use of different DG methods and time-integrators of varying elaborateness, since this thesis is a compilation of multiple years with ever increasing technical developments. Numerical details of specific applications are outlined in Appendix A and are referred to in the next chapters.

# CHAPTER 6

## Complex effective actions and phase transitions

*This chapter is based entirely on [4], all figures are taken from the publication. It sets up a formalism to compute complex effective action from the fRG and has the aim to determine the location of Lee-Yang singularities in the complex plane. We hope to report on an application to QCD and an extrapolation of the critical endpoint in future works.*

The phase structure of interesting relativistic quantum theories such as QCD, or non-relativistic ones in atomic and condensed matter physics such as graphene or spin-imbalanced fermionic gases, exhibits many interesting physics phenomena, ranging from critical end points to competing order regimes. In many cases these phenomena are related to the task of resolving complex structures in the theories at hand. Most prominently, this concerns partition functions with complex actions or Hamiltonians that typically lead to sign problems in a statistical approach. Moreover, constraints for the phase structure can be derived by considering complex external fields or parameters such as a complex magnetic field in spin systems. The latter extension gives rise to Lee-Yang zeros [297, 298] in the complex (magnetisation) plane. These singularities restrict the radius of convergence of expansion schemes as well as providing at the same time much wanted information about the location of singularities on the real axis such as critical end points. For related works on the lattice, see [299–303], with the functional renormalisation group this has been studied in [304–307]. A further exciting possibility is the expansion of quantum field theories in trans series based on the expansion about complex saddle points.

These investigations require the computation of the partition function or free energy of the theories at hand at complex couplings or sources. In the present work we discuss functional renormalisation group approaches to complex action problems. We argue that this task is best formulated in terms of Wegner's flow equation [131], see also Chapter 3, for general flows of an effective Hamiltonian or Wilsonian effective action, or in terms of the general flow for the 1PI effective action derived in [127]. These flows encompass the standard Polchinski equation [68] for the Wilsonian effective action and the Wetterich equation [67] for the 1PI effective action as specific cases. The generality is pivotal for setting up complex action flows adapted to the theory at hand.

In theories with complex actions and an intricate phase structure as discussed above, the

solution of functional flows requires the use of advanced numerical methods. Moreover, different representations of functional flows may have advantages over others for specific problems, as they yield different types of parabolic equations. More specifically, we obtain parabolic partial differential equations reminiscent of convective heat equations for Wegner's flow [131], reaction-diffusion equations for the Polchinski flow [68], and hyperbolic equations in case of the Wetterich equation [67]. We solve this broad range of PDEs with the Discontinuous Galerkin methods which we introduced in Chapter 5. This work now expands these considerations not only to a more general RG-context, but also to a complex setting.

Specifically we study the flow equation for scalar field theories in $d = 0$ to 4 dimensions with a complex source term. The $d = 0$ case can be solved exactly by other means and hence offers benchmark tests for our functional flows. We consider flows for the complex one particle irreducible (1PI) effective action, standard Polchinski flows for the Wilsonian effective action, as well as RG-adapted flows for the Wilsonian effective action derived from Wegner's flow equation. With the present formulation of these approaches, we find that the RG-adapted flows show best convergence in the complex plane. For the complex 1PI effective action we set up and discuss a complex Legendre transform. We show that the results obtained from the complex 1PI flows pass the benchmark tests in $d = 0$. In higher dimensions it is compatible with the results for the Wilsonian effective action.

With the results for the effective potential for complex fields we determine the location of the Lee-Yang zeros as a function of the coupling parameters. We follow these locations towards their intersection with the real axis at the phase transition of the real theory.

We close this chapter with a discussion of extensions and further applications of the present setup for complex functional flows, in particular to QCD and the location of its critical end point.

## 6.1. Complex functional flows

The phase structure of theories with complex action parameters is quite intricate. In particular, the partition function may vanish at Lee-Yang zeros or exhibits cuts in the complex plane that start at the Lee-Yang zeros. As discussed in the introduction, in the present work we aim at setting up a functional approach that is flexible enough to generically deal with these structures.

While the derivations in this section and the following one, Section 6.1.1, apply to general theories, they are formulated in terms of a real scalar $\phi^4$ theory in $d$ dimensions for the sake of simplicity. The numerical results in Section 6.2 are also achieved for this theory in zero to four dimensions. In the smallest dimension, $d = 0$, the generating functional collapses to a simple one-dimensional integral and serves as a benchmark case. In turn, $d = 4$ is the critical dimension of the theory.

The classical action of the real scalar $\phi^4$ theory in $d$ dimensions is given by

$$S[\varphi] = \int_x \left\{ \frac{1}{2}\varphi(x)\left[-\partial_\mu^2 + m^2\right]\varphi(x) + \frac{\lambda}{4!}\varphi(x)^4 \right\}, \tag{6.1}$$

with the real scalar field $\varphi \in \mathbb{R}$, and the real mass and coupling $m, \lambda \in \mathbb{R}$. The $d$-dimensional space-time integral in (6.1) is abbreviated with

$$\int_x = \int d^d x\,. \tag{6.2}$$

The present formulation allows for the computation of complex effective actions deduced from complex masses and couplings, $m, \lambda$ as well as complex sources $J$ in the source term $\int_x J\varphi$. For the numerical application in the present work we consider consider complex sources $J$ and keep real masses and couplings.This allows for some numerical simplifications and covers the interesting case of Lee-Yang zeros. The more general situation will be discussed elsewhere.

In the present work we shall consider complex currents $J$, which may be interpreted as a complex magnetic background field. In the presence of such a current and more generally also complex $m, \lambda$, the generating functional $Z[J]$ is also complex, as is the expectation value of the field and the higher correlation functions. However, it is a function of the complex variable $J$, and does not depend on its complex conjugate $\bar{J}$. Moreover, for real $m, \lambda$, the complex-valued generating functional $Z[J]$ and hence also the correlation functions are real functions of the complex variable $J$,

$$\overline{Z[J]} = Z[\bar{J}], \qquad m, \lambda \in \mathbb{R}. \tag{6.3}$$

This property of the generating functional $Z[J]$ translates to all derived functionals discussed in Section 3.1. Here, we make use of the the property that their functional flow equations constitute different general diffusion equations with different properties. This can be used to our advantage for the present task of solving them for complex effective actions.

### 6.1.1. RG-adapted flows

We now employ general RG kernels, introduced in Section 3.3, for the construction of *RG-adapted* flows. To begin with, we remark that the kernel of functional flows is given by the full field-dependent propagator $G_k[\phi]$, and hence any expansion scheme always implies also an expansion about $G_k[\phi]$. This property has been exploited in [140], and within conceptual considerations and applications on optimisation in functional flows, see [129,130,308]. In particular this led to functional optimisation as set up in [127,128] as well as the recent development of essential RG-flows [136,309,310]. This idea has also been picked up for Machine Learning applications to functional renormalisation in [141].

The above suggests to use RG kernels and currents that are constructed from the full field-dependent propagator. Here we briefly discuss a natural choice: In analogy to (3.27) we are led to the implicit definition,

$$J[\phi] = G_k^{-1}[\phi]\phi\,, \tag{6.4a}$$

and generalisations thereof. A respective RG kernel (3.20) is defined by

$$\mathscr{C}_k[\phi] = -G_k[\phi]\,\partial_t R_k[\phi]\,G_k[\phi] \tag{6.4b}$$

and generalisations thereof. The latter generalisations are deduced from further optimisation conditions, that take into account the complex structure of the theory. Such an *RG-adapted* choice is very similar in spirit to the *dynamical RG* setup in [140]. The fully developed conceptual framework there will be very useful for the computational implementation, which is deferred to future work.

In this context we remark, that the implicit definition in (6.4) with the *field*-dependent propagator introduces a non-linear relation between the current and the field and requires an iterative solution of the flow. While it is precisely the non-linearity which is at the root of the optimisation, its practical use asks for a more comprehensive analysis. Hence, a full discussion

of general optimised RG-flows is deferred to a future publication. There we will also examine choices of (3.33d) and (6.4), that trigger stabilising positive diffusion terms (see Section 6.2) in either the flow of the Wilson effective action or the 1PI effective action.

### 6.1.2. RG-adapted expansion

In the current work we resort to a ready-to-use variant of (6.4): the theory is expanded about the full propagator on a fixed background. This leaves us with a linear relation between the current and the field,

$$J[\phi,\phi_0] = G_k^{-1}[\phi_0]\phi\,, \tag{6.5a}$$

with a field-independent infrared regulator $R_k$ and the respective RG kernel

$$\mathscr{C}_k[\phi_0] = -G_k[\phi_0]\,\partial_t R_k\,G_k[\phi_0] \tag{6.5b}$$

For the background $\phi_0$ in (6.5a) a convenient choice is a solution to the equations of motion (EoM). The above definition (6.5) can be understood as an RG-improvement of (3.27): at each RG-step the respective full propagator is used to define the field $\phi$. This is an RG-adapted definition of the current or rather an RG-adapted expansion of the field.

With (6.5) we are led to the RG-adapted Wilsonian effective action

$$S_{\mathrm{ad},k}[\phi,\phi_0] = -W_k\Big[G_k^{-1}[\phi_0]\phi\Big], \tag{6.6}$$

with the fluctuation field $\phi$, being the difference to $\phi_0$, for more details see Appendix B.5.2. From now on we suppress the dependence on the expansion point $\phi_0$ in (6.6) and simply write $S_{\mathrm{ad},k}[\phi]$. This definition entails an expansion of correlation functions and their flow about the full two-point function, and can be understood as an improvement in the sense of functional optimisation in [127].

The flow equation for the Wilsonian effective action $S_{\mathrm{ad},k}$ reads

$$\left(\partial_t + \int_x \phi\,\gamma_{\mathrm{ad},k}\,\frac{\delta}{\delta\phi}\right) S_{\mathrm{ad},k}[\phi] = \frac{1}{2}\,\mathrm{Tr}\;\mathscr{C}_k\left[S^{(2)}_{\mathrm{ad},k}[\phi] - \left(S^{(1)}_{\mathrm{ad},k}[\phi]\right)^2\right], \tag{6.7}$$

with $\mathscr{C}_k$ provided in (6.5a) and the anomalous dimension

$$\gamma_{\mathrm{ad},k}[\phi_0] = -\left(\partial_t G_k^{-1}[\phi_0]\right) G_k[\phi_0] = \partial_t \log G_k[\phi_0]\,. \tag{6.8}$$

The generalised anomalous dimensions $\gamma_{\mathrm{ad},k}[\phi_0]$ is an operator and carries the change of the full (inverse) propagator with the cutoff scale. In any case, the flow equation (6.7) is well-defined for all complex fields $\phi$.

The RG-adapted setup with the flow (6.7) admits a natural split of $S_{\mathrm{ad},k}$ in the kinetic part and the dynamical interaction part with

$$S_{\mathrm{ad},k}[\phi] = S_{\mathrm{dyn},k}[\phi] - \frac{1}{2}\int_x \phi\,G_k^{-1}[\phi_0]\,\phi + \mathscr{S}_0[\phi_0]\,, \tag{6.9}$$

with the constant part

$$\mathscr{S}_0[\phi_0] = \frac{1}{2}\int_\Lambda^k \frac{dk'}{k'}\,\mathrm{Tr}\,\partial_t R_k G_k[\phi_0] + S^{(2)}_{\mathrm{ad},k}[0]\text{-terms}\,. \tag{6.10}$$

With the choice (6.10) we have $S_{\mathrm{dyn},k}[0]=0$. Moreover, the RG-adapted field expansion entails that $S^{(2)}_{\mathrm{ad},k}[\phi_0]$ is (minus) the full inverse propagator in this background, see also (B.77). Hence, it follows from (6.9) that,

$$S^{(2)}_{\mathrm{dyn},k}[0]=0\,. \tag{6.11}$$

Consequently, if we choose $\phi_0$ as a solution to the equation of motion with

$$S^{(1)}_{\mathrm{dyn},k}[0]=0\,,\qquad \text{for}\qquad \phi_0=\phi_{\mathrm{EoM}}\,, \tag{6.12}$$

the dynamical interaction part $S_{\mathrm{dyn},k}[\phi]$ is of order $\phi^3$ and indeed only carries interactions in an expansion about $\phi=0$, and is an expansion about the physical mean field $\langle\varphi\rangle=\phi_0$, the full field being $\phi_0+\phi$.

By inserting the split (6.9) into (6.7) we are led to the final form of the RG-adapted flow, which is also used for most of the numerical results in the present work. The flow for the dynamical part of the RG-adapted Wilsonian effective action reads,

$$\begin{aligned}\left(\partial_t+\int_x\phi\,\gamma_{\mathrm{dyn},k}\,\frac{\delta}{\delta\phi}\right)S_{\mathrm{dyn},k}[\phi]+\frac{1}{2}\int_x\phi\,\partial_t\Gamma^{(2)}_k[\phi_0]\,\phi&\\ =\frac{1}{2}\,\mathrm{Tr}\,\mathscr{C}_k\left[S^{(2)}_{\mathrm{dyn},k}[\phi]-\left(S^{(1)}_{\mathrm{dyn},k}[\phi]\right)^2\right],&\end{aligned} \tag{6.13a}$$

with

$$\gamma_{\mathrm{dyn},k}[\phi_0]=-\,\partial_t\Gamma^{(2)}_k[\phi_0]G_k[\phi_0]\,. \tag{6.13b}$$

where $\partial_t\Gamma^{(2)}_k[\phi_0]$ is the flow of the two-point function at $\phi=\phi_0$. This flow can be disentangled from that of the correlation functions $S^{(n>2)}_{\mathrm{dyn}}$, see Appendix B.5.2.

## 6.2. Numerical approach

In Section 3.1 and Section 6.1.1 we have discussed general flows for generating functionals. They are reminiscent of different types of (functional) partial differential equations (PDE), i.e. of parabolic and hyperbolic types. In the following, we will use this analogy to those types of PDEs to better understand the behaviour of the equations. We shall consider the flow of the generating functional or path integral measure (3.20), the Wilsonian effective action, (3.30) and (6.13), and the 1PI effective action (3.35). Our main results are achieved with the RG-adapted flow (6.13) for the Wilsonian effective action. We show in Section 6.3.2 that within the current approximation and the lack of RG-adapted reparametrisations for the 1PI effective action, the RG-adapted flow for the Wilsonian effective action is the most stable one for computing complex effective actions that originate from a complex source term. Thus we evaluate the stability of the other flows with this as a benchmark.

While the following considerations concerning the type of PDE are independent of the approximation, it is instructive to consider a simple approximation as a showcase example, the 0th order of the derivative expansion or local potential approximation (LPA). For a detailed discussion of this approximation scheme see e.g. [104]. This is also the approximation we will use in the numerics in Section 6.2. In short, the LPA only considers the classical dispersion in the generating functional under investigation and includes a full effective potential.

We start with the RG-adapted Wilsonian effective action, which is predominantly used for the numerical results in the present work. It is given by

$$S_{\mathrm{ad},k}[\phi] = \int_x \Big[ -\frac{1}{2}\phi(x)\Big(-\partial_\mu^2 + m_k^2 + R_k\Big)\phi(x) + V_{\mathrm{dyn},k} \Big], \tag{6.14}$$

where the dynamical part $V_{\mathrm{dyn},k}$ of the effective potential only contains interaction terms, that is $\phi^n$ with $n \geq 3$ in a Taylor expansion about $\varphi = 0$.

The standard Wilsonian effective action in LPA is a variant of (6.14), where the full mass term with $m_k^2$ is frozen at $k = \Lambda$, and hence the remnant effective potential $V_{\mathrm{int},k}$ also contains $\varphi^2$ terms,

$$S_{\mathrm{eff},k}[\phi] = \int_x \Big[ -\frac{1}{2}\varphi(x)\Big(-\partial_\mu^2 + m_\Lambda^2 + R_k\Big)\varphi(x) + V_{\mathrm{int},k} \Big]. \tag{6.15}$$

For the Wegner flow of the path integral measure we consider $\exp\{-S_{\mathrm{ad/eff},k}[\phi]\}$ with the approximations (6.14) and (6.15) for the exponent. However, the complex Wegner flow has the issue of highly oscillatory initial conditions at high imaginary fields, see Appendix C.3.4 for more details.

The 1PI effective action in LPA reads

$$\Gamma_k[\phi] = \int_x \Big[ -\frac{1}{2}\phi(x)\,\partial_\mu^2\phi(x) + V_{\mathrm{eff},k} \Big]. \tag{6.16}$$

We emphasise again, that $\Gamma_k$ is the Legendre transform of the Wilsonian effective action. Therefore, the two effective potentials are not identical but are related by a Legendre transform. Hence, a given approximation of the respective generating functionals does not necessarily constitute the same approximation for the flows:

The $d = 0$ dimensional theory lacks the momentum dependence, and the LPA is exact. Hence, all flows have to agree with the full integral (after the Legendre transform is taken into account), if the initial conditions describe the same theory.

In turn, for $d > 0$ the LPA drops the non-trivial momentum-dependence of all terms. Accordingly, in LPA the Wilsonian effective action and the 1PI effective action differ genuinely.

In all cases the flow equations for the effective potential considered, (3.20), (3.30), (6.13), (3.35), can be formulated as convection-diffusion equations for the $\phi$-derivative of the effective potential or its interaction part,

$$u(\phi) = \frac{\partial V_{\mathrm{dyn/int/eff}}(\phi)}{\partial\phi}. \tag{6.17}$$

With (6.17) the generic form of the functional flows is given by

$$\partial_t u(z) - \partial_z\left[F(t,z,u(z)) - a(t,z,u(z))\,\partial_z u(z)\right] = 0, \tag{6.18}$$

where $t \in \mathbb{R}$ is the (negative) RG-time and $z \in \mathbb{C}$ is the complex field, triggered by a complex current or magnetisation in the path integral (3.2). In contrast to most of the DG literature, see [251,274,311,312], our formulation picks up an additional minus sign, due to the negative RG-time integration. As discussed there, all the generating functionals and hence their flows are real functions of a complex (field) variable $z$. The RG-adapted flow in LPA is derived in Section 6.2, see (6.29) and (6.30). The Polchinski flow and Wetterich flow in LPA can be found in Appendix B.5.1 and Appendix C.3.3 respectively.

The convection functional $F$ and the diffusion coefficient $a$ in (6.18) are structurally different in the functional flows considered here. Hence, already for real generating functionals, each of these systems of partial differential equations offers different numerical as well as conceptual challenges. Flows for complex generating functionals and the ensuing numerical evaluation of real generating functionals for complex fields add yet another layer of complexity.

In Section 6.2.1 we discuss the different types of partial differential equations encountered for the flows of the different generating functionals. In Section 6.2.2 we provide some details on the numerical approach with Discontinuous Galerkin (DG) methods. Finally, in Section 6.2.3 we discuss some features of the formation of DG for complex effective actions which allow to simplify the computation significantly.

### 6.2.1. Parabolic- and hyperbolic-type functional flows

Here we discuss the different types of partial differential equations (PDEs) we encounter for the three classes of functional flows put forward in Section 3.1 and Section 6.1.1. The emergent structure of singularities present in the different types of PDEs not only depends on the given type but also on the initial conditions. In the case of functional flows the set of allowed initial conditions is determined by RG-consistency [61, 127] and the physics at hand. This is discussed further in Section 6.3.1.

The flow of the path integral measure (3.20) is discussed in Section 6.2.1, that of the Wilson effective action (3.30) and the RG-adapted flow (6.13) are discussed in Section 6.2.1, and the flow for the 1PI effective action (3.35) is discussed in Section 6.2.1.

#### Parabolic-type flow I: Flow of the path integral measure

The Wegner flow of the path integral measure (3.20) with the typical RG kernel (3.22) is reminiscent of a *linear-parabolic equation*. Parabolic differential equations are common in heat conduction or particle diffusion processes. Generally speaking, real linear heat equations are well behaved. An initial solution $u(x, t_0)$ is smoothened out as the RG-time progresses and solutions exist for all times $t > t_0$. In an RG context, the diffusion coefficient is usually dependent on the RG-scale. Thus, the smoothing can freeze out at a certain RG-scale and a final structure survives. The amount of smoothing is therefore decided by the physical scales in the system which are introduced via the initial conditions.

Functional flows for the path integral measure on the real axis are showcased in Appendix C.3.4 as a consistency check. In a complex setting, we find that the main intricacy in this formulation are the initial conditions. As the complex part increases, the exponential function shows the characteristic oscillations which need to be resolved at a high numerical cost.

#### Parabolic-type flow II: Flow of the Wilsonian effective action

General flows for the Wilsonian effective action, and specifically the standard Polchinski flow for the effective action (3.30) and the RG-adapted flow (6.13) derived in Section 6.1.1 structurally resemble non-linear parabolic equations of the *reaction-diffusion* type. Subject to their specific form and the initial conditions, non-linear parabolic equations can generate so called *blow-ups* [311, 312]. These blow-ups may result in singularities, shocks or jumps at some finite time $t_0 < t_1 \leq \infty$. A prominent example for this flow is the Ricci-flow [313], which has been used to prove the Poincaré-conjecture.

We find that the initial conditions within the RG-setting belong to the class of initial conditions that potentially produce these blow-ups. Again, the RG-scale dependence of coefficients can prevent the *blow up* by freezing out the system. Therefore, their occurrence or absence depends on the the details of the setup, in other words on the physics at hand. For a numerical investigation of blow-ups within the equations see Appendix C.3.1.

In the complex plane, this formulation is very similar to *two-component reaction–diffusion systems*. These types of systems are most prominently used to describe biological pattern formation, for a review see [314]. An interplay of differing diffusive contributions, as well additional source terms, can destabilise a homogeneous system, resulting in the formation of a periodic, static pattern [315]. This effect is primarily found in *activator-inhibitor systems* [316], which do not contain any convective contributions. However, these convective contributions can be found in RG-flows and are given by $F$ in (6.18). We therefore do not expect any static pattern formation.

Blow-ups in the lower dimensional ($d \leq 2$) solutions are directly related to the Lee-Yang zeroes [297, 298]. They are expected to show up as divergences in the Wilsonian effective action, simply by their definition as zeroes or cuts of the exponential. We demonstrate in Appendix C.3.1, that our RG-adapted flow (6.13) allows us to narrow down the position of the blow-up and leads to a quantitative estimate. Our present numerical scheme is not fully adapted for resolving such a singularity, and the resolution of this intricacy is subject of ongoing work in a fully RG-adapted setup.

In higher dimensions, $d > 2$, the Lee-Yang singularity is directly linked to a physical phase transition. Here, the singularity is related to a cut in the complex plane, which we cannot resolve in the present setup, as in the present approximation we enforce holomorphicity within the flow, see Section 6.2.2. Still, we are able to infer the position of the Lee-Yang in Section 6.4.2, since it lies at the beginning of the cut. This information is not tainted by our enforcement of holomorphicity. Numerical inaccuracies linked to a potential smudging out of a cut are also subject to further investigations.

### Hyperbolic-type flow: Flow of the 1PI effective action

General flows for the 1PI effective action (3.33), including the Wetterich flow (3.35), are qualitatively very different from the previously discussed parabolic equation lookalikes. This qualitative difference is induced by the Legendre transform that connects the 1PI flows to that of the Wilsonian effective action and the path integral measure.

The 1PI flows are mostly dominated by strong convective movements and display characteristics of hyperbolic equations. Specifically, the information flows with a wave-like behaviour towards the infrared as has been studied in [1, 5, 65]. This structure of the information flow induces stabilising properties as does the dependence on the inverse 1PI two-point function. These stabilising properties are one of the main reasons why to date 1PI flows are used in most numerical applications. However, 1PI flows display non-linear and even negative diffusive contributions, which appear at high densities, or large complex fields in the present setting. For an in depth analysis we refer to Appendix C.3.3.

### Wrapup

The above investigation of the properties of the PDEs for the different functional flows suggests that the RG-adapted flows derived in Section 6.1.1 are very well-suited for the numerical computation of complex flows. The advantage is a combination of the structure of the PDE and

the simple implementation of RG-adapted variable changes. We rush to add that this evaluation is based on the current state of the investigation of functional flows for complex effective actions. A full comprehensive investigation is deferred to a future work. The general setup put forward in the present work suggests that it is rather a combination of well-chosen initial condition and RG-adaptation that is important. We expect that within such a combination all different functional flows can be used equally well.

In summary, we will predominantly show numerical results obtained with the flow (6.13a) derived in Section 6.1.1 with the PDE-type discussed in Section 6.2.1. These results are also used as benchmark for the numerical results obtained with the other functional flows.

### 6.2.2. Discontinuous Galerkin

Our numerics is done with Discontinuous Galerkin methods, which have been applied in the context of parabolic blow-ups, e.g. [317]. Therefore, we use the Local Discontinuous Galerkin method (LDG) [251] and implicit time stepping. This method has been set up for the fRG, and the corresponding numerical framework using the DUNE-project has been set up in Chapter 5.

In the present chapter we extend this method to complex systems of flow equations. The explicit form of each of these equations has already been displayed in (6.18). There we have introduced the complex field variable $z = x + \mathrm{i}\, y$, which can be interpreted as a 'spatial' variable for the given type of PDEs. The form (6.18) is essential for the convergence of the LDG method. Importantly, $u, F \in \mathbb{C}$ are real functions of a complex variable $z$. This leaves us with a two component system of PDEs for two one-dimensional variables $t, z$. It is discussed in detail in Section 6.2.3 how this property facilitates the numerical implementation. In short, the one-dimensional spatial coordinate is resolved within a numerical approximation, while the time dependence is integrated via an implicit time stepping scheme.

The requirement $a \geq 0$ ensures a strictly positive diffusion, which is a necessary requirement for the convergence of the LDG method [251]. Positive diffusion is a very restrictive requirement on the general form of a system of PDEs. In particular, this requirement is not always met in the complex 1PI flows. In Appendix C.3.3 the instability of a naive implementation of the 1PI flow in a complex setting is demonstrated numerically. In turn, the RG-adapted flow (6.13) was constructed with this property in mind.

### 6.2.3. Complex structure

The present set-up and in particular the final flow equation (6.18) can be readily applied to complex action problems with general complex couplings. Then, (6.18) is a partial differential equation for a general complex function $u(z)$ of a complex variable $z$. For complex classical couplings we find

$$\overline{u(z)} \neq u(z)\,. \tag{6.19}$$

Accordingly, (6.18) has to be solved for its imaginary and real part, while also implementing the holomorphicity constraint $\partial_{\bar{z}} u(z) = 0$.

From now on we restrict ourselves to the case of complex currents. Then, (6.18) is a partial differential equation in the RG-time t and the complex spatial variable $z$. In principle, one could simply use the split of $z$ into its real and imaginary part, $z = x + \mathrm{i}\, y$, and the respective split of the derivative, $\partial_z = \frac{1}{2}(\partial_x - \mathrm{i}\, \partial_y)$, for solving the equation on a two-dimensional grid. However, this is a two-dimensional representation of a one-dimensional system, additionally necessitating the implementation of the holomorphicity constraint.

Naturally, it is much more efficient for the numerical implementation to utilise the complex structure: the generating functional (3.2) and all derived quantities are defined for real field variables $\phi$. They become complex with $\phi \in \mathbb{R} \to \phi \in \mathbb{C}$. Thus, we can exploit the fact, that we compute real functions of a single complex variable $z$. For the generating function this leads to (6.3). For a general real function $f(z)$ this simply reads

$$\overline{f\big(z\big)} = f\big(\bar{z}\big). \tag{6.20}$$

with the real and imaginary part satisfying

$$\begin{aligned} \mathrm{Re}\big[f(x,y)\big] &= \frac{1}{2}\big(f(x,y)+f(x,-y)\big), \\ \mathrm{Im}\big[f(x,y)\big] &= \frac{1}{2\mathrm{i}}\big(f(x,y)-f(x,-y)\big). \end{aligned} \tag{6.21}$$

The Cauchy-Riemann differential equations allow to reformulate the $z$ derivative as a derivative of only the real variable $x$,

$$\begin{aligned} \partial_z \mathrm{Re}\big[f(z)\big] &= \frac{1}{4}\Big(f^{(1,0)} + \overline{f^{(1,0)}} - \mathrm{i}\left(f^{(0,1)} - \overline{f^{(0,1)}}\right)\Big) = \frac{1}{2}\Big(f^{(1,0)} + \overline{f^{(1,0)}}\Big), \\ \partial_z \mathrm{Im}\big[f(z)\big] &= \frac{1}{4\mathrm{i}}\Big(f^{(1,0)} - \overline{f^{(1,0)}} - \mathrm{i}\left(f^{(0,1)} + \overline{f^{(0,1)}}\right)\Big) = \frac{1}{2\mathrm{i}}\Big(f^{(1,0)} - \overline{f^{(1,0)}}\Big), \end{aligned}$$

where we used $\partial_z = \frac{1}{2}(\partial_x - \mathrm{i}\partial_y)$. The validity of the Cauchy-Riemann equations is assumed on the computational grid, which does not contain the blow-ups. Note that this assumption artificially smoothens out non-analyticities (cuts) around critical regions, since it enforces holomorphicity.

In summary we can replace $\partial_z \to \partial_x$ without loss of generality if the solution is holomorphic. After this replacement (6.18) does not contain any dependency on $\partial_y$, which allows for the computation at constant $y$. Therefore, the complex plane can be resolved on slices of constant $y$, i.e. a one-dimensional numerical grid in $x$-direction. The $y$-slices are then put together after the computation and we interpolate between them. Note that this procedure allows to resolve the entire RG-time and $x$ dependence for $\mathrm{Im}[z] \neq \mathrm{Im}[z_c]$, where $z_c$ is the position of the blow-up, whereas the computation of the $\mathrm{Im}[z_c]$ slice freezes in at $t_1 < \infty$. This separation also illustrates nicely how the extension of the formalism to the complex plane does not affect the computation on the real axis.

### 6.2.4. Separating the equations

The real and complex part of (6.18) are now separated, and we use the replacement $\partial_z \to \partial_x$ as suggested by the previous section. Here, we solely focus on parabolic-type flows, where the diffusive contribution is completely independent of $z$ and thus a real function $a(t) \in \mathbb{R}$. In the LDG formulation, this translates to system of two instationary and two stationary equations,

$$\begin{aligned} \partial_t u_x - \partial_x \left(\mathrm{Re}\left[F\left(t,z,u_x,u_y\right)\right] - a(t)\, q_x\right) &= 0\,, \\ \partial_t u_y - \partial_x \left(\mathrm{Im}\left[F\left(t,z,u_x,u_y\right)\right] - a(t)\, q_y\right) &= 0\,, \end{aligned} \tag{6.22}$$

and

$$q_x = \partial_x u_x\,, \qquad q_y = \partial_x u_y\,, \tag{6.23}$$

where we used the notation $u = u_x + \mathrm{i}\, u_y$ and a negative RG-time $t$. Alternatively, one could have used the replacement $\partial_z \to -\mathrm{i}\,\partial_y$. The proof for this replacement works analogously to Section 6.2.3. This procedure maps $\partial_z^2 \to -\partial_y^2$, effectively changing the sign of the diffusion term.

In principle, a mapping of $\partial_z$ to a mixed expression of $\partial_x$ and $\partial_y$ is also possible. In this case the computation would be performed on certain trajectories in the complex plane instead of straight lines.

Applying the LDG formulation to the 1PI flow is much more challenging. The diffusion coefficient $a(t, z, u(z))$ is not only field-dependent and thus requires an additional numerical flux, but it is also complex and hence creates mixing terms. For a formulation of the 1PI LDG formulation in a real setting see [5]. The complex LDG 1PI setup is outlined in Appendix C.3.3.

## 6.3. Convergence in the complex plane

In this section we present numerical results for the effective potential of the $\phi^4$ theory with a (classical) real scalar field and the action (6.1). The RG-adapted flow equation for the dynamical part $V_{\mathrm{dyn}}$ of the effective potential is derived in Section 6.3.1, including a discussion of the initial conditions. The derivation of the standard Polchinski flow and the 1PI Wetterich flow are deferred to Appendix C.3.2 and Appendix C.3.3 respectively. These appendices also include further numerical details and results.

A first benchmark test is given by the computation of the effective potential in $d = 0$ in Section 6.3.2. In zero dimensions the effective action agrees with the effective potential and LPA gives the full result. Hence, this analysis provides us with a non-trivial numerical benchmark for the convergence of the different flows. As a next step, the RG-adapted scheme is investigated on the real axis and compared with flows for the effective Wilsonian action, as well as the 1PI results.

### 6.3.1. Flow of the dynamical potential

As already discussed before, we consider the 0th order derivative expansion or local potential approximation (LPA), in which the full effective action is approximated by a classical dispersion term and a full effective potential. This is a low momentum approximation and is well-tested, see e.g. the recent review [104] for a comprehensive overview. In LPA the Wilsonian and 1PI effective action take the form (6.14), (6.15) (Wilsonian), and (6.16) (1PI). For the convenience of the reader we have provided a tabular summary of the different schemes, and where to find them, in Table 6.1.

#### Flow equation

In this section we apply the RG-adapted scheme from Section 6.1.1 to the real scalar field theory in $d$-dimensions. Solving (6.13a) for a single current $J = G_k[\phi_0]\phi$ requires knowledge of the full propagator at the expansion point $\phi_0$, which is given by

$$G_k[\phi_0] = \left(\Gamma_k^{(2)}[\phi_0](p) + R_k(p^2)\right)^{-1} = \left(m_k^2 + p^2 + R_k(p^2)\right)^{-1}, \tag{6.24}$$

where the regulator $R_k$ is given by a flat cutoff, that is optimised for the 0th order in the derivative expansion, [127, 129, 130], see Appendix B.7.1.

| Scheme | Effective Action (EA) | Effective Potential | Flow eq. | Current |
|---|---|---|---|---|
| *RG-adapted* | RG-adapted EA (6.6) | $V_{\rm dyn}$ (6.14), $m_k^2$ (6.25) | (6.29), (6.26) | (6.4b) |
| *Polchinski* | Wilsonian EA (3.6) | $V_{\rm int}$ (6.15) | (C.20) | (3.27) |
| *1PI* | 1PI EA (3.7) | $V_{\rm eff}$ (6.16) | (5.22) | (B.88) |

Table 6.1.: Summary of the different schemes used throughout this work. We indicate the Effective Action (EA), the Effective Potential which is used, as well as the respective flow equation, and definition of the current.

In the RG-adapted scheme, the two-point contribution at the expansion point $\phi_0$ is separated from the field-dependent dynamical potential $V_{\rm dyn}$ (6.14), see also (6.11). Thus, in the RG-adapted scheme we have to solve two distinct equations. At every RG-time step, we first compute the two-point contribution at the expansion point, which is just the RG-time dependent mass $m_k^2$. Secondly, we solve the field-dependent flow of the dynamical potential $V_{\rm dyn}$. To derive the flow of RG-time dependent mass, we use its direct link to the 1PI two-point function,

$$m_k^2 = \Gamma_k^{(2)}[\phi_0](p)|_{p=0}\,, \tag{6.25}$$

which in turn can be inferred from the flow of the RG-adapted effective action. This is evaluated in Appendix B.5.2 by using the relations for the two-point functions, (B.77), and the flow of $\Gamma_k^{(2)}$ in terms of the RG-adapted effective action, (B.79). The latter is now used to obtain the flow of the RG-time dependent mass,

$$\partial_t m_k^2 = \frac{1}{2}\int_p \left\{ \frac{\left(V_{\rm dyn}^{(3)} V_{\rm dyn}^{(1)} - V_{\rm dyn}^{(4)}\right)\partial_t R_k(p^2)}{\left[m_k^2 + p^2 + R_k(p^2)\right]^2} \right\} = \frac{v(d)k^{d+2}}{\left(m_k^2+k^2\right)^2}\left(V_{\rm dyn}^{(3)} V_{\rm dyn}^{(1)} - V_{\rm dyn}^{(4)}\right), \tag{6.26}$$

where

$$v(d) = \frac{2\pi^{d/2}}{\Gamma(d/2)d}(2\pi)^{-d}\,. \tag{6.27}$$

In (6.26), the nth derivatives

$$V_{\rm dyn}^{(n)} = V_{{\rm dyn},k}^{(n)}[\phi_0]\,, \tag{6.28}$$

are the corresponding n-point function of the RG-adapted effective action at the expansion point $\phi_0$. The full solution of $V_{{\rm dyn},k}$ is computed within the Local Discontinuous Galerkin method. This method captures the field dependence on $\phi$ using non-overlapping cells. Within each cell $V_{{\rm dyn},k}$ is then projected onto a higher order polynomial basis $N > 4$ (where $N$ is the polynomial order) around the expansion point. This basis ensures a precise computation of derivatives. Hence we can infer all vertices up to the four-point functions from the field-dependent potential with a very high numerical precision. The extraction of higher order derivatives from the full solution is expanded on in Appendix A.1.3.

The dynamical potential is a real function of a complex variable. We pick $\phi_0 = 0$ on the real axis, in order to ensure that this property is not spoiled by out choice of expansion point $\phi_0$.

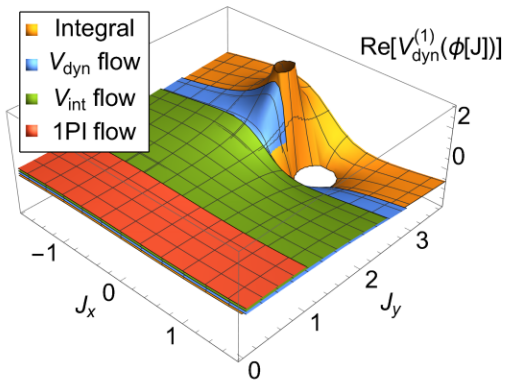


(a) Graphical comparison of the real part of $V^{(1)}_{\mathrm{dyn}}$.

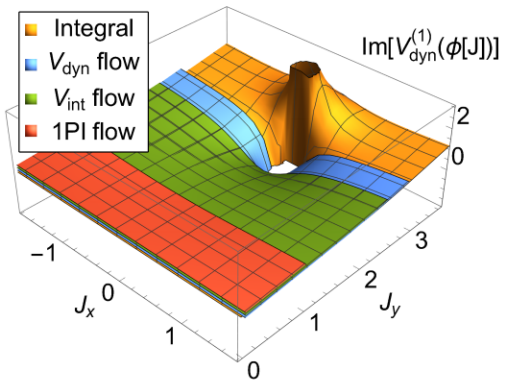


(b) Graphical comparison of the imaginary part of $V^{(1)}_{\mathrm{dyn}}$.

Figure 6.1.: Numerical convergence in the complex plane for the different expansion schemes. The results of all flows (*red*: 1PI, *green*: Polchinski ($V_{\mathrm{int}}$), *blue*: RG-adapted ($V_{\mathrm{dyn}}$)) agree with the results of the numerical integration, and for a better visualisation the different data are shown with a slight offset. We show results for the first derivative of the dynamical potential $V^{(1)}_{\mathrm{dyn}}$, which is raw output of the numerical computation in (6.29). Definitions and fluxes of the different schemes are summarised in Table 6.1. All units are given in terms of the UV mass $m = 1$ with an initial cutoff $\Lambda = 5$.

Thus all vertices $V^{(n)}_{\mathrm{dyn}}$ are also real, implying $m_k^2 \in \mathbb{R}$. This reasoning can be extended even further by making use of the $Z_2$ symmetry of the effective dynamical potential $V_{\mathrm{dyn},k}(\phi)$. We deduce that $\mathrm{Re}[V_{\mathrm{dyn},k}(\phi)]$ is an even function in the real variable $\phi_x$, whereas $\mathrm{Im}[V_{\mathrm{dyn},k}(\phi)]$ is odd in $\phi_x$. Furthermore, we find that $\mathrm{Re}[V^{(1)}_{\mathrm{dyn},k}(\phi)]$, $\mathrm{Im}[G_k^{-1}[\phi]]$, $\mathrm{Re}[V^{(3)}_{\mathrm{dyn},k}(\phi)]$, $\mathrm{Im}[V^{(4)}_{\mathrm{dyn},k}(\phi)]$ are odd in $\phi_x$ as well. This implies purely real or imaginary values, for even and odd vertices respectively, if the expansion point is chosen at $\phi_x = 0$. Since odd vertices only appear as a product, we find that choosing any expansion point along the imaginary axis does not introduce any complex parts in the flow equation. By also choosing $\phi_0 = 0$, we deduce $V^{(3)}_{\mathrm{dyn}} = V^{(1)}_{\mathrm{dyn}} = 0$. Accordingly, the respective terms in the equations are dropped in the following.

Next, we derive the field-dependent flow of the dynamical potential $V_{\mathrm{dyn}}$. For this purpose, (6.14) is inserted in the flow (6.13a). Using the expression for the propagator in (6.24) with the flat cutoff, we arrive at

$$\partial_t V_{\mathrm{dyn}}(\phi) = v(d) k^{2+d} \left[ \frac{\left[V^{(1)}_{\mathrm{dyn}}(\phi)\right]^2 - V^{(2)}_{\mathrm{dyn}}(\phi)}{\left(m_k^2 + k^2\right)^2} + \frac{V^{(4)}_{\mathrm{dyn}}}{\left(m_k^2 + k^2\right)^2} \frac{\phi^2}{2} - \frac{V^{(4)}_{\mathrm{dyn}}}{\left(m_k^2 + k^2\right)^3} V^{(1)}_{\mathrm{dyn},k}(\phi)\phi \right] . \tag{6.29}$$

We now proceed to adjust this equation to the numerical framework presented in Section 6.2.2 and map $\partial_\phi \to \partial_{\phi_x}$. Equation (6.29) can be reformulated as a one-dimensional non-linear diffusion equation by taking an additional $\phi_x$-derivative. In a complex framework we make use of Section 6.2.3. With $u = \partial_{\phi_x} V_{\mathrm{dyn}}(\phi)$ as defined in (6.17), we obtain

$$\partial_t u = A(k, d, \phi_0)\, \partial_{\phi_x} \Big( F[u, \phi, \phi_0, k] - \partial_{\phi_x} u \Big) . \tag{6.30a}$$

The real, positive diffusion coefficient is given by

$$A(k,d,\phi_0) = v(d)k^{2+d}\frac{1}{\left(m_k^2+k^2\right)^2}\,, \tag{6.30b}$$

and the complex valued convective flux

$$F[u,\phi,\phi_0,k] = u^2 + u'''(\phi_0)\left[\frac{\phi^2}{2} - \frac{1}{\left(m_k^2+k^2\right)}u\,\phi\right]. \tag{6.30c}$$

This highlights a convenient property of the RG-adapted expansion for the evaluation of complex effective potentials or even effective actions: for any expansion point along the imaginary axis the propagator remains real, i.e. positive diffusion is ensured.

### Initial conditions

All dimensionful quantities are measured in powers of the mass at the initial UV scale $k = \Lambda$, in particular implying $m = 1$. The initial or bare classical coupling at $k = \Lambda$ is also set to unity, to wit

$$m^2 = 1\,, \qquad \lambda = 1\,. \tag{6.31}$$

The initial conditions are obtained via the Legendre transformation of the classical action, which is the initial condition for the 1PI flow. Details of this derivation are given in Appendix B.5.3. Furthermore, the choice of the initial cutoff scale $\Lambda$ in the UV requires special care: the algebraic structure of the Wilsonian effective action flow has no built-in suppression at high field values, as present for the 1PI flows. In fact, the flow of couplings and the mass increases at larger field values. Moreover, the structure of the flow is such that for $d > 2$ potential numerical inaccuracies in this fine-tuning problem are enhanced by powers of the cutoff scale.

In this work, an initial cutoff scale $\Lambda = 5$ is used, for which we find coinciding results from various methods for dimensions $d = 0,\ldots,4$, see Section 6.3.3.

## 6.3.2. Benchmark results in d=0

In this section, the numerical convergence of the different functional flows towards the full result is tested. For this purpose we use the zero-dimensional theory, where the partition function (3.2) is a simple one-dimensional integral. This integral can be solved numerically, and in some limiting cases even analytically. For related works for real-valued effective actions and flows see [248–250]. We remark, that in $d = 0$ the partition function indeed develops zeros that are particularly difficult to resolve. In turn, in higher dimensions we expect cuts which may facilitate the numerical treatment. This has been already observed within lattice simulations with complex Langevin dynamics [299].

The dynamical potential $V_{\mathrm{dyn}}$ is computed using the flow of the RG-adapted scheme, the Polchinski flow and the 1PI flow, see Table 6.1 for a summary of relevant equations in the different schemes. Detailed derivations of the latter two flows are found in Appendix C.3.2 and Appendix C.3.3 respectively. Computations are, as discussed in Section 6.2.3, performed on slices of constant $\phi_y$, using 1d-numerical grid, ranging from $\phi_x \in [-3,3]$. On each slice a grid of $K = 60$ cells is used with a polynomial of order $N = 2$ in each cell. Afterwards, results need to be mapped from the fields to the current $\phi \to J$. In the RG-adapted scheme, this is done via

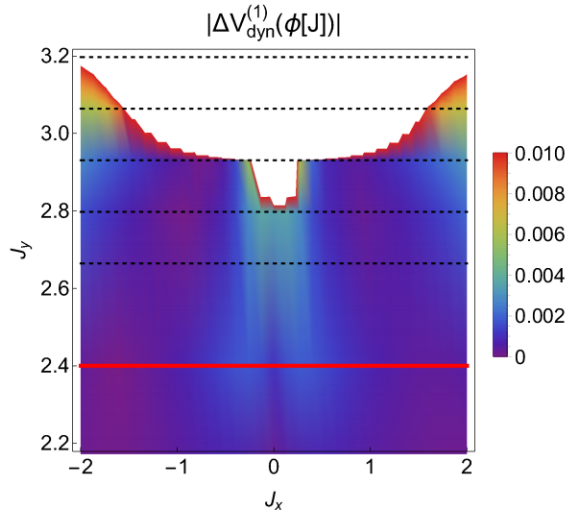


Figure 6.2.: Absolute value of the numerical error of $V^{(1)}_{\mathrm{dyn}}$ computed with the RG-adapted flow. The error is measured by subtraction from the numerically performed integral, the definition is given in (6.32). The pole position is inferred from the numerical evaluation of the integral and situated at at $J_y = 3$. The flow is solved on the slices along the black dashed lines, remaining values are interpolated. The red line is drawn in as a reference. It indicates the last convergent computation using the Polchinski flow, see Appendix C.3.2. All units are given in terms of the UV mass $m = 1$ at an initial cutoff $\Lambda = 5$.

the definition of the current in (6.5a), the approximation of the propagator in (6.24) and the contained mass term $m_k^2$ (6.25). The mass term is computed from (6.26). This computation is explained further in the following Section 6.3.3, see also Figure 6.5.

Figure 6.1 shows results up to their maximal $J_y$ value, where the computation still converges. We find that the RG-adapted scheme retains a very high numerical accuracy in a very close proximity of the pole in comparison to the Polchinski flow and the 1PI flow. The convergence pattern is shown in Figure 6.2 and we find satisfying numerical accuracy of the RG-adapted scheme up to $J_y = 2.8$. The numerical error is given by the absolute value of $\Delta V^{(1)}_{\mathrm{dyn}}(\phi[J])$ with,

$$\Delta V^{(1)}_{\mathrm{dyn}}(\phi) = \Delta V^{(1)}_{\mathrm{dyn,int}}(\phi) - \Delta V^{(1)}_{\mathrm{dyn,flow}}(\phi)\,. \tag{6.32}$$

Equation (6.32) is the difference of the numerical result for the first derivative of $V_{\mathrm{dyn}}$ obtained from the direct numerical evaluation of the integral in (3.2), $V_{\mathrm{dyn,int}}$, and the integration of the RG-adapted flow, $V_{\mathrm{dyn,flow}}$.

From the numerical integration of (3.2) the pole position is found at

$$J = 3\mathrm{i}\,. \tag{6.33}$$

A computation of the Polchinski flow (C.20) on the same numerical grid, only converges up to $J_y = 2.4$, which is indicated by the red line in Figure 6.2. This significant increase in accuracy between the RG-adapted scheme and the Polchinski flow supports the expansion about $\phi_0$.

Within the current scheme, the 1PI flow is only convergent in the symmetric phase, i.e. for $\phi_y \leq 1$, where $V^{(2)}_{\mathrm{eff,k}} \geq 0$ with our initial conditions discussed in Section 6.3.1. A detailed discussion is given in Appendix C.3.3, an alternative formulation of the 1PI flow is subject to further investigation.

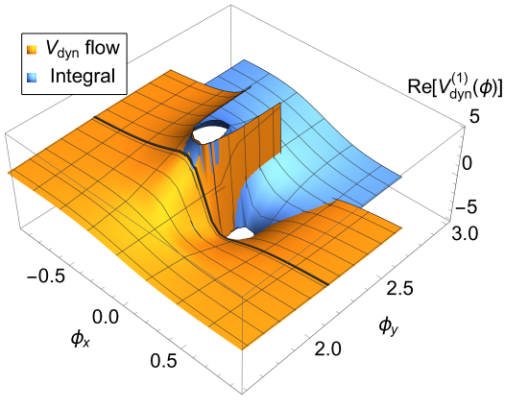


(a) Real part of $V^{(1)}_{\mathrm{dyn}} = \partial_\phi V_{\mathrm{dyn}}$ from the RG-adapted flow (6.30) in comparison to the exact numerical result.

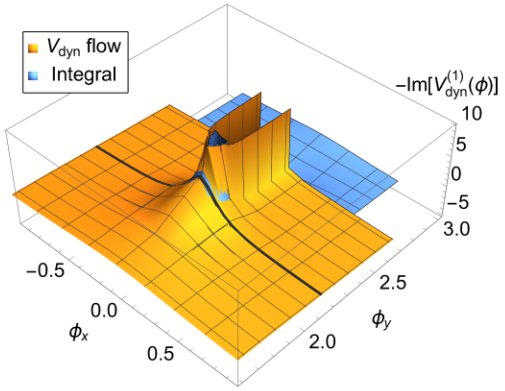


(b) The imaginary part of $-V^{(1)}_{\mathrm{dyn}} = -\partial_\phi V_{\mathrm{dyn}}$ from the RG-adapted flow (6.30) in comparison to the exact numerical result.

Figure 6.3.: The plots show the first derivative of the dynamical potential $V^{(1)}_{\mathrm{dyn}}(\phi)$ in $d = 0$ dimensions in the vicinity of the first Lee-Yang singularity. We compare results generated by the RG-adapted flow (6.29), (6.30) to the numerically integrated expression in (3.2). The numerical data has a slight offset which allows for a better graphical presentation. Both calculations are in agreement for $\phi_y$ smaller than the black line. The absolute difference between both results is shown in Figure 6.2. At the Lee-Yang singularity the RG-adapted flow freezes in and we see an un-physical continuation of the singularity. All units are given in terms of the UV mass $m = 1$ at an initial cutoff $\Lambda = 5$.

Beyond the Lee-Yang zero, an expansion about $\phi_0$ is no longer feasible. For all values $\phi_y > \phi_c$, where $\phi_c$ is the position of the Lee-Yang singularity, the flow runs into a *blow-up*, i.e. a singularity, compare to the raw data in Figure 6.3. A detailed discussion of the *blow-up* is given in Appendix C.3.1. The use of possible expansion points beyond the first pole are subject of ongoing investigations.

### 6.3.3. Convergence for $d \geq 0$ on the real axis

For higher dimensions, d> 0, the local potential approximation is indeed an approximation. Moreover, the LPA differs for the different schemes and we expect small deviations in the effective potentials.

Within a first application of the RG-adapted scheme to a quantum-field theory, i.e. $d > 0$, we investigate its behaviour on the real axis in comparison to established methods such as the Polchinski flow and the 1PI flow.

The raw LPA data in the RG-adapted scheme is converted by using the relations in Table 6.1. It provides us with the density of the Schwinger functional $w[J]$,

$$w[J] = W[J]/\mathcal{V}_d \quad \text{and} \quad \mathcal{V}_d = \int \mathrm{d}^d x\,. \tag{6.34a}$$

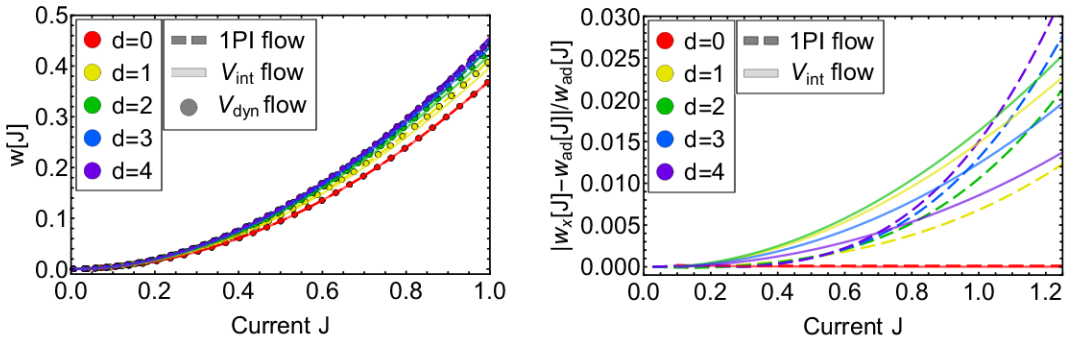


(a) Graphical comparison of the desity of the Schwinger functional $w[J]$ (6.34) as a function of the real current J.

(b) The relative error of the density of the Schwinger functional $w_x$ in relation to the RG-adapted result $w_{\text{ad}}$. Where $x$ indicates the result from the Polchinski and 1PI flow as indicated by the legend.

Figure 6.4.: Full potential of the Schwinger functional (6.34) on the real axis for different dimensions $d = 0, \ldots, 4$. We compare numerical results from the RG-adapted flow ($V_{\text{dyn}}$), the Polchinski flow ($V_{\text{int}}$) and the 1PI flow. The data was then used to compute the density of the Schwinger functional $w[J]$ using (6.34) and the information linked in Table 6.1. The results in $d = 0$ are exact, whereas the solutions for $d > 0$ start differing more strongly with increasing field values. All units are given in terms of the UV mass $m = 1$ at an initial cutoff $\Lambda = 5$.

It follows,

$$\begin{aligned} w[J] &= \frac{1}{2} m^2_{k=0}\, \phi^2 - V_{\text{dyn}}(\phi)|_{\phi = G_k[\phi_0]J} \\ &= \frac{1}{2}\phi^2 - V_{\text{int}}(\phi)|_{\phi = \left(S^{(2)}\right)^{-1} J} \\ &= J\ \phi - V_{\text{eff}}(\phi)|_{\phi = \left(\frac{\partial V_{\text{eff}}}{\partial \phi}\right)^{-1}(J)} . \end{aligned} \tag{6.34b}$$

The first, second and third line are given in terms of the RG-adapted result, the result of the Polchinski flow and the 1PI flow respectively. The different definitions of the current make use of the RG-adapted propagator $G_k[\phi_0]$ and the classical dispersion $S^{(2)}$. The coordinate change in the 1PI scheme follows directly from the Legendre transformation. The results from the different flows agree remarkably well, as is shown in Figure 6.4: the results agree necessarily in $d = 0$. In $d > 0$ we notice a deviation in the percent range for currents $J < 0.8$, which keeps increasing for even higher fields. Interestingly, we find that the results obtained from the 1PI flow, are in better agreement with that from the RG-adapted scheme for currents $J \lesssim 0.7$. This is likely related to the similar definition of RG-adapted currents, since in the 1PI case we have

$$J = \frac{\partial V_{\text{eff}}}{\partial \phi} + k^2 \phi = (V^{(2)}_{\text{eff}} + k^2)\ \phi\,, \tag{6.35}$$

due to the $Z_2$ symmetry of the potential. In this picture, the 1PI effective action is related to the RG-adaptation the current suggested in (6.5), using the full field-dependent propagator. Hence it is suggestive, that an RG-adapted scheme using the fixed field value $\phi_0$ compares well at small fields.

The behaviour shown in Figure 6.4 also suggests to compare the two-point function at the origin, the mass parameter $m^2_k$ (6.25) as it constitutes the defining difference in the presented

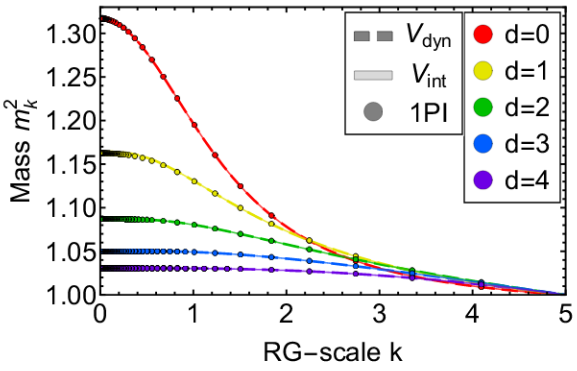


Figure 6.5.: RG-scale dependence of the mass $m_k^2$ at the expansion point, as it is defined in (6.25), for dimensions $d = 0, \ldots, 4$. Results are obtained from computations of $V_{\text{dyn}}$ (RG-adapted scheme), $V_{\text{int}}$ (Polchinski flow) and the 1PI flow, see Table 6.1. All units are given in terms of the UV mass $m = 1$ at an initial cutoff $\Lambda = 5$.

schemes. In the RG-adapted scheme, it is computed in a separate equation from the potential using (6.26), whereas it can be read off of $V_{\text{int}}^{(2)}[0]$ (Polchinski) and $V_{\text{eff}}^{(2)}[0]$ (1PI). The results compare well for all dimension and are shown in Figure 6.5. This check shows that physical values can be extracted consistently from the various schemes in all dimensions.

## 6.4. Complex effective potential and Lee-Yang zeroes in $d = 4$

We now proceed with a comprehensive analysis of results for the complex effective potential and the properties of the Lee-Yang zeros in the $d = 4$ dimensional scalar field theory. As mentioned before, this theory or rather its O(4) variant is (part of the) scalar-pseudoscalar meson sector in the fRG approach to QCD with dynamical hadronisation, see [44, 45, 49, 51]. Roughly speaking, its embedding in QCD leads to additional driving forces in the present setup and hence this extension is covered by the general discussion of the types of differential equations in Section 6.2. Finally we are interested in such a QCD analysis at finite temperature and density. There the respective phase transitions and Lee-Yang zeros are related to the O(4) theory in $d = 3$ dimensions. We have performed such a numerical analysis also in $d = 3$ and $d = 1, 2$. However, a discussion of the location of the Lee-Yang zeros, their parameter dependence and the critical physics goes beyond the scope of the present paper, and will be presented elsewhere. Here we only state, that the present numerical analysis is also converging in $d = 1, 2, 3$.

In Section 6.4.1 we initiate the analysis with the discussion of the effective potential and its scaling properties. In Section 6.4.2 we evaluate the properties of the Lee-Yang singularity. In particular we compute the mass dependence of its location and the intersection point with the real axis at the phase transition point of the real scalar theory.

### 6.4.1. Scaling properties and Lee-Yang singularities

For the evaluation of the scaling properties in the vicinity of the Lee-Yang singularities we evaluate the full effective potential in the complex plane. The computations are performed on $\phi$ slices with constant imaginary part $\phi_y$ with a spacing of 0.1 until $\phi_y = 3.2$. At $\phi_y = 3.2$ we are in the proximity of the *blow-up*, investigated in Appendix C.3.1. Furthermore, we increase

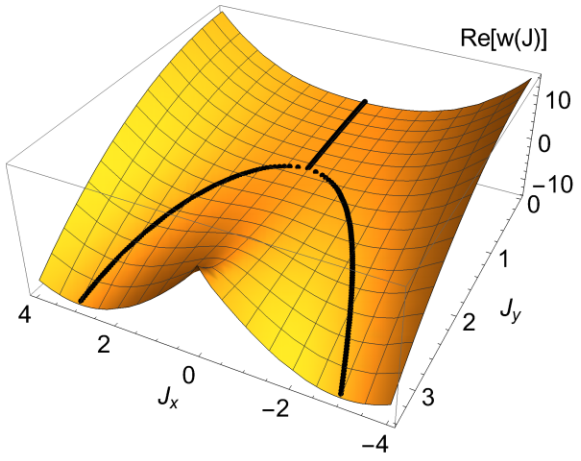


Figure 6.6.: Real part of the density of the Schwinger functional $w[J]$. The data is obtained from the RG-adapted scheme. The raw data was computed in Section 6.4 and integrated using the path described in Appendix B.5.5 and (6.34). The black dotted line indicates the expectation value for the magnetisation, compare (6.36), and is evaluated for all $\phi_y$ using (6.36b) with $H = 0$. The critical value for the spontaneous breaking of symmetry is clearly visible at $J_0 \approx 1.37$. All units are given in terms of the UV mass $m = 1$ at an initial cutoff $\Lambda = 5$.

the resolution in the critical area between $\phi_y \in [1.3, 1.4]$ to 0.01. The slices are interpolated in $\phi_y$ direction after the evaluation. Lastly, the effective potential is computed from the raw data, following the integration procedure described in Appendix B.5.5.

Performing calculations in the complex plane is tantamount to scanning the theory for different initial masses, since $m^2[0, \phi_y] = m^2 - \frac{\phi_y^2}{2}$ on each slice. In $d = 4$, the $\phi^4$ theory is evaluated in its critical dimension, and hence we expect mean field scaling at the Lee-Yang singularity.

In the present case, mean field scaling occurs in a relatively big scaling regime, which allows for very accurate fits. Once the scaling amplitudes are determined, the location of the Lee-Yang singularity is estimated in Section 6.4.2. The order parameter is given by the average magnetisation $M$ which is the solution of the equation of motion (EoM),

$$M(\phi_y, H) = \phi_{\text{EoM}}\,. \tag{6.36a}$$

The solution to the EoM, $\phi_{\text{EoM}}$ is determined from

$$\left.\frac{\partial w[J(\phi_x, \phi_y)]}{\partial \phi_x}\right|_{\phi_x = \phi_{x,\text{EoM}}} = H\,. \tag{6.36b}$$

The solution $\phi_{\text{EoM}}$ in (6.36) depends on the effective mass $m^2[0, \phi_y]$ of the corresponding $\phi_y$-slice and the external field $H$. The magnetisation (6.36) follows the minimum of the density $w$ and is depicted in Figure 6.6. There, the critical value $J_0 \approx 1.37$ is clearly visible as the bifurcation point of the minimum.

For the extraction of the scaling exponents we use the scaling relations in the vicinity of the

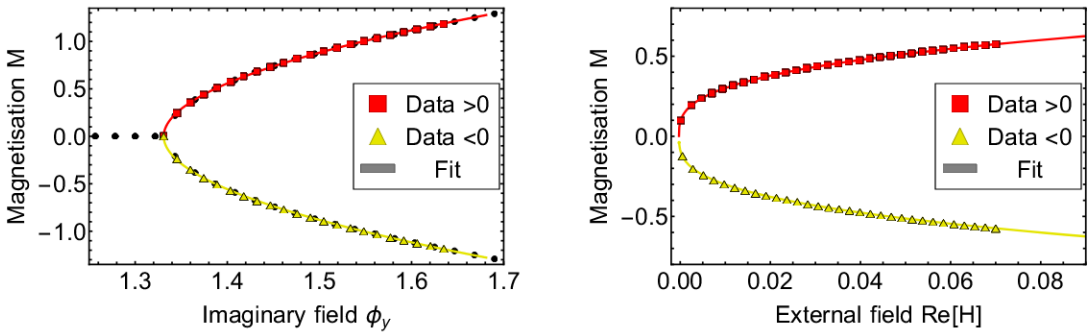


(a) Real part of the magnetisation as a function of $\mathrm{Im}\,\phi$. (b) Real part of the magnetisation as a function of $\mathrm{Re}\,H$.

Figure 6.7.: Real part of the average magnetisation $M$ as a function of the imaginary part $\phi_y$ of the field (left) and the real part $\mathrm{Re}\,H$ of the external field (right). The fits are based on the scaling functions (6.37) with the fit parameters in Table 6.2. Both branches of the magnetisation are fitted separately, and the overall error of the fit parameters is obtained by averaging over both branches and taking the fit error into account. All units are given in terms of the UV mass $m = 1$ at an initial cutoff $\Lambda = 5$.

critical $\phi_y$-slice

$$\mathrm{Re}\big[M(\phi_y, H=0)\big] = B\left(\frac{\phi_y - \phi_c}{\phi_c}\right)^{\beta},$$

$$\mathrm{Re}\big[M(\phi_y = \phi_c, H)\big] = B_c H^{1/\delta}, \tag{6.37}$$

where $\phi_c$ is the critical field that signals the onset of symmetry breaking. The amplitudes $B, B_c$ are used later for computing universal quantities.

A $\chi$-squared fit is performed separately on both branches and the difference between fits is used for an error estimate of the numerical error.

The fit parameters are given in Table 6.2 and the result is plotted in Figure 6.7. From the scaling fits we obtain

$$\beta = 0.505(23), \qquad \delta = 2.992(18), \tag{6.38}$$

which corresponds well to the expected mean field scaling parameters $1/2$ and $3$ respectively. The error is estimated by dropping the last five data-points. Since we do not aim at a precise estimate of the scaling parameters in this work, we refrain from an in-depth error analysis. Possible sources of error are the interpolation of data in $\phi_y$-direction, as well as the determination of the minimum.

A further,derived, scaling exponent is given by,

$$\gamma = \beta(\delta - 1), \tag{6.39}$$

and governs the scaling of the susceptibility $\chi$.

$$\chi(\phi_y, H=0) = \frac{\partial M}{\partial H}(\phi_y, H)|_{H=0}. \tag{6.40}$$

We include an additional subleading quadratic term in our fit to allow for a bigger fit-interval and a better fit to the data. The fit function reads

$$\chi(\phi_y, H=0) = C_{\pm}\left(\frac{\phi_y - \phi_c}{\phi_c} + D\left(\frac{\phi_y - \phi_c}{\phi_c}\right)^2\right)^{-\gamma}, \tag{6.41}$$

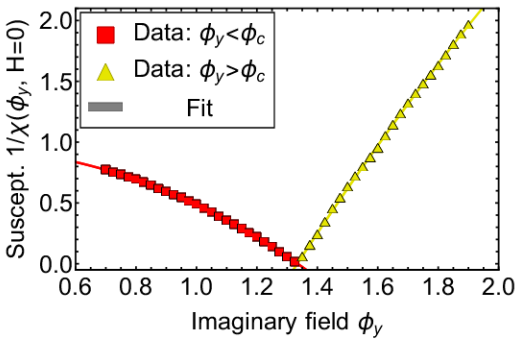


Figure 6.8.: Inverse of the susceptibility $\chi$ as a function of field $\phi_y = \mathrm{Im}\,\phi$. Fits to the data are performed with (6.41), where we use $\gamma = 1$. The resulting scaling amplitudes are given in (6.42). Small wiggles in the data-points originate from an 2D-interpolation of the raw data. All units are given in terms of the UV mass $m = 1$ at an initial cutoff $\Lambda = 5$.

where $\gamma = \beta(\delta - 1) = 1$ is the mean field scaling exponent. $C_\pm$ are the scaling amplitudes in the symmetric and spontaneously broken phase respectively. The susceptibility is obtained from $\partial^2_{\phi_x} V_{\mathrm{dyn}}(\phi_x, \phi_y)$, for details see Appendix B.5.4.

We have applied a $\chi$-squared fit to the inverse of the susceptibility $\chi(\phi_y, H = 0)^{-1}$. The fit with (6.41) and the data-points are shown in Figure 6.8. The overall amplitudes $C_\pm$ and the relative factor $D$ of the subleading term from the fits are given by

$$\begin{aligned} C_+ &= -0.4369(11), \quad C_- = 0.2025(21), \\ D_+ &= -0.256(20), \quad D_- = 0.6117(88). \end{aligned} \tag{6.42}$$

In mean field, the amplitudes $C_\pm$ are related with $|C_+| = 2|C_-|$. This relation is violated by approximately 8%. The deviation in $C_\pm$ also persists for smaller fit-intervals. The numerical errors may be caused by a small true scaling regime as well as the interpolation of $\phi_y$ slices. This behaviour may also be linked to a faulty smoothing out of an cut for $\phi_y > \phi_c$. All these potential sources are currently investigated.

Gathering all scaling parameters, we obtain the universal scaling amplitude

$$R_\chi = \frac{C_+ B^{\delta-1}}{B_c^\delta} = 1.035(25), \tag{6.43}$$

This agrees well with the expected value in mean field computations $R_\chi = 1$. Computing $R_\chi$ from $C_-$ yields $R_\chi = 0.931(22)$. This result also suggests, that the potential smoothing out

| | $\beta$ | $\delta$ | $\lvert B\rvert$ | $\lvert B_c\rvert$ | $\phi_0$ |
|---|---|---|---|---|---|
| $\phi_{x,\mathrm{EoM}} > 0$ | 0.5050(40) | 2.9830(88) | 2.520(20) | 1.408(40) | 1.331 |
| $\phi_{x,\mathrm{EoM}} < 0$ | 0.5060(43) | 3.000(11) | 2.526(22) | 1.3933(55) | 1.331 |

Table 6.2.: Fit parameters for the fit (6.37) applied to the data-set in Figure 6.7. The error is the $\chi^2$ error of the fit. We keep fits of both branches to get an estimate for the error of the overall scaling. The error on $T_c$ is $\leq 10^{-5}$ and not indicated.

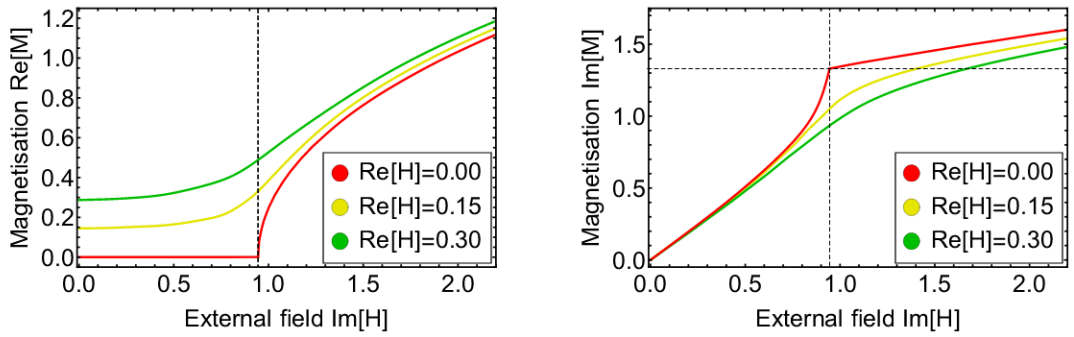


(a) Real part of the magnetisation.

(b) Imaginary part of the magnetisation.

Figure 6.9.: Real and imaginary part of the average magnetisation $M$, defined in (6.36), at $\phi_y = \phi_c$ as a function of the imaginary part $\mathrm{Im}\,H$ of the external field. The magnetisation is shown for different values of the real part $\mathrm{Re}\,H = 0,\ 0.15,\ 0.30$ of the external field. The dashed lines highlight the position of the cusp at $M = 1.33\mathrm{i}$ and $\mathrm{Im}\,H = 0.9448$. The Lee-Yang singularity is clearly visible at $\mathrm{Re}\,H = 0$ and is increasingly smudged out for higher values of the real external field. All units are given in terms of the UV mass $m = 1$ at an initial cutoff $\Lambda = 5$.

of the cut does not strongly affect the solution of the equations of motion. The fit result also provides an error for the critical field with

$$\phi_c = 1.3340(10)\,, \tag{6.44}$$

where we have taken the mean of both fits (6.42) and their respective error.

### 6.4.2. The Lee-Yang singularity

Finally, we discuss the location of the Lee-Yang edge singularity. This is chiefly important for an application of the current approach to QCD: the extrapolation of the location of the Lee-Yang singularity in QCD as a function of baryon chemical potential onto the real axis constrains the location of a potential critical end point. More generally it constrains the location of the onset of new physics.

In the present $\phi^4$ model case, the edge singularity in $d = 4$ corresponds to a kink in the magnetisation. As an example, we use the data-set from the previous section with the initial conditions from Section 6.3.1 with a UV-mass $m^2 = 1$. We evaluate the magnetisation $M$ defined in (6.36) at critical $\phi_y = \phi_c$ and imaginary external field $H$. Both the real and imaginary part of the magnetisation are shown in Figure 6.9. The exact position of the Lee-Yang edge singularity is located at $M_{\mathrm{crit}} = 1.3320(20)\mathrm{i}$ and $\mathrm{Im}\,H = 0.9448$. It can be identified by the

| $\Delta$ | $m_c^2$ | $A$ |
|---|---|---|
| 1.4969(66) | −0.03943(17) | 0.913(12) |

Table 6.3.: Fit parameters to the scaling fit of the Lee-Yang location in (6.45) and plotted with the data-set in Figure 6.10a. The error to the fit is obtained by removing the last data point.

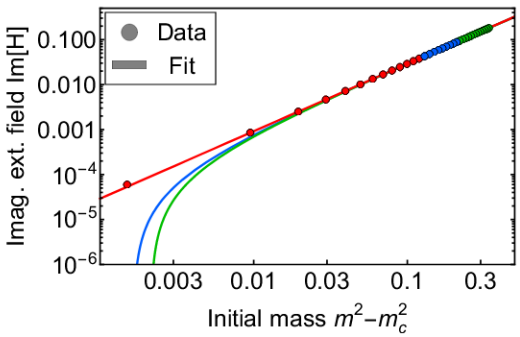


(a) Location of the Lee-Yang singularity in the complex plane as a function of the difference of the square of the initial UV-mass $m^2$ and the critical mass squared, $m_c^2 = -0.03943(17)$. Fits are perfomed separately on the red, blue and green data-points with the (mean field) leading scaling form (6.45). The red data-points show the expected scaling-behaviour and yield a critical initial mass for the real phase transition. The corresponding fit data is given in Table 6.3. The blue and green data-points contain a small subleading contribution to the scaling, see Figure 6.10b and thus result in higher estimates of $m_c^2$.

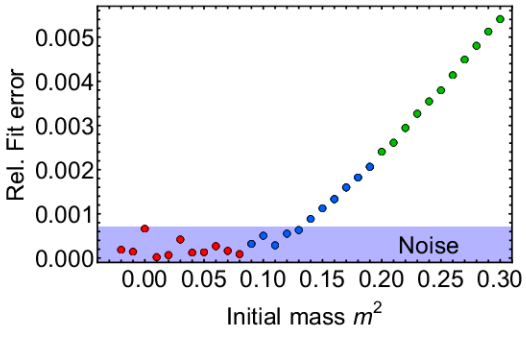


(b) Relative error between data-points and the fit obtained close to $m_c$: red fit-function in Figure 6.10a with the parameters Table 6.3. The first few data-points are exempt from the plot, since their absolute value is smaller than the fit-accuracy. The red, blue and green color corresponds to that of the data-points in Figure 6.10a. The noise is linked to a numerical error on the data, whose absolute value is smaller than $10^{-5}$. We find a subleading behaviour to the scaling for initial masses $m^2 \gtrsim 0.14$.

Figure 6.10.: Location of the phase transition on the real axis from an extrapolation of the location of the Lee-Yang zeros. All computations use an initial cutoff $\Lambda = 5$.

second order phase transition in the real part $\mathrm{Re}\, M$, as well as the cusp in the imaginary part $\mathrm{Im}\, M$.

We have done a similar analysis in $d = 3$, where we find the position of the Lee-Yang edge singularity at $M_{\mathrm{crit}} = 1.3136(31)\mathrm{i}$ and $\mathrm{Im}\, H = 0.9589$ for an UV-mass $m^2 = 1$. For a comprehensive analysis of the theory in $d = 3$, including also a discussion of the size of the (small) scaling regime is deferred to a work in preparation.

More generally, for initial masses $m^2 > m_c^2$ and fixed initial self coupling $\lambda = 1$, the expectation value of the real field $\phi_x$ vanishes, $\phi_x(m^2 > m_c^2) = 0$. Accordingly, the $Z_2$ symmetry is preserved on the real axis. In turn, for smaller $m^2$, the $Z_2$ symmetry is spontaneously broken, $\phi_x(m^2 < m_c^2) \neq 0$. The critical value $m_c^2$ determines the location of the second order phase transition.

This allows us to determine the $m$-dependence of the critical field value $\phi_c(m)$, and in particular its endpoint with $\phi_c(m_c) = 0$. The result is shown in Figure 6.10a, were we show the value of the imaginary part of the magnetisation or solution of the equation of motion, $\phi_y = \mathrm{Im}\, M$, at the Lee-Yang singularity as a function of the initial UV-mass squared. We extract the critical UV-mass $m_c^2$ by fitting the universal scaling behaviour,

$$\mathrm{Im}\, H = A(m^2 - m_c^2)^{\Delta} . \tag{6.45}$$

The scaling fit with the fit parameters in Table 6.3 is based on the data-points with initial masses $m_c^2 < m^2 < 0.1$. We recover a critical UV-mass $m_c^2 = -0.03943(17)$. For all UV-input masses higher than $m_c^2$, we are in the symmetric phase, which can be seen from the IR-mass on the real axis. For example, performing a computation at a UV-mass of $m^2 = -0.039$, yields an IR-mass $m_0^2 = 4.2\ 10^{-4}$. We also recover the mean-field scaling $\Delta = \beta\delta = 3/2$ remarkably well with our estimate given by $\Delta = 1.4969(66)$.

Finally, we investigate the size of the scaling regime. Scaling fits to data-points from initial masses $m^2 > 0.09$ yield a higher estimate for $m_c^2$, which hints at a small subleading contribution to the scaling behaviour (blue and green curves in Figure 6.10a). The relative error between the scaling-fit and the data-points is depicted in Figure 6.10b. We find a subleading contribution to the scaling for $m^2 > 0.14$ which grows in importance for higher initial masses $m^2$. At $m^2 = 1$ the relative fit error on the Lee-Yang location is only $\approx 3\%$. Hence, we deduce a large scaling regime in $d = 4$.

## 6.5. Summary and outlook

In the present work we have set up general fRG approaches for computing complex actions. To that end we have compared different general fRG flows for the Wilsonian effective action and the 1PI effective action, based on the general flows for both, (3.20) and (3.33). The analysis suggests that the construction of adapted fRGs is key to constructing systems of partial differential equations whose types support flows towards the infrared, see Section 6.2.

The present conceptual results allow for a systematic construction of these flows within the theory and truncation at hand. Our explicit numerical computations of the effective potential in scalar theories in zero to four dimensions have aimed at resolving Lee-Yang zeroes, and are based on the RG-adapted flow for the Wilsonian effective action constructed here. The setup allowed us to compute the full effective potential in the complex magnetisation plane, see in particular Figure 6.6. These results give access to the position as well as the mass-dependence of the Lee-Yang zeroes, see Figure 6.10a.

This evaluation of the mass dependence allowed us to predict the location $m_c^2$ of the phase transition from the symmetric into the broken phase in terms of an extrapolation of the Lee-Yang singularity and its intersection point with the real axis. It can be seen as a precursor of a respective computation in QCD, where the present scalar potential or rather scalar sector is linked to the scalar-pseudoscalar meson sector obtained via dynamical hadronisation in functional QCD. Then, the dependence of the location of the Lee-Yang zero on the chemical potential can be used to constrain the location of the critical end point or the onset of new physics within first principle QCD. We hope to report on the respective investigation in the near future.

# CHAPTER 7

# Applications of general RG transformations

In Chapter 3 we have outlined some of the computational challenges of the fRG. Firstly, we have addressed the issue finding an approximation scheme for the intricate momentum and field dependence of the generating functional $\Gamma[\phi]$, which allows for a quantitative description of physics, recall Section 3.2.2. This issue goes hand in hand with finding a regulator that is optimised for the truncation, see Section 3.2.3. The second challenge becomes apparent in real-time applications. Ideally, one would like to find a regulator which implements a causal, Lorentz-covariant theory. Until now, the only regulator which has been found to allow this, fails to implement UV-finiteness in the RG-flows. This has been discussed in [3] or in Section 3.4.

In this chapter we present two applications of the generalised RG-flow (3.33) to scalar theories, which address these challenges. The respective works represent an important step in method development of the fRG. Whilst they are aimed at a quantitative description of QCD, these developments can also be applied in a broader context.

Section 7.1 aims at an expansion of the theory about the ground state of the theory by an RG-scale dependent redefinition of the effective mean field $\phi$. This way we are able to reduce the complexity of the approximation scheme by absorbing part of the RG-flow into the definition of the field.

Section 7.2 presents an application of the CS-flow introduced in (7.45). Here, the RG-flow was adapted for the computation of spectral functions.

Previously, in Chapter 6, we have already applied generalised flows to implement an RG-adapted flow of the Wilsonian effective action, which showed great numerical stability for computations with complex external fields.

## 7.1. Optimal RG-flows and flowing fields

*This section is based on [8]. We make use of the generalised RG-flow derived in (3.33) to compute the full wave function renormalisation.*

Renormalisation group approaches are ideally suited for resolving the intricate phase structure of physical systems, ranging from condensed matter and statistical systems over Quantum Chromodynamics, particle physics, cosmology to quantum gravity. They are set-up for mon-

itoring the change of physical phenomena and degrees of freedom under changing intrinsic scales such as mass and more generally couplings, as well as external parameters such as temperature, density or external fields. Renormalisation group approaches provide a relatively easy access to the mechanisms or dynamics behind intricate physical phenomena already in simple approximations of the system at hand, even for strongly correlated systems. Often, simple approximations already lead to semi-quantitative results.

In turn, fully quantitative results and, equally important, a small systematic error estimate require far more effort. Moreover, the phase structure of many systems, including many condensed matter systems and QCD, exhibits regimes with competing order effects. There, quantitative precision as well as the inclusion of the full vacuum structure is mandatory for obtaining even qualitative results. Accordingly, the quest for quantitative precision and small systematic error estimates is of vital importance for the reliability of the RG-approach, and the present work aims at adding to this important endeavour.

A specifically appealing feature of RG-approaches is their adaptive flexibility that originates in the successive resolution of the theory at hand, and Wilsonian fRG approaches are tailor made in this respect. In the present work we aim at a description of the one particle irreducible (1PI) effective action of free energy $\Gamma$ in terms of the emergent dynamical degrees of freedom. This corresponds to an expansion of the theory about its ground state, and in terms of the effective action this is tantamount to an expansion about the full covariance or inverse propagator. In the fRG approach this idea is implemented within a successive RG-adapted reparametrisation of the dynamical field, which evolves from the microscopic field at large momentum scales to the emergent dynamical field at low momentum scale. This requires an fRG flow equation for the effective action that encompasses general reparametrisations, which has been set-up in [127, 140], and was discussed in Section 3.3.2. The underlying idea dates back to [131] and has recently also been used for the construction of the essential fRG, [136, 143].

In the current section we use the flowing field approach to reduce the full dispersion of the field to a classical one at each RG-step. In Section 7.1.2 we briefly describe our numerical setup, and we present numerical results for the three-dimensional O(4)-theory in the broken phase (in Section 7.1.3) as well as for the thermal phase transition of the O(4)-theory in four dimensions (in Section 7.1.4). We summarise our findings in Section 7.1.5.

### 7.1.1. Flowing fields for scalar O(N) theories

In the following we explore the thermal phase transition in a scalar O(N) theory with the scalar field $\varphi^T = (\varphi_1, ..., \varphi_N)$. This model has a thermal phase transition from a symmetric phase at high temperatures $T > T_c$ to a spontaneously broken phase for low temperatures $T < T_c$ with one radial mode and $N-1$ massless Goldstone modes.

As discussed in Section 3.3.3, we use the reparametrisation freedom stored in the flowing fields (3.41) to transform the full dispersion into a classical one for all field values, while keeping the pole mass fixed. To that end we consider the following approximation of the effective action in the presence of an infrared cutoff scale,

$$\hat{\Gamma}_k[\varphi] = \int_x \Big[\frac{1}{2} Z_\varphi(\rho_\varphi)(\partial_\mu \varphi)^2 + V_k(\rho_\varphi)\Big], \tag{7.1}$$

with the notation

$$\int_x = \int_0^\beta dx_0 \int_{\mathbb{R}^3} d^3x\,, \qquad \rho_\varphi = \frac{\varphi^2}{2} = \frac{\varphi^a \varphi^a}{2}\,, \tag{7.2}$$

where $\beta = 1/T$ with the temperature $T$, and $a = 1, ..., N$. Equation (7.1) corresponds to the first order of the derivative expansion for the O(N) model.

For $N = 4$ this model is a simple low energy effective theory for the chiral dynamics in QCD, and the phase transition is that of strong chiral symmetry breaking, as also discussed in the last section. The radial scalar $\sigma$-mode is obtained from the quark bilinear $\bar{q}q$. The three (peudo-)Goldstone bosons are related to the three pseudoscalar pions $\boldsymbol{\pi}$ obtained from $\bar{q}\gamma_5\boldsymbol{\sigma}q$ with the Pauli matrices $\boldsymbol{\sigma} = (\sigma^1, \sigma^2, \sigma^3)$. The masses $m_\pi \approx 140\,\text{MeV}$ of the latter are generated by an explicit symmetry breaking term linear in the radial field. This simple model emerges dynamically as part of the full QCD effective action within the fRG approach to first principle QCD with dynamical hadronisation, for recent works see [51, 60] and the reviews [104, 126]. While we will use the results of this specific application in a forthcoming QCD related work, the approach and results here are far more general.

Now we use a transformation, that maps the effective action $\hat{\Gamma}_k[\varphi]$ to one with a classical dispersion in terms of the transformed field $\phi$ with

$$\Gamma_k[\phi] = \int_x \Big[\frac{1}{2}(\partial_\mu\phi)^2 + V_k(\rho) - c_\sigma\sigma\Big], \tag{7.3}$$

where

$$\phi = \begin{pmatrix} \sigma \\ \boldsymbol{\pi} \end{pmatrix}, \qquad \rho = \frac{\phi^2}{2} = \frac{\sigma^2 + \boldsymbol{\pi}^2}{2}. \tag{7.4}$$

and $\boldsymbol{\pi}^T = (\pi_1, ..., \pi_{N-1})$. In (7.3) we have introduced an explicit linear breaking term for the radial mode $\sigma$. Note that such a term drops out of the flow and only shifts the (constant) solution $\phi_{\text{EoM}}$ of the equation of motion,

$$\sigma\partial_\rho V_k(\rho_0) = c_\sigma\,. \tag{7.5}$$

Accordingly, this linear term is only a spectator in the following derivations and computations. We emphasise that the form of (7.3) does not signal an approximation with the assumption $Z_\phi \approx 1$, but a formulation with flowing fields with the constraint

$$Z_\phi(\rho) \overset{!}{\equiv} 1\,, \tag{7.6}$$

which is the momentum-independent reduction of (3.41).

We also envisage (7.3) with (7.6) as the intermediate reparametrisation of the theory, before the Goldstonisation of [139, 142] is applied. This combined application is deferred to future work.

### RG-adapted field transformations

It is left to derive the flowing fields $\dot{\phi}$, that absorbs the full field dependence of $Z_{\phi,k}$ into the field $\phi$ and leads to

$$\partial_t Z_\phi(\rho) = 0\,, \tag{7.7}$$

where we have dropped the subscript $_k$ indicating the $k$-dependence. To begin with, both actions, (7.1) and (7.3) are invariant under linear O(N) transformations, so we only have

to consider field transformations that carry a linear representation of O(N). Consequently, a general parametrisation of $\dot{\phi}$ is given by

$$\dot{\phi} = -\frac{1}{2}\eta_\phi(\rho)\,\phi\,, \tag{7.8}$$

with a general $\rho$-dependent function $\eta_\phi(\rho)$, which is indeed absorbing the anomalous dimension of the field, hence the notation.

In order to determine (7.8), we compute the flow of $Z_\phi$ from that of the two-point function, $\partial_t\Gamma_k^{(2)}[\phi](p)$, the second field derivative of the functional flow with flowing fields, (3.33). The wave function is directly extracted from the two-point function of the Goldstone fields at $\boldsymbol{\pi} = \mathbf{0}$. The general form of the Goldstone two-point function for constant fields $\phi = (\sigma, \mathbf{0})$ and $\rho = \sigma^2/2$ is given by

$$\Gamma^{(2)}_{k,\pi_i\pi_j}[\phi](p) = Z_\phi(\rho,p)\left[p^2 + m_\phi(\rho)\right]\delta^{ij}\,. \tag{7.9}$$

It is diagonal in field space and the mass parameter $m_\phi(\rho)$ is the pole mass of the theory. While the pole mass can be accessed within the fRG approach, in particular within spectral flows, see e.g. [3], we will use an additional approximation in the present work with

$$Z_\phi(\rho,p) \approx Z_\phi(\rho)\,. \tag{7.10}$$

With (7.10) the flow of $Z_\phi(\rho)$ is computed by taking a $\boldsymbol{p}^2$ derivative of $\partial_t\Gamma_k^{(2)}[\phi](p)$ at $p=0$, as all mass terms drop from the flow of (7.9). In combination we arrive at

$$\partial_t Z_\phi(\rho) = \frac{\partial}{\partial \boldsymbol{p}^2}\partial_t\Gamma^{(2)}_{k,\pi_1\pi_1}[\phi](p)\bigg|_{\substack{p=\ 0\\ \boldsymbol{\pi}=\ \mathbf{0}}}\,. \tag{7.11}$$

The details of the explicit computation are deferred to Appendix B.4.1, and the final flow for $p=0$ and $\boldsymbol{\pi}=\mathbf{0}$ reads

$$\partial_t Z_\phi = \frac{1}{2}\frac{\partial}{\partial \boldsymbol{p}^2}\,\mathrm{Tr}\left[G^{(2)}_{,\pi_1\pi_1}\left(\partial_t + 2\frac{\delta\dot{\phi}}{\delta\phi}\right)R_k\right] - \frac{\delta^2}{\delta\pi_1\delta\pi_1}\left[\dot{\phi}\,\phi\left(\rho Z_\phi' + Z_\phi\right)\right], \tag{7.12}$$

where $Z_\phi' = \partial_\rho Z_\phi$ and $G^{(2)}_{\pi^1\pi^1}$ stands for the second derivative of the propagator w.r.t. the Goldstone $\pi_1$, and we have in general

$$G^{(m)}_{\phi_i\phi_j,\phi_{n_1}\cdots\phi_{n_m}}(p_1,\ldots,p_{m+2}) = \frac{G_{\phi_i\phi_j}(p_1,p_2)}{\delta\phi_n(p_3)\cdots\delta\phi_m(p_{m+2})}\,. \tag{7.13}$$

We shall also use the short-hand notation $G_{\phi_i\phi_j,\phi_n\phi_m}$, $G_{ij,nm}$ as well as $G_{,\phi_n\phi_m}$ and extensions to more derivatives for the sake of readability.

Using $Z_\phi = 1$, due to the constraint imposed in (7.6), at any given $k$, all derivatives of $Z_\phi$ vanish. Moreover, for the choice

$$\frac{\delta^2}{\delta\pi_1\delta\pi_1}(\dot{\phi}\,\phi) = \frac{1}{2}\frac{\partial}{\partial \boldsymbol{p}^2}\,\mathrm{Tr}\left[G^{(2)}_{,\pi_1\pi_1}\left(\partial_t + 2\frac{\delta\dot{\phi}}{\delta\phi}\right)R_k\right], \tag{7.14}$$

for $p=0$ and $\boldsymbol{\pi}=\mathbf{0}$ we obtain $\partial_t Z_\phi = 0$ and hence (7.6) is sustained for all $k$. In (7.14), we have used the short hand notation $G^{(2)}_{,\pi_1\pi_1}$, where we have dropped the indices that are involved in the trace.

Comparing (7.14) with the $\pi_1$-derivative of (7.8) at $p=0$ and $\boldsymbol{\pi}=\mathbf{0}$ leads us to

$$\eta_\phi+\rho\,\eta'_\phi=-\frac{1}{2}\frac{\partial}{\partial \boldsymbol{p}^2}\,\mathrm{Tr}\Big[G^{(2)}_{,\pi_1\pi_1}\Big(\partial_t-\eta_\phi-2\rho\,\eta'_\phi\Big)R_k\Big]\,, \tag{7.15}$$

where $\eta'_\phi=\partial_\rho\eta_\phi$. It is worth noting that (7.15) with $\eta'_\phi=0$ is also obtained, if $R_k$ in the standard fRG approach without flowing fields is augmented with a field-dependent wave function,

$$R_k(\rho,p)=Z_\phi(\rho)R_k^{(0)}(p)\,. \tag{7.16}$$

Equation (7.16) is at the root of the background approximation in scalar theories, gauge theories and gravity. However, (7.16) leads to higher loop terms in the flow equation. In the background approximation the higher loop terms are simply dropped. Then we are led to (7.15) as well as the flow (3.33) with (7.8), where we consistently approximate $\eta'_\phi\approx 0$. This holds true in the limit of slowly varying $\eta_\phi$, which is analogous to the local density approximation. Note that while the validity regime of this approximation is difficult to estimate, as the size of $\eta'_\phi$ is not the relevant quantity, but rather its impact if fed back to the flow. The latter impact can be estimated in the fRG within a (linear) self-consistency analysis: we can feed back the $\eta'_\phi$ obtained in the $\eta'_\phi\approx 0$ approximation into the right hand side of the flow and use the difference as an error estimate.

Consequently, the fRG approach with flowing fields supports the background field approximation within the approximation (7.10) in the limit of slowly varying $\eta_\phi$. Importantly, within the approach with flowing fields, this approximation can be systematically lifted without leading to higher order loop terms. In particular, momentum-dependent $Z_\phi(\rho,p)$ can be implemented straightforwardly.

The full RG-adapted reparametrisation of the theory in terms of a non-linear transformation in field space (7.14) is linked to linear ones, if further approximations are used. Already in the derivation of (7.14) we have dropped the momentum dependence of the wave function. While not necessary, it simplifies the final transformation (7.14) significantly. A further significant simplification is achieved if we drop the field dependence in (7.14), which linearises the RG-adapted transformation and reduces it to a cutoff-dependent rescaling of the field. This approximation is a commonly used one, the local potential approximation (LPA) with cutoff-dependent but field-independent wave functions, called LPA′. In contrast, the full RG-adapted fields with (7.14) encode the full first order of the derivative expansion. However, the flows in the latter depend on derivatives of $Z_\phi(\rho)$ which are absent here, due to the RG-adaptation.

The LPA′ approximation is obtained by (7.1) with $Z_\varphi(\rho_\varphi)\to Z_\varphi(\rho_0)$ with a specific $\rho_0$,

$$\Gamma_k^{\mathrm{LPA}'}[\varphi]=\int_x\Big[\frac{1}{2}Z_\varphi(\rho_0)(\partial_\mu\varphi)^2+V_k(\rho_\varphi)-c_\sigma\sigma\Big]. \tag{7.17}$$

Typically, $\rho_{0,k}$ is chosen as the cutoff-dependent solution of the equations of motion (6.36b). The rescaling of the field is then given by,

$$\dot\phi=-\phi\,\frac{\eta_\phi(\rho_0)}{2}\,,\qquad\qquad \eta_\phi(\rho_{0,k})=-\frac{\partial_t Z_\varphi(\rho_{0,k})}{Z_\varphi(\rho_{0,k})}\,. \tag{7.18}$$

In short, in LPA′ the flowing fields leading to (7.6) are simply implementing the rescaling $\phi=Z_\varphi^{(1/2)}(\rho_0)\varphi$. Conceptually, the difference between the full field-dependent reparametrisation

and the LPA′ one is the additional assumption, that the field dependence of $Z_\varphi$ is negligible, $\partial_{\rho_\varphi} Z_\varphi \approx 0$. This is the analogue of a local density approximation in density functional theory. This relation of the fRG flows with flowing fields to the well-studied LPA′ approximation allows us to gauge the impact of fully field-dependent reparametrisations. Consequently, in Section 7.1.3 we shall compare the full results with that obtained in LPA′.

### Flow equations

In the present approximation we are left with two flow equations, one for the effective potential and that for the flowing field. With the underlying O(N) symmetry we can formulate the flows in terms of $\rho$ instead of $\phi$. Here we provide the explicit forms of the two flows in the present setting of a thermal O(N) model. In comparison to the flow of the effective potential in LPA, the flow carries additional terms proportional to $\eta_\phi(\rho)$ and its $\rho$-derivative,

$$\partial_t V_k - \eta_\phi \rho V' = k^{d+1} A_d \left[ \left( 1 - \frac{\eta_\phi + 2\rho\,\eta_\phi'}{1+d} \right) \frac{\coth\left(\frac{\epsilon_\sigma}{2T}\right)}{2\,\epsilon_\sigma} + \left( 1 - \frac{\eta_\phi}{1+d} \right) \frac{(N-1)\coth\left(\frac{\epsilon_\pi}{2T}\right)}{2\,\epsilon_\pi} \right], \tag{7.19}$$

with $V' = \partial_\rho V$, $V'' = \partial_\rho^2 V$, $\eta_\phi' = \partial_\rho \eta_\phi$ and

$$A_{d+1} = \frac{2\pi^{d/2}}{(2\pi)^d \Gamma(d/2) d}\,. \tag{7.20}$$

The dispersion relations $\epsilon_{\sigma/\pi}$ are given by

$$\epsilon_{\pi/\sigma} = \sqrt{k^2 + m^2_{\pi/\sigma}}\,, \tag{7.21}$$

and the radial and Goldstone masses

$$m_\pi^2 = V'\,, \quad m_\sigma^2 = m_\pi^2 + 2\rho V''\,. \tag{7.22}$$

The RG-adapted flow of the field basis is given by (7.15) and has the explicit form in terms of $\eta_\phi$,

$$\eta_\phi + \rho\eta_\phi' = 4A_d\,\bar{\rho}(\bar{V}'')^2 \left( 1 - \frac{\eta_\phi + 2\,\rho\,\eta_\phi'}{1+d} \right) BB_{(2,2)}\,, \tag{7.23}$$

with the dimensionless threshold function $BB_{(2,2)}$ defined in Appendix B.7.2, and dimensionless fields $\bar{\rho} = k^{d-2}\rho$ and potential $\bar{V} = k^d\,V$. Note that the the right hand side of (7.23) tends towards zero in the large N limit with N$\to\infty$. This is consistent with the vanishing anomalous dimension in this limit.

We close this analysis with the comment that this setup can be used as a starting point for an additional transformation of the field basis into polar coordinates in the broken phase, with or without a consequent absorption of the emergent wave function $Z_\theta(\rho)$. Such a set-up is fully adapted to the ground state or covariance of the O(N) theory.

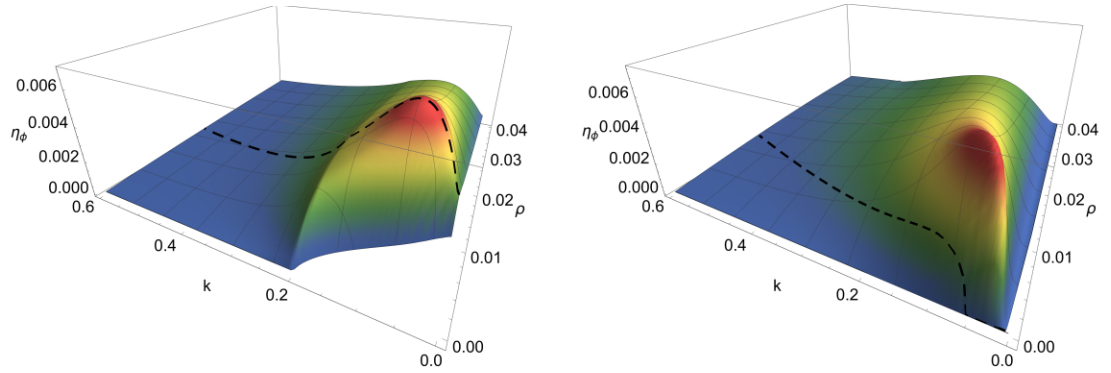


(a) Anomalous dimension in the broken phase for $T = 0.100$ deep in the broken phase.

(b) Anomalous dimension in the symmetric phase for $T = 0.270$ close to the critical temperature.

Figure 7.1.: Field and RG-time dependence of the anomalous dimension in the broken phase, Figure 7.1a, and in the symmetric phase, Figure 7.1b, in four dimensions at finite temperature. The critical temperature is $T_c \approx 0.260$ and the initial conditions are given in Section 7.1.4. All units are given in terms of the UV-cutoff $\Lambda = 1$, and the dashed black line indicates the equations of motion in the limit of massless Goldstone bosons. The solution of the differential equation (7.23) for $\eta_\phi$ depends on a boundary condition that is in general $k$-dependent. The kink at about $k \approx 0.2$ in Figure 7.1a originates in a strong $k$-dependence of the boundary condition when entering the broken phase, see Appendix B.4.4. The figure does not show negative values of $\eta_\phi(\rho)$, which appear in the unphysical part of the potential in the broken phase.

## 7.1.2. Numerical setup

With the introduction of the RG-adapted, field-dependent flow of the anomalous dimension $\eta_{\phi,k}(\rho)$, (7.23), we add an additional ordinary differential equation to the RG-time integration of the field-dependent effective potential $V_k(\rho)$. We solve this system numerically: The RG-time evolution is started at a UV-scale $k = \Lambda$ and we use small, discrete RG-steps $k \to k - \Delta k$ until the final RG-scale $k = k_{\text{fin}} \approx 0$ is reached. At every RG-step the computation is then separated into two stages, where we consider the field dependency of both functions on an interval $\rho \in (0, \rho_{\text{UV}}]$.

At first, we solve the evolution equation of the flowing fields for $\eta_{\phi,k}(\rho)$, (7.23), using the effective potential $V_k(\rho)$. The second stage then computes the flow of the field-dependent potential $\partial_t V_k(\rho)$, (7.19), using a Discontinuous Galerkin discretisation and prepares the next RG-step, i.e. $V_k(\rho) \to V_{k-\Delta k}(\rho)$.

### Solving the RG-adapted flow

We solve the RG-adapted flow (7.23) at each RG-step. The flow is a first order ordinary differential equation (ODE). As such, we obtain a general solution to this ODE by the *variation of constants* method, see Appendix B.4.2. From this general solution we derive a particular solution by specifying a *boundary condition*.

The choice of this condition requires some care when computing on a finite numerical interval $\rho \in (0, \rho_{\text{UV}}]$. We recall, that the anomalous dimension $\eta_\phi(\rho)$, i.e. the solution to (7.23), is a non-linear reparametrisation of the field. In terms of a numerical interval with a fixed length $\rho_{\text{UV}}$, this implies a changing coordinate interpretation in terms of the initial field $\rho_\Lambda$. Or differently said, the numerical interval zooms in/out of, or moves through, specific regions

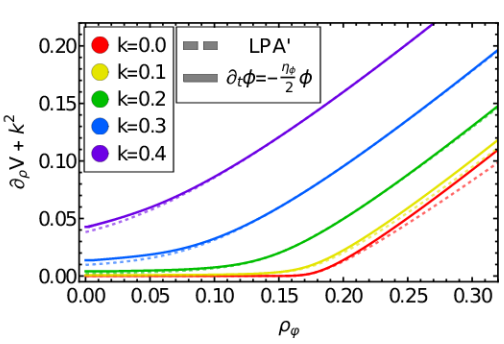


(a) (1PI) First field derivative $\partial_\rho V(\rho)$ of the potential.

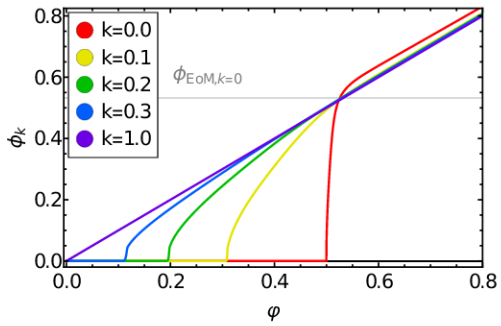


(b) Flowing field $\phi_k(\varphi)$ as a function of the UV field $\varphi = \phi_{k=\Lambda}$.

Figure 7.2.: Comparison of the RG-scale dependence of the (1PI) effective potential derivative $u = \partial_\rho V$ (a) and the flowing field $\phi_k$ (b). Results are shown in the broken phase in $d = 3$ at $T = 0.05$ for the initial conditions specified in Section 7.1.3. We compare results of the approximation with field-dependent $Z_\phi(\rho)$ to LPA$'$ (dashed lines) and indicate the field dependence in terms of $\rho_\varphi = \rho_\Lambda$. All units are given in terms of the UV-cutoff $\Lambda = 1$.

of the initial field dependency. This is depicted at a later point in Figure 7.2b, where we show the transformation of the flowing field $\phi_k$ in terms of the initial field $\phi_\Lambda$ at the UV-cutoff scale. The subtlety lies in fixing the integration constant such, that the numerical interval zooms into the physically interesting regions, which we discuss in Appendix B.4.4. A solution for the anomalous dimension $\eta_{\phi,k}(\rho)$ for $d = 4$ dimensions for temperatures $T > T_c$ in the symmetric and $T < T_c$ in broken phase is depicted in Figure 7.1. The figure shows the particular solution for $\eta_\phi(\rho)$, which is used in the computation.

### RG-time integration of the effective potential

After solving the RG-adapted flow, we can proceed to use $\eta_{\phi,k}$ in the computation of the effective potential $V_k(\rho)$. The flow of the potential (7.19) defines a second order differential equation, which is dependent on its first and second derivatives $\partial_\rho V(\rho)$ and $\partial_\rho^2 V(\rho)$ respectively. It can be rewritten as a convection-diffusion equation along the lines of [1, 5, 65], by taking a $\rho$ derivative. Hence we solve for $u = \partial_\rho V(\rho)$, with,

$$\partial_t u = \partial_\rho \left( \rho \eta_\phi \, u + F \right), \tag{7.24}$$

where the flow $F(u, u', \rho, \eta_\phi, \eta_\phi')$ is given by the right hand side of (7.19).

Equation (7.24) is solved numerically using Discontinuous Galerkin methods. We build on the *dune-FRGDG* framework put forward in [5], more specifically we make use of the local-DG scheme put forward in [9]. For further applications and convergence tests in the fRG see also e.g. [4, 6].

## 7.1.3. Flowing fields in the broken phase

In this section we present results in $d = 3$ dimensions, where the flow is initiated deep in the broken phase. The initial conditions of the RG-time integration are given by a $\phi^4$-potential at an initial RG-scale of $\Lambda = 1$, to wit

$$u(\rho) = \partial_\rho V(\rho) = \rho\lambda + m^2 . \tag{7.25}$$

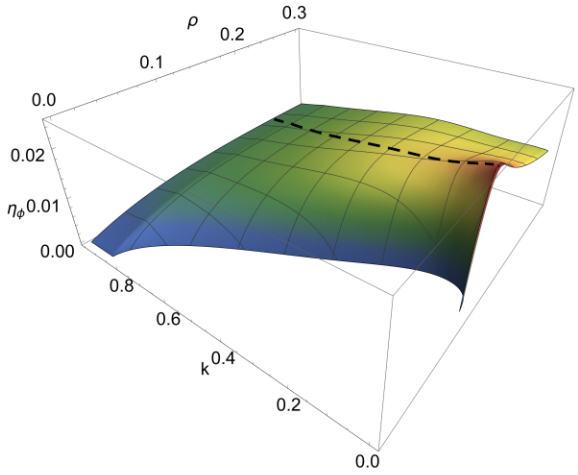


Figure 7.3.: Anomalous dimension in $d = 1+2$ deep in the broken phase ($T = 0.05$). With the onset of strong, convexity restoring dynamics at $k \approx 0.85$, it diverges as $\rho \to 0$. The divergence is situated in the unphysical (flat) part of the potential $\rho < \rho_0$, where the latter is the solution to the equations of motion ((7.5)), and does not affect the results in the physical regime $\rho > \rho_0$. The numerical treatment of this divergence is discussed in Appendix B.4.3. The dashed black line indicates $\rho_0$ in the limit of massless Goldstone bosons. All units are given in terms of the UV-cutoff $\Lambda = 1$.

with $\lambda = 1$ and $m^2 = -0.25$.

We depict the RG-scale dependence of the solution to the flow of the potential derivative (the Goldstone mass) (7.24) in Figure 7.2a. This result is compared to an LPA′ computation with the same initial conditions. In comparison to the LPA′ computation we see deviations in the unphysical regime of the effective potential during the flow, i.e. for $\rho < \rho_0$, where $\rho_0$ is the solution to the equations of motion (7.5) in the chiral limit $c_\sigma \to 0$. These are caused by the strong field dependence of the anomalous dimension in the flat part of the potential, see Appendix B.4.4. These deviations are further impacted by the implementation of a numerical cut-off of the anomalous dimension in this regime, see Appendix B.4.3.

Now we turn our focus to the regime $\rho > \rho_0$ at small RG-scales in Figure 7.2a. Here, the deviations emphasise the improvement that comes with the flowing fields formulation or rather its more complete field-dependences: while LPA′ results match the flowing fields on the equations of motion (EoM), we see a deviation away from $\rho_0$. In summary, the current result, in a qualitatively improved approximation, validates the use of the LPA′ approximation for the physics questions under investigation: both methods agree on the EoM, where the physical correlation functions are obtained. This is not surprising, as the anomalous dimension on the EoM is relatively small and flat in the vicinity of $\rho_0$, see Figure 7.3. We expect this to change for increasingly more dynamical settings, such as e.g. fermionic models with finite density. Note also, that the deviations away from the EoM indicate, that higher correlation functions may differ even on the EoM.

The flowing field formalism introduces a $k$-dependence to the coordinate space via the relation (7.8). The underlying transformation $\phi_k[\varphi]$ is obtained by integrating the flow $\dot{\phi}$,

$$\phi_k = \phi_\Lambda + \int_k^\Lambda \frac{\mathrm{d}k}{2k}\, \eta_{\phi,k}\, \phi_k\,, \tag{7.26}$$

with $\varphi = \phi_\Lambda$. The anomalous dimension $\eta_\phi$ is maximal on the equations of motion, see

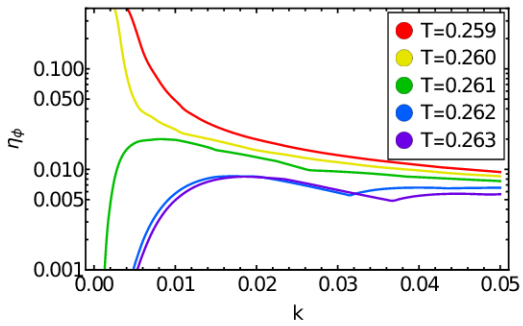


Figure 7.4.: RG-scale dependence of the anomalous dimension $\eta_\phi(\rho_0)$ on the equations of motion (7.5), in the vicinity of the critical temperature $0.260 < T_c < 0.261$. The current result is compatible with a scaling solution $\eta_{\phi,c} \approx 0.042$.

Figure 7.3. This increases the resolution in its vicinity, which is discussed in more detail in Appendix B.4.4. In Figure 7.2b, we show the integrated flowing fields as a function of the initial UV-fields. The emergent regime with a steep drop about the EoM entails´ that a rather small interval in the UV field $\varphi$ stretches over a large interval in the emergent composite field $\phi$. This zooming-in on the equations of motion is a numerically very welcome feature in the presence of symmetry breaking:

Within LPA or LPA′ we find the formation of a *non-analyticity* or *kink* at $\rho_0$. The formation of this structure in $\partial_\rho V$ is smoothened out significantly in the flowing field approach, as the non-analyticity is at least partially stored in the map to the dynamical fields.

We close this discussion with a comment on the flattening of the coordinate transformation in $\phi_k(\phi_\Lambda)$ at small values of $\phi$. It is linked to the divergence of the anomalous dimension $\eta_\phi(\rho \to 0)$ in Figure 7.1a, which indicates a coordinate singularity. This is discussed in detail in Appendix B.4.4. Note that the converse of the magnification of the regime around the solution $\phi_0$ of the EoM with magnification point $\phi_0$ is the compression of the interval $\rho < \rho_0$. There the flowing fields describe the reparametrisation

$$\phi_{k\to 0}(\varphi) = 0\,, \quad \text{for} \quad \varphi \in [0, \sqrt{2\rho_0} - \epsilon) \tag{7.27}$$

with some small $\epsilon > 0$. In fact, with each RG-step $\Delta k$ a new coordinate $\phi_k$ is set to 0 when it reaches the singularity of the flow. In the numerical implementation, the singular reduction $\phi_{k\to 0}(\varphi) = 0$ is only achieved with an accuracy of

$$\phi_{k\to 0}(\varphi)|_{\text{num}} < 10^{-9}\,, \quad \text{for} \quad \phi_\Lambda \neq 0\,, \tag{7.28}$$

which is due to the numerical cut-off for the anomalous dimension, see Appendix B.4.3.

### 7.1.4. Thermal phase transition in $d = 4$ dimensions

In this section we apply the flowing field approach to the thermal phase transition in the four-dimensional $\phi^4$ theory. The effective action at the initial scale $\Lambda = 1$ is given by the classical potential (7.25) with the coupling $\lambda = 1$ and the mass parameter $m^2 = -0.025$. All units are measured in terms of the UV-cutoff scale $\Lambda$.

Note that this choice of the initial effective action as the classical one is not fully RG-consistent [61, 127] due to the relatively large coupling. However, the second order thermal

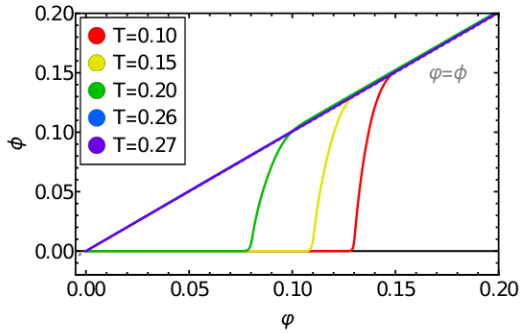


Figure 7.5.: Temperature dependence of the dynamical fields as a function of the UV-field at $k = 0.01$. All units are given in terms of the UV-cutoff $\Lambda = 1$.

phase transition in this theory occurs at sufficiently low temperature $T_c \approx \Lambda/4$, and hence potential ultraviolet effects due to the choice of the classical action as the initial effective action have decoupled. Moreover, in low energy effective theories of QCD the initial $\phi^4$ coupling is typically even larger.

### Phase transition regime

We have computed the effective potential around the phase transition with a temperature spacing of $\Delta T = 10^{-3}$ for both the full $Z_\varphi(\rho_\varphi)$ dependence and in LPA′ down to a minimal RG-scale of $k_{\min} = 0.005$. From this investigation we can determine the location $T_c$ of the phase transition in the chiral limit in the present approach with flowing fields in comparison to the location $T_{c,\mathrm{LPA}'}$ in LPA′,

$$T_c = 0.2605(05)\,,$$
$$T_{c,\mathrm{LPA}'} = 0.2605(05)\,. \tag{7.29}$$

The critical temperatures in both approximations agree within their error, which again provides a much desired systematic error estimate for a $T_c$-predictions in $T_{c,\mathrm{LPA}'}$ in the current model class. The fine temperature resolution $\Delta T = 10^{-3}$ or rather $\Delta T/T_c \approx 0.0038$ used in the present computation allows for a crude estimate of the size of the critical region. To begin with, we find that the used temperature spacing is not small enough for a reliable extraction of the critical exponents. Note that $\Delta T$ is readily reduced without problems given the numerical accuracy of the present framework. However, the present numerical approach is set-up for computing the effective potential in the phase structure, and is not tailor made for the extraction of critical exponents, which is best done within a fixed point analysis. When determining the scaling of $m_\pi^2 \propto |T - T_c|^\nu$, our estimate of the region that is *dominated* by critical scaling, is

$$\left|1 - \frac{T_c}{T}\right| \lesssim 5 \times 10^{-3}\,. \tag{7.30}$$

Note that a fit with sub-leading scaling terms and regular terms may be compatible with our results for a far larger regime, but still the extraction of the critical exponents from $|1 - T_c/T| \gg 5\ 10^{-3}$ requires a rapidly increasing precision as the scaling contributions get suppressed. In any case we remark, that the critical exponent obtained from a naive interpolation of the potential in the regime (7.30) is compatible with $\nu \approx 0.7 - 0.8$. Finally, we consider the anomalous

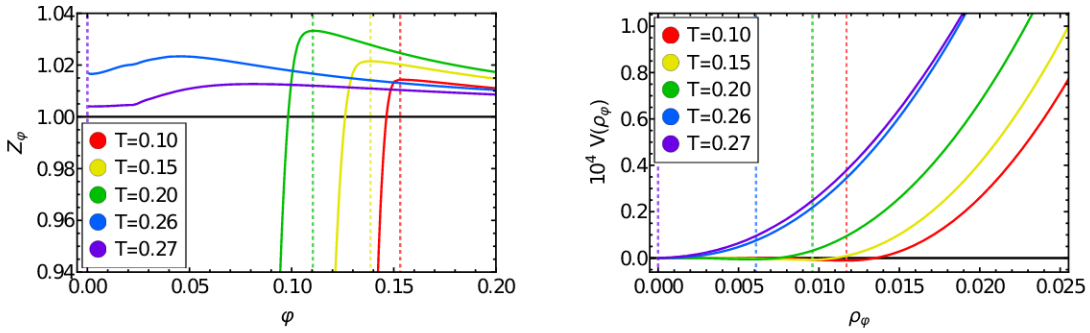


(a) Wave function $Z_\varphi(\varphi)$ at $k = 0.005$.

(b) Potential for different temperatures at $k = 0.005$.

Figure 7.6.: Transformation of the field basis and potential in $d = 1+3$ at different temperatures. We show results in terms of the coordinates at the initial cut-off scale $\Lambda$. The solution to the equation of motion (6.36b) is indicated by the dashed lines. The critical temperature is given by $T_c \approx 0.26$. Hence the *(purple)* line is located in the broken phase. All units are given in terms of the UV-cutoff $\Lambda = 1$.

dimension $\eta_\phi(\rho_0)$ on the equations of motion $\rho_0$, in the vicinity of the phase transition, see Figure 7.4. Here, we have plotted the regular solution, see Appendix B.4.2. Our computations support a critical value $\eta_{\phi,c}(\rho_0) \approx 0.042$. Again, it is very apparent from Appendix B.4.2, that a determination of the critical exponents, rather than the present crude estimate, requires a far higher resolution of the scaling regime.

### Consistency of flowing fields

We close the discussion of the thermal properties of the O(4) model within the flowing field approach with a discussion of the field transformation $\phi(\varphi)$ and the self-consistency of the approach. The anomalous dimension in the symmetric phase at $T = 0.270$ and in the broken phase at $T = 0.100$ is depicted in Figure 7.1. In the symmetric phase the map to the flowing fields encounters no coordinate singularity for $k \to 0$ as the latter originates in the non-convexity of the effective potential only present in the broken phase for $k \to 0$. Figure 7.5 shows the field transformation at $k \to 0$ for different temperatures. The field-dependent wave function can be obtained from the coordinate reparametrisation at $k \to 0$ using

$$\phi = Z_\varphi(\rho_\varphi)^{1/2}\varphi\,, \tag{7.31}$$

and is depicted for various temperatures in Figure 7.6a. Most notably, $Z_\varphi$ increases as we near the phase transition from the broken phase. By construction, it is maximal on the equations of motion $\phi_{\text{EoM}}$ and thus $\partial_\rho Z_\varphi|_{\text{EoM}} = 0$ in the broken phase, as suggested by the finite density approximation. Figure 7.6b shows the potential at $k \to 0$ for various temperatures. Here we can see the the transformation of UV coordinates onto zero in the flat region (i.e. to the left of the EoMs).

Finally we discuss the self-consistency and stability of our explicit solutions for the flowing fields. We have explained in Section 7.1.2, that the anomalous dimension is given by a solution to an ODE. We then identified a particular solution for our numerical computation in Appendix B.4.4, which is displayed in Figure 7.1a. This particular choice of boundary condition is a hybrid-scheme which allows to resolve phase transitions.

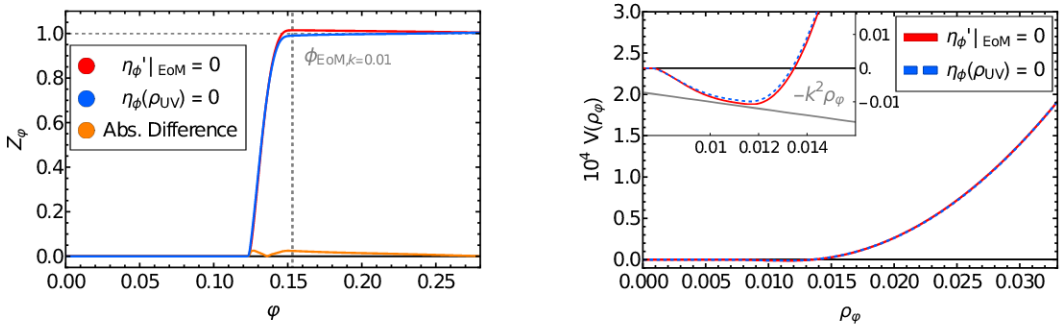


(a) Wave function renormalisation $Z_\varphi(\varphi)$: The absolute difference of both solutions is indicated in *(orange)*, it is $\approx 0.03$ on the equations of motion.

(b) Potential: We use a shift $Z_\varphi \to Z_\varphi \pm \Delta Z_\varphi$, where $\Delta Z_\varphi = 0.0011\, Z_\varphi$, on the *(blue)* (+) and *(red)* (-) solution to obtain coinciding potentials at $\rho_\varphi = 0.03$. This shift serves also as an error estimate for $Z_\varphi$.

Figure 7.7.: Potential and wave function renormalisation at $k = 0.01$ for different boundary conditions of the anomalous dimension: The *hybrid scheme* in *(red)*, see Appendix B.4.4 and and additionally the *UV-boundary conditions* (7.32) in *(blue)*. The solution for the potential deviates genuinely in the un-physical domain to the left of the minimum. As $k \to 0$ the negative part of the potential will flatten out and we expect agreement within numerical errors for the physical part of the potential, whereas the $Z_\phi$ genuinely differ for $\varphi > \varphi_{\text{EoM}}$: By definition the *(red)* solution is $> 1$ and *(blue)* $< 1$. All units are given in terms of the UV-cutoff $\Lambda = 1$.

To confirm that the physical quantities do not depend on the specific choice of boundary condition, we solve the flow at $T = 0.10$ up to an RG-scale $k_{\text{min}} = 0.01$ for both the hybrid-scheme and another particular solution, given by the boundary condition

$$\eta_\phi(\rho_{\text{UV}}) = 0\,, \tag{7.32}$$

where $\rho_{\text{UV}} = 0.05$ is the right boundary of the numerical grid.

In Figure 7.7a we compare the wave function $Z_\varphi$ at the final RG-scale for both the hybrid boundary conditions and (7.32). On the equations of motion we find relative deviation of $\approx 3\%$ and a deviation of $\approx 2\%$ at $\rho_{\text{UV}}$. Quantitatively, these solutions do not deviate much from one another to the right of the solution to the equations of motion, since the numerical stability of our scheme only allows for a small set of boundary conditions, see Appendix B.4.4. However, the deviation is still significant and qualitative:

- The *hybrid scheme*, with $\eta_\phi'(\rho_{0,k}) = 0$ as $k \to 0$ in the broken phase, has a positive anomalous dimension to the right of the equations of motion, i.e. $Z_\varphi > 1$ at all RG-scales $k < \Lambda$. See also the *(red)* solution in Figure 7.7.
- The *UV-boundary conditions* (7.32) have a negative anomalous dimension for all field values $\rho$ and all RG-times $k$. Hence $Z_\varphi < 1$ at all RG-scales $k < \Lambda$. See the *(blue)* solution in Figure 7.7.

Figure 7.7b shows the effective potential at $k = 0.01$ for both initial conditions, as a function of the shared initial field $\varphi = \phi_\Lambda$. We require the solutions for the effective potential to be identical at large values of the field $\rho = 0.03$. From this requirement we infer a global error estimate on $Z_\varphi(\rho_\varphi)$ at $k = 0.01$ of

$$\Delta Z_\varphi = \pm 0.0011\, Z_\varphi\,. \tag{7.33}$$

This error accumulates during the integration (7.26) and is of numerical origin. Figure 7.7b also shows that the potential $V$ is identical within this error estimate, whenever $V > 0$.

### 7.1.5. Summary and outlook

In this work we put forward an application of the generalised flow equation (3.33) to an O(4) theory, which implements the idea of an expansion of the effective action about the ground state of the theory. Technically, this is done by reducing the full dispersion with a field-dependent wave function $Z_\varphi[\varphi]$ of the fundamental scalar field $\varphi$ to a classical one at each flow step. This is achieved by a dynamical reparametrisation of the field $\varphi \to \phi_k(\varphi)$, introducing an emergent composite or flowing field via the differential reparametrisation $\dot{\phi}[\phi]$ with $Z_\varphi \to Z_\phi \equiv 1$ at each RG-step. We have shown that the constraint of a trivial dispersion does not fix this reparametrisation completely, and we are left with a one-parameter family of field-reparametrisations. This freedom is used to optimise the numerical implementation of the flowing fields.

As a first application we have computed the effective potential in the three-dimensional theory in the broken phase within this optimised expansion scheme. The results have been compared to the commonly used LPA′ approximation scheme, in which the wave function $Z_\varphi$ is only computed on the cutoff-dependent solution of the equation of motion. Our results provide a non-trivial reliability check of the LPA′ approximation in the broken phase, which turns out to be quantitatively reliable in the present setup. However, the sizeable deviations of the solutions away from the equation of motion depicted in Figure 7.2 indicate, that higher correlation functions may differ in LPA′. For this reasons we also expect inaccuracies of the LPA′ scheme in the presence of highly dynamical flows. For instance, we hope to report in the near future on an application of flowing fields to shock-development processes, as e.g. present at large densities and low temperatures in the QCD phase diagram.

Finally, we have applied the flowing field approach to the thermal phase transition of the four-dimensional $\phi^4$ theory. As for the three-dimensional case we found an impressive reliability of the LPA′ approximation for the observables considered. For example, the critical temperatures agreed in both approximations agree within their small respective error. This result has an immediate consequence for the systematic error estimate of state of the art fRG computations for the chiral phase transition up to $\mu_B/T \approx 4$: the current work supports the quantitative accuracy of the LPA′ scheme used e.g. in [51] for the chiral part of QCD.

Moreover, we found that the field-dependence of the wave function $Z_\varphi$ increases towards the phase transition temperature, see Figure 7.6a. This highlights its importance for quantitative accuracy for critical exponents and other universal properties, for a respective application to the O(1) model see [136]. As a self-consistency check of the present approach we have checked that different field-reparametrisations $Z_\varphi \to Z_\phi \equiv 1$ implement the same effective potential, with slight deviations in the unphysical regime at finite RG-scale $k$. This is yet another self-consistency check of the sub-leading nature of truncation artefacts.

The present approach can be readily implemented in the fRG approach to first principles QCD, leading to a flowing optimised expansion scheme around the cutoff-dependent ground state in the mesonic sector. This improves the truncation scheme at finite temperature and density in the quest for quantitative precision for high density QCD. The latter application also has to take into account potential spatial inhomogeneities such as a moat regime [318, 319]. This requires momentum-dependent wave functions, and hence the implementation of a momentum-dependent flowing field transformation.

## 7.2. The spectral functional renormalisation group

*This section is based on [7]. We make use of the CS-flow derived in Section 3.4 to compute spectral functions.*

In this section, we set up the spectral functional renormalisation group (fRG) for a scalar $\phi^4$-theory in three spacetime dimensions. The spectral fRG is a non-perturbative functional real-time approach for the direct computation of correlation functions in Minkowski spacetime. It is based on the general functional real-time setup introduced in [168,169,320,321], first applied to Dyson-Schwinger equations (DSE). The approach is based on the Källén-Lehmann spectral representation [322,323] for the two-point function, which allows to analytically access the momentum structure of functional diagrammatic expressions. The setup has been extended to the fRG approach by using a masslike Callan-Symanzik (CS) regulator in [3] and has been applied to gravity in [166]. The CS regulator sustains spectral representations alongside with Lorentz invariance, and allows for a spectral renormalisation consistent with all symmetries at hand; for more details see [3,168]. Moreover, in [3] the concept of flowing renormalisation has been introduced, which allows for an on-shell renormalisation at each renormalisation group scale. For further real-time applications of the fRG in a broad variety of research fields, see e.g., [147–152,154–156,158–167,324].

In the present work, we accompany the conceptual progress made in [3] with a non-perturbative application to spectral functions in the three dimensional $\phi^4$-theory. This allows to directly compare our results with those obtained in [168] within the spectral DSE approach. Both functional approaches implement different resummation schemes for the correlators of the given theory through infinite towers of one-loop (fRG) or two-loop (DSE) exact diagrammatic relations. Within an fRG implementation, the successive momentum-shell integration of loop momenta $p^2 \approx k^2$ with the infrared cutoff scale $k$, already provides an average momentum dependence within simple approximations. Due to their intricate spectral representation, this is particularly beneficial for including non-trivial vertices into the flow, e.g., via momentum-independent but cutoff-dependent approximations.

The organisation is as follows: In Section 7.2.1, we briefly discuss the spectral functional approach. In Section 7.2.2 we set up its application to the functional renormalisation group for a scalar theory. We present our results in Section 7.2.3. This includes a detailed comparison to those obtained with the spectral DSE in [168]. Our findings are summarised in Section 7.2.4. For technical details we defer to Appendix B.4 and the corresponding publication [7].

### 7.2.1. Spectral functions and functional equations

One of our main motivations for using the CS flow is that Lorentz invariance and the existence of spectral representations are manifest, see Section 3.4.1. We exploit in particular the latter property for defining spectral, Lorentz invariant fRG flows in real time, based on the CS flow (3.53).

Most of the relations in the present section can be generalised other field theories. For the sake of simplicity we restrict ourselves to a $\phi^4$-theory in $(1+2)$ dimensions. Its classical action reads

$$S[\phi] = \int \mathrm{d}^3x \left\{ \frac{1}{2}\phi\left(-\partial^2 + \mu\right)\phi + \frac{\lambda_\phi}{4!}\phi^4 \right\}. \tag{7.34}$$

For $\mu > 0$, the minimum of the classical potential is at vanishing field. Then, the mass parameter can be identified with the classical mass squared, $m_\phi^2 = \mu$. For $\mu < 0$, the full potential exhibits non-trivial minima, and the classical mass of the theory is given by $m_\phi^2 = -2\mu$.

### Spectral representation of the propagator

The basic ingredients of spectral fRG flows are the spectral representations of the correlation functions, and foremost the Källén-Lehmann (KL) spectral representation of the propagator,

$$G(p_0, \vec{p}) = \int_{0_-}^{\infty} \frac{\mathrm{d}\lambda}{\pi} \frac{\lambda \rho(\lambda, \vec{p})}{\lambda^2 + p_0^2}, \tag{7.35a}$$

where $0_-$ ensures that massless poles are integrated over. The spectral function $\rho(\lambda)$ is the probability density of creating a Fock state with energy $\lambda$ from the vacuum in the presence of the quantum field $\phi$. It is related to the propagator via

$$\rho(\omega, \vec{p}) = 2 \operatorname{Im} G\left(p_0 = -\mathrm{i}(\omega + \mathrm{i}0^+), \vec{p}\right). \tag{7.35b}$$

where $p_0$ denotes the Euclidean and $\omega$ the Minkowski frequency. In this application, the propagator is a function of $p^2$ due to Lorentz symmetry. Hence we drop any explicit $\vec{p}$-dependence from now on and identify $p_0^2 = p^2$. The spectral function is defined by (7.35b) but the relation (7.35a) does not always hold.

For the two-point function of asymptotic states, the spectral function is positive semidefinite and normalised to unity, if the states are normalised. In general this is not the case, since (7.35b) and (7.35a) are mere statements about the causal propagation of the associated operator. In the absence of higher order resonances, the spectral function of the $\phi^4$-theory is given by

$$\rho(\omega) = \frac{2\pi}{Z_\phi} \delta(\omega^2 - m_{\text{pole}}^2) + \theta(\omega^2 - m_{\text{scat}}^2) \tilde{\rho}(\omega), \tag{7.36}$$

with $\rho(\omega) = \rho(\omega, 0)$, and $\tilde{\rho}(\omega) = \tilde{\rho}(\omega, 0)$ for the scattering continuum $\tilde{\rho}$. The mass $m_{\text{pole}}$ in (7.36) is the pole mass of the full quantum theory, defined by $G^{-1}(\pm m_{\text{pole}}, 0) = 0$.

The scattering continuum begins at $\lambda^2 = m_{\text{scat}}^2$. In the case of a non-vanishing background field, the theory admits $1 \to 2$ scattering (broken phase), and we have $m_{\text{scat}} = 2m_{\text{pole}}$. Figure 7.8a shows the full scattering tail of the propagator as a function of the frequency $\omega$ and spatial momentum $|\vec{p}|$ in the broken phase. Higher thresholds of $1 \to N$ scattering processes lead to further discontinuities of the scattering tail and are strongly suppressed.

If the spectral representation (7.35) holds, all non-analyticities of the propagator lie on the real frequency axis. These non-analyticities are given by either poles or cuts. Poles originate from asymptotic states that overlap with the propagator of the field $\phi$, while cuts represent scattering states.

From the normalisation condition we also obtain the relation,

$$\frac{1}{Z_\phi} = 1 - \int_{m_{\text{scat}}}^{\infty} \frac{\mathrm{d}\lambda}{\pi} \lambda \tilde{\rho}(\lambda, \vec{p}). \tag{7.37}$$

which implies $Z_\phi \geq 1$ on shell, since the scattering tail carries part of the total probability.

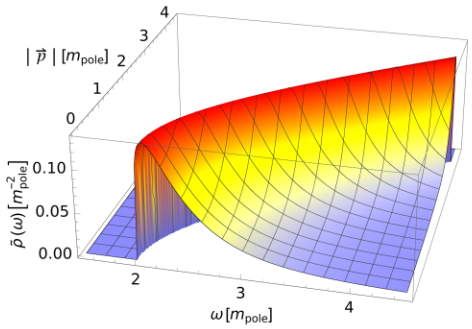


(a) Scattering tail of the propagator spectral function as a function of frequency and spatial momentum in the $(1+2)$-dimensional $\phi^4$-theory in the broken phase. It features a sharp onset at the $1 \to 2$ particle onset and explicit Lorentz invariance. Higher scattering onsets are strongly suppressed.

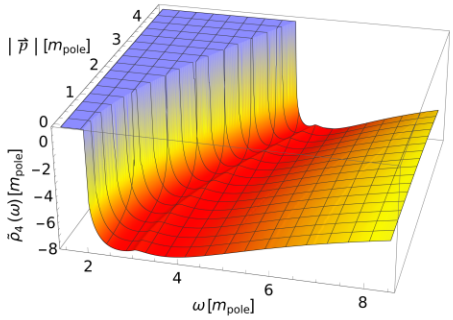


(b) Spectrum of the resummed four-vertex in an $s$-channel approximation as a function of frequency and spatial momentum. It features Lorentz invariance and exhibits a sharp onset at the two-particle threshold. The scattering spectrum also has a visible three-particle onset at $3m_{\text{pole}}$.

Figure 7.8.: Propagator and vertex scattering spectra in a $(1+2)$-dimensional $\phi^4$-theory in the broken phase. All quantities are measured in units of the pole mass, with a coupling strength $\lambda/m_{\text{pole}} = 20$.

### Spectral properties of the four-point function

Vertices also admit spectral representations, which get increasingly complicated for higher order correlation functions. In the present case, we consider an $s$-channel approximation of the full one-particle irreducible (1PI) four-point function or vertex. It is given by the fourth field derivative of the effective action $\Gamma[\phi]$, whose $n^{\text{th}}$ field derivatives $\Gamma^{(n)}[\phi]$ are the 1PI $n$-point functions. We use a spectral representation for this $s$-channel vertex [168],

$$\Gamma^{(4)}(p_0,\vec{p}\,) = \lambda_\phi + \int_\lambda \frac{\rho_4(\lambda,\vec{p}\,)}{\lambda^2 + p_0^2}\,,$$
$$\rho_4(\omega,\vec{p}\,) = 2\,\mathrm{Im}\,\Gamma^{(4)}(p_0 = -\mathrm{i}(\omega + \mathrm{i}0^+),\vec{p}\,)\,, \tag{7.38}$$

where $\lambda_\phi$ is the classical vertex in (7.34) and

$$\int_\lambda = \int_{0_-}^{\infty} \frac{\mathrm{d}\lambda}{\pi}\lambda\,. \tag{7.39}$$

The spatial momentum dependence of spectral function $\rho_4(\omega,\vec{p}\,)$ follows from a Lorentz boost of $\rho_4(\omega) = \rho_4(\omega,0)$.

Figure 7.8b shows the spectrum of the four-point function in the $s$-channel approximation discussed in Appendix B.4.6. It shows the $2 \to 2$ scattering onset at twice the pole mass $m_{\text{pole}}$ of the field $\phi$. The next threshold from the $2 \to 3$ scattering is also visible, but the result also contains the strongly suppressed threshold of higher order scattering processes.

### Structural properties of diagrams

In the spectral functional approach, spectral representations are used to rewrite diagrams in terms of momentum loop integrals over classical propagators with spectral masses and

residual spectral integrals; for a general discussion see [168]. In the present work, we apply this approach to the functional renormalisation group using the CS-flow (3.53). This leads to one-loop exact relations for correlation functions in terms of full propagators and vertices. In addition, we use a one-loop closed, resummed Bethe-Salpeter kernel to compute the four-point function.

As discussed above, the spectral fRG leads to perturbative one-loop momentum integrals in diagrams, which can be solved analytically. The non-perturbative information of the diagrams such as pole masses and thresholds is stored in the remaining spectral integrals. For the present purpose, it is sufficient to consider a single external momentum argument, which is either that of the propagator or the $s$-channel momentum of the four-point function. However, the generalisation to diagrams with several external momenta is straightforward.

We consider diagrams of the general form

$$D[p] = g \int_q \mathrm{Vert}(p,q) \prod_{j=1}^{N} G(l_j) \quad \text{with} \quad \int_q = \int \frac{\mathrm{d}^d q}{(2\pi)^d}\,, \tag{7.40}$$

and where $l_i = q, q \pm p$ are the momenta of the $N$ propagators. $\mathrm{Vert}(p,q)$ carries the momentum dependence of all vertices, which we assume to be either a polynomial or rational function of $p$ and the $l_i$, or to admit a spectral representation. All prefactors are collected in the overall prefactor $g$. By inserting the spectral representation (7.35) for each propagator, the momentum integrals acquire a standard perturbative form, where the masses are the respective spectral parameters squared, $\lambda_i^2$. Finally, the spectral parameters are integrated over and weighted by the respective spectral function,

$$D[p] = g \prod_{j=1}^{N} \int_{\lambda_j} \rho(\lambda_j) I(\lambda_1, .., \lambda_n, p)\,, \tag{7.41}$$

with

$$I(\lambda_1, .., \lambda_n, p) = \int_q \mathrm{Vert}(p,q) \prod_{j}^{N} \frac{1}{\lambda_j^2 + l_j^2}\,. \tag{7.42}$$

The momentum integral in (7.42) is readily solved and the resulting analytic expression holds true for $p \in \mathbb{C}$. This gives us access to the spectral function (7.35) via the limit $p \to -\mathrm{i}(\omega + \mathrm{i}0^+)$. We remark that in the present spectral fRG approach to the (1+2)-dimensional scalar theory, all integrals are finite, and we can safely change the order of integration even prior to renormalisation. In general the interchange of momentum and spectral integration performed in (7.41) assumes a suitable regularisation of the full integral, which can be done with *spectral renormalisation* [168].

The spectral structure of the diagrams allows for a simple discussion of the emergent scattering thresholds that can be easily tracked within spectral functional approaches. An illustrative example is given by the contribution of the vacuum polarisation diagram to the spectral function of a single scalar field: It features a branch cut that opens at the sum of the spectral masses of the two propagators. The spectral function entering the diagram consists of a mass pole at $m_{\text{ pole}}$ and a sum of scattering continua $\rho_N$ starting at $N m_{\text{ pole}}$ with $N \geq 2$. It follows straightforwardly from the analytic structure of that diagram that substituting scattering contributions $\rho_N$ and $\rho_M$ for the two internal lines directly yields a contribution to $\rho_{N+M}$. This demonstrates how any scattering structure, once seeded, gives rise to higher scattering contributions.

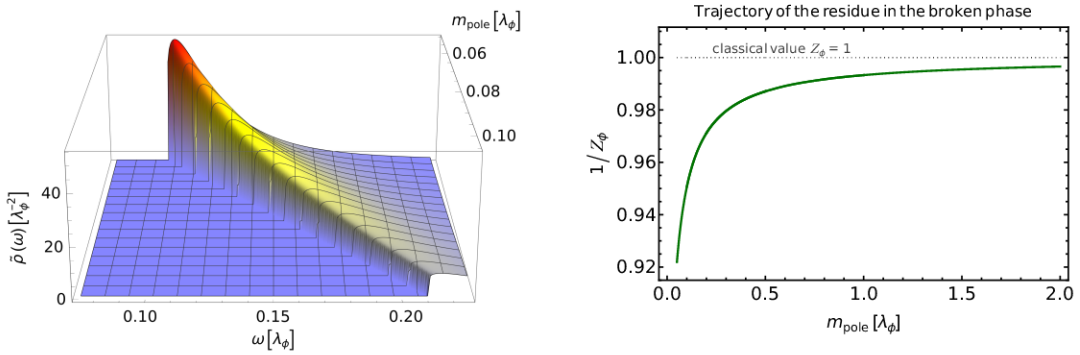


(a) Scattering tail $\tilde{\rho}_k$ for vanishing spatial momentum $\vec{p} = 0$ as a function of the spectral value $\omega$ and the pole mass $m_{\text{pole}}$ for $1/20 \leq m_{\text{pole}}/\lambda_\phi \leq 1/10$.

(b) Amplitude $1/Z_\phi$ of the pole contribution of the spectral function (7.52) as a function of the pole mass $m_{\text{pole}}$ for $1/20 \leq m_{\text{pole}}/\lambda_\phi \leq 1/2$. The classical value for $Z_\phi$ is indicated in grey.

Figure 7.9.: Spectral function $\rho$, (7.52), for different pole masses $m_{\text{pole}}/\lambda_\phi$, measured in the fixed coupling $\lambda_\phi$.

### 7.2.2. The CS-flow at work

In the spectral fRG approach put-forward in [3, 166] and summarised in Section 3.4, the quantum effective action of the theory at hand is obtained by starting with a theory with an asymptotically large classical pole mass $m_\phi \to \infty$, and then lowering the mass successively until the physical point is reached. The respective classical action is given by (7.34) with

$$S[\phi] = \int \mathrm{d}^3x \left\{ \frac{1}{2}\phi\left(-\partial^2 + Z_\phi\,\mu\right)\phi + \frac{\lambda_\phi}{4!}\phi^4 \right\}, \tag{7.43}$$

with positive or negative $\mu$. The wave function $Z_\phi$ has been introduced for convenience, anticipating the emergence of a wave function. For asymptotically large pole masses we have $Z_\phi \to 1$, see Figure 7.9b. Then, (7.43) reduces to (7.34), and the pole mass is given by

$$m_\phi^2 = \mu - 3\mu\,\theta(-\mu), \tag{7.44}$$

capturing both the symmetric and broken phase. This setup captures both, theories deep in the symmetric phase with $\mu \to +\infty$ and theories deep in the broken phase with $\mu \to -\infty$.

#### Functional Callan-Symanzik equation

The infinitesimal change of the quantum effective action $\Gamma[\phi]$ under a change of the mass $\mu$ is governed by the manifestly finite *renormalised* Callan-Symanzik equation, (3.53), or [3, 166],

$$\mu\partial_\mu\Gamma[\phi] = \frac{1}{2}\left(1 - \frac{\eta_\phi}{2}\right) Z_\phi \mu\,\mathrm{Tr}\Big[\,G[\phi] + \phi^2\Big] - \frac{1}{2}\,\mu\partial_\mu S_{\text{ct}}[\phi]\,, \tag{7.45a}$$

with the anomalous dimension

$$\eta_\phi = -2\frac{\mu\partial_\mu Z_\phi}{Z_\phi}\,, \tag{7.45b}$$

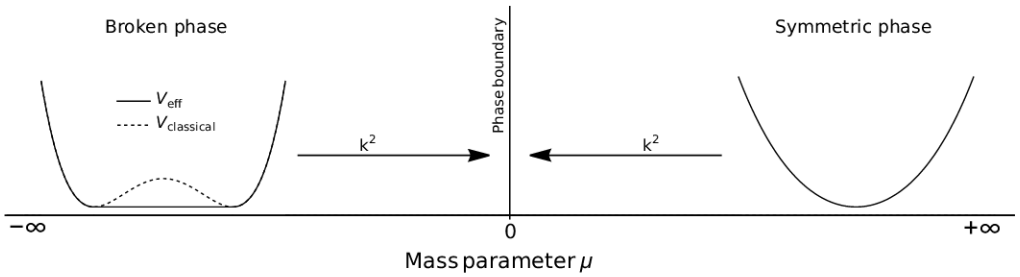


Figure 7.10.: Schematic phase diagram with respect to the mass-parameter $\mu$. The phase boundary is located at $\mu = 0$. The flow is initiated in the deep UV, i. e. $|\mu| = k^2 \to \infty$ with the respective (classical) initial effective potential.

The factor 2 in (7.45b) takes into account that $\mu$ has mass dimension 2, and the anomalous dimension 'counts' dimensions and not 1/2 dimensions. The argument $\phi$ in (7.45) is the mean field. The term $\mu\partial_\mu S_{\text{ct}}[\phi]$ in the second line of (7.45a) is the flow of the counter terms that renders the flow equation finite, where the factor 1/2 was added for convenience. The loop term on the right-hand side depends on the full field-dependent propagator. In the momentum basis it is given by

$$G[\phi](p,q) = \langle\varphi\varphi\rangle_c(p,q) = \frac{1}{\Gamma^{(2)}[\phi]}(p,q), \tag{7.45c}$$

where the subscript $_c$ refers to the connected part of the two-point function and the mean field $\phi$ is given by the expectation value of the quantum field $\varphi$, i.e., $\phi = \langle\varphi\rangle$. In the momentum basis, the trace in (7.45a) corresponds to a momentum integral. Note that the effective action $\Gamma[\phi]$ in (7.45) includes the full mass term $1/2\int_x \mu\,\phi^2$ in contradistinction to the effective action used in standard fRG momentum-shell flows. There, the momentum dependent regulator part of the mass term is subtracted, and the physical theory is reached when it vanishes. In the present setup, the $\mu$-dependent effective action is that of a physical theory with mass parameter $\mu$, and the flow is one in (physical) theory space.

Moreover, compared to the Wetterich equation [67] with a momentum-dependent infrared regularisation, the novel ingredient in the functional Callan-Symanzik equation (7.45) is the explicit counter term flow $\mu\partial_\mu S_{\text{ct}}[\phi]$. The counter term flow has been derived in a manifestly finite limit of standard momentum cutoff flow equations as discussed in detail in [3]. The derivation entails that the flow of the counter term originates from a closed one-loop expression such as the trace in (7.45) itself, i.e., $\mu\partial_\mu S_{\text{ct}}[\phi] \sim$ diagramms. Accordingly, the counter term flow contains no tree-level contributions to the respective correlation functions. This entails that classical values of the correlation functions are solely given by the respective choice of tree-level values specified in the classical action (7.43), and in particular cannot be further changed by specification of renormalisation conditions. In consequence, the latter can only be used to renormalise the flow contributions, but not the initial conditions of the flow. This excludes, for example, that the counter term flow rearranges the theory from the symmetric into the broken phase or vice versa by $\mu\partial_\mu S_{\text{ct}} \propto \pm\text{const.}\,\mu\int\phi^2$. However, the counter term can contain similar terms proportional to $\lambda_\phi/m_{\text{pole}} = \lambda_{\text{eff}}$.

In particular, the counter term flow allows for *flowing renormalisation conditions*, and we shall use it to adjust a *flowing on-shell renormalisation*, based on the spectral on-shell renormalisation put forward in [168]. Then, the pole mass $m_{\text{pole}}$ is identified with $m_\phi$ in (7.44) in both phases,

$m^2_{\text{pole}} = \mu - 3\mu\,\theta(-\mu)$. In this physical RG scheme the phase transition between the symmetric and broken phase happens for $m^2_\phi = 0$. Hence, we approach the phase transition both from the broken and the symmetric phase in the limit $\mu \to 0$, and the flows are taking place in the one or the other phase, see Figure 7.10. This also avoids flows through the phase transition as are present in momentum cutoff flows.

In the present work, we consider the flow of the inverse propagator within the spectral representation. The flow is given by

$$\mu\partial_\mu \Gamma^{(2)}(p^2) = \left(1-\frac{\eta_\phi}{2}\right) Z_\phi \mu \left[D_{\text{pol}}(p^2) - \frac{1}{2} D_{\text{tad}}(p^2)\right] + \left(1-\frac{\eta_\phi}{2}\right) Z_\phi \mu - \frac{1}{2}\mu\partial_\mu S^{(2)}_{\text{ct}}, \quad (7.46)$$

where $D_{\text{tad}}$ and $D_{\text{pol}}$ refer to the tadpole and polarisation diagram, for more details see [7]. Moreover, all quantities in (7.46) depend on the chosen background $\phi$. For general space-time dependent backgrounds $\phi(x)$ this would lead to $\Gamma^{(2)}[\phi](p,q)$. In the explicit computations we consider the background $\phi_0$, which is the constant solution of the equation of motion

$$\left.\frac{\delta\Gamma[\phi]}{\delta\phi}\right|_{\phi=\phi_0} = 0\,. \quad (7.47)$$

With this physical choice for the background, the general field-dependent propagator (7.45c) reduces to the physical propagator $G(p^2)$ in the absence of source terms,

$$G(p^2) = \frac{1}{\Gamma^{(2)}[\phi_0](p^2)}\,. \quad (7.48)$$

In the symmetric phase, we have $\phi_0 = 0$, while $\phi_0 \neq 0$ signals the broken phase. At constant fields the propagator (7.45c) reduces to $G(p,q) = G(p^2)(2\pi)^d\delta(p+q)$. Similarly we have $\Gamma^{(2)}[\phi_0](p,q) = \Gamma^{(2)}[\phi_0](p^2)(2\pi)^d\delta(p+q)$.

In three dimensions the two phases are separated by a second order phase transition in the Ising universality class. From now on we drop the field argument $\phi_0$. It is implicitly understood that all correlation functions are evaluated at $\phi = \phi_0$.

In a final step, we substitute $\mu$ with $\pm k^2$, to keep the relations to standard fRG flows with momentum cutoffs simple, where $k$ is commonly used. This facilitates the comparison and benchmarking of the real-time results obtained with the spectral fRG. For example, the three-dimensional $\phi^4$-theory has been studied abundantly within the Euclidean fRG, including systematic studies of the convergence of approximation schemes, for a recent review see [104]. These results carry over straightforwardly to the present approach, and the Euclidean correlation functions obtained from the spectral functions can be directly compared. This substitution leads us to

$$k^2 = |\mu|\,, \qquad \partial_t = k\,\partial_k = 2\mu\partial_\mu\,, \quad (7.49)$$

where the (negative) RG-time $t = \log(k/k_{\text{ref}})$ is measured relatively to a suitable reference scale or mass.

### Spectral on-shell renormalisation

We proceed with discussing the on-shell spectral renormalisation, using the direct access to Minkowskian momenta. In (1+2)-dimensions, both diagrams in the CS flow (7.46) are

manifestly finite, and the flow of the counter term action $\mu\partial_\mu S_{\rm ct}$ only guarantees the implementation of the chosen renormalisation conditions. The (1+2)-dimensional $\phi^4$-theory is super-renormalisable, and one only has the renormalisation condition for the mass. Now we use on-shell renormalisation to keep the full pole mass on the classical input mass (7.44) with $m^2_{\rm pole} = k^2$ in the symmetric phase, and $m^2_{\rm pole} = 2k^2$ in the broken phase. This leads us to

1. symmetric phase:

$$\Gamma^{(2)}[\phi_0]\Big|_{p^2=-k^2} = 0\,, \tag{7.50}$$

2. broken phase:

$$\Gamma^{(2)}[\phi_0]\Big|_{p^2=-2k^2} = 0\,. \tag{7.51}$$

In the symmetric phase the first allowed scattering process is the $1 \to 3$ scattering, and the onset of the scattering continuum is located at three times the pole mass. In turn, in the broken phase with $1 \to 2$ scattering, the onset of the scattering continuum of the spectral function is located at twice the pole mass. Thus, the spectral function (7.36) reads

$$\rho(\lambda) = \frac{2\pi}{Z_\phi}\delta(\lambda^2 - m^2_{\rm pole}) + \theta(\lambda^2 - m^2_{\rm scat})\tilde\rho(\lambda)\,, \tag{7.52}$$

with $m_{\rm scat} = 3m_{\rm pole}$ (symmetric phase) and $m_{\rm scat} = 2m_{\rm pole}$ (broken phase). In Figure 7.9, we show the scale evolution of the spectral function $\rho$ in the broken phase: in Figure 7.9a we depict the scattering tail $\tilde\rho$, and in Figure 7.9b we depict the amplitude of the pole contribution. All quantities are measured relative to the coupling $\lambda_\phi$.

The spectral tail is rising towards smaller pole masses for a fixed classical coupling, and in turn the amplitude $1/Z_\phi$ of the pole contribution is decreasing. In combination the sum rule holds during the evolution. The growing importance of the scattering processes can be understood from the fact that the dynamics of the theory only depends on the dimensionless ratio $\lambda_\phi/m_\phi$ with $m_\phi \propto k$. Hence, the effective coupling grows strong for smaller pole masses and on the other hand the dynamics of the theory are vanishing for asymptotically large pole masses.

In contrast to the Callan-Symanzik or mass regulator used here, commonly used regulators in Euclidean flows decay for momenta larger than the IR cutoff $k$. This provides manifestly finite flows without the need of further renormalisation. Moreover, for Euclidean momenta, the respective flows of lower order correlation functions decay faster than for a CS regulator. In Minkowski space, however, the CS or mass regulator has the welcoming property, that the one-loop flow of $\rho(\omega)$ contains only classical correlation functions and is maximally local. While this is trivial in the symmetric phase where the one-loop flow only shifts the pole mass and does not generate a scattering continuum, it is non-trivial in the broken phase. There, the flow of the scattering continuum is given by a single delta function at the onset of the scattering spectrum, which originates from $\partial_t \operatorname{Im}\Gamma^{(2)} \propto \delta(\omega^2 - 4m^2_{\rm pole})$. Since the mass pole constitutes the dominant part of the propagator, the flow of the spectral function at spectral values larger than the flowing onset $2m_{\rm pole}$, which is solely induced by the scattering tail, is sub-leading.

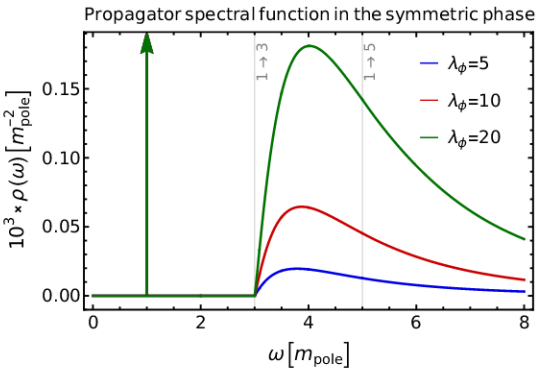


Figure 7.11.: Spectral functions for vanishing field value as a function of the frequency. All quantities are measured in units of the pole mass. $1 \to 3$ and $1 \to 5$ onsets are indicated in grey.

### 7.2.3. Results

In this section, we present results for the non-perturbative spectral functions of the scalar propagator in the symmetric and broken phase. The discussion of the numerical implementation is deferred to Appendix B.4. The results allow for an investigation of the scattering processes in both phases. The present results are in remarkable quantitative agreement with that obtained with the spectral DSE in [168]. This agreement of the spectral functions from these two different functional approaches hold true for a large range of effective couplings $\lambda_\phi/m_\phi$, see Figure 7.12a. In this coupling regime this agreement provides a non-trivial reliability check for both functional approaches, thus decreasing the respective systematic error.

#### Symmetric phase

In the symmetric phase with $\phi_0 = 0$ we are left with the tadpole diagram in the flow of the two-point function (7.46). The resummation (B.47) introduces a non-trivial momentum dependence to the four-point function and, in consequence, also to the tadpole diagram. This allows to calculate the propagator spectral function in the symmetric phase, i. e., at vanishing field value, where the polarisation diagram is absent. For the respective flow equation on the real frequency axes see (B.53). The resulting spectral function is shown in Figure 7.11. In the symmetric phase, the scattering continuum starts at $3m_{\text{pole}}$. As mentioned above, the dynamic tadpole contribution carries the momentum structure of the polarisation diagram, resembling the $s$-channel structure of the four-vertex. Still, the onset of its imaginary part is at thrice the pole mass, since the bubble resummed vertex represents a series of $2 \to 2$ scatterings which leads to a generic two-particle onset of $\rho_4$. The quantum corrections to the symmetric phase propagator are small compared to the broken phase. The amplitude on the mass pole is close

| $\lambda_\phi/m_{\text{pole}}$ | $1/Z_\phi$ (fRG) | $1/Z_\phi$ (DSE) | $1/Z_\phi(\phi_0 = 0)$ |
|---|---|---|---|
| 5 | 0.971 | 0.969 | 0.9998 |
| 10 | 0.950 | 0.945 | 0.9995 |
| 20 | 0.921 | 0.907 | 0.9986 |

Table 7.1.: Amplitudes $1/Z_\phi$ of the pole contribution for given effective couplings, corresponding to the scattering tails displayed in Figure 7.12a and Figure 7.11.

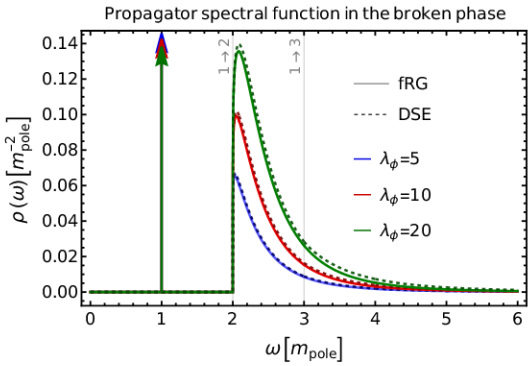


(a) Spectral function of the propagator. The $1 \to 2$ and $1 \to 3$ particle scattering onsets are indicated in grey.

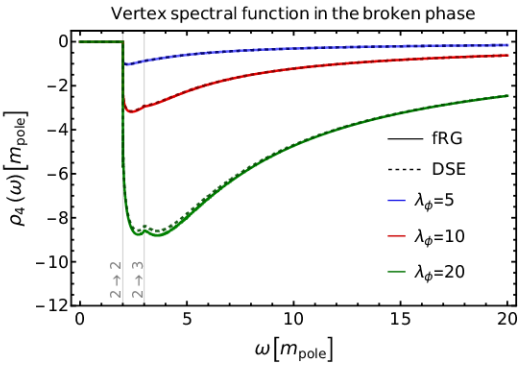


(b) Spectral function of the four-point function. The $2 \to 2$ and $2 \to 3$ particle scattering onsets are indicated in grey.

Figure 7.12.: Spectral functions as a function of Minkowski frequency in comparison to DSE results from [168]. In contrast to Figure 7.9, all quantities are measured in units of the pole mass to facilitate the comparison with the DSE results.

to one compared to the respective values in the broken phase, see Table 7.1. This is expected, since the first dynamic contribution is of two-loop order and corresponds to the sunset topology.

### Broken phase

In the broken phase the condensate is non-vanishing, $\phi_0 \neq 0$. To compute the spectral function, the flow equation is evaluated on the real frequency axes see (B.62).

The $N$-particle onset positions of the spectral scattering tail are governed by the imaginary part of (B.62). For the polarisation diagrams, where only propagators come into play, the flow exhibits an onset at the sum of the two mass-poles. In contrast, the contribution of the tadpole leads to an onset at thrice the pole-mass, as the four-point spectral function only consists of a scattering continuum starting at $2m_{\text{ pole}}$, cf. Figure 7.12b.

In Figure 7.12a the spectral function from the current fRG approach is compared to spectral DSE results from [168]. Every quantity is measured relative to the respective pole mass to facilitate comparison with the DSE results. This allows to compare the relative magnitude of the scattering continua for different coupling strengths. For effective couplings $\lambda_\phi / m_{\text{ pole}} \lesssim 20$, the spectral weight of the scattering continuum is sub-leading, as can be inferred from the combination of Figure 7.9b and the sum rule (7.37). The amplitudes of the pole contributions are listed in Table 7.1.

We find a remarkable agreement of both methods in the tested coupling range. For effective couplings $\lambda_\phi / m_{\text{ pole}} \approx 20$, the deviations start growing, specifically at the thresholds. Deviations between both methods arise due to differences in the resummation structure of the two functional equations in the current truncation. The convergence of functional techniques for a large range of couplings is non-trivial and strengthens our confidence in spectral functional approaches.

In general, the tail of the propagator spectral function is enhanced for stronger couplings, while the residue of the mass pole decreases as the scattering states become more accessible due to the rising dimensionless interaction strength. The three- and higher $N$-particle onsets are graphically not visible in the full spectral functions of Figure 7.12a, but present in the data. In the limit of large couplings we expect the three-particle onset to become more pronounced

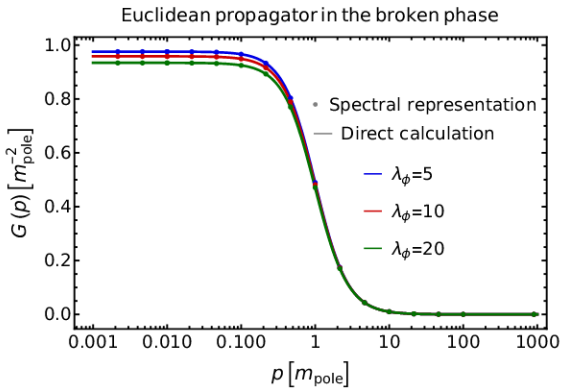


Figure 7.13.: Propagator as function of Euclidean frequency. This result serves as a cross-check between a direct computation via the flow and a calculation using the spectral functions.

as the tadpole contribution becomes large.

The four-point spectral function shown in Figure 7.12b consists of only a negative scattering tail corresponding to a $2 \to 2$ scattering process. For higher couplings, the three-particle onset becomes visible. The different suppression of higher $N$-particle thresholds in the propagator- and four-point spectrum are explained by dimensional analysis. While for the propagator spectral function, higher $N$-particle onsets are suppressed by their squared energy threshold, the four-point spectral function decays only with $\lambda^{-1}$, leading to a suppression linear in their respective energy thresholds. In both cases, four-particle or higher onsets are strongly suppressed, since they come with at least one additional loop each.

Figure 7.13 shows the Euclidean propagators corresponding to the spectral functions of Figure 7.12a. As a cross-check, we compare the Euclidean propagator calculated from the spectral representation to the propagator directly obtained from the integrated Euclidean flow. We find the spectral representation to hold.

### 7.2.4. Conclusion

In the present work, we computed single particle spectral functions of a scalar $\phi^4$-theory within the spectral functional renormalisation group approach, put forward in [3]. This approach leads to renormalised spectral flows with flowing renormalisation, and facilitates a fully self-consistent computation of non-perturbative spectral functions. We derived full flow equations for the inverse propagator in both, the symmetric and broken regime of the theory, for a detailed discussion see Appendices B.4.5 and B.4.6.

Our setup is manifestly Lorentz invariant and sustains the causal properties of the theory throughout the flow. Every point on the Callan-Symanzik RG trajectory is a physical theory of scale $k$. Trajectories in the symmetric and broken regime each start from an infinitely heavy theory in the respective phase and meet at the phase boundary in the strongly interacting massless limit of the theory, see Section 7.2.2 and Figure 7.10. Thereby, our setup avoids flows through the strongly interacting phase transition regime, which are usually present in momentum cutoff flows. This minimises the systematic error stemming from the strong dynamics in the vicinity of a phase transition, where the flows are highly sensitive to truncation artefacts. Furthermore, the implementation of a flowing renormalisation condition eliminates the need of fine-tuned initial conditions and allows for monotonous mass flows.

The explicit results in the broken phase are in impressive agreement with those obtained

in [168] within the spectral DSE, see Section 7.2.3. This affirms the reliability of the spectral functional approach for the non-perturbative computation of fundamental Minkowski spacetime correlation functions.

In contrast to DSE, the fRG approach captures average momentum dependencies of vertices via their scale dependence. This allows to include non-trivial vertex dynamics without resorting to intricate spectral representations of higher correlation functions. Furthermore, the current spectral fRG approach is straightforwardly and easily extended to include the flow of the full effective potential. This work represents an important step towards unravelling real-time correlations in QCD from first principles with spectral functional approaches. We hope to report on respective results in the near future.

# CHAPTER 8

## The quark-meson model

*This chapter we investigate the quark-meson model, which is essential to a quantitative description of QCD within functional methods. We present a compilation of results from [1, 10, 11]. Figures are taken from [1] unless indicated differently in the respective (sub)section.*

In Chapter 2, we pointed out the importance of a Fierz-complete basis of the four-quark scattering vertex and the importance of quantitative access to the respective order parameter potentials for homogeneous and inhomogeneous condensates. The latter allows to locate phase transition lines and discuss the question of the symmetry breaking pattern and the order of phase transitions. It has been shown in the past decade that functional QCD flows towards QCD-assisted low energy effective models for energy scales below 1 GeV, for a detailed discussion see in particular the recent works [51, 104] and also Chapter 9. With dynamical hadronisation [102, 123, 127, 219] the low energy effective theory is the (Polyakov-loop enhanced) quark-meson model (QM model), see Section 2.3, or more generally the quark-hadron model. For recent fRG-works with the (P)QM model on the phase structure of QCD relevant for the present work see e.g. [46, 58, 118, 279, 280, 306, 325–344], for a recent overview see [104]. This emergence of LEFTs from first principle QCD flows is well understood and quantitatively explored in the vacuum, see [42, 44, 45, 48, 102, 103]. It entails that the infrared critical dynamics is dominated by the low energy fluctuations of quarks and hadrons. For small baryon-chemical potentials, $\mu_B/T \lesssim 4$, the relevant hadronic degrees of freedom are simply the pseudo-scalar pions and the sigma mode, see [19, 51, 56, 64, 100]. In turn, for baryon-chemical potentials $\mu_B \lesssim 4/T$ the situation is less clear, but we expect sizeable diquark contributions, see [64].

In the following we present results which combine two important technical advances from the past years: The first one was the development of self-consistent approximations for the computation of order parameter potentials, [58]. The second one was the development of a numerical approach for solving flow equations that also enables us to discuss discontinuities in the flows such as shocks that are potentially relevant for the correct description of first and second order phase transitions, [65] see also Chapter 5. In the present chapter we compute the phase structure of the quark-meson model (QM model) at finite temperature and density.

An important benchmark is already provided in the large-$N_f$ limit with an infinite number of flavors. It is argued that within an 't Hooft-type limit we can mimic the two-flavor QM model

well (or any other flavor), and in particular reproduce well it's non-universal properties such as the location of the phase boundary. Moreover, in this limit the numerical approach also allows for a full computation of higher quark-mesonic scattering processes and allows to gauge therir quantitative importance in QCD. The respective results are compared with the currently most advanced approximation (including shocks) to the self-consistent approximation including the order parameter potentials in [58] for the $N_f = 2$-flavor quark-meson model. The results include also the regime $\mu_B/T \gtrsim 4$.

In Section 8.1 we discuss the QM model in an fRG setting and how this low energy effective model relates to QCD. This is followed by an investigation of the results, considering only higher mesonic scattering orders in Section 8.2. Here, we investigate the phase structure and scaling parameters for both the large-$N_f$ limit and at finite $N_f$. The former also sets up the investigation of higher quark-mesonic scattering orders in Section 8.3. We give a brief summary in Section 8.4.

## 8.1. The quark-meson model within the functional renormalisation group

*This section is based on [1, 11]. All figures are taken from [1].*

We briefly recapitulate the fRG-approach to the (Polyakov-enhanced) quark-meson model (QM model). In the present chapter, the inclusion of dynamical mesons as low energy effective degrees of freedom has to be seen as an efficient and convenient book-keeping device for the respective resonant interaction channels. In particular, this substitutes the rather tedious inclusion of the resonant parts of the higher-order scattering processes of quarks. Still, if used on a quantitative level, even for large UV-cutoff scales its effective action does not reduce to a simple local classical actions. For more details and in particular its quantitative properties as an emergent low energy theory in QCD we refer to [44, 45, 48, 51] and Chapter 9. Validity checks, benchmarks and bounds in comparison to QCD have been provided in [103].

Here, we restrict ourselves to qualitative approximations to the effective action. We are predominantly concerned with the quantitative access to the effective potential of the chiral order parameter. The systematic inclusion of the present quantitative setup within functional QCD flows is straightforward due to the modular nature of the fRG-approach and is considered in Chapter 9.

A careful study of QCD correlation functions, as done in [51, 103, 345], reveals that the QM model incorporates QCD fluctuations only below a momentum scale of $k_{\rm UV} \approx 300$ MeV: for this analysis one uses QCD results at a given momentum scale $k_{\rm UV}$ as the UV effective action of the QM model and compares the results from the model and QCD in the deep infrared. Evidently, the QM model only incorporates QCD fluctuations if the results agree.

In turn, initiating the QM model at a larger UV scale $k_{\rm UV}$, the effective action at this scale has to include part of the QCD gluon fluctuation still present for lower scales. Typically, this is done in the vacuum at $T, \mu_B = 0$, and one may estimate that the model can be used as a low energy effective model for momentum scales $k_{\rm UV} \approx 700$ MeV, hence roughly of the order of 1 GeV. However, one has to be aware of the fact that the model does not match full quantitative QCD even for temperatures and densities that are well below 1 GeV: gluonic fluctuations are present above $k \approx 300$ MeV and they are only modelled well in the vacuum and their thermal and density modifications are missing. In summary, the QM model gradually looses quantitative

precision, if $T, \mu_B$-fluctuations significantly modify the momentum dependence above $k \approx 300$ MeV. We shall use these considerations for our evaluation of the regime of validity of the results obtained here.

The scales of the present (qualitative) LEFT are gauged by the pion decay constant in the chiral limit. We use $f_{\pi,\chi} = 88\,\text{MeV}$ and measure all other scales with these units. We choose the UV-cutoff scale of the QM model as $\Lambda \approx 700\,\text{MeV}$. We consider this to be a good compromise between integrating-out as many momentum-fluctuations as possible and stretching the validity-bound of the LEFT. The momentum fluctuations with momentum scales $k \leq \Lambda$ are included with the functional renormalisation group (fRG). This approach has been used intensively in the past 25 years for the inclusion of low energy dynamics of the QM model. For the setup of the flow equation for the effective action, and the derivation of the respective flow equations for (field-dependent) couplings we refer to the fRG-reviews see [104, 202, 203, 229, 346]. Applications relevant for the present work can be found in [58, 64, 347], the derivations and flows for the present approximation can be found in [58].

### 8.1.1. The local potential approximation

In the zeroth order derivative expansion the effective action $\Gamma_k[q, \bar{q}, \phi]$ of the $N_f$-flavor QM model is given by,

$$\Gamma_{LPA,k}[q, \bar{q}, \phi] = \int_x \left\{ \bar{q}(\gamma_\mu \partial_\mu - \gamma_0 \mu_q) q + \frac{1}{2}(\partial_\mu \phi)^2 + h_k(\rho)\, \bar{q}(\tau^0 \sigma + \boldsymbol{\tau}\boldsymbol{\pi}) q + V_k(\rho) - c_\sigma \sigma \right\}, \tag{8.1}$$

with $\tau^\mu$ being related to the Pauli matrices, $\tau = 1/2(\mathbb{1}, i\gamma_5 \boldsymbol{\sigma})$, and the quark-meson coupling incorporates the SU(2) $\cong$ SO(3) symmetry of the pseudoscalar subgroup. The O(4)-scalar field $\phi$ and the respective O(4)-invariant $\rho$ are given in (2.36) and (2.37) respectively. We have also $\int_x = \int_0^{1/T} dx_0 \int d^3x$ as an abbreviation for the finite temperature spatial integration.

Here, the Yuakwa coupling $h_k(\rho)$ is indicated with a full field dependence. It multiplies the O(4)-invariant operator $\bar{q}\,\tau\phi\, q$, hence it only depends on the O(4)-invariant $\rho$. The field-dependence of the Yukawa-coupling takes into account higher-order point-like scatterings of the resonant scalar-pseudoscalar channels with the quark–anti-quark pair. The inclusion of these processes is necessary for a fully consistent zeroth order derivative expansion, and has been introduced in [58]. For further works in Yukawa models with field-dependent Yukawa coupling see [341, 348–351]. This necessity is easily seen by performing a perturbative one-loop computation within the QM model. Then, the quark loop with $h(\rho)$ contributes to the full effective potential. Of course higher terms in the derivative expansion also contribute to the effective potential, but the Yukawa-term contains no derivatives. Accordingly, its full field-dependence should be accounted for in a consistent lowest order derivative expansion.

Finally, the scalar effective potential $V_k(\rho)$ takes into account the remaining part of the higher scattering orders of the mesons. The linear term $c_\sigma \sigma$ introduces explicit chiral symmetry breaking. Evidently, it drops out on the right hand side of the flow equation and does not run with the RG-scale. Consequently, the full flow and hence the full effective potential $V_k$ does not know anything about explicit chiral symmetry breaking.

In the zeroth order derivative expansion, the wave function renormalisations $Z_q(\phi), Z_\phi(\phi)$ for quarks and mesons are dropped. Here, we concentrate on the quantitative discussion of the full effective potential. Hence, with (8.1) we assume implicitly,

$$Z_{q,k}(\rho) = 1 = Z_{\phi,k}(\rho)\,. \tag{8.2}$$

The flow equation for the complete set of couplings, $h_k(\rho), V_k(\rho)$, and wave function renormalisations, can be found in [58]. We use the same setup here, including the choice of regulators, three-dimensional flat or Litim regulators, [308] or see Appendix B.7.1.

For the effective potential we simply evaluate the flow for $\Gamma_k[q,\bar{q},\phi]$ for constant scalar fields $\phi$ and vanishing quark fields, $q,\bar{q}=0$, similarly to the procedure in Section 5.1.1. This leads us to,

$$\begin{aligned}\partial_t V_k(\rho) =& \frac{k^5}{12\pi}\bigg[-\frac{4N_f N_c}{\epsilon_k^q}\Big(1-n_f(\epsilon_k^q+\mu)-n_f(\epsilon_k^q-\mu)\Big)\\ &+\frac{N_f^2-1}{\epsilon_k^\pi}\Big(1+2n_B(\epsilon_k^\pi)\Big)+\frac{1}{\epsilon_k^\sigma}\Big(1+2n_B(\epsilon_k^\sigma)\Big)\bigg],\end{aligned} \tag{8.3}$$

with $\rho$-dependent quark- and meson-dispersion relations,

$$\epsilon_k^\phi(\rho)=\sqrt{k^2+m_{\phi,k}^2(\rho)}\,,\quad \epsilon_k^q(\rho)=\sqrt{k^2+m_{q,k}^2(\rho)}\,, \tag{8.4}$$

and the (negative) RG-time $t=\ln k/\Lambda$. The RG-time involves a reference scale in the logarithm, which we have set to be the initial scale. The masses $m_q, m_\phi$ are obtained by evaluating the respective two-point functions at constant fields. Note that $m_q, m_\phi$ are the curvature and not the pole or screening masses of quarks and mesons, for respective definitions and discussions see [333].

The meson curvature masses are defined with

$$\begin{aligned}m_{\pi,k}^2(\rho) =& \partial_\rho V_k(\rho)\,,\\ m_{\sigma,k}^2(\rho) =& \partial_\rho V_k(\rho)+2\rho\,\partial_\rho^2 V_k(\rho)\,,\end{aligned} \tag{8.5a}$$

and hence are curvature-coefficients of the effective potentials. In turn, the quark mass is proportional to the Yukawa-coupling,

$$m_{q,k}^2(\rho)=2h_k(\rho)^2\rho\,. \tag{8.5b}$$

It is left to discuss the flow equation for the field-dependent Yukawa coupling, for details we again refer to [58]. We can project the flow for $\Gamma_k$ onto the Yukawa coupling $h(\rho)$ by evaluating the quark two-point function at vanishing quark and pion fields, $q,\bar{q},\pi=0$, and constant $\sigma$. With (8.1) we arrive at

$$\Gamma^{(2)}_{q\bar{q},k}[\sigma](p)\delta_{p,p'}=\left.\frac{\delta^2\Gamma[q,\bar{q},\phi]}{\delta q(p)\delta\bar{q}(p')}\right|_{q,\bar{q},\boldsymbol{\pi}=0}\simeq i\not{p}-\gamma_0\mu+\frac{1}{2}h_k(\rho)\sigma-c_\sigma\sigma\,, \tag{8.6}$$

where we have dropped the momentum conservation $\delta_{p,p'}$ in the last line with $\delta_{p,p'}=(2\pi)^4\delta(p-p')$ in the vacuum.

Equation (8.6) reflects the fact that the Yukawa term simply is the $\rho$-dependent mass quark term, $m_{q,k}(\sigma)=h_k(\rho)\sigma/2$. Accordingly, the flow of the Yukawa coupling $h_k(\rho)$ can be derived from that of the scalar part of the quark two-point function: it is simply $\sigma/2\,\partial_t h_k(\rho)$ as $\partial_t c_\sigma=0$ by definition. Thus we get,

$$\partial_t h_k(\rho)=-\frac{1}{4N_cN_f}\frac{1}{\sigma}\mathrm{ReTr}\,\Gamma^{(2)}_{q\bar{q},k}[\sigma](p=0)\,. \tag{8.7}$$

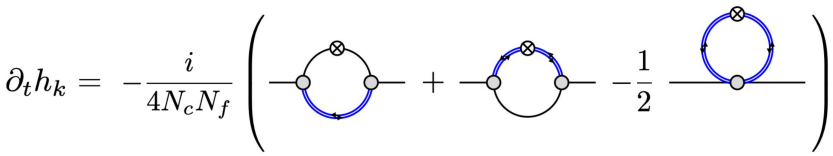

Figure 8.1.: Diagrammatic representation of the flow of the Yukawa coupling. The circled cross ⊗ depicts the regulator insertion $\partial_t R_k(\boldsymbol{p}^2)$ and the gray dots denote full vertices. The double lines depict the mesons, whereas the single line indicates the quark content. The arrows depict the quark number flow.

In (8.7) we have used that $\rho = \sigma^2/2$ for $\boldsymbol{\pi} = 0$. The flow (8.7) is depicted in Figure 8.1. From (8.7) and the approximation (8.1) we finally get,

$$\begin{aligned}\partial_t h_k(\rho) = {} & 4v_3 h_k^3(\rho)\big[L^{(4)}_{(1,1)}(m^2_{q,k}, m^2_{\sigma,k}; T, \mu) - (N_f^2 - 1) L^{(4)}_{(1,1)}(m^2_{q,k}, m^2_{\pi,k}; T, \mu)\big] \\ & + 16 v_3 h_k(\rho) h_k'(\rho)\rho\big[h_k(\rho) + \rho h_k'(\rho)\big] \times L^{(4)}_{(1,1)}(m^2_{q,k}, m^2_{\sigma,k}; T, \mu) \\ & - 2v_3 k^2\big[(3h_k'(\rho) + 2\rho h_k''(\rho)) l_1^{(B,4)}(m^2_{\sigma,k}; T) + (N_f^2 - 1) h_k'(\rho) l_1^{(B,4)}(m^2_{\pi,k}; T)\big].\end{aligned}$$

with

$$v_{d-1} = \frac{1}{2^{d+1}\pi^{\frac{d}{2}}\Gamma\left(\frac{d}{2}\right)}. \tag{8.8}$$

The threshold functions $l_1^{(B,4)}$ originate in the bosonic loops in 4 dimensions. The $L^{(4)}_{(1,1)}$ originate in the mixed fermionic and bosonic contributions, again in 4 dimensions. Both functions are defined in Appendix B.7.2. The two four lines from (8.8) are contributions of the first two diagrams with mixed fermionic and bosonic loops in Figure 8.1, whereas the last line corresponds to the bosonic loop with the four-vertex.

Similarly to the flow of the effective potential (8.3), the flow of the Yukawa coupling (8.8) is a non-linear partial differential equation. Contrary to the effective potential however, the interpretation of the Yukawa flow in terms of fluid-dynamics, compare Section 5.1.2, is not easy. In fact, we were not able to find a conservative formulation for (8.8) and defer a full solution of this equation to future work. Hence, we only solve the flow of the Yukawa coupling in the large-$N_f$ limit, see Appendix B.6.1, where we are able to find a stable numerical discretisation of (8.8) in terms of non-conservative fluxes, see Appendix B.6.1.

### Beyond LPA

*This subsection is taken from [11].*

The reliability of the QM model is not only influenced by its overlap or lack thereof with full QCD, it also depends on the truncation used. At very low momentum scales $p^2 \lesssim m_\pi^2$ we enter the realm of chiral perturbation theory and expansions in orders of $k^2/m_\pi^2$ work. For that reason QCD physics in the deep infrared can be systematically accessed within a derivative expansion in $p^2/m_\pi^2$, to lowest order this corresponds to LPA.

| Observable | Value [MeV] | Parameter at $\Lambda_{\mathrm{UV}} = 0.65\,\mathrm{GeV}$ |
|---|---|---|
| $m_\sigma$ | 317.1 | $\lambda_\Lambda = 71.6$ |
| $m_q$ | 310.8 | $h_{\phi,\Lambda} = 3.6$ |

Table 8.1.: Low energy observables and related EFT couplings at the initial cutoff scale $\Lambda_{\mathrm{UV}} = 0.65\,\mathrm{GeV}$. The scales are fixed with the pion decay constant in the chiral limit $f_{\pi,\chi} = 88\,\mathrm{MeV}$, that is $m_\sigma/f_{\pi,\chi} \approx 3.603$ and $m_q/f_{\pi,\chi} \approx 3.532$. In the present approximation we have $f_{\pi,\chi} = \sigma_0$, and in the model the dimensionless ratios are simply $m_\sigma/\sigma_0$ and $m_q/\sigma_0$. In the chiral limit we also have $m_\pi = 0$.

Within the fRG approach, discussed in Chapter 3, LPA still captures an average momentum dependence for momenta $p \leq k_{\mathrm{UV}} \approx 700\,\mathrm{MeV}$, but a full momentum resolution of the scalar-pseudoscalar interaction channel is missing. The momentum truncation could be improved on, by considering the $s$-channel momentum dependence of the scalar-pseudoscalar interaction, which is fully encoded in the momentum dependence of the mesonic two-point functions. The respective truncation of the effective action $\Gamma[q, \bar{q}, \phi]$ has been suggested in [333]. In summary the truncation contains two additional independent coefficients, the two momentum dependent meson dressings. This addition goes in hand with an introduction of smooth regulator functions, which also allow an analytic continuation to the complex plane and hence access to real-time physics and spectral functions. This approach is investigated in upcoming work [11].

The inclusion of fully momentum dependent wave function renormalisation can also be considered in the context of flowing fields, as we have outlined in Section 3.3.3.

### 8.1.2. Initial conditions and numerical setup

The field dependent flow equations ((8.3), (8.8) and their large-$N_f$ limit) are solved using Discontinuous Galerkin methods. The numerical procedure is analogous to Chapter 5, where we solve for the first $\rho$ derivative of the potential $u(\rho) = \partial_\rho V(\rho)$, which corresponds to the pion mass (8.5). Additionally, we solve for the quark mass $w(\rho) = 2\rho h^2$. Details on the derivation of the large-$N_f$ limit of the flows, and the numerical procedure are provided in Appendix B.6.

We initiate the flow at a cutoff scale $k = \Lambda \approx 0.650\,\mathrm{GeV}$ with the classical action of the QM model, see (2.38). Then, the parameter in the initial effective action $\Gamma_\Lambda$ is the $\phi^4$-coupling in the classical potential (2.38a),

$$u_\Lambda(\rho) = \frac{\lambda_\Lambda}{2}\rho \qquad w_\Lambda(\rho) = 2h_\Lambda^2\rho\,. \tag{8.9}$$

as well as the Yukawa coupling $h_\Lambda$. For the sake of simplicity we use a initial meson quark mass, $m_\phi^2 = 0$. All our scales are measured in the pion decay constant in the chiral limit $f_{\pi,\chi} = 88\,\mathrm{MeV}$. Within the present approximation of the QM model we have $f_\pi \approx \sigma_0$, and hence we define $\sigma_0 = 88\,\mathrm{MeV}$. Here $\sigma_0$ is the solution to the equations of motion in the chiral limit, i.e.

$$\partial_\rho V(\rho)|_{\rho=\sigma_0^2/2} = 0\,. \tag{8.10}$$

which corresponds to the minimum of the effective potential $V(\rho)$ for vanishing quark masses at the initial scale $\Lambda$. By definition, the pion mass (8.5) on the equations of motion in the

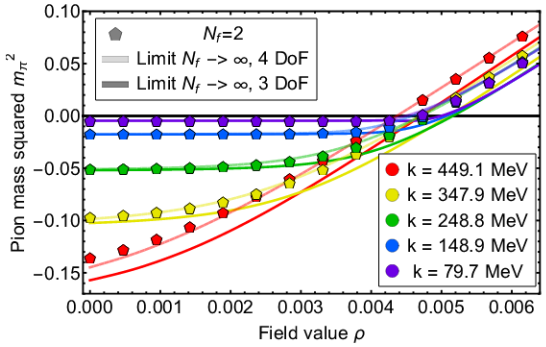


Figure 8.2.: RG-scale evolution of the field-dependent pion mass $m_\pi^2(\rho)$ in LPA (constant Yukawa coupling) in the vacuum. We compare results for $N_f = 2$, and the large-$N_f$ limit with 3 and 4 degrees of freedom, see Appendix B.6.1.

chiral limit (8.10) is always 0 in the symmetry broken phase. They are massless Goldstone-bosons in this case. In Section 8.2.3, we discuss the physical equations of motion, where we introduce an additional explicit symmetry breaking term $c_\sigma \neq 0$, which accounts for the finite up- and down-quark masses, already at the initial scale. The pions now correspond to pseudo-Goldstone-bosons with a small, but finite mass $m_\pi$ in comparison to the $\sigma$-mode $m_\sigma$.

Unless explicitly stated otherwise, we investigate the QM model in the chiral limit $c_\sigma = 0$. Then, the two model parameters $\lambda_\Lambda, h_\Lambda$ are fixed such that they lead to a 'physical' constituent quark mass $h\sigma_0/\sqrt{2}$, and a 'physical' mass of the sigma resonance, $m_\sigma$. The parameters for the couplings of the effective theory and their relation to physical observables are summarised in Table 8.1. The dimensionless ratios in the models at $k = 0$ are given by

$$\frac{m_\sigma}{\sigma_0} \approx 3.605\,, \qquad \frac{m_q}{\sigma_0} \approx 3.532\,, \tag{8.11}$$

and follow from the initial parameters in Table 8.1.

## 8.2. Higher mesonic scattering orders

In this section we present and discuss our results for the phase structure of the QM model. Specifically we only consider a field dependent order parameter potential $V(\rho)$ and constant $h$. We have chosen our initial conditions such that the quark mass and the pion decay constant reproduce physical values in the vacuum, see Section 8.1.2. Note however, that it is not the main objective of the present work to produce quantitatively reliable results. The vacuum benchmark simply facilitates the understanding of our results. In the present work we focus on the qualitative behaviour of the matter sector of QCD at large densities, quantitatively reliable results require full QCD flows and will be considered in Chapter 9. Such a set-up entails, that while we compute and present a phase structure at large densities, the low energy effective theory gradually looses predictability for larger $\mu_B/T$. An estimate in functional QCD leads to a predictability bound of $\mu_B/T \lesssim 4$, if the currently existing state of the art computations are combined, [51, 56, 100] and estimates for missing channels and effects are considered as well, [51, 64, 352]. In the present class of low energy effective theories (QM, NJL-type, PQM, PNJL), a respective estimate leads to $\mu_B/T \lesssim 2$.

We proceed to investigate the QM model at finite $N_f = 2$ and the large-$N_f$ limit with three and four degrees of freedom (DoF). Those DoFs correspond to the effective number of pions

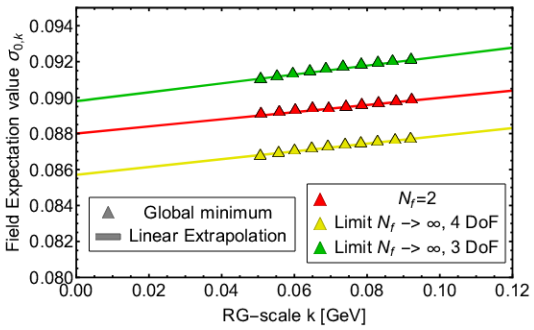


Figure 8.3.: Linear extrapolation of the expectation value $\sigma_0$. The corresponding fit parameters to (8.12) can be found in Table 8.2.

and allow to approximate if the sigma meson drops out of the flow (3 DoF) or behaves as a pion (4 DoFs). The large-$N_f$ limit serves as a benchmark for the more advanced approximations discussed in Section 8.3. Furthermore, the finite $N_f = 2$ computations also serve as benchmark for results in the literature within the QM- and Polyakov loop-enhanced QM models, in particular at large density, where DG-methods or similar numerical approaches are mandatory for reliable results.

We first discuss the asymptotic regimes: vacuum, large temperatures, and large chemical potential, Section 8.2.1. Then we show that the chiral phase transition, or rather its non-universal properties, agree quantitatively for all models, Section 8.2.2. In investigation of the crossover regime in the presence of an explicit symmetry breaking term is done in Section 8.2.3. The shock-development at large chemical potential is discussed in Section 8.2.4. Finally, we compare the phase structure for all three cases in Section 8.2.5.

### 8.2.1. Asymptotic regimes

We begin with an evaluation of the asymptotic regimes: the vacuum with $\mu_q, T = 0$, large temperatures with $\mu_q = 0$, and large chemical potentials with $T = 0$. For these cases we show the field-dependence of the pion mass $m_{\pi,k}(\rho) = \partial_\rho V_k(\rho)$. This resolves the effective potential, obtained from an integration over $\rho$, in terms of a physical observable.

The benchmark case is the vacuum, where the present models are anchored, see Section 8.1.2. The field-dependence of the pion mass is shown in Figure 8.2. For the initial cutoff $k = \Lambda$, the pion mass is simply a straight line, $m_{\pi,\Lambda}(\rho) = \lambda_\Lambda \rho/2$, where the slope is determined by the initial mesonic self-coupling, $\lambda_\Lambda$. With decreasing cutoff scale, the pion mass develops a flat regime, which is related to the emergence of non-trivial minima $\rho_0 = \sigma_0/2$ in the potential, indicating chiral symmetry breaking.

We also conclude, from the comparison of the pion masses in the different models, that the cutoff-dependence of the physical two-flavor case is best mimicked by the large-$N_f$ limit with four degrees of freedom: most of the dynamics takes place in the symmetric regime or close to it. Technically, this regime is described with $1 + m_\sigma^2(\rho_0)/k^2 \approx 1 + m_\pi^2(\rho_0)/k^2$, owing to the fact that the total mass of the respective modes is $k^2 + m_{\pi/\sigma}^2$.

Finally, we determine the relative values of the pion decay constants in the chiral limit, $f_{\pi,\chi} = \sigma_0$, in the different models. All scales are measured in the pion decay constant $f_\pi = 88$ MeV in the two-flavor case. The expectation value $\sigma_0$ or $\rho_0 = \sigma_0^2/2$ follows from (8.5a) as the maximal field value with $m_\pi(\rho_0) = 0$. However, since we stop the numerics at a small but finite cutoff

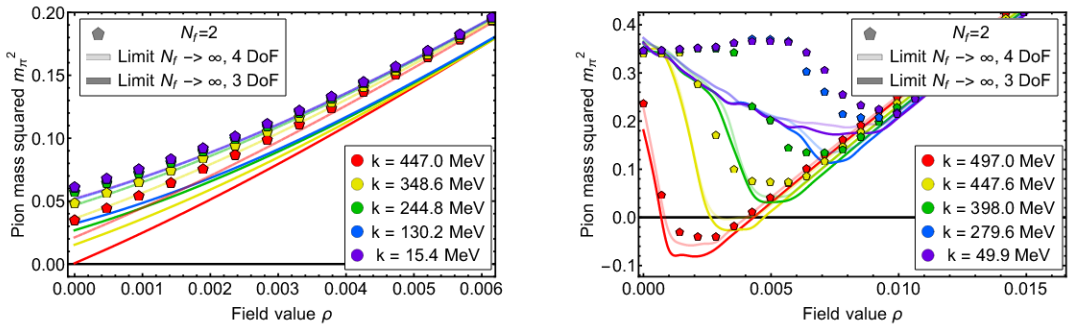


(a) Pion mass at zero density and high temperature ($T = 280$ MeV). The flow is washed out by the temperature fluctuations.

(b) Pion mass at zero temperature and high density ($\mu = 500$ MeV). The density onset introduces a sharp edge to the flow.

Figure 8.4.: RG-scale evolution of the field dependent pion mass $m_\pi^2$ in the symmetric phase. In this figure we compare results for the finite $N_f$ case and the large-$N_f$ limit with 3 and 4 degrees of freedom respectively. The Yukawa coupling is kept at a constant value.

value, $k_{\min} = 50\,\text{MeV}$, we extrapolate the expectation value $\sigma_0(k_{\min})$ to $\sigma_0(0)$ within a linear fit: we use data from 10 equally spaced RG-scales from $k = 90\,\text{MeV}$ to $k = 50\,\text{MeV}$, and fit

$$\sigma_{0,k} = \sigma_0 + \text{const}\, k\,. \tag{8.12}$$

The self-consistency of this linear fit is checked by the perfect agreement of the linear fit with the data, see Figure 8.3. The respective values for $\sigma_0$ are given in Table 8.2. The mass $m_\sigma$ of the scalar mode is extrapolated to $k = 0$ from the same data. Note however, that once the kink enters the cell in which $\sigma_0$ is located, the precise determination of the derivative is difficult. Therefore, the flattening of the potential most likely causes an underestimation of $m_\sigma$.

For large temperatures we safely stay in the symmetric regime and the mesons simply acquire a thermal Debye mass. This is seen in Figure 8.4a. In the symmetric regime we have four mesonic degrees of freedom in the two-flavor case. This is consistent with our expectations: the cutoff-dependence of the pion mass in the model with four degrees of freedom in the large-$N_f$ limit has the best agreement with the two-flavor case.

We close with a discussion of the large chemical potential asymptotics. The respective pion mass (squared) is depicted in Figure 8.4b. The sudden increase of the pion mass for $k \lesssim k_{\text{on}}$ with $k_{\text{on}} \approx \mu$ in Figure 8.4b is related to the Silver Blaze property, [353], for the discussion in

| | $\sigma_0$ [MeV] | const | $m_\sigma$ [Mev] |
|---|---|---|---|
| $N_f \to \infty$, 3 DoF | 89.8(17) | 0.0755(32) | 335(15) |
| $N_f \to \infty$, 4 DoF | 85.7(18) | 0.0752(35) | 311(10) |
| $N_f = 2$ | 88.0(20) | 0.0360(26) | 317(12) |

Table 8.2.: Expectation value $\sigma_0$ for the three models obtained by a fit of (8.12) to the zero point at 5 equally spaced RG-scales $k = 90$ MeV to $k = 50$ MeV. The error is computed from the grid resolution and the error to the fit parameters. The mass $m_\sigma$ is extrapolated from the same data points as the fit. The error of $m_\sigma$ is obtained analogously to the one of $\sigma_0$, it might be underestimated due to the kink developing at $\sigma_0$.

the fRG-approach see [46, 354, 355]. This property entails that correlation functions below the density onset are simply functions of $p_0 \mp i\mu_q$ for quark and anti-quark frequencies respectively. Accordingly, observables do not depend on the chemical potential for $\mu_q < \mu_{q,\mathrm{on}}$, where $\mu_{q,\mathrm{on}}$ is the onset chemical potential. For $\mu_q > \mu_{q,\mathrm{on}}$, the medium leads to deformations of the quark-meson scattering processes, comprised in medium meson-dispersions. In the presence of thermal fluctuations this onset is washed out with increasing temperature.

Note also, that the onset cutoff scale depends on the field value, as in the present approximation the onset chemical potential is given by $\mu_{q,\mathrm{on}}^2 = k^2 + m_q^2$.

In summary, the results in the asymptotic regimes show the expected physics phenomena. Moreover, the comparison of the large-$N_f$ models with the two-flavor case quantifies the similarities between the large-$N_f$ limit models and the physical two-flavor model.

### 8.2.2. Chiral phase transition at vanishing density

These similarities are furthered by a study of the chiral phase transition at vanishing density, $\mu_q = 0$. In particular we present a detailed comparison of the temperature-dependence of the chiral order parameter $\sigma_0$ in the $N_f = 2$-flavor case with the large-$N_f$ limits with 3 and 4 degrees of freedom. The numerical results for $\sigma_0(T)$ are displayed in Figure 8.5a and Figure 8.5b.

The order parameter $\sigma$ is obtained by a linear extrapolation as described in Equation (8.12). The data in proximity of the transition point are compatible with the scaling law,

$$\sigma(T) = \begin{cases} c_{\mathrm{cr}} |T - T_{\mathrm{crit}}|^{\beta}, & T \leq T_{\mathrm{crit}} \\ 0, & T \geq T_{\mathrm{crit}} \end{cases}, \tag{8.13}$$

where in the large-$N_f$ limit we have $\beta = 1/2$, the mean field critical exponent. In turn, for the present LPA-study of the Yuakwa model with the O(4)-universality class we have used the three-dimensional spatial flat or Litim regulator, [308], for both quarks and mesons. See also Appendix B.7.2, (B.113), (B.114). This leads us to $\beta \approx 0.40$, see [282] with [356, 357] and in particular the recent work in the QM model, [120]. Note, that more advanced approximations of the fRG provide $\beta \approx 0.39$ consistent with conformal bootstrap and Monte-Carlo results. For a recent compilation see [268], for the QM model see [120] that also includes an investigation of the $Z_2$-universality class.

The respective scaling regimes are already very small in the $O(4)$-model and even shrink in the presence of the (driving) fermion loop, see the discussion in [120]. While possible, we do not aim at a precision estimate of critical exponents here, as we focus on the location of the phase boundaries. Accordingly, we have simply checked the consistency of the scaling law (8.13) with $\beta \approx 0.4$ ($N_f = 2$) and $\beta = 1/2$ ($N_f \to \infty$) for small reduced temperatures $1 - T/T_c \to 0_+$. This also allows us to determine the respective scaling regimes. Consistent with the observation above that they should be even smaller as the already small scaling regime in $O(N)$-models we find scaling for

$$0 < 1 - T/T_c \lesssim 2\ 10^{-1}\,. \tag{8.14}$$

Moreover, a scaling fit with (8.13) in the regime (8.14) allows us to determine $T_c$ as well as the prefactor $c_{\mathrm{cr}}$.

We see from Table 8.3, that the two-flavor critical temperature agrees well with the large-$N_f$ limit with four degrees of freedom. This is expected from the theoretical analysis and our results on the asymptotics in Section 8.2.1. This good agreement extends to the full temperature

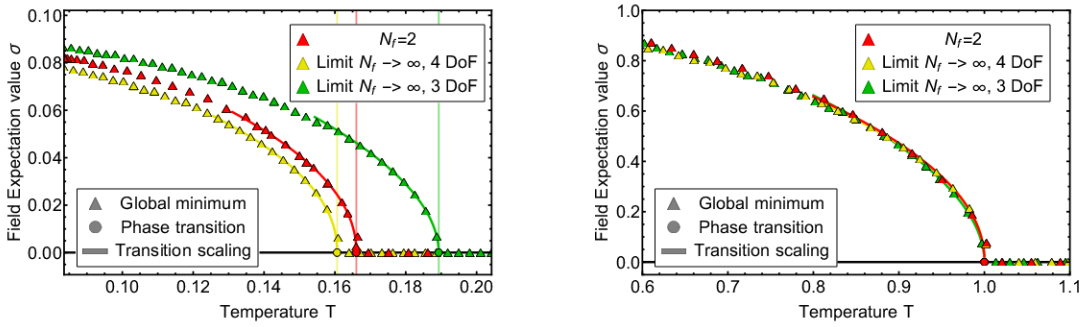


(a) Absolute values of the field expectation value $\sigma$. Units are given in GeV.

(b) Axes rescaled by the respective expectation values and critical temperatures.

Figure 8.5.: Temperature dependence of the mesonic field expectation value $\sigma_0$. The figure shows a second order phase transition at fixed chemical potential $\mu = 0$ GeV. We compare the case for finite $N_f$ and the large-N limit with 3 and 4 degrees of freedom with a constant Yukawa coupling. Fitting (8.13) to the data gives values for the critical temperatures and exponents of the transition, with the parameters given in Table 8.3. Deviations to the fit values are due to the low resolution in the extrapolation of the zero point on the numerical grid.

dependence, as can be seen from Figure 8.5a. In turn, the order parameter from the large-$N_f$ limit with three degrees of freedom seemingly shows a slightly different behaviour.

However, the two large-$N_f$ models are obtained by a simple rescaling of the fields and hence are identical to each other. They can be mapped onto each other by the relative rescaling. Put differently, the temperature dependence of the order parameters should agree if plotted in dimensionless units, $\sigma(T)/\sigma(0)$ and $T/T_c$. This comparison is shown in Figure 8.5b: as expected, the temperature-dependence of the order parameter of the large-$N_f$ models agree. More importantly, also the two-flavor case agrees quantitatively, though with small deviations. Trivially, the non-trivial critical scaling of the two-flavor case does not agree with the trivial mean-field scaling for $N_f \to \infty$, but the scaling regimes are very small, see (8.14).

In summary, the thermal properties of the models in the large-$N_f$ limit and the physics case $N_f = 2$ agree very impressively.

### 8.2.3. A crossover transition

The presence of finite quark masses in the UV-action explicitly breaks chiral symmetry. This manifests in the presence of a linear term $-c_\sigma\sigma$ in the effective action, and has been discussed

| Model | $c_{\mathrm{cr}}$ | $T_{\mathrm{crit}}$ |
|---|---|---|
| $N_f \to \infty$: 3 DoF | 0.2985(24) | 0.18929(11) |
| $N_f \to \infty$: 4 DoF | 0.3010(33) | 0.16139(10) |
| Finite $N_f$ | 0.2126(61) | 0.16618(19) |

Table 8.3.: Parameters obtained from a $\chi^2$-fit of (8.13) to the mean field expectation values in Figure 8.5a which are underlined by the transition scaling. The error in the data is expected to be higher, since the numerical precision is limited by the grid resolution.

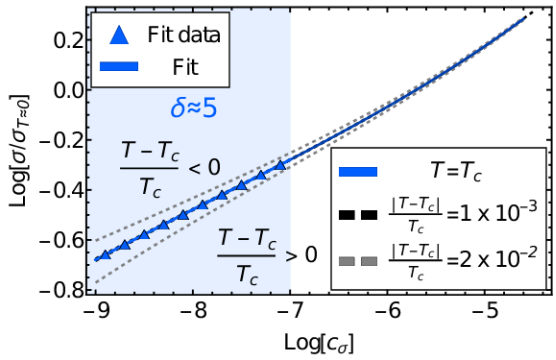


Figure 8.6.: Solution to the equations of motion $\sigma$ (8.15) as a function of the explicit chiral symmetry breaking parameter $c_\sigma$. The scaling function (8.16) is fit in the highlighted area (blue background). We indicate curves for different temperatures around $T_c$ in the chiral limit. The indicated dashed lines visualise the small scaling regime, which was already pointed out in (8.14). $\sigma$ is given in terms of its value in the chiral limit in the vacuum $\sigma_{T\approx 0} = 88\,\text{MeV}$, $c_\sigma$ is given in units of the cutoff.

in Section 2.3.2. This term does not factor into the RG-flow (8.3), since the latter only depends on the two-point functions. It comes into play at a later stage when evaluating the physical equations of motion (EoM), which lie at the minimum of the effective potential $V(\rho)$. In the current approximation scheme of the effective action, the equations of motion, away from the chiral limit, are given by

$$\sigma \partial_\rho V(\rho)|_{\sigma=\sigma_0} = c_\sigma \,. \tag{8.15}$$

with $c_\sigma \neq 0$. As a direct consequence of (8.15), we obtain finite pion masses $m_\pi \neq 0$.

In the presence of an explicit symmetry breaking term, we can fit another scaling law to the finite $N_f$ data, where we evaluate the EoMs on the critical temperature $T_c$

$$\sigma_0(c_\sigma)|_{T=T_c} \propto c_\sigma^{1/\delta} \,. \qquad \log\left(\frac{\sigma_0(c_\sigma)}{\sigma_{T\approx 0}}\right)\Big|_{T=T_c} = A + 1/\delta \, \log(c_\sigma/\Lambda^3) \,. \tag{8.16}$$

with $\sigma_{T\approx 0} = 0.088\,\text{GeV}$ and the fit coefficients

$$A = 1.112(10)\,, \qquad \delta = 5.029(50)\,, \tag{8.17}$$

where we obtain an error estimate by fitting for $T_c \pm \Delta T_c$, which is indicated in Table 8.3. The fit parameters agree well with the $O(4)$-model in LPA, i.e. $\delta \approx 5$, see [358]. We show the fit in Figure 8.6. The figure also shows deviations from the scaling relation for $T \neq T_c$. This highlights the very small scaling regime already discussed in (8.14).

### 8.2.4. Phase transitions at high densities

In this section we discuss shock development and propagation at intermediate densities and very low temperatures. This is also used to discuss the first order regime.

We first note, that the running of the pion mass stops quickly below the onset RG-time $t_{\text{on}} = \ln \frac{\Lambda}{\mu}$: the RG-flow is proportional to the Fermi-distribution. Hence it stops at $k_{\text{on}}$ at $T = 0$, for finite $T$ the Fermi-distribution is softer but for small temperatures there is still a strong exponential suppression for $k \leq k_{\text{on}}$. This suppression leads to two competing effects at finite densities:

- At high densities the suppression of the quark-contribution creates positive meson masses $m^2_{\pi,k}(\rho)$ and determines the value of $m^2_\pi(\rho_0)$ in the symmetric phase (compare to Figure 8.4b). The quark contribution dominates initially, but due to the constant Yukawa coupling it is quickly suppressed with $k^5$, decreasing the effect of the suppression at lower densities.

- For field values with positive meson masses $m^2_{\pi,k}(\rho)$ the meson loop in the flow is suppressed with $k^5$. In turn, for negative meson masses the meson loop is suppressed with $k^4$. Additionally the flow increases with decreasing values of $m^2_{\pi,k}$, which is closely linked to the restoration of convexity. The mesonic flow contribution is reminiscent of the spreading of waves in hydrodynamics, where its value corresponds to the wave velocity: if we consider the solution $m^2_\pi(\rho)$ as a wave packet, it flows with the RG-time in the direction of smaller field values with a $\rho$-dependent propagation velocity.

The interplay of both effects leads to the creation of shocks and a first order phase transition at low temperatures. The increased propagation speed of negative modes is blocked by the slowed propagation of positive modes. The shock travels towards smaller field values during the RG-time evolution, but eventually freezes when the shock amplitude is too high. An illustration of this process can be found in Appendix C.2.

Naturally, the occurrence of shock development depends on the choice of initial conditions, specifically those that trigger stronger dynamics of the system, for a respective discussion in the $O(1)$-model see [65]. With physical initial conditions we find shock development in the large-$N_f$ limit with 3 DoF, whereas the dynamics for 4 DoFs are not strong enough to generate a shock at finite temperature $T > 10$ MeV. This is an important observation: we have used the same initial conditions for all models, fixed within the two-flavor case. As discussed before, the two models in the large-$N_f$ limit only differ by a rescaling of the fields and parameters. Accordingly, they can be interpreted as the same model with different initial conditions, as we do not apply any rescaling to the initial condition. However, these changes are marginal, as can be seen from the small variation of the pion decay constants and $\sigma$-masses in the vacuum, see Table 8.2. In conclusion the physical case is very close to the situation where shocks may form during the RG-time evolution. Whether or not this also occurs in QCD requires further investigation:

(i) The embedding of the present model as part of the matter sector will lead to additional driving forces in the flow. This may be mimicked with a $T, \mu$-dependent change of the initial conditions here. naturally these changes can go either way, they may support the shock development or soften it.

(ii) The additional diffusion terms in the finite-$N_f$ case structurally soften the RG-time evolution and remove any shock development from the pion mass $m^2_\pi = \partial_\rho V$. However, an O(N) model study shows that shock development may be transported to higher derivatives Appendix C.2. Then, the shock appears in the mass of the sigma meson $m^2_\sigma = \partial_\rho V + 2\rho\partial^2_\rho V$.

The resolution of these aspects is crucial for an access to the QCD phase boundary at large chemical potential and low temperatures. Especially the observation that shock development is strongly connected to initial conditions, recall the 3 DoF and 4DoF large-$N_f$ comparison, hints at the importance of (i).

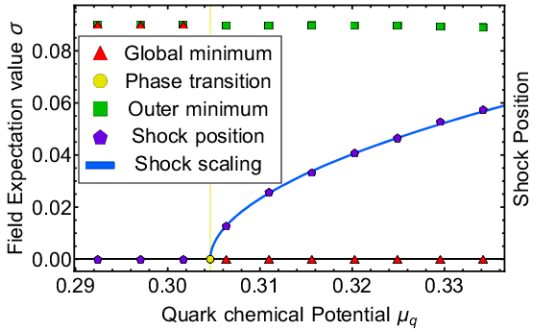


Figure 8.7.: Density dependence of the mesonic field expectation value $\sigma_0$ at $T \approx 0$ for the large-$N_f$ model with 3 DoFs in LPA (constant Yukawa coupling). The figure shows a first order phase transition of the field expectation value at zero temperature. The solution now contains a local outer minimum and shock development between the outer local and inner global minimum. The extrapolated shock position at $k = 0$ GeV is plotted at different densities. We find that the shock position, in the vicinity of the first order transition, obeys the scaling law in (8.18). The parameters of a scaling fit, see (8.18), are given in Table 8.4.

In the following, we analyse shock development in the 3 DoF large-$N_f$ case and its connection to the first order transition. We then proceed to investigate the high density phase transition at finite $N_f$. Here we find that the initial conditions are not strong enough to generate shocks.

### Shock development as a mechanism for first order phase transitions

In the large-$N_f$ limit with 3 DoFs we can use the shock development at low temperatures for an accurate determination of the phase transition line. The shock position $\xi_{\text{final}}$ at $k = 0$ is extrapolated by fit, utilizing the exponential decay of the flows,

$$\xi(t) = \xi_{\text{final}} + \text{const}\, e^{-t}\,.$$

We use the shock position at 6 equally spaced time steps between RG-times $t = 3$ and $t = 3.5$. We expect the same power law behaviour as in [65] for the final shock position as a function of chemical potential,

$$\xi_{\text{final}} = \begin{cases} \beta\,|\mu - \mu_{\text{crit}}|^{\zeta}, & \mu \geq \mu_{\text{crit}} \\ 0, & \mu \leq \mu_{\text{crit}} \end{cases}\,. \tag{8.18}$$

As an explicit example we concentrate on $T = 10$ MeV. The coefficients of the $\chi^2$-fit are provided in Table 8.4. Next to the first order phase transition at small temperatures the position of the shock as function of the control parameter, the chemical potential, is well approximated by the function in (8.18). This scaling form is the same used to describe the order parameter

| Parameter | Prefactor $\beta$ | Crit. exponent $\zeta$ | Crit. density $\mu_{\text{crit}}$ |
|---|---|---|---|
| $\chi^2$-Fit | 0.391(45) | 0.524(31) | 0.30460(33) |

Table 8.4.: Parameters obtained from a $\chi^2$-fit of (8.18) to the shock positions in Figure C.6.

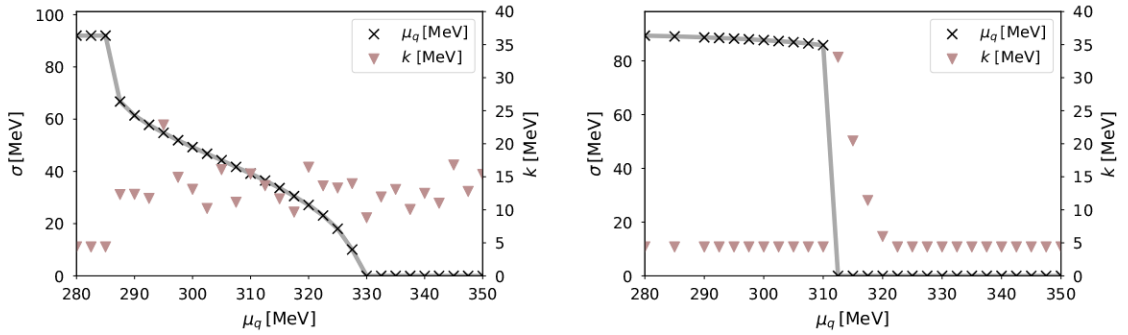


(a) T = 2 MeV (b) T = 30 MeV

Figure 8.8.: Density dependence of the mesonic field expectation value $\sigma_0$ at low temperatures at finite-$N_f$ in LPA (constant Yukawa coupling). The figures show a phase transition of the field expectation value: At $T = 30\,\text{MeV}$ we can see a first order phase transition. Lowering the temperatures further yields a combination of both, a jump indicating a first order transition and a subsequent second order transition. The convergence of our results by indicating the final RG-scale $k$ of each point.

next to a second order phase transition. In this sense the shock position behaves like an order parameter of a second order phase transition when the system experiences a first order phase transition. From the scaling form of the shock position (8.18) we obtain an accurate estimate for the critical chemical potential of $\mu_{\text{crit}} = 0.30460 \pm 0.00033\,\text{GeV}$. The phase transition and shock positions are depicted in Figure 8.7. Shock formation occurs only in a relatively small area of the $(T, \mu)$ plane, being confined to intermediate densities 290 MeV $<$ 360 MeV and small temperatures up to $T = 20\,\text{MeV}$.

### Phase transition at finite $N_f$

*This section and its figures are taken from [10].*

In the finite-$N_f$ case we do not find shock development using the present initial conditions. The presence of the sigma-loop in the flow introduces a diffusion term to the flow of the pion mass $m_\pi^2 = \partial_\rho V$, recall Section 5.1.2. Hence shocks in the first derivative $\partial_\rho V$ are smoothed out by the diffusion. Curiously, they can now appear in the second derivative $\partial_\rho^2 V$, as was found in an O(N) model computation Appendix C.2.

In the current setting, however, the interplay between the positive and negative modes (or meson masses) is not strong enough to create a shock, even in the second derivative. Instead we find a simple first order transition without shock development at temperatures below the critical point. This transition is plotted for $T = 30\,\text{MeV}$ in Figure 8.8b. We find a first order phase transition followed by a second order transition at very low temperatures $T = 2\,\text{MeV}$, see Figure 8.8a. This curious behaviour has already been found in similar studies of the quark-meson model [151, 347].

In the absence of a shock a very fine grid has to be used to pin down the phase transition line for low temperatures. In the present work we have simply narrowed down the location of the phase transition to a small interval. We refrain from an in-depth analysis, since the present expansion scheme and regulator used are not adjusted to physics in the high density regime: In this area, momentum dependent quantum fluctuations become relevant and the current LPA

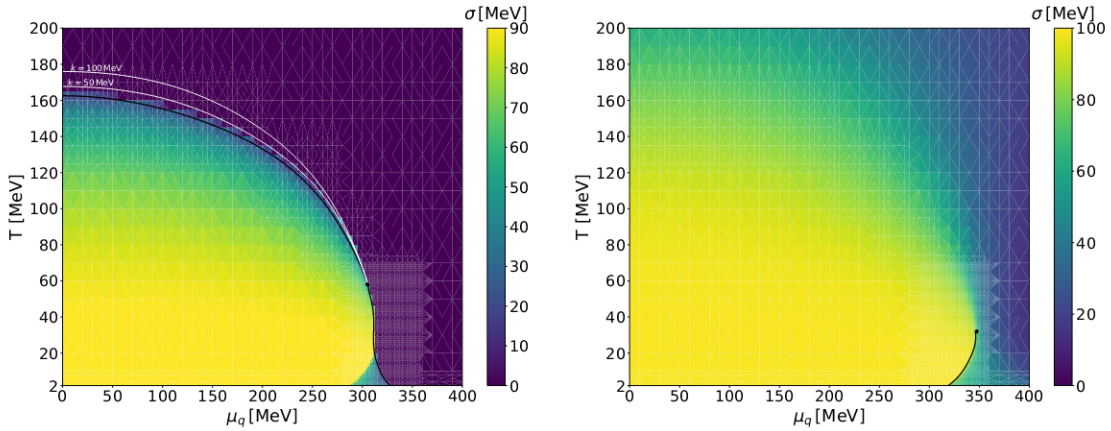


(a) $c_\sigma = 0$, CEP at $(T,\mu) = (58, 305)\,\mathrm{MeV}$. (b) $c_\sigma = 1.89{\cdot}10^{-3}\,\mathrm{GeV}^3$, CEP at $(T,\mu) = (32, 347.5)\,\mathrm{MeV}$.

Figure 8.9.: The phase diagram of the QM model in the chiral limit (a) and with explicit chiral symmetry breaking $c_\sigma = 1.89{\cdot}10^{-3}\,\mathrm{GeV}^3$ (b). We show the condensate expectation value $\sigma$ in MeV.The critical endpoints are indicated by small black dots. The extrapolated phase transition line as $k \to 0$ is also indicated in black.

setting is not a good approximation any more. Additionally, the sharp onset of density effects, c.f. Figure 8.4b, suggests the use of smooth regulator functions. Lastly, we recall that the QM model alone is not an accurate description of the matter sector of QCD at high densities.

### 8.2.5. Phase diagrams

*This section and its figures are taken from [10].*

Finally, we display phase diagrams at finite temperature $T$ and quark density $\mu_q$ in Figure 8.9. We show results both in the chiral limit and for physical pion masses $m_\pi = 138.1\,\mathrm{MeV}$. The latter results is obtained by setting the explicit symmetry break term $c_\sigma = 1.89 \cdot 10^{-3}\,\mathrm{GeV}^3$.

The chiral limit ($c_\sigma = 0$) shows a second order phase transition until the critical endpoint is reached. This is followed by a short first order regime at high densities around $T = 30\,\mathrm{MeV}$ and we see the splitting into a first and second order transition at very low temperatures, which was already commented on in Figure 8.8a.

Away from the chiral limit ($c_\sigma \neq 0$) the phase transition is softened and we recover a crossover regime at high temperatures, which is similar to the high temperature transition in QCD. As we go to higher densities we can identify a critical endpoint, but the jump in the order parameter is much smaller.

The respective critical endpoints are indicated in the figure and are located at

$$\begin{aligned} \mathrm{CEP}_{c_\sigma=0}: &\quad (T,\mu) = (58, 305)\,\mathrm{MeV}, \\ \mathrm{CEP}_{c_\sigma\neq0}: &\quad (T,\mu) = (32, 347.5)\,\mathrm{MeV}. \end{aligned} \tag{8.19}$$

Again, we note that the location of the CEP in QCD is expected to be heavily influenced by other resonances in the matter sector.

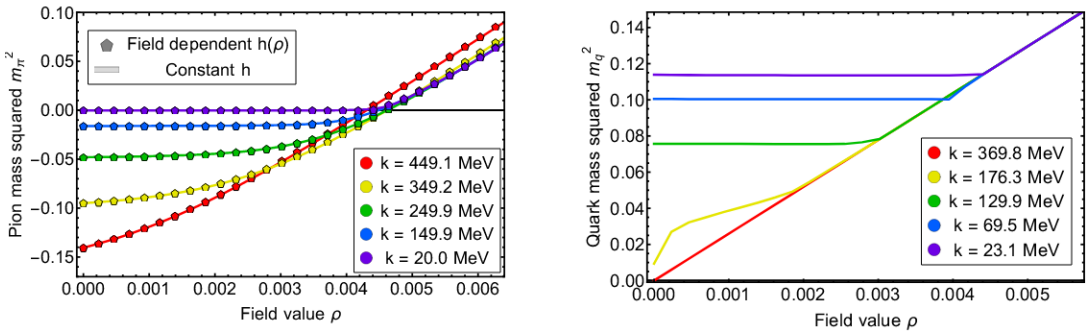


(a) Comparision of the RG-running of the pion mass with constant and field dependent Yukawa coupling.

(b) Field-dependence of the quark mass. A flat regime emerges for $k \to 0$, related to that in the effective potenial.

Figure 8.10.: RG-scale evolution of the field-dependent quark and pion masses in approximate vacuum in the large-$N_f$ limit with 4 DoF.

## 8.3. Higher quark-meson scattering orders

The discussion of the results in LPA with a constant Yukawa coupling have revealed a very intricate structure at about onset chemical potentials and low temperatures. In particular the occurrence of shocks is very sensitive to the details of the dynamics. Moreover, we expect quark-meson scatterings to be important in the vicinity of a potential critical end point in QCD.

We now present our results for the QM model with a field-dependent Yukawa coupling in the large-$N_f$ limit with four DoFs, based on the combined numerical solution of the flows in Appendix B.6.1.

### 8.3.1. Dynamics in the vacuum

Figure 8.10 depicts the solutions of the pion and quark masses in approximate vacuum, the pion mass in comparison to the case with constant Yukawa coupling. We can see that in approximate vacuum the pion mass remains unchanged for both models. An exponential fit is performed on the position of the zero point of $\partial_\rho V_k(\rho)$ using 5 equidistant RG-scales from $k = 65$ MeV to $k = 25$ MeV and we obtain

$$\sigma_{0,\pi} = 87.4(17)\,\mathrm{MeV}\,. \tag{8.20}$$

This is consistent with the results in the previous sections with a constant Yukawa coupling (LPA). Consequently, this confirms previous findings in [58], that LPA or rather higher orders in the derivative expansion are a good approximation for vacuum QCD.

Figure 8.10b depicts the field-dependent quark mass $m^2_{q,k}(\rho)$ for different RG-times. As argued in [58], the quark mass flattens for meson fields $\rho \leq \rho_0$. The computation in the present work puts these conceptual and preliminary numerical findings on a sound numerical footing. In summary, at vanishing cutoff scale $k = 0$, this leaves us with a field-dependent quark mass $m^2_q(\rho)$ with

$$m^2_q(\rho) \geq m^2_q(\rho_0)\,. \tag{8.21}$$

Note that while conceptually the field value $\rho_{0,q}$, below which the mass function flattens, has to agree with $\rho_0$, the solution of the EoM, numerically this is not fully guaranteed. Hence,

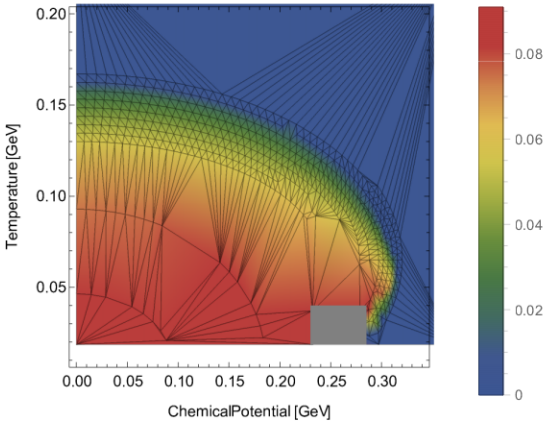


Figure 8.11.: Phase diagram for the quark-meson model in the large-N limit with four DoFs with field dependent Yukawa coupling. The gray box indicates the points that did not converge. The mesh indicates the discrete data points.

this provides a further consistency check of the present scheme. For performing the respective reliability check, we have determined the position of the kink by subtracting $-\rho$ from the solution and taking the minimum. An exponential fit gives,

$$\sigma_{0,q} = 86.0(17)\,\mathrm{MeV}\,, \tag{8.22}$$

which coincides within its error $\sigma_0$ in (8.20). The error is computed from the grid resolution and the error to the fit parameters.

The quark mass in the flattened area in Figure 8.10b is computed as follows: one computes the average value of the quark mass up to the kink for the previously mentioned 5 RG-scales and performs an exponential fit. This leads to the physical quark mass,

$$m_q(\rho_0) = 309.635(85)\ \mathrm{MeV}\,. \tag{8.23}$$

The linear $\rho$-dependence of $m_q^2(\rho)$ in Figure 8.10b for $\rho > \rho_0$ entails, that the Yukawa coupling is constant with $\partial_\rho h(\rho) \approx 0$, already observed in [58] for finite $N_f$. The constant approximation for these field values works so well, that we can use the input Yukawa coupling $h_\Lambda$ to confirm $\sigma_0$ with the consistency relation $\sigma_0 = m_q(\sigma_0)/h_\Lambda$. This leads us to $\sigma_{0,q'} = 86.01(24)\,\mathrm{MeV}$, where we take the error from the fit and the mean deviation in the flattened region.

In summary the present numerical analysis quantitatively confirms the conceptual and preliminary numerical analysis in [58]: In the broken phase, the flattening-out of the field-dependent quark-mass $m_q^2(\rho)$ is triggered by the flattening of the effective potential. In turn, in the symmetric phase the field dependent quark mass does not flatten-out and the quark mass vanishes on the solution of the equation of motion, $\rho_0 = 0$. Importantly, apart from the flattening of the quark mass, they do not deviate significantly from the results in LPA. In particular this applies to their values on the equations of motion. Note however, that this is bound to change for finite $N_f$.

### 8.3.2. Phase structure

As in LPA with a constant Yukawa coupling, we finally present our results on the phase diagram of the QM model in the large-$N_f$ limit including quark-meson scatterings via a field-dependent

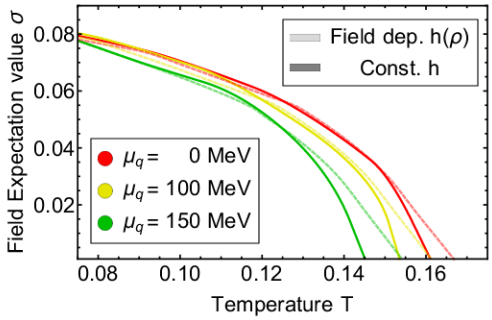


Figure 8.12.: Chiral order parameter $\sigma_0(T)$ in the large-$N_f$ limit with four DoFs as a function of temperature and quark chemical potential. We compare the LPA results with quark-meson scatterings encoded in $m_q(\sigma)$ for different densities. The data is interpolated from the phase diagrams.

quark mass or Yukawa coupling, see Figure 8.11. The computations did not complete the time integration for $\mu \geq 0.3$ GeV, respective numerical upgrades are currently investigated.

As already discussed in the last section, Section 8.3.1, in the phase with chiral symmetry breaking the field-dependent quark-mass $m_q^2$ is necessarily flattened for $\rho \leq \rho_0$. In turn, The quark mass function does not flatten in the symmetric phase, and the quark mass is found to be zero in the symmetric phase. The field dependence of the quark mass $m_q^2$ and pion mass $m_\pi^2$ for high values of temperature and density do not significantly deviate from the results with a constant Yukawa coupling.

We close this section with a comparison of the phase structure in Figure 8.11 with that of a constant Yukawa coupling, in the same setting: large-$N_f$ limit with four DoFs. While the phase boundaries do not change significantly, the crossover gets softened, if quark-meson scatterings are taken into account. This is clearly visible in Figure 8.12, where we depict the chiral order parameter as a function of temperature for different densities with $\mu_q = 0, 100, 150$ MeV. This entails, that the quark-meson scatterings considered here give sizeable contributions to important observables measured in heavy ion collisions. First of all, fluctuation observables will be sensitive to such a widening of the crossover. These effects may be even more prominent at large chemical potential where the freeze-out line most probably deviates from the chiral crossover line. Moreover, it can also be deduced from Figure 8.12, that the quark-meson scatterings may have a sizeable delaying effect on a possible critical end point. We conclude, that these scatterings have to be taken into account for a quantitative prediction for the location of the CEP.

## 8.4. Conclusions

We have presented a study of the QM model with an emphasis on quantitative access to order parameter potentials at finite temperature and chemical potential using Discontinuous Galerkin methods. We discussed the location of phase transition lines and recovered scaling exponents of the O(4) universality class.

We have used the large-$N_f$ limit with an infinite number of flavors as an important benchmark. We argued that within an 't Hooft-type limit we can mimic the two-flavor QM model well (or any other flavor), and in particular reproduce its non-universal properties such as the location

of the phase boundary.

In this limit we found shock-development and propagation in the order parameter potential in the vicinity of the first order regime at high chemical potential. Since the QM model is an important ingredient to a functional description of QCD matter even low densities, we cannot exclude the occurrence of shocks in QCD. Hence it is essential to use numerical methods which are adapted to shock development in a quantitative study of the QCD phase structure, see Chapter 9.

Furthermore, we investigated the importance of higher orders of quark mesonic scatterings. We found that they give already sizeable contributions in the vicinity of the second order regime and cannot be neglected in the computation of observables.

However, already for smaller ratios $\mu_q/T$ close to the crossover line we have to also improve the current approximation of the matter sector of QCD. This follows already from [51, 64]. The results there indicate the potential relevance of non-trivial meson dispersions as well as the diquark channel at larger chemical potentials, $\mu_q/T \gtrsim 4/3$. Moreover, in the vicinity of a potential critical end point we also have to take into account the density channel, that mixed with the critical $\sigma$-mode. This is work in progress and we hope to report on it in the near future.

# CHAPTER 9

## Towards quantitative precision in QCD

*This chapter is taken from [9]. It is a first application of the technical developments and insights of Chapter 5 and Chapter 8 to a full computation in QCD.*

In the past two decades, functional QCD has been established as a versatile approach for the description of QCD. Its particular strength is its universal applicability to all research areas of QCD, ranging from first principle studies of the hadron spectrum over scattering processes and decays to the phase structure of QCD at finite temperature and density as well as its non-equilibrium dynamics. This universal applicability is rooted in its diagrammatic, modular structure. As an analytic method, it does not suffer from the sign problems on the lattice, which are present for the description of QCD at finite density, as well as real-time processes. This advantage is paid for with an intricate systematic error control present in all diagrammatic approaches for strongly correlated systems. The most successful and most used systematic expansion scheme to date is a combination of the vertex expansion and the derivative expansion, recall Section 3.2.2. In the vertex expansion, QCD scattering processes are expanded in the number of single scatterings, including the full momentum dependent distribution functions of the respective scattering process. In the derivative expansion part, all scattering orders are taken into account, but their momentum distribution is expanded in powers of momenta. In the fRG approach this scheme is sustained by the fact, that the theory is solved by integrating out scattering events momentum-shell by momentum-shell, and momenta can be measured in the respective infrared cutoff $k$, the expansion being one in $p^2/k^2$.

Both expansion schemes come with their own systematics, which has been tested in a plethora of different models with intricate dynamics, covering that present in QCD. Moreover, the combination allows for an almost full scan of the convergence properties.

In the present work we make progress towards the completion of the derivative expansion part of this combined scheme. Analogously to Chapter 8, we take the full meson field-dependence of all considered vertices into account using Discontinuous Galerkin methods (DG methods). In contrast, the momentum dependence is limited to that required for semi-quantitative accuracy. This was tested and proven in a comparison of functional QCD with full momentum dependences, [44, 47, 48], and functional QCD with an emphasis on meson field dependences [42, 43, 45, 51, 59, 102, 117].

In this first implementation within the Discontinuous Galerkin framework, recall Chapter 5, we implement the vertices analogously to the local density approximation of the wave function, i.e. we neglect the respective mesonic field derivatives. This approximation will be lifted in a subsequent work. In the following we use this local density approximation to obtain an estimate on the importance of higher (quark-meson) scattering orders in a full QCD setting. This is benchmarked with a computation which only considers simple scatterings, i.e. uses constant couplings, to emphasise quantitative changes.

In Section 9.1 we introduce the derivative expansion part of this combined scheme and discuss the relevant approximations and quantities. The model and derivations of the flows are based on [51]. Hence, we refrain from giving a detailed derivation and briefly introduce the relevant definitions and quantities. We proceed to discuss the novelties of our field dependent implementation with DG methods in Section 9.2 and present results taking higher quark-mesonic scattering orders into account. This is benchmarked with a computation at constant couplings. Finally we close in Section 9.3 with a brief summary and a discussion of the next steps towards a full quantitative description of the QCD phase structure.

## 9.1. A functional description of QCD

The classical action of QCD was introduced in (2.20), in terms of the gluon field $A$, the ghost fields $\bar{c}, c$ and 6 species of quarks $\bar{q}, q$ with $N_c = 3$ color charges. This was followed by a discussion in Section 2.3.2, where we found that the gluonic dynamics decouple at low energies and the emergence of composite particles, created by resonances of the four-quark interaction, become the relevant dynamic degrees of freedom.

We identified the scalar-pseudoscalar four-quark scattering, (2.34), as the dominating process. Its resonance corresponds to the creation of mesons, and consequently the breaking of the (approximate) chiral symmetry of the two light quark flavors. This scattering was found to be the dominant and decisive process for chiral symmetry breaking throughout the majority of temperatures $T$ and baryonic chemical potential $\mu_B = 3\mu_q$ until approximately $\mu_B/T \lesssim 6$. Hence, for a quantitative investigation of the chiral phase structure within this region, we need to combine the low energy dynamics of the lightest quark flavors, which we previously studied in Chapter 8, with the gluonic interactions. In the present setting we consider the superfield $\Phi$ consisting of

$$\Phi = \left(\Phi_f, \phi\right), \quad \Phi_f = (A, c, \bar{c}, q, \bar{q}), \quad \phi = (\sigma, \pi), \tag{9.1}$$

where the $\Phi_f$ contains the fundamental fields and $\phi$ is the scalar-pseudoscalar mesonic field. Its introduction is done by dynamical hadronisation and follows along the lines of (2.35). The current approximation considers the $N_f = 2$ flavor case, which describes (approximate) chiral symmetry breaking for the two lightest quark flavors. As a next step towards quantitative precision, future work will consider a $N_f = 2+1$ study, where chiral symmetry is investigated for the light quarks $u$ and $d$ (i.e. a $SU(2)$ flavor symmetry) and the heavier strange quark is only considered in the flow, but not for the symmetry investigations and formation of condensates. Since the gluons decouple from the low energy dynamics, we can make use of quantitative vacuum QCD results for the gluon and ghost propagators [44], which are used as an input to set the stage for the dynamics in the low energy regime.

Finally, the Euclidean scale dependent effective action of QCD is approximated by

$$\begin{aligned}\Gamma_k = \int_x \Big\{ &\frac{1}{4} F^a_{\mu\nu} F^a_{\mu\nu} + \frac{1}{2\zeta} \left(\partial_\mu A^a_\mu\right)^2 + \frac{1}{2} \int_p A^a_\mu(-p) \left(\Gamma^{(2)ab}_{AA\mu\nu}(p) - Z_A \Pi^\perp_{\mu\nu} \delta^{ab} p^2\right) A^b_\nu(p) \\ &+ Z_c \left(\partial_\mu \bar{c}^a\right) D^{ab}_\mu c^b + \bar{q} Z_q \left(\gamma_\mu D_\mu - \gamma_0 \hat{\mu}_q\right) q - \lambda_q(\rho) \left[\left(\bar{q}\tau^0 q\right)^2 + \left(\bar{q}\boldsymbol{\tau} q\right)^2\right] \\ &+ h(\rho) \bar{q} \left(\tau^0 \sigma + \boldsymbol{\tau}\cdot\boldsymbol{\pi}\right) q + \frac{1}{2} Z_\phi \left(\partial_\mu \phi\right)^2 + V(\rho) - c_\sigma \sigma \Big\} . \end{aligned} \tag{9.2}$$

With the integration $\int_x = \int_0^{1/T} dx_0 \int d^3x$, where $T$ is the temperature and $\hat{\mu}_q$ the finite (quark) density, see also Appendix B.1. The ghost and gluon dynamics are computed in Landau gauge. They correspond to the first four terms on the left-hand side in (9.2) and contain the field strength $F_{\mu\nu}$, a gauge fixing term, the ghost and gluon two-point functions and the respective dressing functions $Z_c$ and $Z_A$. They are purely input in the present work and are part of the vertex expansion part of the combined scheme. Their adaption to the current setting follows along the lines of [45]. This setting was further verified in [51], which already provided results for vacuum masses in agreement with [44].

The last five terms in (9.2) introduce the mesons to the effective action. In the two flavor case we have $\tau = 1/2(\mathbb{1}, i\gamma_5\boldsymbol{\sigma})$. $c_\sigma \neq 0$ is an explicit chiral symmetry breaking term and corresponds to a finite current quark mass and physical pion masses, recall Section 2.3.2. The derivative expansion translates to a field dependence of the effective mesonic potential $V$ and the couplings on the mesonic fields. It is given in terms of the chiral invariant $\rho = \frac{(\sigma+\boldsymbol{\pi})^2}{2}$, following the argumentation in Section 2.3.2. We distinguish between the massive-mode, the $\sigma$-meson and the pseudo-Goldstone bosons, the pions $\boldsymbol{\pi}$. In the current approximation, all couplings to the quarks, i.e. the Yukawa coupling $h(\rho)$, the four-quark coupling $\lambda_q(\rho)$ and the quark-gluon coupling $g_{\bar{q}Aq}(\rho)$ have this field dependency within a local density approximation, which neglects higher scattering orders of the mesons in the diagrams. This is commented on in the following. Lastly, we consider the wave function renormalisations of quarks and mesons $Z_q$ and $Z_\phi$, which are evaluated at a constant mesonic field $\rho_0$ and are outfitted with an appropriate momentum dependency specified below (9.12) and (9.13) respectively. In this approximation we assume $\partial_\rho Z_\phi(\rho) = 0$ and hence $Z_\pi = Z_\sigma = Z_\phi$. The higher derivatives of the wave function renormalisation account for momentum dependent mesonic-self scatterings. We drop them in this calculation, since these momentum dependent scatterings are heavily suppressed at low energy scales and at high energies the mesonic dynamics do not factor in at all.

In the following we comment on the derivation flows in the matter sector and the implications of the gluonic input within this truncation of the effective action.

### 9.1.1. Quarks, mesons and dynamical hadronisation

For the derivation of RG-flows in the matter sector, we make use of the generalised flow equation (3.33). For completeness we state the generalised flow in terms of the super-field $\Phi$ and the RG-transformation $\dot{\phi}$ of the emergent mesonic field $\phi$,

$$\partial_t \Gamma_k[\Phi] + \int \dot{\phi} \left( \frac{\delta \Gamma_k[\Phi]}{\delta \phi_i} + c_\sigma \delta_{i\sigma} \right) = \frac{1}{2} \mathrm{Tr}\left[ G_k[\Phi] \partial_t R_k \right] + \mathrm{Tr}\left[ G_{\phi\Phi_j}[\Phi] \frac{\delta \dot{\phi}}{\delta \Phi_j} R_\phi \right] , \tag{9.3}$$

where $t = \ln(\Lambda/k)$ is the RG-time, $G_k$ the propagator and $R_k$ the standard, block-diagonal regulator matrix, see Appendix B.7.1 for the regulator choice in this work. Equation (9.3) is

completely $c_\sigma$ independent, which is ensured by the subtraction in the second term on the left-hand side.

We use the generalised RG-transformations $\dot{\phi}$ in (9.3) to implement dynamical hadronisation, analogously to [51, 144]. In contrast to the application to purely scalar theories in Chapter 7, the dynamical hadronisation relation for $\dot{\phi}$ is given in terms of the $\phi$ and the condensate $\bar{q}\tau q$, which has the same transformation properties,

$$\dot{\phi} = \dot{A}_k \bar{q}\tau q + \dot{B}_k \phi \,. \tag{9.4}$$

The hadronisation functions $\dot{A}_k$ and $\dot{B}_k$ can, in principle, be chosen freely. Here, they are used to absorb the flow of the quark four-point $\lambda_q$ and the wave function renormalisation $Z_\phi$ respectively. In this way, momentum channel of the scalar-pseudoscalar four-quark vertex is captured entirely by the momentum dependence of the emergent effective field $\phi$. This is done using constraints on the flow as given in (3.36) and briefly outlined below in (9.21).

$\dot{B}_k$ is used to absorb the wave function renormalisation $Z_{\phi,k}$, at an average momentum $\boldsymbol{p}^2 \approx k^2$, into the field via the anomalous dimension $\eta_{\phi,k}$, which is derived at a later point in (9.13). It follows

$$\dot{B}_k = -\frac{1}{2}\eta_{\phi,k} \,. \tag{9.5}$$

This effectively implements $Z_\phi \equiv 1$, for more detail see Section 7.1 and in particular (7.18) for wave function renormalisations without field dependence.

With the definition of the effective field $\phi$ we are finally able to specify the propagator matrix $G_k$ in (9.3), which is given by

$$G_k[\Phi] = \left(\Gamma_k^{(2)}[\Phi] + R_k\right)^{-1} , \quad G_{\Phi_i\Phi_j} = (G_k[\Phi])_{\Phi_i\Phi_j} \,. \tag{9.6}$$

The two point functions $\Gamma_k^{(2)}$ for the quarks and mesons are derived from the full effective action (9.2). They are evaluated at constant field configuration $\phi = (\sqrt{2\rho}, \mathbf{0}) = (\sigma, \mathbf{0})$ and $\bar{q} = q = 0$, along the lines of Section 5.1, and are given by

$$\begin{aligned}
\Gamma^{(2)}_{\bar{q}q}[\phi](p) &= Z_q(p)\left(\tilde{\not{p}} + \bar{h}(\rho)\sigma\right) , \\
\Gamma^{(2)}_{\pi_i\pi_j}[\phi](p) &= \delta_{ij}\Big[p^2 + \partial_\rho V(\rho)\Big] \\
\Gamma^{(2)}_{\sigma\sigma}[\phi](p) &= p^2 + \partial_\rho V(\rho) + 2\rho\partial_\rho^2 V(\rho) ,
\end{aligned} \tag{9.7}$$

with the four momentum that already contains the density $\tilde{p} = (p_0 + i\mu, \boldsymbol{p})$. We note that due to (9.5), $Z_\phi$ is completely absorbed into the field $\phi$ and does not appear in the two-point function of the mesons any more. We have also introduced the renormalised Yukawa coupling

$$\bar{h}(\rho) = \frac{h(\rho)}{Z_q} , \tag{9.8}$$

where we have already used $Z_\phi \equiv 1$. The current setup includes the full field dependency of the mesonic potential $V(\rho)$. This allows to take all orders of momentum independent mesonic self-scatterings into account. Specific vertices can be computed from the derivatives of the potential. For example, the mesonic masses are given by

$$m_\pi^2 = \partial_\rho V(\rho) , \quad \text{and} \quad m_\sigma^2 = \partial_\rho V(\rho) + 2\rho\partial_\rho^2 V(\rho) \,. \tag{9.9}$$

Equation (9.9) already indicates renormalised masses, due to the redefinition of fields (9.4). However, the definition of physical mesonic masses (pole masses) requires an closer look at the momentum dependence of the anomalous dimension (9.5), which follows suit.

### Wave function renormalisations and anomalous dimensions

The wave function renormalisations, or their absorption into fields (9.5), are computed from their anomalous dimensions, which is usually defined by

$$\eta_{\Phi_i,k}(\rho_0,p) = -\frac{\partial_t Z_{\Phi_i,k}(\rho_0,p)}{Z_{\Phi_i,k}(\rho_0,p)}\,, \tag{9.10}$$

for any super-field component $\Phi_i$ or, in case of an absorption into flowing fields, recall Section 7.1.1. Generally the $\eta_{\Phi_i,k}$ carry a RG-scale dependence, as well as a momentum and field dependence. The latter is dropped in the current setting: the quality of this approximation was verified in an O(N) model in Section 7.1. Here, the wave function renormalisation is evaluated on the scale dependent solution to the equations of motion $\rho_{0,k}$, which is given by

$$\left(\sigma\partial_\rho V(\rho) - c_{\sigma,k}\right)|_{\rho=\rho_{0,k}} = 0\,, \tag{9.11a}$$

where the RG-scale dependence of the explicit symmetry breaking term is given by

$$\partial_t c_{\sigma,k} = \frac{\eta_{\phi,k}}{2} c_{\sigma,k}\,, \tag{9.11b}$$

and the anomalous dimension $\eta_{\phi,k}$ is defined in (9.13).

We proceed by discussing the momentum dependences of the anomalous dimensions. The quark anomalous dimension only carries a small momentum dependence [19, 44, 48, 359] and we use $\eta_{q,k} \approx \eta_{q,k}(p_0,\mathbf{0})$, where $p_0$ is a small, non-vanishing frequency accounting for the lowest fermionic Matsubara mode, see [51] Appendix J. From this we can project onto the flow of $Z_{q,k}$ via

$$\eta_{q,k}(p_0,\mathbf{0}) = \frac{1}{4Z_{q,k}}\mathrm{Re}\left[\, i\frac{\partial}{\partial \boldsymbol{p}^2}\mathrm{tr}\,\boldsymbol{\gamma}\cdot\boldsymbol{p}\,\partial_t\Gamma^{(2)}_{\bar{q}q,k}[\phi](p)\right]_{\boldsymbol{p}=0}. \tag{9.12}$$

The full expression of the flow is also given in [51] Appendix J.

Next, we consider the anomalous dimension of the mesons: its full momentum dependence is given by

$$\eta_{\phi,k}(0,\boldsymbol{p}) = -\frac{\delta_{ij}}{3Z_{\phi,k}}\frac{\partial_t\Gamma^{(2)}_{\pi_i\pi_j}[\phi](0,\boldsymbol{p}) - \partial_t\Gamma^{(2)}_{\pi_i\pi_j}[\phi](0,\mathbf{0})}{\boldsymbol{p}^2}\,. \tag{9.13}$$

During the flow, the full momentum dependence of the mesonic wave function renormalisation is approximated with the averaged momentum dependence $p^2 \approx k^2$. This is a good approximation during the flow with our current choice of a flat 3d regulator, see Appendix B.7.1.

However, for the evaluation of physical meson masses, we need to introduce a correction $\Delta Z_\phi$, which accounts for the momentum dependence of the anomalous dimension at the pole of the propagator. The physical pole mass is situated on the real time axis, hence in an Euclidean setting it is defined by an extension to the complex plane

$$\Gamma^{(2)}_{\pi_i\pi_i}[\phi](\tilde{p}^0 = i\,m_{\pi,\mathrm{pol}},\mathbf{0}) = 0\,. \tag{9.14}$$

The current truncation scheme is not equipped for a continuation of momentum dependencies to the complex plane. Hence, we use $p_0 = 0$ as an approximation, since the momentum

dependence of the anomalous dimension is found to be very small at low momentum scales $|p|^2 \lesssim m^2_{\pi,\mathrm{pol}}$, [333]. The corrective factor is then obtained from an integration of

$$\partial_t \Delta Z_\phi = \eta_{\phi,k}(0,\mathbf{0}) - \Delta Z_\phi \eta_{\phi,k}(0,\boldsymbol{p})|_{\boldsymbol{p}^2\approx k^2}\,. \tag{9.15}$$

The explicit expressions for $\eta_{\phi,k}(0,\mathbf{0})$ and $\eta_{\phi,k}(0,\boldsymbol{p})$ are again indicated in [51] Appendix I.

Using (9.15), the mesonic pole masses are evaluated on the equations of motion (9.11) and are given by

$$m_{\pi,\mathrm{pol}} \approx \sqrt{\frac{\partial_\rho V(\rho)}{\Delta Z_\phi}}\bigg|_{\rho=\rho_0}, \quad \text{and} \quad m_{\sigma,\mathrm{pol}} \approx \sqrt{\frac{\partial_\rho V(\rho) + 2\rho\partial^2_\rho V(\rho)}{\Delta Z_\phi}}\bigg|_{\rho=\rho_0}. \tag{9.16}$$

### Yukawa interaction

The constituent quark mass is directly linked to the mesonic field $\sigma$, which couples to the quarks though the Yukawa coupling. In our truncation, its definition can be read off (9.7) and is given by

$$m_q = \sqrt{2\rho}\bar{h}(\rho) = \sigma\bar{h}(\rho)\,. \tag{9.17}$$

Consequently, the flow of the Yukawa coupling is derived from the quark two-point function, analogously to (8.7). For a detailed derivation and the full expressions for the flows see [51]. Here we only state the essential steps in the derivation within the current approximation and discuss the dynamical hadronisation process in the context of (3.36).

The generalised flow (9.3) is projected onto the scalar part $\bar{q}\tau^0 q$, which corresponds to the renormalised quark mass, and obtain

$$\partial_t \bar{h} - \eta_{q,k}\bar{h} + \bar{h}\dot{B}_k + m_\pi^2\dot{\bar{A}}_k = \frac{1}{4N_c N_f Z_q}\frac{1}{\sigma}\mathrm{tr}\Big[\partial_t \Gamma^{(2)}_{\bar{q}q}\Big]\,. \tag{9.18}$$

In contrast to (8.7) the flow now also contains the (renormalised and dimensionful) hadronisation function $\dot{\bar{A}}_k$ and $\dot{B}$. In contrast to (8.7) the flow on the right-hand side of (9.18) now contains loops with mesonic and gluonic interactions. Furthermore, the field dependency is evaluated in a *local density approximation*, hence we use $\partial_\rho \bar{h} = 0$ in the derivation of the equations. The flow of the quark-two point function is indicated in [51] Appendix K.

Similarly, we deduce the flow for the four-quark coupling, by projecting onto the quark-bilinear $(\bar{q}\tau q)(\bar{q}\tau q)$,

$$\partial_t \bar{\lambda}_q(\rho) - 2\big(1+\eta_q\big)\bar{\lambda}_q(\rho) - \bar{h}\dot{\bar{A}}_k = \overline{\mathrm{Flow}}^{(4)}_{(\bar{q}\tau q)(\bar{q}\tau q)}\,. \tag{9.19}$$

The renormalised and dimensionless quantities are given by

$$\bar{\lambda}_q = \frac{\lambda_q k^2}{Z_q^2}, \quad \dot{\bar{A}}_k = \frac{Z_\phi^{1/2}}{Z_q}\dot{A}_k k^2, \quad \text{and} \quad \overline{\mathrm{Flow}}^{(4)}_{(\bar{q}\tau q)(\bar{q}\tau q)} = \frac{k^2}{Z_q^2}\mathrm{Flow}^{(4)}_{(\bar{q}\tau q)(\bar{q}\tau q)}, \tag{9.20}$$

and the projected flow can be found in [51] Appendix L. We recall the flowing fields Section 7.1, where we chose $\dot{\phi}$ such that the flow of the wave function is cancelled out. Now we make a similarly choice for $\dot{\bar{A}}$, i.e. we chose it such, that $\lambda_q \equiv 0$ at all RG-scales. It follows that

$$\dot{\bar{A}} = -\frac{1}{\bar{h}}\overline{\mathrm{Flow}}^{(4)}_{(\bar{q}\tau q)(\bar{q}\tau q)}, \tag{9.21}$$

which effectively absorbs the momentum dependence of the quark-bilinear $(\bar{q}\tau q)(\bar{q}\tau q)$ into kinetic term $(\partial_\mu\phi)^2$ of the emergent field $\phi$.

### 9.1.2. Gluonic interactions

For the purely gluonic interactions we resort to the efficient expansion scheme that has been set-up and used in [51,117]. At its heart lies the advantageous flexibility of functional approaches, that one can use external results as input. This input can either be obtained from other functional computations or from lattice results. In short, one can outsource part of the computation without loss of reliability. This external input comes with its own systematic and, in the case of lattice results, with an additional statistical error. Consequently, the statistical and systematic errors of such a mixed approach then depend on the quantitative precision and statistical and systematic errors of the external input as well as the intrinsic systematic error of the given expansion order of the fRG computation. This scheme has been extended, tested and used in Dyson-Schwinger equations. In [56,57,100,227], for related earlier work see also [360].

The most straightforward use of external input is to simply substitute correlation functions in the loops on the right hand side of functional relations by that obtained from other computations. In the past decades this has often been done with low order lattice correlation functions, mostly in Yang-Mills theory in the vacuum. Evidently, if the systematic and statistical error of the input is significantly smaller than that of the approximation level used in the computation at hand, one does not have to consider it in the error analysis.

#### Quark-gluon interactions

The flow equation of the coupling $g_{\bar{q}Aq}$ of the classical tensor structure of the quark-gluon vertex shows a direct $\rho$-dependence via that of the quark-meson Yukawa coupling and quark mass function. We will take into account the meson field dependences in all couplings, except for the Yukawa coupling and the purely mesonic couplings, in the analogue of the local density approximation: while all couplings such as $g_{\bar{q}Aq}$ are taken to be $\rho$-dependent we shall neglect all derivatives, $\rho\partial_\rho g_{\bar{q}Aq} \approx 0$. This approximation certainly holds true for mildly varying $\rho$-dependences which is present for most $\rho$ and $k$. Furthermore, even for $\rho\partial_\rho g_{\bar{q}Aq} \neq 0$ the respective diagrams are sub-leading or negligible for all cutoff scales and $\rho$.

It has been discussed in detail in [51], that the current approximation allows for semi-quantitative accuracy. Key to full quantitative precision is the inclusion of the relevant tensor structures of the quark-gluon vertex, for a detailed analysis see the fRG and DSE-analyses in [48,227]. In short, the quark-gluon vertex accommodates three relevant tensor structures, the chirally symmetric classical one and a further chirally symmetric one as well as one that breaks chiral symmetry and is only present for a non-vanishing value of the quark mass function. Importantly, in the fRG approach the dynamics of the non-classical tensor structures is partially taken into account via the four-quark interactions, and the dominant contribution of the latter is comprised in the scalar-pseudo-scalar channel. This entails that dropping the direct contribution from the non-classical tensor structure as well as further four-quark interaction channels is leading to a small drop in the strength of chiral symmetry breaking. In the present work we compensate this with a minor infrared enhancement by a few precent of the quark-gluon coupling strength $\alpha_{Aq\bar{q}}$ in the deep infrared.

This approach follows those used in [45,51] and consists of a phenomenological infrared enhancement of the classical tensor structure. The flow is enhanced by

$$\begin{aligned}\partial_t \bar{g}_{\bar{q}Aq}(\bar{\rho}) \to & \bar{g}_{\bar{q}Aq}(\bar{\rho})\partial_t \zeta_{a,b}(k) \\ & + \zeta_{a,b}(k)\partial_t \bar{g}_{\bar{q}Aq}(\bar{\rho}),\end{aligned} \tag{9.22a}$$

where the infrared enhancing function is given by

$$\zeta_{a,b}(k) = 1 + a\frac{(k/b)^2}{\exp[(k/b)^2]-1}\,. \tag{9.22b}$$

and the enhancement factors $a$ and $b$ are fitted to suit the constituent quark mass. They depend on the truncation used and will be indicated with the result. The strength of the enhancement, encoded in $a$, lies in the percent range.

In contradistinction, in the DSE-approach the direct contributions to chiral symmetry breaking from the non-classical parts of the quark-gluon vertex dominate by far, and dropping them leads to a qualitative drop of the strength of chiral symmetry breaking or even the lack thereof. Compensating these missing dynamics by an enhancement of the couplings strength $g_{\bar{q}Aq}$ of the classical tensor structure requires enhancement factors larger than two. Note however, that including the two most relevant tensor structures in the computation already provides full quantitative results both in the vacuum and at finite temperature and density, see [57, 100].

This qualitative difference between DSE and fRG approaches in the given approximations originates in the very different resummation schemes both offer in rather similar approximations to the effective action. Indeed, this fact offers a further systematic error control: if the results within theses two functional approaches agree quantitatively, this is a highly non-trivial self-consistency check.

## 9.2. Systematic errors in QCD computations

The current work has two aims, necessitating differing approximations which are easily implemented in the current setting.

Firstly, we give an estimate for the constituent quark mass in vacuum, using an improved approximation of the effective action (5.1), by taking higher quark-mesonic scattering orders into account in a finite density approximation, recall (9.18). Secondly, we provide a numerical benchmark for computations which only consider the lowest quark-mesonic scattering order. This benchmark also provides an error estimate for state of the art computations of the QCD phase structure [51].

These two implementations are discussed in Section 9.2.1 and we present results for the pole masses in Section 9.2.2 and for the field dependent couplings in Section 9.2.3. Currently, we only present results in the broken phase, at low temperatures $T = 1\,\mathrm{MeV}$ and vanishing density $\hat{\mu}_q = 0$. A study of the full phase structure is deferred to future work.

### 9.2.1. Implementation

In the previous section we outlined our current truncation, with an emphasis on notation and the relevant definitions. Firstly, Section 9.1.1 introduced flows in the matter sector, i.e. the mesonic masses, the Yukawa coupling to the quarks and their anomalous dimensions. Secondly Section 9.1.2 gave a brief outline of the gluonic-overhead. The gluon dynamics are completely input, with the exception of the quark-gluon vertex $g_{\bar{q}Aq}$, whose field dependence plays a sub-leading, but important role for quantitative accuracy. To summarise, we give an overview of all quantities within the current truncation and discuss their numerical implementation.

### Implementation of the mesonic potential $V(\rho)$

The mesonic potential $V(\rho)$ is used to derive the mesonic masses, see (9.9). Its full field dependence is implemented using the Discontinuous Galerkin (DG) framework put forward in Chapter 5, more precisely the local DG method outlined in Appendix A.1.2. By computing the full field dependence, the current truncation takes all higher purely mesonic scattering orders into account. This is of great importance for quantitative precision in the chiral limit and later on in even the qualitative access to the phase structure at high densities. In this regime, non-analyticities appear in the RG-flow of the potential, as well as in the potential itself at $k \to 0$, see e.g. [1] or Chapter 8 for an investigation in the quark-meson model. Thus higher derivatives of the potential - which correspond to higher mesonic scattering orders - cannot be neglected. Following the reasoning of Section 5.1.2, the RG-flow is computed in terms of its first derivative $u = m_\pi^2 = \partial_\rho V(\rho)$. To wit

$$\partial_t u = \partial_\rho \left( \frac{k^4}{4\pi^2} \big[ (N_f^2 - 1) l_0^{(B,4)}(\bar{m}_{\pi,k}^2, \eta_{\phi,k}; T) + l_0^{(B,4)}(\bar{m}_{\sigma,k}^2, \eta_{\phi,k}; T) \right.$$
$$\left. - 4 N_c N_f \, l_0^{(F,4)}(\bar{m}_{q,k}^2, \eta_{q,k}; T, \mu_q) \big] + \eta_{\phi,k} \rho u \right) . \tag{9.23}$$

where the threshold-functions $l_0^{(B,4)}$ and $l_0^{(F,4)}$ perform the momentum integration and Matsubara summation and are given by (B.125) and (B.126) in Appendix B.7.2. The dimensionless masses are given by $\bar{m}_i = m_i / k$.

### Implementation: Field dependent couplings

To make a quantitative statement about the importance of higher quark-mesonic scattering orders in a full QCD setting we consider two different implementations of the Yukawa coupling $h$ and the quark-gluon vertex $g_{\bar{q}Aq}$.

(i) **Field dependent couplings $h(\rho), g_{\bar{q}Aq}(\rho)$ in a finite density approximation**, i.e. $\partial_\rho h \approx 0$ and $\partial_\rho g_{\bar{q}Aq} \approx 0$: This approximation allows for different coupling strengths at different mesonic field values, but does not explicitly take higher scattering processes (diagrams) into account in the flows. The finite density approximation allows to implement a field dependence without adding instabilities by introducing a second partial differential equation. We implement the field dependence by using a Discontinuous Galerkin discretisation, consisting only of a source term, recall (5.10).

(ii) **Couplings constant in the field $\rho$**: Couplings are evaluated on the solution to the physical equations of motion (9.11), analogously to the anomalous dimensions. This implementation is identical to state of the art results of the QCD phase structure, see [51], and is numerically very efficient and stable.

Both approximations are contrasted by the study of the full field dependence of the Yukawa coupling within the low energy effective model in Section 9.1.1.

Inarguably, the main, novel result in this work is obtained from (i), but we emphasise again, that (ii) provides an important benchmark to existing results. Furthermore (ii) may be a desired approximation for computations considering multiple condensates, such as diquarks and vector-mesons.

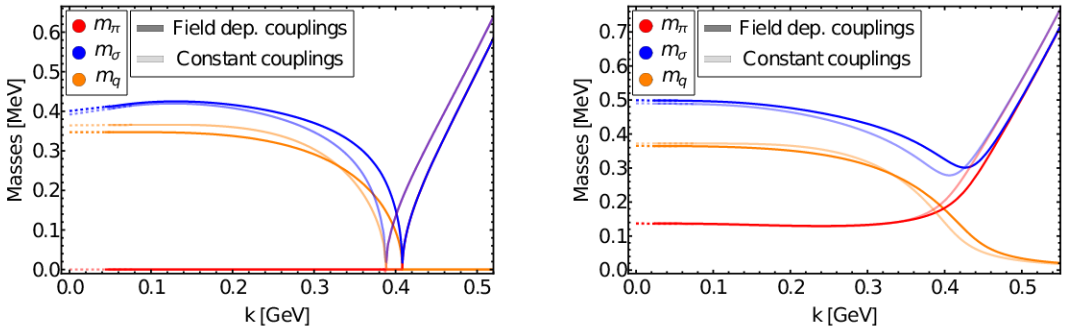


(a) Pion, sigma and quark masses in the chiral limit, where we use $c_\sigma = 0$.

(b) Pion, sigma and quark masses on the physical equations of motion.

Figure 9.1.: RG-time dependence of pion, sigma and quark masses in the IR. Results and tuning parameters for the masses are indicated in Table 9.2 for the computation with field dependent couplings (i) and in Table 9.1 at constant couplings (ii). Fits to extrapolate the masses at $k \to 0$ are indicated by the dashed lines.

### Initialisation of flows

The computation is initialised at an RG-scale of $k = 20\,\text{GeV}$. At this scale, the important input parameters are those of the gluonic sector, which need to match the input data [48]. Hence the quark-gluon coupling at $k = 20\,\text{GeV}$ is set to $g_{\bar{q}Aq} = 0.21$ for the present two flavour case.

To fix the initial conditions in the mesonic sector, we make use of the pseudo-fixed point behaviour of the flow at intermediate RG-scales [102]. The pseudo-fixed point ensures that results at $k \to 0$ are independent of the initial mesonic masses and Yukawa coupling, as long as the initial four-fermi coupling $\lambda_q$ is smaller than the strong coupling $\alpha_s$ [45]. For completeness we state the initial values in our computation: the potential is simply given by a mass term

$$V_\Lambda(\rho) = \rho m_\phi^2 \,. \tag{9.24}$$

where $m_\phi = 4 \times 10^6\,\text{GeV}$ is initiated at a very high value to ensure that all mesonic loops are additionally suppressed. The Yukawa coupling at the initial scale is set constant, to $h = 1$. Furthermore, the mesonic and quark wave function renormalisations are initialised at $Z_\phi = Z_q = 1$.

## 9.2.2. Masses

As a first result in our investigation, we compute the quark mass (9.17), as well as the mesonic masses (9.9). Results converge up to an RG-scale $k_{\text{min}} = 0.03\,\text{GeV}$. A linear extrapolation is used to extract the values at $k \to 0$, a similar procedure was applied in Figure 8.3. The explicit symmetry breaking term $c_\sigma$ is used to fix the pion mass to its physical value and is indicated with the respective results, see Table 9.1 or Table 9.2. Similarly we adjust the IR-enhancement of the quark-gluon vertex, which allows to tune the strength of chiral symmetry breaking, recall (9.22a), to obtain a physical constituent quark mass. The initial parameters for the computation using constant couplings, as well as the corresponding quark and mesonic pole masses are given in Table 9.1. Results and initial parameters using field dependent couplings are indicated in Table 9.2.

### Benchmark results

Table 9.1 gives results for the mesonic and quark masses in both the chiral limit and the physical case for the benchmark computation (ii) at constant couplings. We use the values of the tuning parameters from [51], to obtain an estimate on the improvement obtained by using a fully field dependent potential $V(\rho)$ instead of a Taylor expansion about the equations of motion. The physical pion mass is nearly identical at $m_\pi = 136\,\text{MeV}$, whereas the quark mass is slightly increased to $m_q = 372\,\text{MeV}$. The biggest deviation is in an decreased mass of the sigma meson, which is at $m_\sigma = 490\,\text{MeV}$ in a fully field dependent setting. This is unsurprising, because the full field dependent potential is expected to be more precise in the computation of higher derivatives. In conclusion, this analysis supports the Taylor expansion scheme of the potential in vacuum. However, it also calls for a more cautious investigation in regimes of the phase structure where the sigma mode becomes more important, i.e. in the vicinity of the conjectured critical point.

An additional computation in the chiral limit, i.e. $c_\sigma = 0$ yields the expected decrease in masses. In such a scenario, the pion is a real Goldstone boson with $m_\pi = 0\,\text{MeV}$, the quark mass $m_q = 364\,\text{MeV}$ as well as a sigma meson at $m_\sigma = 392\,\text{MeV}$. The study of the chiral limit is especially interesting when investigating scaling properties in critical regions and in the context of chiral expansion schemes of the magnetic equation of state [57].

### Full truncation

We now consider results for field dependent couplings, outlined in (i). We tune the initial parameters to obtain physical masses [78]. We increase the explicit symmetry breaking term to $c_\sigma = 3.7\,\text{GeV}^3$ and increase the strength of the IR-enhancement of the quark-gluon coupling to $a = 0.012$. We discuss the IR-enhancement at a later point in connection with the field dependent couplings. With this we obtain the physical pion mass $m_\pi = 137\,\text{MeV}$, sigma mass $m_\sigma = 499\,\text{MeV}$, as well as the quark mass $m_q = 365\,\text{MeV}$. In the chiral limit we obtain a lowered quark mass $m_q = 347\,\text{MeV}$ as well as a bigger sigma meson at $m_\sigma = 404\,\text{MeV}$ in comparison to the evaluation at constant couplings. For a condensed summary of the results see Table 9.2.

The most significant difference between calculations with constant and fully field dependent couplings is the shift of the onset-scale of chiral symmetry breaking $k_\chi$. This is visualised for both the chiral limit and physical observables in Figure 9.1. An earlier onset of chiral symmetry breaking in the flow will have a significant effect on the location of the crossover transition at high temperatures and we suspect to report on an increase of the critical temperature $T_c$ in future publications.

| Observable | chiral limit | physical EoM | Ref. [51] | Parameter in $\Gamma_\Lambda$ |
|---|---|---|---|---|
| $m_{\pi,0}$ [MeV] | 0 | 136.0 | 137 | $c_\sigma = 3.6\,\text{GeV}^3$ |
| $m_{\sigma,0}$ [MeV] | 392.0 | 490.0 | 531 | - |
| $m_q$ [MeV] | 364.4 | 371.9 | 367 | $a = 0.008$ $b = 2\,\text{GeV}$ |

Table 9.1.: IR-Observables and adjustable parameters for the computation with constant couplings. Parameters in $\Gamma_\Lambda$ are used to adjust the pole masses (9.16) and (9.17) on the physical equations of motion (9.11). The quark mass is adjusted using an enhancement of the quark-gluon vertex which is indicated in Equation (9.22a). The results correspond to a calculation in a comparable truncation from [51].

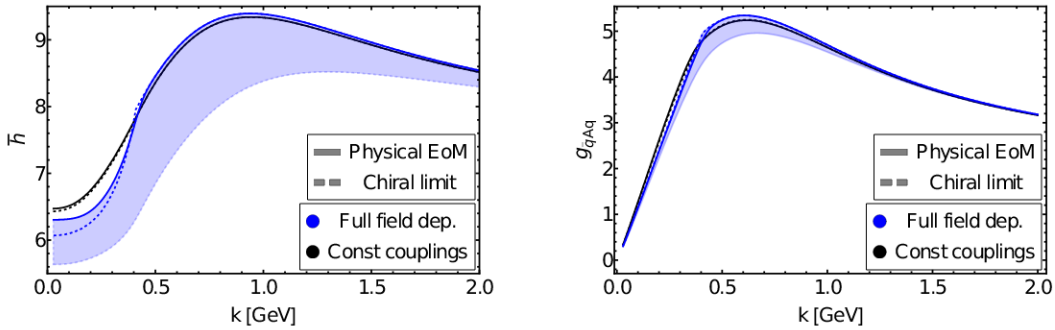


(a) Yukawa coupling.

(b) Quark-gluon coupling.

Figure 9.2.: Couplings as a function of RG-scale $k$ on the equations of motion. We compare both calculations on the physical equations of motion as well as in the chiral limit. Furthermore, we consider calculations within the truncations (i) and (ii). The light blue area indicates values for the field-dependent couplings at higher field values $\rho_0 < \rho < \rho_{\mathrm{UV}}$ where $\rho_{\mathrm{UV}} = 0.015 \approx 2\rho_{0,k\to 0}$ is the length of the numerical computation interval.

### 9.2.3. Field dependent couplings

The field dependence of the couplings is almost vanishing up until $k \approx 2.5\,\mathrm{GeV}$. Then, it gains importance around $k \approx 3k_\chi$, where $k_\chi \approx 0.4\,\mathrm{GeV}$ is the approximate scale at which chiral symmetry breaks.

We have already established that this field dependence of couplings has a quantitative effect on the meson masses. The difference between truncations becomes apparent, when considering the RG-scale dependence of the couplings themselves: Figure 9.2 shows a comparison between the computations at constant fields and the field dependent results. Firstly one can see the difference in IR-enhancement between the computation of type (i) and (ii), by the difference in maximum value reached by the quark-gluon vertex $g_{\bar{q}Aq}$ around 0.6 GeV.

In spite of the stronger IR-enhancement of the coupling, the physical quark mass $m_q$ is smaller in (i). This effect is linked to the couplings generally decreasing towards higher field values $\rho$, which is discernible from the light blue tube in Figure 9.2. This quantitatively relevant effect cannot be captured with truncation (ii).

| Observable | chiral limit | physical EoM | Parameter in $\Gamma_\Lambda$ |
|---|---|---|---|
| $m_{\pi,0}$ [MeV] | 0 | 137.0 | $c_\sigma = 3.7\,\mathrm{GeV}^3$ |
| $m_{\sigma,0}$ [MeV] | 404.3 | 499.0 | - |
| $m_q$ [MeV] | 347.1 | 364.9 | $a = 0.012$ $b = 2\,\mathrm{GeV}$ |

Table 9.2.: IR-Observables and adjustable parameters for the computation with field dependent couplings couplings. Parameters in $\Lambda_\Gamma$ are used to adjust the pole masses (9.16) and (9.17) on the physical equations of motion (9.11). The quark mass is adjusted using an enhancement of the quark-gluon vertex which is indicated in Equation (9.22a), in comparison to Table 9.1 the IR-enhancement is slightly bigger.

## 9.3. Conclusion and outlook

In this chapter, we investigated the dynamics of chiral symmetry breaking in QCD in at low temperatures and densities. To this aim we used input data for the gluonic interactions from [44], which were used to compute an order parameter potential in terms of a quark-condensate, formed by a resonance in the scalar-pseudoscalar four-quark interaction. From this effective potential we were able to obtain quantitative masses for the mesons and the current quark mass of the light quarks, see Table 9.2. The field dependence of the order parameter potential was computed using the Discontinuous Galerkin (DG) framework put forward in Chapter 5. Using the DG methods, we were able to reproduce the vacuum results from [51] with an improved truncation scheme.

The result for the current quark mass in vacuum was adjusted by the introduction of an IR-enhancement of the quark-gluon vertex, to match the Particle data group [78]. This IR-enhancement accounts for non-classical tensor structures of the quark-gluon vertex, which were neglected in the current approximation. We plan to include them in future applications and thereby remove the artificial IR-enhancement.

Furthermore, we considered the quantitative error caused by neglecting higher quark-mesonic scattering orders, as investigated for the quark-meson model in Chapter 8. In the current work we make use of a local density approximation for the couplings and find significant quantitative deviations, most notably a shift in the onset scale for chiral symmetry breaking in comparison to a computation with constant couplings: In the presence of field dependent couplings, onset of chiral symmetry breaking occurs at an earlier RG-time in the vacuum, see Figure 9.1. A naive extrapolation of this argument to the finite temperature transition at low densities, predicts a higher critical temperature than the one computed in current functional state of the art computations using constant couplings, see [51] or Figure 2.2.

The current work did not consider computations at finite temperature. To do so in a quantitative way, it remains to include the temperature dependence of the gluonic dynamics, as well as the interactions with the strange quark, see [51].

The introduction of Discontinuous Galerkin methods was an important step towards the computation of the QCD phase structure at finite densities. However, there is still a long path ahead: First and foremost, the current truncation needs to be improved, since the scalar-pseudoscalar interaction is no longer the dominant four-quark interaction at high densities. We have discussed this issue in Section 2.3. We aim to include the computation of order parameter potentials in term of diquark and vector-meson condensates.

# CHAPTER 10

## Summary, conclusion and outlook

In this work, we investigated nuclear matter and other possible phases of quark-matter. This was motivated by the interpretation of heavy ion collisions, the physics of the early universe or neutron stars. To this end, various approaches towards a systematic, quantitative computation of the underlying first-principle theory Quantum Chromodynamics (QCD) and its phase structure were explored. In doing so, we have made many methodological developments within the functional renormalisation group (fRG) which also find application in a broader quantum field theory context.

In Chapter 2, we gave a brief introduction to QCD and outlined its distinctive features. We considered the perturbative nature of QCD at high energies, linked to asymptotic freedom. This stands in contrast to the low energy regime, in which the strong interaction of quarks and gluons makes for an interesting phase structure across different temperatures and densities. The phase structure is determined by the confinement/deconfinement transition, as well as the process of chiral symmetry breaking, both of which we set out to investigate throughout this thesis. For this purpose, we proceeded to discuss the range of validity of common low energy effective theories for the four-quark scattering processes. Importantly, we introduced an effective description of the dynamics in the matter sector of QCD in terms of a scalar O(4) model. This also explains our general interest in the O(N) model for QCD computations.

The functional renormalisation group was put forward as our method of choice for non-perturbative computations in the low energy regime of QCD. The general idea behind a functional formulation in terms of the effective action $\Gamma[\Phi]$ was outlined in Chapter 3, together with the commonly used functional flows, the Wetterich and Polchinski flows. We commented on appropriate expansion schemes of the effective action in QCD, also in the context of an optimisation of the RG-flow. We proceeded with a discussion of general RG reparametrisations in terms of dynamical 'flowing' fields in Section 3.3 and possible applications thereof to the process of Goldstonisation, the improvement of expansion schemes and in the context of dynamical hadronisation. Lastly, we considered the CS-flow as an important real-time application of generalised RG-flows in Section 3.4.

A first computation was presented in Chapter 4, where we explored the dynamical emergence of the Yang-Mills mass gap in terms of spontaneous symmetry breaking. We used the fRG to compute an effective potential of a colourless gluon condensate. From this we obtained an

estimate for the mass gap of $m_{\text{gap}} = 322(34)\,\text{MeV}$, which compares very well to the lattice estimate $m_{\text{gap}}^{(\text{lattice})} = 0.3427(8)\,\text{MeV}$ from [192, 194, 234]. This estimate should be understood as an incentive to further investigate this promising mechanism for mass (gap) generation in Yang-Mills theory. It also highlights a very important feature of the fRG, which we have continued to explore throughout this thesis: its modular structure, which allows to use external results for gluonic correlation functions in the computation of an order parameter potential. In this case, the order parameter was the expectation value of a gluon condensate which indicated confinement.

We continued to explore the concept of order parameter potentials in Chapter 5, in the context of scalar O(N) theories and spontaneous symmetry breaking. This chapter developed a rigorous numerical approach, which was applied to investigate chiral symmetry breaking in Chapter 8 and Chapter 9. The derivative expansion was used to translate the renormalisation group flow of an effective potential, in terms of the (locally constant) scalar field $\phi$ and RG-scale $k$, into the language of fluid dynamics and partial differential equations (PDE). To solve the ensuing highly non-linear PDEs, we introduced the Discontinuous Galerkin method (DGM) to discretise the field dependence in $\phi$ and proceeded to investigate the creation of non-analyticities and shock waves in the RG-flow of the effective potential. Their occurrence implies the importance of higher scattering orders of the scalar field and emphasises the necessity of advanced numerical discretisation schemes in the fRG. This applies not only to achieve quantitative accuracy but already for qualitative aspects! For this reason, all results in the following chapters of the main text, with the exception of Section 7.2, make use of DGMs. We also point out the wide range of applicability of fluid dynamical methods in the context of derivative expansions in the fRG. The introduction of DGMs in Chapter 5 is accompanied by Appendix A, which discusses technical details, such as efficient (RG-)time-integration algorithms, and containes a guide to a freely available implementation on github [12].

In Chapter 6 and Chapter 7 we discussed applications of generalised RG transformations to O(N) theories. We have not applied them to the matter sector of QCD yet, but aspire to do so in the future. These chapters contain novel technical developments, which can also be used in a condensed matter, cosmology or beyond the standard model context, to name a few. In Chapter 6 we set up functional flows for complex effective actions and compared results for different formulations in terms of the Wilsonian effective action and the 1PI effective action. We made use of generalised RG transformations to construct an RG-adapted flow which allowed to compute the effective potential of an O(1) model in the presence of complex sources, for example magnetisations. In this setting, we were able to locate Lee-Yang singularities in the complex magnetisation plane and to investigate their scaling behaviour. We were also able to precisely extrapolate the phase transition on the real axis from the location of the Lee-Yang singularities in the complex plane and found a very large scaling regime in our study within four dimensions. We hope to apply this procedure to the QCD phase structure in the future, possibly for an extrapolation of the critical endpoint of QCD. Section 7.1 discusses an expansion scheme of the effective action about its ground state and Section 7.2 an application of the CS-flow to spectral functions.

The last two chapters focussed on the investigation of chiral symmetry breaking. We studied the quark-meson phase structure in Chapter 8, using DGMs. We were able to precisely resolve the competing order effects, which are decisive for the location of phase transition lines within this low-energy effective theory of QCD. This study provides further proof of the relevance of higher scattering orders in an investigation of the large-$N_f$ limit: We found shock development in the first order regime at high densities, hinting at the relevance of higher mesonic scattering

orders. Furthermore, this full implementation of quark-mesonic scatterings emphasised their quantitative significance in the vicinity of phase transitions.

Lastly, the qualitative improvement by the DGMs was also applied to a full QCD computation of the mesonic part of the matter sector in approximate vacuum. In Chapter 9, we provided estimates for the mesonic masses and current quark mass of the light quarks and investigated the importance of higher quark-mesonic scatterings in this context. Though technically our estimates are in agreement with the known masses from e.g. the Particle Data group [78], the computation still contains tuning parameters which are included in the truncation to compensate for scattering processes that are not accounted for in the truncation yet. Nevertheless, this tuned vacuum-framework can be applied to make predictions about the phase-structure, as was done in [51].

The next tasks are obvious: to achieve quantitative precision and predictability, the QCD setup from Chapter 2 needs to be upgraded with quantitative corrections provided by e.g. the contributions of non-classical tensor structures of the quark-gluon vertex, which removes the tuning parameter for the quark mass. Moving away from approximate vacuum, we hope to use the modular structure of the fRG to extend the QCD setup beyond the mesonic part of the matter sector at high densities, such as the formation of vector mesons, diquark-condensates and baryons. The foundation for such an investigation has been laid in this thesis, by the improvement of the derivative expansion scheme via the general RG transformations and by an intensive development of the numerical method: DGMs, and fluid dynamical methods in general, are well suited to solve higher dimensional PDEs, which are inevitable in the computation of order parameter potentials of multiple condensates. With such a setup, we are excited to gain insights on the connection between shock-development, first order phase transitions and the formation of quark-matter at high densities in upcoming years.

# Appendix

# APPENDIX A

# Details on Discontinuous Galerkin

In this chapter of the appendix, we outline some numerical details. Appendix A.1 focusses on different DG methods or extensions of the ones presented in Chapter 5 that were used for specific problems in other chapters. Appendix A.2 focusses different time-integration schemes we have used in this work. Finally we give detailed instructions to a simplified version of our numerical framework in Appendix A.3, at the example of the LDG implementation discussed in the main text, accompanied by a code which is accessible in [12].

## A.1. DG methods: Misc

### A.1.1. Non-conservative product

*This Appendix is taken from [1].*

In this section the extension of direct DG-methods to non-conservative flow equations is set up. To this end we consider a system of differential equations of the form,

$$\partial_t u_i + \partial_x f_i(\boldsymbol{u}, x, t) + a_{ij}(\boldsymbol{u}, x, t)\partial_x u_j = s_i(\boldsymbol{u}, x, t)\,, \tag{A.1}$$

where $\boldsymbol{u} = (u_1, u_2)^T$ and $i, j \in \{1, 2\}$. The $s_i$ are source terms and $f_i$ conservative fluxes. In (A.1) we also allow for non-conservative terms $a_i$.

In the full quark-meson model the flux $f_i$ is additionally separated into a convective and a diffusive contribution depending also on $\partial_x u_i$. We note that the splitting into conservative and non-conservative terms is not unique in these equations. Here, we need an additional expression for $\partial_x u_i$. We obtain this expression by taking another $x$ derivative of the polynomial basis functions $\psi_p$, compare (5.13).

The presence of the diffusion modifies the numerical flux significantly and is discussed in Section 5.2.2. However, in the convection dominated regime, and in the absence of a discontinuity, it is possible to neglect this diffusion numerical fluxes and formulate the Discontinuous

Galerkin method for this equation as follows,

$$\int_{D^k} \Big( (\partial_t u_{i,h} + a_{i,h}\partial_\rho u_{i,h} + s_{i,h})\psi_p + f_{i,h}\partial_x \psi_p \Big) dx = -\int_{\partial D^k} \psi_p \Big( f_i^* \hat{\boldsymbol{n}} + \boldsymbol{D}(u_{i,h}^+, u_{i,h}^-, \hat{\boldsymbol{n}}) \Big) dx \,. \tag{A.2}$$

where $a_{i,h}$, $s_{i,h}$ and $f_{i,h}$ are computed form the field $u_i$ and their local approximation of the derivative, no other numerical fluxes are introduced into the numerical scheme. The absence of numerical fluxes for the extra derivative present in the equation at finite $N_f$, corresponds to the assumption of continuity of this field and the DG scheme reduces to a pseudo spectral method. This approximation is acceptable, whenever the flow is rather smooth and no shock or rarefaction wave are generated during the simulation. In turn, this scheme will fail in the vicinity of a first order phase transition. There we expect shock-formation and propagation in the flow equation. In conclusion, for the rest of the phase diagram the present approximation can be considered as a sufficiently accurate solution of the flow equation due to the local high order accuracy of the DG scheme.

The additional non-conservative flux across a boundary is given by $\boldsymbol{D}$. The theory of non-conservative fluxes was developed in [361, 362] and is applied in the context of Finite Volume and Discontinuous Galerkin schemes [271, 363–370]. To compute this quantity we need to consider the general form of a flux across an interface. For this purpose we consider a path $\phi_i(s)$ along the solution $u_i$, with start and endpoint $u_i^L$ and $u_i^R$ respectively and the parameter $s \in [0,1]$. The formal definition of the flux along this path for a non-conservative flux contribution $a_i \partial_\rho u_j$ (see (A.1)) is then given by:

$$f_{i,\mathrm{nc}} = \int_0^1 a_i(\phi_i(s), \phi_j(s), s)\partial_s \phi_j(s) ds \,. \tag{A.3}$$

We remark that in the non-conservative case the flux is dependent on the chosen path.

By choosing the right and left sides of a boundary $u^R = u^+$ and $u^L = u^-$ we are able to compute the flux from one cell to another. Similar to the numerical flux, $\boldsymbol{D}$ has to satisfy the jump property for consistency,

$$\boldsymbol{D}(u^+, u^-, \hat{\boldsymbol{n}}) + \boldsymbol{D}(u^+, u^-, -\hat{\boldsymbol{n}}) = \int_0^1 a(\phi(s))\hat{\boldsymbol{n}} \frac{\partial \phi}{\partial s} ds \,,$$

which implies $D(u,u,\hat{\boldsymbol{n}}) = 0$ when there is no jump.

This condition can be obtained by integrating the equation around a discontinuity. It generalizes the so called Ranking Huginot Condition for non-conservative systems of equations. The numerical fluxes are,

$$\boldsymbol{D}(u^+, u^-, \hat{\boldsymbol{n}}) = \frac{1}{2}\int_0^1 a(\phi(s))\hat{\boldsymbol{n}} \frac{\partial \phi}{\partial s} ds + \frac{1}{2}\int_0^1 |a(\phi(s))\hat{\boldsymbol{n}}| \frac{\partial \phi}{\partial s} ds \,. \tag{A.4}$$

$|a(\phi(s))\hat{\boldsymbol{n}}|$ is intended as the absolute value of the matrix namely $|a| = U^{-1}\mathrm{diag}(|\lambda_1|, \cdots, |\lambda_N|)U$, with $\lambda_i$ the eigenvalue of the matrix. It is possible to prove that this choice of flux reduces to the Lax-Friedrichs flux in the conservative case. If the dominant convection part of the equation is given by the conservative flux this extra term can be neglected. The non-conservative flux under this assumption can therefore be computed from

$$\boldsymbol{D}(u^+, u^-, \hat{\boldsymbol{n}}) = \frac{1}{2}\int_0^1 a(\phi(s))\hat{\boldsymbol{n}} \frac{\partial \phi}{\partial s} ds \,. \tag{A.5}$$

The last remaining degree of freedom are the boundary conditions for the outer boundary of $\Omega_h$. In our case they are given by the in- /out-flowing flux, which is implemented by setting $u^+_{i,h} = u^-_{i,h}$ at the outer boundaries, effectively adding an imaginary additional cell. It follows that the non-conservative flux is not fit for flux-boundary conditions, since the non-conservative flux vanishes at the outer boundaries due to the jump property. Therefore the equations need to be reformulated such that the boundary-conditions can be met using the conservative flux. This is done in Appendix B.6.1.

## A.1.2. An alternative LDG formulation

*This Appendix is taken from [10].*

In contrast and/or in addition to the LDG method presented in Section 5.2.2, this section focuses on a LDG method using left- and right-sided derivatives as detailed in [371]. The stability and correctness of the solution has been checked in [371] on the example of various higher-order convection-diffusion equations. It is a variation of the standard LDG method put forward in [372], which has already been successfully applied to the fRG in [5]. In contrast to the standard LDG method, the current method is specifically designed to stabilize second order derivatives and allows for the computation of large diffusive flows which may be highly non-linear also in the derivatives. Furthermore, is allows for a more flexible structure of the equations.

The main idea is to replace the higher-order object $F(u, \partial_\rho u, \rho)$ with a mathematical operator $\mathscr{F}(u, g_\eta, w_{\eta\xi}, \rho)$ which behaves in a more controlled way. We introduce the right and left derivatives $g_1$ and $g_2$ via the respective numerical flux. From $g_1$ and $g_2$ we can then reconstruct $\partial_\rho u$ in order to get a well-conditioned derivative. Similarly we use the four second-derivative terms from the left and right, $w_{\eta\xi}$, for the second derivative and also to correct errors in $\partial_\rho u$.

### Spatial discretisation

We introduce additional stationary equations to the standard dDG discretisation (5.14) for new variables $g_\eta$ and $w_{\eta\xi}$ accompanying the instationary one,

$$\begin{aligned} \partial_t u + \partial_\rho \mathscr{F} &= 0\,, \\ g_\eta &= \partial_\rho u\,, \\ w_{\eta\xi} &= \partial_\rho g_\eta\,, \end{aligned} \tag{A.6}$$

with $\eta, \xi \in \{1, 2\}$ and the operator $\mathscr{F}$ dependent on all variables and to be specified later. We choose $g_\eta$ and $w_{\eta\xi}$ to be projections of first and second order derivatives of $u$ respectively. The aim is then to build projections which are in analogy to right- and left-side derivatives and use them to reconstruct the (continuum) derivative by averaging.

Next, we apply the standard DG spatial discretization to (A.6), i.e. we integrate (A.6) against

local test functions $\psi_p$ on each cell and perform a partial integration. From this we obtain

$$\begin{aligned}
\int_{D_k} \left( (\partial_t u_h + s_h)\,\psi_p + \mathscr{F}(u_h, (g_\eta)_h)\,\partial_x \psi_p \right) &= -\int_{\partial D_k} \widehat{\mathscr{F}}(u_h^-, u_h^+)\cdot \hat{n}\,\psi_p\,, \\
\int_{D_k} (g_\eta)_h \psi_p - \int_{D_k} u_h \partial_x \psi_p &= \int_{\partial D_k} \widehat{g}_\eta(u_h^-, u_h^+)\cdot \hat{n}_k\,\psi_p = 0\,, \qquad \eta \in \{1,2\}\,, \\
\int_{D_k} (w_{\eta\xi})_h \psi_p - \int_{D_k} (g_\eta)_h \partial_x \psi_p &= \int_{\partial D_k} \widehat{w}_{\eta\xi}((g_\eta)_h^-, (g_\eta)_h^+)\cdot \hat{n}_k\,\psi_p = 0\,, \qquad \eta \in \{1,2\}
\end{aligned} \tag{A.7}$$

for each grid cell $D_k$ separately. Here we have introduced the outward-facing normal vector $\hat{n}_k$ on the cell surface $\partial D_k$ as well as the value of $u_h$ on the cell surface from the inside, $u_h^-$ and from the outside $u_h^+$. We proceed by specifying the numerical fluxes $\widehat{\mathscr{F}}$, $\widehat{g}_\eta$, and $\widehat{w}_{\eta\xi}$, which connect solution variables across cell boundaries and are a crucial ingredient to formulating a consistent DG method.

In order to get analogons of right- and left-derivatives, the choice of fluxes $\widehat{g_\eta}$ is to use up- and downwind fluxes, respectively, and similarly for the second derivatives $\widehat{w}_{\eta\xi}$, i.e.

$$\begin{aligned}
\widehat{g}_1(u_h^-, u_h^+) &= u_h^+\,, \quad \widehat{g}_2(u_h^-, u_h^+) = u_h^-\,, \\
\widehat{w}_{\eta 1}((g_\eta)_h^-, (g_\eta)_h^+) &= (g_\eta)_h^+\,, \quad \widehat{w}_{\eta 2}((g_\eta)_h^-, (g_\eta)_h^+) = (g_\eta)_h^-\,.
\end{aligned} \tag{A.8}$$

Effectively, this means that $g_1$ is a right-sided derivative and $g_2$ a left-handed one, whereas the $w_{\eta\xi}$ give all combinations of two either right- or left-sided derivatives. In doing this, we provide the instationary equation with information on all possible jumps in derivatives between cell borders. We can now go on to devise a scheme on how to introduce this information to the flow in a consistent, stabilizing manner.

For the collective flux of $\mathscr{F}$, i.e. $\widehat{\mathscr{F}}$, we utilize the standard Lax-Friedrichs flux,

$$\widehat{\mathscr{F}} = \{\{F\}\} + \frac{c}{2}[[u]]\,, \tag{A.9}$$

where $c$ is the local wavespeed in the system, i.e. the largest eigenvalue of $\frac{\partial F}{\partial u}$.

The only thing to complete the picture, is the definition of $\mathscr{F}$. In order to get a non-oscillatory derivative contribution to the flow, set it to

$$\mathscr{F} = F\left(u, \frac{g_1+g_2}{2}, \frac{w_{12}+w_{21}}{2}, \rho\right) + \alpha\big(w_{11} - w_{12} - w_{21} + w_{22}\big)\,. \tag{A.10}$$

This choice of derivative $\partial_\rho u \simeq \frac{g^+ + g^-}{2}$ is elaborated on in [371], where one sees that it can be viewed as analogous to the central difference derivative operator on a Cartesian grid. The convergence and stability of this method has been shown and tested in [372] for a set of toy problems.

The correction term

$$\alpha\big(w_{11} - w_{12} - w_{21} + w_{22}\big)\,, \tag{A.11}$$

that has been added to (A.10) in order to define the numerical operator can be viewed as

$$\alpha h^2 \frac{\big(w_{11} - w_{12} - w_{21} + w_{22}\big)}{h^2} \to \alpha h^2 \partial_\rho^4 u\,, \tag{A.12}$$

in the limit of small $h$. Effectively, this is a source term added to the flow of $u$ which exerts a force that pushes the second derivatives $w_{\eta\xi}$ onto each other, leading to (local) continuity in the first and second derivatives of $u$.

Framed differently, we are approximating our parabolic problem by a fourth-order problem which reduces to the original equation in the limit of $h \to 0$. This has been shown to work well for certain classes of non-linear second-order equations [373], stabilizing their high-order contributions in a controlled manner. Additionally, (A.11) implements a penalty for jumps in $g^+$, $g^-$, thus stabilizing the solution at the cell borders.

The choice of $\alpha$ should be such, that $\alpha > |\frac{\partial F}{\partial(\partial_\rho^2 u)}|$. We will however define it to be constant in time and by choosing it through experiment: One wants it to be as small as possible, but large enough to suppress oscillations in the derivatives. We comment that a choice of $\alpha = c|\frac{\partial F}{\partial(\partial_\rho^2 u)}|$ with some constant $c > 1$ is possible, but works in numerical experiments worse than choosing $\alpha$ globally constant.

### A.1.3. Higher derivatives around expansion points

*This Appendix is taken from [4].*

In this section we explain how to extract quantitatively precise higher order derivatives of the solution, evaluated at an expansion point $x_0$. These terms are directly evaluated from the solution by taking the $n$-th derivative of the functional basis,

$$\partial_x^n u_h^k(t,x)|_{x=x_0} = \sum_{p=1}^{P+1} u_p^k(t)\partial_x^n \psi_p(x)|_{x=x_0}\,, \tag{A.13}$$

and feed back into the flow in a trivial manner. All computations generating data at the expansion point are therefore preformed using an appropriately high polynomial order $P > n$. For specific, strongly dynamical scenarios, the second procedure may lead to apparent convergence towards a false solution. In Chapter 6 we test convergence of the derivatives by making use of some known symmetry properties. The $Z_2$ symmetry of the potential $V$ requires $\partial_x^n V|_{x=x_0} = 0$ for odd $n$, thus we track the numerical values of $\partial_x V|_{x=x_0}$ and $\partial_x^3 V|_{x=x_0}$ throughout the $d = 0$ computation, which displays the highest dynamics and generates the highest numerical error for this check. We find that

$$\begin{aligned} 1.02476e-13 \leq |\partial_x V|_{x=x_0}| \leq 2.18304e-12\,,\\ 2.7792e-10 \leq |\partial_x^3 V|_{x=x_0}| \leq 9.13647e-09\,, \end{aligned} \tag{A.14}$$

for a polynomial order $P = 6$.

## A.2. Time stepping

Throughout this thesis we have used various time-stepping schemes, which have continuously been improved and fitted to the purpose. We begin with a brief explanation of our explicit time-stepping implementation, before discussing implicit steppers which are more adapted to the fRG.

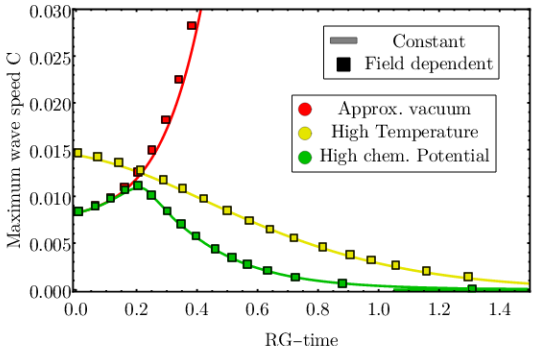


Figure A.1.: Comparison of the maximal information propagation speed $f_{max}$ for constant and field dependent Yukawa couplings at different places in the phase diagram. Both computations were performed with $K = 100$ cells and a local approximation order $N_p = 2$.

### A.2.1. Explicit stepper and CFL-conditions

*This Appendix is taken from [1].*

The solution is computed by an explicit third-order time-stepping scheme from the *dune-pdelab* module, where we additionally implemented Courant-Friedrichs-Lewy (CFL-)conditions. The time step $\Delta t$ is thus limited by the propagation speed of the flow,

$$\Delta t \leq \frac{\Delta x}{(2P+1)} \frac{1}{f_{max}}, \tag{A.15}$$

where $\Delta x$ is the size of the grid cell, $P$ the polynomial degree used in the computation, such that the denominator indicates the total amount of grid points within the respective cell. $f_{max}$ is the maximal propagation speed of the information and was defined in (5.16). This quantity is plotted in Figure A.1 for a computation in the quark-meson model (compare Chapter 8) and in approximate vacuum in the broken symmetry phase and for high temperatures and chemical potential in the symmetric phase.

#### Approaching convexity in the broken symmetry phase

It can be observed from Figure A.1 that the broken symmetry phase has a steadily increasing maximum wave speed. This corresponds to steadily decreasing time steps and leads to long computation times. This behaviour is caused by the time-steps inverse proportionality to the flux,

$$\Delta t \propto (k^2 + u)^{n/2},$$

for some positive integer value of $n$. The two-point function $\Gamma^{(2)}$ can have negative eigenvalues during the RG-flow, which is what happens to the computed function $u = m_\pi^2 = \Gamma^{(2)}_{\pi_i \pi_i}$, the pion mass, in approximate vacuum. The flow is self-regulating, ensuring that the expression in the square root in the proportionality remains positive: The closer the root gets to becoming negative, the stronger the flow increases $u$, causing the modulo $|u|$ to always be slightly smaller than $k^2$. This must hold for $k \to 0$ from which it follows that $u \to 0$, such that $\Gamma^{(2)} = 0$ at infinite RG-time and convexity is restored. $|u|$ teeters on the edge of becoming bigger than $k$ during the entire integration which results in a big flux between grid cells and very small explicit time steps.

#### Convexity in the symmetric phase

The pion mass becomes positive at some point during the computation in the symmetric phase and convexity is restored before $k = 0$. Positive values of $u$ also significantly decrease the flux between grid cells as can be seen from Figure A.1 and increase the size of time steps.

### A.2.2. The necessity for implicit steppers

*This Appendix is taken from [6]. In this work, a plethora of implicit time-stepping schemes was tested in a simple finite difference implementation using Julia. Here, we only present a brief summary of the most significant results in the context of this thesis.*

The problem concerning the exponential decay of the time-step we outlined in the previous section, can be solved with a vast landscape of implicit algorithms. In the following, we benchmark the accuracy and efficiency of different time-stepping schemes for future applications. For a detailed introduction see e.g., [374,375], here we only state their rough features.

The popular family of Runge-Kutta schemes splits into two different classes. The first and most commonly used class of algorithms are the Diagonally Implicit Runge-Kutta (DIRK) methods, it includes well-known algorithms such as Implicit Euler or the Trapezoid/Implicit Midpoint algorithm used in the Crank–Nicolson scheme. The second class contains the Fully Implicit Runge-Kutta (FIRK) schemes. While in DIRK schemes for each internal stage the system of equations can be solved subsequently, in FIRK schemes a coupled system of equations has to be solved. To be more precise, in explicit RK schemes each stage is obtained from previous stages only, while in DIRK methods the right-hand side of each stage can contain itself. In FIRK methods, the right-hand side may contain all stages. As a direct consequence, DIRK schemes are a lot easier and cheaper to implement and are typically also faster, if they capture the stiffness of the system. Consequently, DIRK methods are the most commonly implemented implicit methods in toolboxes for PDEs.

The next big class of algorithms under investigation in this work are the Rosenbrock methods, including their derived Rosenbrock-W extensions. They incorporate the Jacobian directly in the timestep update, essentially performing the step of a Newton iteration, and they can be seen as an extension of the DIRK methods. As a consequence, for non-autonomous equations also the RG-time gradient of the flux appears in the formula. They show impressive stability and accuracy properties for a wide range of problems, but their implementation is comparatively tedious. In schemes collected as Rosenbrock-W, the Jacobian and time gradient are not updated at every step, but in a lazy manner, depending on the algorithm.

The last big class of implicit algorithms are the implicit multistep schemes. Compared to the RK schemes, no internal stages are evaluated, but the information from previous steps is used in the update step. Some of the most used libraries to solve stiff systems of ODEs, including the `SUNDIALS` library [376,377] or the `ODEPACK` package [378], focus on implicit multistep methods. Both of the aforementioned libraries are also included via their Julia interface [379]. A big advantage of implicit multistep methods is that they easily allow for adaptive choice of order, greatly improving performance.

#### Error norms

Both for the purpose of checking if a Newton solver has converged, as well for choosing the size of an adaptive time-step, an error norm of the residual is used. For large problems, where

a LU decomposition is not feasible, such a norm is also needed to check if an iterative algorithm has converged.

To be more explicit, consider absolute and relative precision limits $s_{\text{abs}}$ and $s_{\text{rel}}$. For a residual vector $r$ and a solution vector before the iteration ($u$) and after ($\tilde{u}$) on a grid of size $N$, we could define the normalized error using an $l_2$-norm as,

$$e_{l_2} = n_{l_2} \frac{\|r\|_2}{s_{\text{abs}} + s_{\text{rel}} \max(\|u\|_2, \|\tilde{u}\|_2)}, \tag{A.16}$$

with $n_{l_p} = N^{\frac{1}{p}}$. Generically, this is the standard kind of error norm implemented in many discretisation frameworks for finite difference and finite elements. However, such a definition can allow locally large errors in cases where locally strong dynamics occur, which quickly destabilize the system.

Therefore, an error-norm which evaluates the relative precision locally is more pertinent,

$$e_{\text{loc}} = n_{l_p} \left\| \frac{r_i}{s_{\text{abs}} + s_{\text{rel}} \max(|u_i|, |\tilde{u}_i|)} \right\|_p . \tag{A.17}$$

In `DifferentialEquations.jl` and in the `SUNDIALS` suite, the error norm (A.17) is implemented with $p = 2$, which is sufficient for the problems considered in this work. However, we would like to comment that in the presence of spatially localized phenomena with fast dynamics we found it necessary to choose $p = \infty$ in order to ensure stability of the evolution.

### Work-precision

For solving flow equations in everyday applications, the most important quantity measuring the performance is the work-precision relation, i.e., how does the accuracy behave with computing time. Beforehand, a reference solution was generated using the `KenCarp58` algorithm. For this reference solution, the absolute and relative accuracy goals were chosen as $10^{-15}$, the highest accuracy feasible with double-precision floating-point numbers. By comparing different algorithms, i.e., `RadauIIA5`, `QNDF` and `Rodas4`, at this target accuracy, we found the maximally actual achievable accuracy to be roughly $10^{-12}$, measured in the $\ell_2$-norm. Therefore, we excluded all results in the survey with $\|a_i - a_i^{ref}\|_{\ell_2} < 1.25 \cdot 10^{-12}$. Slight remnants of the resulting saturation effect when investigating the work-precision relation are still visible.

In order to investigate the work-precision relation, we scanned all possible combinations of absolute and relative target accuracies in the range $10^{-8} \ldots 10^{-12}$ in steps of one ($\log_{10}$ scale). We excluded all runs that did not reach the final RG-time $t = 6$, which was mostly the case at lower accuracy goals and explains the lower scan range of $10^{-8}$. The DIRK algorithms, here we show the `TRBDF2` algorithm, are looking very promising, considering that they are low-order methods. It is also noteworthy that the popular choices `ImplicitEuler` and `Trapezoid` performed extremely poor.

The Rosenbrock methods are relatively independent of the specific choice of algorithm. While they do require significantly more time to push the high precision boundary, they shine through their remarkable stability and over-performance in actually achieved accuracy.

We turn to implicit multistep methods, for the purpose of this discussion, including `SUNDIALS`' `CVODE_BDF` and `ODEPACK`'s `lsoda`. While being unable to push toward really small accuracies, the variable order BDF implementations, i.e., `QBDF`, `QNDF` and `CVODE_BDF`, are attractive due to their very short run-times. `FBDF` performed similar, but performed worse than `QBDF` and `QNDF` due to reduced stability, i.e., requiring a significantly smaller minimal allowed step size.

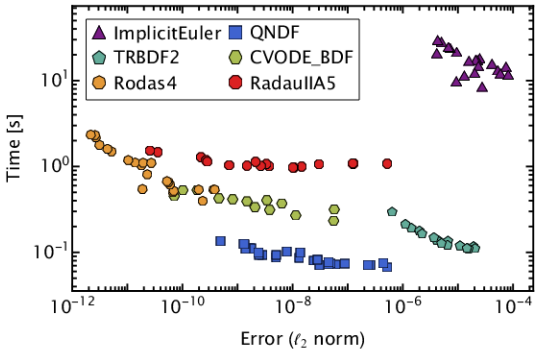


(a) Work-precision diagram. Noteworthy are the very efficient nature of the Implicit Multistep algorithm `QNDF`, the high accuracy of the Rosenbrock algorithm `Rodas4` and the poor performance of `ImplicitEuler`.

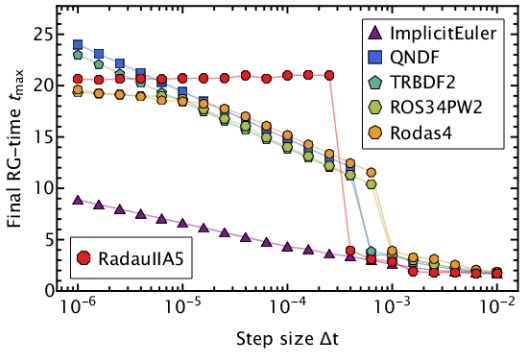


(b) RG-time stability. Noteworthy is the notion of pseudo stability, visible from the jump in final RG-time around $10^{-3}$.

Figure A.2.: RG-time integration survey for different time-steppers in the O(1) model, using the flow (5.7). The computation uses a finite difference implementation in Julia. For more details see the corresponding publication [6].

Turning towards the FIRK methods, we found `RadauIIA5` to be very stable and well-performing, while `RadauIIA3` was one of the worst performing algorithms that still managed to solve the system. We could not find an obvious explanation for the drastic difference between the two very similar algorithms. We suspect it to be related to the lack of a pseudo-stability region for `RadauIIA3`, which will be discussed next.

Finally, the family of implicit extrapolation algorithms performed significantly worse than the other families of algorithms, rendering them irrelevant for normal applications to flow equations.

For the reader's convenience, a collection of well performing algorithms, and `ImplicitEuler` for reference, is shown in Figure A.2a. The depicted algorithms, i.e., `QNDF`, `TRBDF2`, `Rodas4`, `RadauIIA5` and `CVODE_BDF`, can be considered excellent choices when being confronted with a novel problem/equation in the context of derivative expansions in flow equations.

### Stability in the infinite RG-time limit

There is another aspect when solving fRG equations in everyday applications that is highly relevant: The long RG-time stability of the RG-time integration. In order to test this faithfully, we switch to fixed RG-timestep size evolution, where the step size is denoted by $\Delta t$. The flow is integrated until we detect an inconsistency/instability in the flow, i.e., either the solution becomes non-monotonic or the positivity bound is violated. The last successful RG-timestep then determines $t_{max}$. Ideally, there would be some maximal step size $\Delta t_{cr}$, for which all smaller RG-timesteps $\Delta t < \Delta t_{cr}$ provide stable evolution, i.e., $t_{max} \to \infty$. In practice, we cannot integrate until $t_{max} \to \infty$. Therefore, we chose the maximal cutoff at $t = 50$, which is the same for all practical purposes. The external libraries are excluded for technical reasons in this survey, we do not expect them to perform as well as the pure Julia implementations, due to the lack of auto differentiation in the calculation of the Jacobian.

The selection of algorithms is depicted in Figure A.2b. There is an immediate observation: The simulation does not exceed $t_{max} \approx 20 \ldots 25$, i.e., is does not feature stability. However,

there is a sharp increase in $t_{max}$ at a step-size $\Delta t \approx 10^{-3}$. This sharp increase precisely makes the difference between breaking down during the flatting of the potential and being able to properly resolving this essential part of the evolution. We call this notion *pseudo stability*. Luckily, a large part of the investigated algorithms, particularly the Rosenbrock and implicit multistep methods, posses this property. The final RG-time reached by most algorithms in the standard and mass formulation is limited by double precision in the (non-)linear solver part. This can be easily seen by estimating the relevant orders of magnitude in their discrete equations.

Furthermore, for the method `RadauIIA5` the jump in the final RG-time is so large, that we cannot differentiate between pseudo stability and proper stability of the algorithm. One might suspect that the method is stable, but limited by finite numerical precision.

We would like to note that the generalisation thereof to more complicated theories, e.g., a $O(N)$-theory with $N > 1$, is ambiguous and has to be worked out. In general, the notion of pseudo stability hints towards the existence of two different stability criteria. One being related to stability with respect to non-analyticities, i.e., the kink in the current example. The other one being related to the existence of a singularity bound and can be circumvented by, for example, a log formulation, see [6].

## A.3. Local Discontinuous Galerkin: An implementation

*This section is based entirely on [5], all figures are taken from the publication.*

In this section of the Appendix, we describe how to reformulate the O(N) model flow, derived in Section 5.1 and Appendix B.3.1, such that can be solved with the LDG method of [251]. The numerical discretisation is outlined in Appendix A.3.1. An in depth description of the implementation is given in Appendix A.3.2, accompanying the Github repository [12].

### A.3.1. Assumptions on the form of equations

As a guiding example, let us examine the flow equation for an O(N) system, which we will keep in mind when explaining the LDG method. An inherent property of the flow is its dependence on the second derivative of the effective action. This translates to a system of equations containing convection, as well as diffusion. Instead of directly looking at the effective potential $V(x)$ of the theory, we take its first derivative and note that the two unknowns of the system are linked by another derivative

$$u = \partial_x V\,, \quad \text{and} \quad v = \partial_x^2 V\,. \tag{A.18}$$

Thus we introduce $\partial_x u$ as a further unknown, apart from $u$

$$\partial_x u = v\,. \tag{A.19}$$

Having established these definitions we allow for the following general form of the equations

$$\begin{aligned} \partial_t u - \partial_x F_t(u,v) &= 0\,, \\ \partial_t v - \partial_x\big(G_t(u,v) + a_t(s)\partial_x s|_{s=u+b(x)v}\big) &= 0\,, \end{aligned} \tag{A.20}$$

where $u = u(t,x)$, $v = v(x,t)$ are the sought after solutions and we have some initial conditions at $t = 0$ which we evolve in time. This specific form is motivated by the expressions derived in

Section 5.3.1 and Section 5.1. It is given at this point to construct the numerical framework in a general way. $u(t,x)$ is the solution to a purely convective equation with a Lipschitz conservative, RG-time-dependent flux $F_t$, whereas the equation for $v(t,x)$ has a convective (Lipschitz) flux $G_t$ and allows for a diffusive term linear in $\partial_x v$, which inherently depends on the combination $s = u + b(x)v$, with a positive prefactor $a_t$. For simplicity we drop the $(\cdot)_t$ subscript from now on, which indicates the RG-time dependence of the terms. The diffusive term in $\partial_x v$ prevents the use of direct DG methods discussed previously in [1, 65], since there is no sensible formulation of a numerical flux for higher derivative terms. In general the direct DG method is still applicable but has possibly non-negligible errors, as discussed above, if its contribution to the numerical flux is small.

The LDG method, as developed in [251], presents a formulation for this additional diffusive flux, by solving a second, stationary equation. Afterwards, we discuss the introduction of the appropriate numerical fluxes. Note, that introducing $v = \partial_x u$ as an independent unknown does not remedy the problem of having a second-order PDE, but it enables us to fit the framework given by the LDG method and thus construct a convergent and stable scheme for the fRG equations of such systems. The price to pay is a potentially reduced order of convergence due to promoting a dependent quantity into an independent one. However, this effect is practically mitigated by the high order of accuracy the LDG method. Its error is of order $O(\Delta x)^{P+\frac{1}{2}}$, where $\Delta x$ is the grid spacing and $P$ is the maximal order of the trial functions.

### The stationary Equation

We will now present the LDG formulation for the system given in (A.20). The main idea here is to introduce a stationary equation which captures the additional derivative term by rewriting it as $q = \sqrt{a(u+b(x)v)}\,\partial_x(u+b(x)v)$

$$\begin{aligned} \partial_t u + \partial_x(F(u,v)) &= 0\,, \\ \partial_t v + \partial_x\big(G(u,v) - \sqrt{a(u+b(x)v)}q\big) &= 0\,, \\ q - \partial_x j(u+b(x)v) &= 0\,. \end{aligned} \tag{A.21}$$

Supplemented by some initial condition for $u(t=0,x)$ and $v(t=0,x)$. Hence the system (A.20) now contains two *instationary* equations for the RG-time evolution of $u$ and $v$ and one additional *stationary* equation for $q$. The flux of the stationary equation is in a conservative form and given by

$$j(s) = \int_0^s \sqrt{a(s')}\mathrm{d}s'\,, \tag{A.22}$$

which follows simply from applying the chain rule

$$\sqrt{a(s)}\partial_x s = \partial_s j(s)\partial_x s = \partial_x j(s)\,, \tag{A.23}$$

with $s = u + b(x)v$. We note that this particular formulation is insofar different from its original formulation in [251] as $q$ is dependent on two variables through $s$, $u$ and $v$.

### Numerical fluxes

In order to numerically solve the system of conservation equations given in (A.21) over an interval $\Omega$, we introduce a one-dimensional grid over a computational interval $\Omega_h$. $\Omega_h$ is

separated into $K$ non-overlapping elements $D^k$, following the notation from [65]. Consider the full solution to be given by $\boldsymbol{w} = (u, v, q)^t$, then the local, approximate solution $\boldsymbol{w}_h^k = (u_h^k, v_h^k, q_h^k)^t$ is described by a polynomial of degree $P$ in every cell $D^k$,

$$\boldsymbol{w}_h^k(t,x) = \sum_{p=1}^{P+1} \boldsymbol{w}_p^k(t)\psi_p(x). \tag{A.24}$$

Here we also introduce standard notation from the DG literature for the average $\overline{\boldsymbol{w}}$ and the jump $[\boldsymbol{w}]$ across a cell boundary. Supposing some solution $\boldsymbol{w}_h^k$ on the cell $D^k$, we label $\boldsymbol{w}^-$ as the solution inside the cell and $\boldsymbol{w}^+$ as the solution in the neighbour cell.

A solution to (A.21) is only defined in a weak sense, and the resulting system of equations for $\boldsymbol{w}_h^k(t,x)$ reads

$$\begin{aligned}
\int_{D^k} \left((\partial_t u_h^k)\psi_p - F_h^k(u_h^k)\partial_x\psi_p\right) \mathrm{d}x &= -\int_{\partial D^k} \mathrm{h}_{\mathrm{conv},1}\cdot\hat{n}\,\psi_p \,\mathrm{d}x\,,\\
\int_{D^k} \left((\partial_t v_h^k)\psi_p - \left(G_h^k(u_h^k, v_h^k) - \sqrt{a_h^k(u_h^k + b_h^k(x)v_h^k)}\,q_h^k\right)\partial_x\psi_p\right) \mathrm{d}x &= -\int_{\partial D^k} \left(\mathrm{h}_{\mathrm{conv},2} + \mathrm{h}_{\mathrm{diff},2}\right)\cdot\hat{n}\,\psi_p \,\mathrm{d}x\,,\\
\int_{D^k} \left(q_h^k\psi_p + j_h^k(u_h^k + b_h^k(x)v_h^k)\partial_x\psi_p\right) \mathrm{d}x &= -\int_{\partial D^k} \mathrm{h}_{\mathrm{diff},3}\cdot\hat{n}\,\psi_p \,\mathrm{d}x\,,
\end{aligned} \tag{A.25}$$

where $\hat{n}$ is the outwards facing unit normal vector at a cell boundary.

The numerical fluxes, at the right-hand side of (A.25) have been separated into convective and diffusive contributions

$$\boldsymbol{h}(\boldsymbol{w}^-, \boldsymbol{w}^+) = \boldsymbol{h}_{\mathrm{conv}}(\boldsymbol{w}^-, \boldsymbol{w}^+) + \boldsymbol{h}_{\mathrm{diff}}(\boldsymbol{w}^-, \boldsymbol{w}^+). \tag{A.26}$$

For the convective flux we choose the standard LLF-flux, which has already been used in the direct DG implementations [1, 65], given by

$$\boldsymbol{h}_{\mathrm{conv}}(\boldsymbol{w}^-, \boldsymbol{w}^+) = \begin{pmatrix} \bar{F} \\ \bar{G} \\ 0 \end{pmatrix} - \frac{C_{\mathrm{conv}}}{2}[\boldsymbol{w}]. \tag{A.27}$$

$C_{\mathrm{conv}}$ corresponds to the speed of information propagation across the interface and is chosen as the largest eigenvalue (or an approximation thereof) of the Jacobian

$$J = \begin{pmatrix} \partial_{w_1} F & \partial_{w_2} F \\ \partial_{w_1} G & \partial_{w_2} G \end{pmatrix}. \tag{A.28}$$

It produces an additional diffusive smoothing factor, which enforces the continuity of the solution between cells.

The diffusive numerical flux, which ensures continuity when a diffusive flow is present, is given by

$$\boldsymbol{h}_{\mathrm{diff}}(\boldsymbol{w}^-, \boldsymbol{w}^+) = \begin{pmatrix} 0 \\ -\frac{[j(u+b(x)v)]}{[u+b(x)v]}\bar{q} \\ -j(u+b(x)v) \end{pmatrix} - \frac{C_{\mathrm{diff}}}{2}[\boldsymbol{w}], \tag{A.29}$$

Here a smoothing across cell boundaries is being applied using a diffusive wave-speed, for which

$$C_{\text{diff}} = \begin{pmatrix} 0 & 0 & 0 \\ 0 & 0 & c \\ 0 & -c & 0 \end{pmatrix}, \tag{A.30}$$

is chosen to emulate the LLF-flux (A.27) and we use the approximate wave-speed $c = \sqrt{a}$.

## A.3.2. DUNE and the dune-FRGDG module

All results obtained from DG methods have been computed by using DUNE, the Distributed and Unified Numerics Environment [252], which provides a wide range of tools to solve PDEs numerically. The method detailed in this work has been implemented within the *dune-FRGDG* module, an extension of DUNE specially for solving fRG flows using discontinuous Galerkin methods. A build containing the models showcased in this work can be freely accessed on the web [12]. Firstly, we give detailed instructions on the installation of the framework. Next, the general structure of the module is outlined. This is followed by a discussion of different components: The *simulation set*, which allows to specify the general numerical settings of the calculation, such as the numerical grid or the choice of numerical fluxes. The implementation of physical models within the framework is discussed next, and we give some additional remarks on the parameters that can be changed with the `.ini` files after compiling the programs.

### Installation

In the following we give step-by-step instructions to install the *dune-FRGDG* module:
Before setting up the framework, all dependences of dune-FRGDG need to be available. These dependences are:

- CMake $\geq$ 3.13
- Open MPI
- GCC with support for C++17
- pkg-config
- GSL - GNU Scientific Library

The framework itself can be cloned from the public github repository [12],

```
$ git clone https://github.com/satfra/dune-FRGDG.git
```

Next, the user should run an automatic setup script and to build the framework itself:

```
$ cd dune-frgdg
$ bash ./setup.sh
$ bash ./build-release.sh
```

The setup script will clone and modify all necessary DUNE modules for the framework. The script `build-release.sh` will run CMake and make on all modules to produce a release build of the code. Alternatively, if a debug build of dune-FRGDG is needed, the user can run `build-debug.sh` instead. The header files, where most of the code is contained in, can be

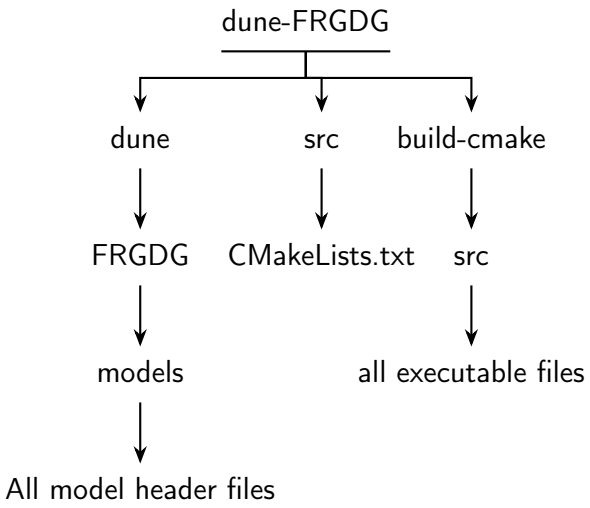


Figure A.3.: Folder structure of the dune-FRGDG module after initial setup.

found at `dune-FRGDG/dune/FRGDG`. All source files are at `dune-FRGDG/src`. After building the project, the binary executable files can be found in `dune-FRGDG/build-cmake/src`. These can be either called single-threaded like

```
$ ./anharmonicOscillator
```

or using MPI with

```
$ mpirun -n 4 ./anharmonicOscillator
```

where one can replace the number 4 used here by the amount of desired MPI nodes.

### Implementation in DUNE

The basic design of the computational framework is outlined. The general structure is built on the basis of the dune-project [252], more precisely the *dune-pdelab* module [286]. The framework is devised such that an end-user is only required to specify equations and some properties of the DG setup in a template. These specifications are then pieced together and used by the backend of the code to perform the simulation.

The general structure of the framework itself is shown in Figure A.4a, the folder structure of the installed module can be seen in Figure A.3. Any simulation consists of the user-specified simulation set (frontend) where all specifics of the simulation are abstracted, and the driver class (backend) where the actual simulation is performed. The simulation set contains information about the chosen grid, finite element space, solver algorithms and the actual DG equations in the form of the numerical fluxes and a model class. The driver class uses a specified scheme that defines the way the equations are handled (in our case, the DG scheme and the LDG scheme) to do time-stepping. Within the schemes the way time-stepping is done is defined, i.e. for the DG scheme one uses a RK scheme to directly solve one instationary PDE, while the LDG scheme incorporates the solving of additional stationary equations into the RK scheme.

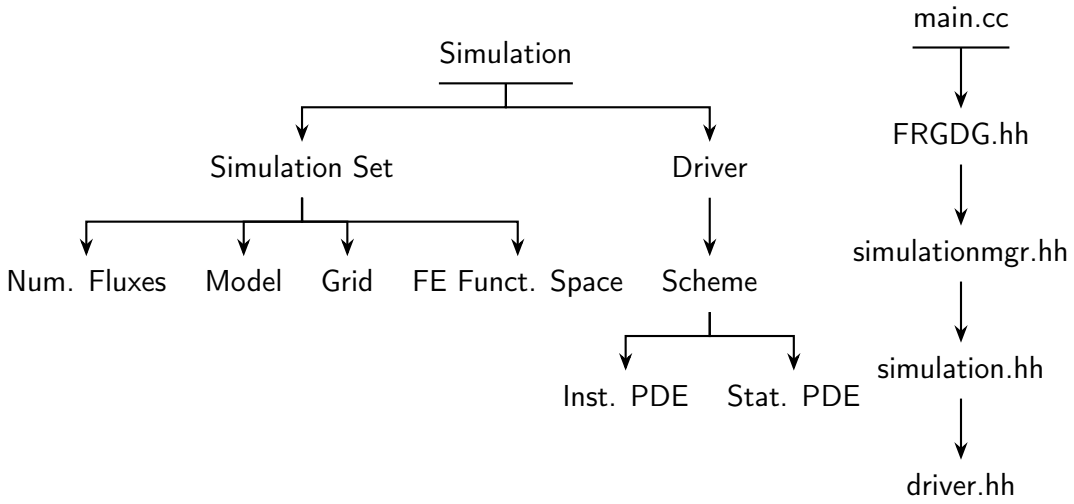


(a) Logical structure of a simulation using the DUNE-FRGDG framework. The Simulation Set contains user-specifics, while the Driver performs the execution of all backend code.

(b) The execution flow of a typical program using the DUNE-FRGDG framework, starting from a file main.cc which contains the main function.

In practice, as any C++ program, the simulation starts with a main-function. Here, we first define a simulation which uses a specific simulation set (here for a large N-model) and then start the backend code execution flow by calling `Dune::startFRGSimulation`.

```
using SIM = Simulation<largeN::SimSet>;
Dune::startFRGSimulation<SIM>(argc, argv,"largeN.ini");
```

The function `Dune::startFRGSimulation` is found in the header file `FRGDG.hh` and does some MPI setup, as well as reading the supplied initialisation file before calling the simulation manager `SimulationMgr`:

```
SimulationMgr<SIM> mgr(ptree,helper);
mgr.run();
```

In the simulation manager a simulation is created and started from the supplied simulation template and initialisation parameters:

```
SIM sim(ptree,mpihelper.getCommunication(),0,log);
sim.start();
sim.finish();
```

Finally, the simulation itself invokes the driver, which goes on to construct the DG system and solve it:

```
DRV<N> driver(gv,fem,pP,ptree,mpicomm,log);
driver.Run();
```

The execution flow is shown in Figure A.4b. Although the step through the `SimulationMgr` may seem superfluous, the structure is designed to allow extending the `SimulationMgr` to do massive parallelisation of simulations and their management.

### Numerical settings

Before implementing a physical model we must specify the numerical setting, i.e. the grid, the integration scheme or the numerical fluxes. This is done in the `SimSet` class in the *models/ON.hh* header file, which also contains the physical equations.

Generally, LDG methods are defined on a domain of arbitrary dimension composed of $K$ cells, $\Omega = \cup_{k=0}^{K} D_k$. Therefore, we must chose an appropriate grid-implementation:

```
using RF = double;
static constexpr unsigned dim = 1;
using GridConstructor = CubicYaspGridConstructor<RF, dim>;
```

Here, we first set all computations to be performed with double precision and then specify a one-dimensional grid to be used. In principle the grid dimension can be set to any integer number. Currently, our computations use cubic grids, i.e. rectangular grid cells.
The next step is to specify the test-function space within each grid cell $D_k$. A numerical approximation using test-functions $\psi_n$, compare (A.24), to the exact solution $\boldsymbol{w}$ of (5.19) reduces the degrees of freedom of $\boldsymbol{w}_h^k$ to a finite number. This test function space is set up in the following way:

```
template<int order>
using FEM = Dune::PDELab::QkDGLocalFiniteElementMap<RF, double,
  order, dim, Dune::PDELab::QkDGBasisPolynomial::legendre>;
static constexpr std::array<int,4> orders {1,2,3,4};
```

The module *dune-pdelab* [286] provides the polynomial space $Q_k$, which is spanned by all polynomials up to order $k$ in the according number of dimensions, for example $Q_1 = \{1, x, y, xy\}$ if `dim=2`. The Legendre polynomials are chosen as a basis of this test-function space. Also, when increasing the dimensionality of the grid, an appropriate tensor-product of one-dimensional function spaces is used. Furthermore the polynomial orders $\{1,2,3,4\}$ are precompiled into the program and are available to chose from in the *.ini* file. We note here that the code can be used for finite volume computations if the polynomial order is set to 0. Similarly, we recover a finite element method (FEM) if continuity is enforced between cells.
The numerical approximation from (A.24) is inserted in (5.19) and projected onto the test function space. This formulation does not account for possible discontinuities at the cell borders. Worse, the solution is effectively double-valued at the cell borders $x_r^{k-1} = x_l^k$. This necessitates the introduction of a numerical flux:

```
using Numflux = utils::static_switch<idx,LLFfluxLDG<Model<idx>>,
LLFfluxLDG<Model<idx>>>;
```

This example uses our standard choice of numerical flux, which is the LLF-flux. Other possible choices are implemented and can be found in the `numericalflux` folder, such as up- and down-winding fluxes, as well as a central flux.

Now, the inside of each cell reduces to a finite element problem where the boundary conditions are given by the numerical flux. An appropriate solver is the key ingredient to FEMs and is provided by the *dune-istl* module [287]. Here we distinguish the solvers given by the `LS_stat` and the `LS_instat` types, for the stationary and instationary equations respectively, in the LDG setting. The correct interplay of both solvers is ensured by the `LDGScheme`.

### Model definitions

The DUNE framework, as well as *dune-FRGDG*, use an object-oriented approach to structuring the code. Thus, a system of LDG equations is represented by classes which contain methods and member variables corresponding to the ingredients detailed in Appendix A.3.1.

When setting up the computation of a specific system of equations, we distinguish between the *instationary* and *stationary* equations, contained in the model classes `iModel` and `sModel` respectively. Every model class is derived from a template class, which is contained in the file `models/modelinterface.hh`. There, every implemented building block of a model is predefined and set to fill the equations with zeros. This way the user can redefine all methods that are needed for a specific physical model in the derived class, whilst everything else defaults to do nothing. Therefore, first of all, we need to choose the correct template from which we derive the model class. The signatures of the two model classes thus read

```
class iModel:public ModelInterfaceLDGinstat<GV,2,1>;
class sModel:public ModelInterfaceLDGstat<GV,2,1>;
```

where also the number of components in each class is specified. `iModel` contains the flow for the two-component vector `Range0 u` $= (u, v)^t$ and `sModel` specifies the equation for the single component vector `Range1 q` $= (q)^t$ - there are two instationary components and one stationary one, corresponding to the LDG system of the O(N) model in Section 5.1. We will use the O(N) model from here on as an implementation example. The model can be found in `models/ON.hh`. The methods in the model-classes are called for every single element and interface separately. This enables the parallelisation of the code: if the grid is split into several sub-grids these only need to communicate on a few interfaces, since in general every cell only depends directly on its Neighbors due to the numerical fluxes.

Let us focus first on the instationary equations in the `iModel` class:
First, we implement the initial conditions. The initial parameters in the UV are determined in the constructor of the model-class, where they are directly pulled from the initialisation file via `ptree` (cf. Appendix A.3.2):

```
iModel(Dune::ParameterTree ptree_): MI(ptree_)
{
  l2 = ptree.get("param.l2", RF(0));
  l4 = ptree.get("param.l4", RF(71.6));
  l8 = ptree.get("param.l8", RF(71.6));
}
```

The method `u0` specifies the initial conditions at the beginning of the simulation, as set in (5.28):

```
Range0 u0(const E &e, const X &x) const
{
  const X xg = e.geometry().global(x);
  Range0 u(0.0);
  u[0] = l2 + xg[0] l4 + powr<3>(xg[0]) l8;
  u[1] = l4 + 3. powr<2>(xg[0]) l8;
  return u;
}
```

In this example `e` is a grid parameter, indicating the specific grid cell on which the method is evaluated, whereas `x` gives the position within the cell. From this we get the global position `xg`, which is a vector in the dimension of the grid.

To get the code formulation of the flow we insert the ingredients from the physical model Section 5.1 into the weak formulation of the equations (A.25), after which ingredient in (A.25) corresponds to a method in the model class. Appendix A.3.1 specified the equations that can be solved within this framework and we will now identify the components of the general mould (5.19) and show their counterpart in the model-classes. The following code-snippets abbreviate the parameter lists of the methods by '...', as they become too lengthy to show here and do not contain important information. We recapitulate the first line of the general mould (5.19)

$$\partial_t u + \partial_x F(u,v) = 0\,. \tag{A.31}$$

The DG discretisation of this equation is the first line in (A.25). The only thing we need here is the definition of the flux $F$ and the numerical flux at the interfaces $F^*$.

```
void flux(...) const
{
  const X xg = e.geometry().global(x);
  const RF F = f<N-1>(u[0]) + f<1>(u[0] + 2.*xg[0]*u[1]);
  const RF G = u[1]    f<N-1,1>(u[0]);

  Flux[0][0] = F;
  Flux[1][0] = G;
}
```

RF is the type of floating point numbers we wish to use - this is aliased to `double` in the implementation shown here.

The numerical flux is implemented in a separate file; the choice is done within the *Simulation Set* where all general parameters of the simulation are fixed (e.g. the grid, basis functions, etc). For specific fluxes one needs additional methods, e.g. for $F^\star$ being an LLF-flux we need to implement a method `maxeigenvalues` whose signature can be found in the base class. In the above code snippet, we have also implemented the first part of the second instationary equation, i.e. for the second variable $v$, as it is also discretized in the standard DG way

$$\partial_t v + \partial_x\big(G(u,v) - \sqrt{a(s)}q\big) = 0\,. \tag{A.32}$$

Next, we need to implement the diffusive component $-\sqrt{a(s)}q$ of the flow of $v$. This is done in the following snippet

```
void diffFlux(...) const
{
  const X xg = e.geometry().global(x);
  const RF s = u[0] + 2.*xg[0]*u[1];

  A[1][0] = -std::sqrt(A_d()) k/(k2 + s)    q[0];
}
```

The variable A corresponds to the diffusive component, where the first index of A labels the respective component of $w = (u,v)^t$ and the second one the 'spatial' direction of the diffusion. As we only solve equations on one-dimensional intervals in this work, the second index is always 0.

The numerical flux (i.e. the flow between neighbouring elements) of the diffusive part is implemented in the following.

```
void numericalDiffFlux(...) const
{
  const X xg_s = inside.geometry().global(x_inside);
  const X xg_n = outside.geometry().global(x_outside);

  const RF s_s = u_s[0] + 2. xg_s[0] u_s[1];
  const RF s_n = u_n[0] + 2. xg_n[0] u_n[1];
  const RF diffusion = std::sqrt(A_d()) k 0.5 (1/(k2 + s_n)+1/(k2 + s_s));

  if (!utils::isEqual(s_s, s_n))
        A[1][0] = -std::sqrt(A_d()) k std::log((k2+s_s)
        /(k2+s_n))/(s_s-s_n)  0.5 (q_s[0] + q_n[0]);
  else
        A[1][0] = - diffusion 0.5 (q_s[0] + q_n[0]);

  beta[1][0] = diffusion (q_n[0] - q_s[0]);
}
```

Here, the method is given the information of the inside and outside cell at the border on which it is being called. The first few lines just calculate the quantities at the inside and outside of the cell border. `A` now plays the role of the first contribution to the diffusive numerical flux in (A.29), whereas `beta` implements the additional smoothing in the numerical flux and corresponds to $C_{\text{diff}}[\boldsymbol{w}]$. A distinction is made for the case when $s$ is identical on both sides of the cell border, in which case we replace $\frac{[j]}{[s]}$ with the derivative $\frac{\partial j}{\partial s}$. Since there is no diffusive flux in the first component $u$, the entries at `A[0][0]` and `beta[0][0]` remain zero.

Lastly, it remains to implement the stationary equation

$$q - \partial_x j(u+v) = 0\,. \tag{A.33}$$

This is done in the second model class `sModel` within the same file. First, we need to implement the flux, analogous to the implementation of the instationary flux

```
void flux(...) const
{
  const X xg = e.geometry().global(x);
  const RF s = u[0] + 2. xg[0] u[1];

  if (s > 0)
        F[0][0] = -std::sqrt(A_d()) k  std::log(k2 + s);
  else
        F[0][0] = std::sqrt(A_d()) k  std::log(1./(k2 + s));
}
```

One more thing is missing: The numerical flux of the stationary equation also contains a smoothing term. This is implemented in the following

```
void numericalDiffFlux(...) const
{
  const X xg_s = inside.geometry().global(x_inside);
  const X xg_n = outside.geometry().global(x_outside);

  const RF s_s = u_s[0] + 2. xg_s[0] u_s[1];
  const RF s_n = u_n[0] + 2. xg_n[0] u_n[1];
```

```
  const RF diffusion = std::sqrt(A_d()) k 0.5 (1/(k2 + s_n) + 1/(k2 + s_s));

  beta[0][0] -= diffusion    (u_n[1] - u_s[1]);
}
```

Here, `beta` corresponds to the stationary, i.e. third, component of $C_{\text{diff}}[\boldsymbol{w}]$.

In general, the code is designed to be easily adaptable and can be fitted to any similar problem. For example, adding another instationary equation for a variable to the system is as easy as increasing the first index of the class signature by one and adding in the flow of this third variable in the equations shown here.

### The initialisation file

In this subsection we comment on the parameters which can be specified after compiling the program, in the initialisation file. The initialisation file is a source file and can be found in the `ini` folder. Running a build script will automatically copy the initialisation files to the location of the corresponding executable. The file is divided into several sections, firstly we start with the grid. Here, it remains to specify the length of the grid, as well as the cell density:

```
[grid]
origin = 0
L = 0.03
N = 30
localRefinement = 0
```

All grid parameters need to be specified for each grid dimension, i.e. the input for a two dimensional grid should be given as `N = 30 30`. `origin` specifies the lower left corner of the grid. `L` and `N` denote the grid length and the number of cells respectively.
The `localRefinement` parameter allows for a finer cell spacing in certain areas of the grid by bisecting all cells $n =$ `localRefinement` times. This feature can be used by setting `localRefinement` to $n > 0$ and specifying the additional parameters `localRefinement` $n$, e.g.

```
[grid]
localRefinement = 2
localRefinement0 = 15
localRefinement1 = 10
```

In this example, all evenly spaced cells of the original grid up to cell 15 are bisected once and afterwards the cells up to (the original) cell 10 are bisected once again.

Next, the finite element properties, i.e. the inside of single cells, are specified:

```
[fem]
degree = 2
torder = 3
```

`degree` sets the polynomial order in each cell. Here, the only available options are those previously specified in the simulation set. The order for the Runge-Kutta time-stepping method is set by the `torder` parameter. The currently available options range from first to fourth order RK methods.
All input parameters for the physical model are specified within the `param` section:

```
[param]
Lambda = 0.65
l = 1
```

Here, all initial UV-parameters, such as the initial cutoff-scale $k_{\mathrm{UV}} = \texttt{Lambda}$ or classical values of the couplings, can be added.
Another important element of the computation is the RG-time integration:

```
[time]
maxTime = 3
maxTimeStep = 3e-3
minTimeStep = 1e-15
safetyfactor = 0.001
timeGrid = 1e-2
```

Starting from $t_{\mathrm{UV}} = 0$ one would ideally like to integrate up to $t_{\mathrm{fin}} \to \log(\frac{0}{\Lambda}) = \inf$. Since this is impractical we usually set a `maxTime` up to which the equations are solved. The final RG-scale is then given by $k_{\mathrm{IR}} = \Lambda \exp(-\texttt{maxTime})$. We limit the maximal step size by `maxTimeStep` as a safety precaution. Similarly, we specify a minimal time step (`minTimeStep`), which causes the computation to abort if the step-size goes below this value. Usually, uncharacteristically small time-steps are caused by non-converging solutions. Therefore, we abort the program to avoid spending a lot of computation time on these computations. Ideally, the code limits the time step using the Courant-Friedrichs-Lewy (CFL) conditions [380]. In case of diffusive systems the condition is usually enforced with an additional safety-factor of about `safetyfactor`$\approx 0.001$. Furthermore, we specify the rate at which the computed data should be saved by `timeGrid`. Lastly, it is specified how the data should be saved:

```
[output]
name = lN
subsampling = 0
```

`name` is prepended to the computation-specific details, which are added to the name of the output-file in the model class. The `subsampling` option allows to increase the amount of data points saved. When setting this to zero, the saved data-points in the output files are minimally sampled according to the polynomial order. For smoother output this option can be increased.

### Simulation Results

The results of any simulation are saved in VTK-files at times specified by the user. These can be displayed and examined either using the open-source vtk file viewer ParaView, or read into python or Mathematica scripts using openly available vtk libraries. All results in this thesis have been processed using Mathematica.

# APPENDIX B

## Definitions and analytical relations

*In this Appendix we discuss formulas and technical derivations which do not fit in the main text. Sections are sorted by the corresponding publication.*

## B.1. Finite temperatures and densities

A main focus point of this work is to get insight into the (chiral) phase structure of QCD at finite temperatures and densities. Therefore we briefly review the concepts behind thermal quantum field theory and use the close connection of the euclidean path integral in quantum field theory to statistical mechanics.

The partition function of the grand canonical ensemble is given by,

$$Z_{\mathrm{GCE}} = \mathrm{Tr}\exp\left(-\beta(\hat{H}-\mu\hat{N})\right), \tag{B.1}$$

which looks very similar to the euclidean path integral in quantum field theory if one can identify the right operators for the Hamiltonian $\hat{H}$ and the particle number operator $\hat{N}$. Furthermore, one needs to introduce the right formulation to include the inverse temperature $\beta = 1/T$ to the theory.

Looking at the grand canonical ensemble from an euclidean (imaginary time) setting, one can directly link the inverse temperature to an imaginary time evolution. Furthermore, the Wick-rotated Lagrangian density becomes an energy density and can be identified with the Hamiltonian $\hat{H}$ from the statistical mechanics picture. Hence, the finite temperature corresponds to a finite imaginary time evolution in a euclidean path integral with $t \in [0, \beta]$. For a correct inclusion of the spin-statistics the periodicity and anti-periodicity of the bosonic ($\phi$) and fermionic ($\psi$) correlation functions, respectively, is used. They read,

$$\begin{aligned}
\langle\phi(x_1)\dots\phi(t_i+\beta,\vec{x}_i)\dots\phi(x_n)\rangle &= \langle\phi(x_1)\dots\phi(t_i,\vec{x}_i)\dots\phi(x_n)\rangle\,,\\
\langle\psi(x_1)\dots\psi(t_i+\beta,\vec{x}_i)\dots\psi(x_n)\rangle &= -\langle\psi(x_1)\dots\psi(t_i,\vec{x}_i)\dots\psi(x_n)\rangle\,.
\end{aligned} \tag{B.2}$$

The finite spatial integration together with the boundary conditions translates to discrete frequencies $p_{0,n}$ and an infinite sum in momentum space. Bosonic frequencies are even $p_{0,n} = 2\pi nT$, fermionic ones odd with $p_{0,n} = 2\pi(n+\frac{1}{2})T$ and $n \in \mathbb{Z}$.

Secondly, we include a fermionic chemical potential to our euclidean field theory. This is achieved, analogously to the grand canonical ensemble, by adding a term proportional to the fermionic density $\mu_\psi$ times the particle number $\mathcal{N}_\psi$ to the generating functional (partition function). Then, the number of particles simply follows as $\mathcal{N}_\psi = \frac{\partial \Gamma[\Phi_{\text{EOM}}]}{\partial \mu}$. Furthermore, the number of fermionic particles follows from the integral $\mathcal{N}_\psi = \int_x \bar{\psi}\gamma_0\psi$, which is just the quark number operator. By a comparison with the classical fermionic action in (2.7), it is evident, that this can be understood as a frequency shift of the time-like momentum to the complex plane,

$$p_0 \to \tilde{p}_0 = p_0 + \mathrm{i}\mu_\psi \,. \tag{B.3}$$

To conclude, the finite temperature and density action for the fermions in $d+1$ dimensions is given by,

$$S_{D,T}[\psi] = i \int_0^\beta dt \int d^d x \Big[\bar{\psi}(x)\cdot(\not{\partial} + m_\psi - \gamma_0\mu)\cdot\psi(x)\Big]. \tag{B.4}$$

We note that the euclidean setting with imaginary time does not describe a real time evolution. All computations in this thesis investigate physics in equilibrium.

## B.2. Formulae: Gluon condensation

*This section is taken from [2] and provides analytic relations.*

### B.2.1. Expansions around condensates and color averages

In this Appendix we discuss the implementation of expansions around non-trivial condensates, and comment on the subtleties of the color-averaging procedure associated with the central mass formula in (4.31). In order to illustrates the properties and subtleties, we employ two simple examples: spontaneous symmetry breaking in a scalar $O(N)$ theory, and (color) center symmetry breaking in finite temperature Yang-Mills theory.

Let us first consider a scalar field theory with an $O(N)$ field $\phi$ (including the discrete $Z_2$ symmetry when $N = 1$ ) in the symmetric phase. In the symmetric phase, both the effective action, $\Gamma[\phi]$, as well as expectation values of observables, are typically expanded around $\phi = \phi_0$, where

$$\phi_0^2 = \lim_{\mathcal{V}\to\infty} \frac{1}{\mathcal{V}} \int_{\mathcal{V}} \langle \phi(x)\phi(0)\rangle \,, \tag{B.5}$$

is defined by the order parameter of the theory. The order parameter (B.5) can also be obtained from

$$\phi_0 = \lim_{J\to 0} \langle \phi \rangle \,, \tag{B.6}$$

where $J$ indicates an external current (or magnetisation) coupled to the field, $\lim_{J\to 0}\int_x J\phi$, which is finally removed. Alternatively, within a finite volume one may use boundary conditions that break the symmetry, and then take the infinite volume limit.

Either way, the effective action $\Gamma$ is invariant under the full symmetry group of the underlying theory by definition, whereas the vacuum state (the solution of the equations of motion) breaks the symmetry.

Thus, quite importantly, the apparent symmetry breaking in $\Gamma$, seemingly induced by the expansion point, is absent for the full effective action. In turn, a given approximation scheme may break this symmetry (for example a finite order of a Taylor expansion about $\phi = \phi_0$). This symmetry can be restored subsequently by averaging the approximated effective action $\Gamma_{\text{app}}[\phi]$ over the symmetry group, $\Gamma[\phi] = \langle \Gamma_{\text{app}}[\phi] \rangle_{\text{av}}$. Note in this context, that in our example case of an $O(N)$ theory the averaged expectation value of the field vanishes, $\langle \phi \rangle_{\text{av}} = 0$, as it must. Moreover, the operator in (B.5) has the full symmetry and hence does not change under the averaging procedure, while $\langle \phi \rangle$ does.

In the case of the effective gluon mass, the underlying symmetry is a gauge-symmetry. For this reason we also consider a second, closer, example, the expectation value of the Polyakov loop $\langle L \rangle$ in finite temperature Yang-Mills theory,

$$L = \frac{1}{N_c} \text{tr}_{\text{f}} \mathscr{P} \exp\{ i g_s \oint A_0(x) \} , \tag{B.7}$$

where the integral $\oint$ in (B.7) is over $x_0 \in [0, 1/T]$. Here, $T$ denotes the temperature and $\mathscr{P}$ is the path ordering operator. The underlying symmetry is the center symmetry $Z_{N_c}$ of the gauge group with $L \to z\, L$ and $z \in Z_{N_c}$. We have the order parameter

$$L_0^2 = \lim_{\mathscr{V} \to \infty} \frac{1}{\mathscr{V}} \int_{\mathscr{V}} \langle L(0) L^\dagger(x) \rangle , \tag{B.8}$$

which is non-vanishing in the confining disordered low temperature phase. Typically, both in functional approaches as well as on the lattice, (B.8) is obtained by an infinitesimal explicit center symmetry breaking in the Cartan direction $t^3$, similar to introducing an infinitesimal explicit breaking of $O(N)$ symmetry described above. In the $t^3$ direction the Polyakov loop takes real values and we get

$$L_0 = \langle L(x) \rangle , \tag{B.9}$$

with a real positive $L_0$, which is a non-trivial solution of the equation of motion (of $A_0$) at finite temperature. The expectation value of the order parameter serves as a physical expansion point for observables as well as the effective action in functional approaches, both in first principle QCD computation and low energy effective theories of QCD. In quantitative approximations the results for observables agree very well with lattice simulations, for the Polyakov loop itself see [231]: The observables are either color blind in the first place and hence do not require a color average and are insensitive to it, or, as in the case of the Polyakov loop, a color direction was singled out for the computation in the first place.

However, the comparison of gauge fixed correlation functions or parts of it is more intricate, as then the averaging is required and may also affect the gauge fixing, for more details and further literature see in particular [48, 381] and the recent review [104]. This intricacy also applies in the present situation and makes a direct comparison of the effective gluon mass difficult.

The lack of a quantitative averaging procedure has forced us to introduce the averaging factor $f_{\text{av}}(N_c)$ in our results, see the definition (4.26) and the definition of the effective gluon mass (4.29) and (4.49). In the present work we have only determined its $N_c$-dependence by resorting to consistency arguments of the large $N_c$ scaling. As mentioned in the main text, the value of $f_{\text{av}}(N_c)$ is the largest source of systematic error for the effective gluon mass.

### B.2.2. Large $N_c$-scaling and self-consistency

The effective gluon masses $m_A^2$ in (4.29) and $m_{\text{gap}}^2$ in (4.49) show an explicit $1/N_c$-scaling, while no $N_c$-scaling is present in the large $N_c$ limit, if the theory is formulated in the 't Hooft coupling

$$\lambda = N_c g_s^2 \,. \tag{B.10}$$

This property serves as a self-consistency check of our computation and specifically our group average used to derive (4.29), (4.49) and entailed in $f_{\text{av}}(N_c)$

An illustrative and relevant example are the functional relations of the two-point function $\Gamma^{(0,2)}_{aa}(p)$. Cast in a relation for the wave function $Z_a(p)$, they read

$$Z(p^2) = Z_{\text{in}} + g_s^2 N_c \,\text{Diags}_1 + \mathcal{O}(N_c^0) \,, \tag{B.11}$$

where the right hand side stands for the typical loop diagrams of e.g. (integrated) fRG flows or Dyson-Schwinger equations. Here, $Z_{\text{in}}$ stands for the input dressing, either the one at the initial UV cutoff scale (fRG) or the classical dressing (DSE). In most cases the $\mathcal{O}(N_c^0)$ term is dropped, for an exception as well as a respective discussion see [125]. The term $\text{Diags}_1$ stands for the loop integral that depends on the wave functions of all the fields and the full vertex dressings. Importantly, the functional relations for all other vertex dressings and wave functions have the same form as (B.11). Accordingly, if dropping the subleading term of the order $O(N_c^0)$, all functional relations only depend on the 't Hooft coupling (B.13), and so do all correlation functions. Respective lattice studies also reveal that the large $N_c$-limit is achieved already for $N_c \gtrsim 3$ for most correlation functions, for a review see [382].

In summary we deduce, that in the large $N_c$-limit the only $N_c$-dependence of the effective gluon masses $m_A^2$ in (4.29) and $m_{\text{gap}}^2$ in (4.49) is implicit in the dependence on the 't Hooft coupling (B.13). This concludes our brief discussion of the $N_c$-scaling of correlation functions.

The relations for the effective gluon mass, (4.29), (4.49), show an even more direct scaling consistency: $Z_{\text{F}}$ is an expansion term in the two-point function of the fluctuating gluon. Moreover, in the presence of the condensate this two-point function approaches the effective gluon for vanishing momentum,

$$\lim_{p\to 0} \Pi^{\perp}_{\mu\nu}(p)\Gamma^{(0,2)}_{aa,\mu\nu}(p) = 3\, m_{\text{gap}}^2 \,. \tag{B.12}$$

Accordingly, both $Z_{\text{cond}}$ and $m_{\text{gap}}$ have the same $N_c$-scaling (only dependent on the 't Hooft coupling in the large $N_c$-limit) as well as the same RG-scaling. In conclusion, the ratio $Z_{\text{cond}}/m_{\text{gap}}^2$ is manifestly RG-invariant as well as $N_c$-independent in the large $N_c$-limit. This implies already, that the RG-invariant information in the effective gluon mass is given by $f_{\text{av}}(N_c)\langle F\rangle^2$. The value of the mass itself depends on the RG-condition and should not be confused with the gluon mass gap. The latter can be defined as the inverse screening length of the gluon propagator which is indeed RG-invariant.

In summary, $f_{\text{av}}(N_c)\langle F\rangle^2$ should be $N_c$-independent in the large $N_c$-limit. This fixes the $N_c$-scaling of $f_{\text{av}}(N_c)$, given that of $\langle F\rangle^2$. The $N_c$-scaling of the latter is obtained by an $N_c$-analysis of the effective potential, whose explicit computation is detailed in Section 4.3 and Appendix C.1.1. Here we only need that it consists out of an ultraviolet classical piece of the form (4.9) and a term that depends on $N_c F^2$,

$$\mathscr{W}_{\text{eff}}(F^a) = \frac{1}{4g_s^2}F^2 + \Delta\mathscr{W}_{\text{eff}}(N_c F^2) \,, \tag{B.13}$$

see Section 4.3.2. In (B.13), $g_s^2$ is the strong coupling at a large momentum scale $k_{\text{UV}}$, and we will use $k_{\text{UV}} = 20\,\text{GeV}$ for this scale later on. We now absorb $N_c$ into the field strength squared amplitude $F^2$, i.e. $\bar{F}^2 = N_c F^2$. With (B.10) this leads us to

$$\mathscr{W}_{\text{eff}}(F^a) = \frac{1}{4\lambda}\bar{F}^2 + \Delta\mathscr{W}_{\text{eff}}(\bar{F}^2)\,, \tag{B.14}$$

and consequently

$$\langle \bar{F}\rangle = \bar{F}_{\text{min}}(\lambda) \qquad \longrightarrow \qquad \langle F\rangle = \frac{1}{\sqrt{N_c}}\bar{F}_{\text{min}}(\lambda)\,. \tag{B.15}$$

The $1/N_c$-scaling for $\langle F\rangle^2$ derived in (B.15), is confirmed numerically in Appendix C.1.1. There, the effective potential and its minimum is computed in a leading order $N_c$ approximation and hence shows the asymptotic $1/N_c$ scaling even for $N_c = 2$. This $N_c$-scaling is rooted in the adjoint representation trace of $n^a t^a$ appearing the definition of the covariantly constant field strength in (4.7), cf. (B.22). We have confirmed its numerical presence in a comparison of $N_c = 2, 3$.

### B.2.3. Flow equation for the effective potential

Here we provide some details of the computation of the integrated flow (4.55) of the effective potential, (4.52a) from the flow equation (4.50) and the propagators (4.53). Inserting the latter into (4.50) yields,

$$\begin{aligned}
\partial_t \mathscr{W}_k(F^a) =& \frac{3}{2}\,\text{Tr}\,\frac{\partial_t R_a^{\perp}(\mathscr{D}_T)}{\mathscr{D}_T Z_{a,k}(\mathscr{D}_T) + R_a^{\perp}(\mathscr{D}_T)} + \frac{1}{2}\,\text{Tr}\,\frac{\partial_t R_a^{\parallel}(-D^2)}{-D^2 + R_a^{\parallel}(-D^2)} \\
&+ \frac{1}{2}\,\text{Tr}\,P_0\frac{\partial_t R_a^{\perp}(-D^2)}{-D^2 Z_{a,k}(-D^2) + R_a^{\perp}(-D^2)} - \text{Tr}\,\frac{\partial_t R_c(-D^2)}{-D^2 Z_{c,k}(-D^2) + R_{k,c}(-D^2)} \\
&- \frac{3}{2}\,\text{Tr}\,\frac{\partial_t R_a^{\perp}(p^2)}{p^2 Z_a(p^2) + R_a^{\perp}(p^2)} - \frac{1}{2}\,\text{Tr}\,\frac{\partial_t R_a^{\parallel}(p^2)}{p^2 Z_a(p^2) + R_a^{\parallel}(p^2)} - \text{Tr}\,\frac{\partial_t R_c(p^2)}{p^2 Z_{c,k}(p^2) + R_{k,c}(p^2)}
\end{aligned} \tag{B.16}$$

where the contributions in the first line are the glue contributions, and $P_0$ denotes the projection on the zero-mode. The traces in (B.16) sum over momenta or space-time, as well as internal and Lorentz indices of the respective field modes. We have three covariant transverse modes and one covariant longitudinal mode, the trivial gauge mode. The term in the second line is the ghost contribution, and the field-independent subtraction in the third line normalises the potential to $\mathscr{W}_k(F^a = 0) = 0$. We choose the regulator in consistency with the input data. The regulators in [47] are defined as,

$$\begin{aligned}
R_{a,k}(p) &= p^2\, r(x)\left(\tilde{Z}_{a,k}\Pi^{\perp}(p) + \Pi^{\parallel}(p)\right), \\
R_{a,k}(p) &= p^2\, r(x)\tilde{Z}_{c,a}\,.
\end{aligned} \tag{B.17}$$

with the projection operators $\Pi^{\perp,\parallel}$ defined in (4.35). In (B.17), $x$ is the dimensionless momentum variable, $x = p^2/k^2$, and the shape function $r(x)$ used in [47] is given by,

$$r(x) = \left(\frac{1}{x} - 1\right)\frac{1}{1 + e^{\frac{x-1}{a}}}\,, \qquad a = 2\times 10^{-2}\,. \tag{B.18}$$

The shape function (B.18) is a smoothened version of the Litim shape function, [129]. The cutoff dependent prefactors $\tilde{Z}_{a/c}$ are given by

$$\tilde{Z}_{a,k} = Z_{a,k}([k^n + \tilde{k}^n]^{1/n}), \qquad \tilde{Z}_{c,k} = Z_{c,k}(k), \tag{B.19}$$

with $k = 1\,\text{GeV}$. The choice (B.19) ensures that the regulators have the same (average) momentum scaling as the two-point functions, regulators proportional to the respective wave function renormalisations of the fields are RG-adapted, see [127]. Moreover, the scale $k = 1\,\text{GeV}$ is introduced for computations convenience; it leads to a gluon regulator, that does not diverge at $p = 0$ for $k \to 0$. While even a singular regulator choice at $p = 0$ does not contribute to the momentum integral, it complicates the numerics.

In [48] the regulator was used as it optimises fully momentum dependent approximations, see [127]. However, the resolution of (B.16) requires the computation of $\mathrm{Tr}\,\mathscr{F}(-D^2)$ and $\mathrm{Tr}\,\mathscr{F}(-D_T)$ in terms of the discrete Eigenvalues or spectrum of the Laplacians $-D^2$ and $D_T$. The spectral properties of the Laplacians are discussed in Appendix B.2.4, see also [211].

The optimisation of the approximation in terms of its momentum dependence as used in [48] comes at the price that soft but sharp regulators delay the onset of the asymptotic ultraviolet scaling in the presence of a discrete momentum spectrum, see [383]. Here, asymptotic UV scaling entails, that the effective action reduces to the classical one with a running prefactor, see (4.56). Indeed, for non-analytic regulators such as the Litim regulator or the sharp regulator the asymptotic UV scaling. In Appendix C.1.1 we investigate the asymptotic UV scaling in the present set up as well as the regulator (in)dependence of our results.

### B.2.4. Spectral properties of Laplace-type operators

In this section we will comment on the background-covariant Laplacians, which were used for the momentum dependence of the Landau-gauge propagators in (4.50) and (B.16). Their explicit form follows from the gauge-invariant background field effective action [384] and is given by

$$\mathscr{D}_{T\,\mu\nu} = -D^2\delta_{\mu\nu} + 2ig\,F_{\mu\nu}, \quad \mathscr{D}_{L\,\mu\nu} = -D_\mu D_\nu, \tag{B.20}$$

and $\mathscr{D}_{\text{gh}} = -D^2$. The transverse Laplacian also contains the spin-1 coupling to the background field.

The traces over the Laplace-type operators in (B.16) can be evaluated upon introduction of Laplace transforms using standard heat-kernel techniques. The subtleties arising from the presence of a self-dual background are discussed in-depth in e.g. [222, 385, 386]. Here, we just quote the relevant spectra in self-dual backgrounds from [211],

$$\begin{aligned}
\mathrm{Spec}\Big\{-D^2\Big\} &= F_l(n+m+1), \quad n,m = 0,1,2,\ldots \\
\mathrm{Spec}\Big\{\mathscr{D}_{\mathrm{T}}\Big\} &= \begin{cases} F_l(n+m+2) & , \quad \text{multiplicity} \quad 2 \\ F_l(n+m) & , \quad \text{multiplicity} \quad 2 \end{cases},
\end{aligned} \tag{B.21}$$

where $F_l = |\nu_l|F/\sqrt{2}$, where dividing by $\sqrt{2}$ accounts for the multiplicity in a self-dual formulation of $F_{\mu\nu}$ and $\nu_l$ are the eigenvalues to the adjoint color matrix $n^a t^a$. The covariant spin-1 Laplacian $\mathscr{D}_{\mathrm{T}}$ has a double zero mode for $n = m = 0$ which is due to the symmetry between colour-electric and colour-magnetic field. The spectral problem of the longitudinal Laplacian $\mathscr{D}_{\mathrm{L}}$ can be mapped onto that of $-D^2$, such that (B.21) is sufficient for the calculation in the

main part of the paper, see e.g. [222, 385, 386]. The trace Tr′ is defined as that without the zero mode, and for a general function $\mathscr{F}$ we get,

$$\begin{aligned}\mathrm{Tr}'\,\mathscr{F}(\mathscr{D}_{\mathrm{T}}) &= 2\sum_{l=1}^{N_c^2-1}\left(\frac{F_l}{4\pi}\right)^2\left\{\sum_{n,m=0}^{\infty}\mathscr{F}\big(F_l(n+m+2)\big)+\sum_{n=0}^{\infty}\sum_{m=1}^{\infty}\mathscr{F}\big(F_l(n+m)\big)+\sum_{n=1}^{\infty}\mathscr{F}\big(nF_l\big)\right\}\\ &= 4\sum_{l=1}^{N_c^2-1}\left(\frac{F_l}{4\pi}\right)^2\sum_{n,m=0}^{\infty}\mathscr{F}\big(F_l(n+m+1)\big) = 4\,\mathrm{Tr}_{xc}\,\mathscr{F}(-D^2),\end{aligned} \tag{B.22}$$

where the trace Tr sums over momentum or space-time, internal indices and Lorentz indices of the respective field mode. Equation (B.22) displays an isospectrality relation between $-D^2$ and the non-zero eigenvalues of $\mathscr{D}_{\mathrm{T}}$. As a consequence, all gluon and ghost modes except for the two zero modes couple in the same fashion to the selfdual background. This allows us to compute (B.16).

## B.3. Formulae: O(N) model in LDG

*This section is taken from [5] and provides the reformulation of the flow to fit the LDG-scheme.*

### B.3.1. Linearising the diffusion

The flow equation of the $O(N)$ model (5.23) is a highly non-linear convection diffusion equation. Therefore, an application of the LDG method presented in Section 5.2.2 requires a few manipulations of the equation. Linearity in the second derivative is achieved by computing the RG-flow of the first potential derivative $\partial_\rho V_k(\rho)$ and separately of the second $\partial_\rho^2 V_k(\rho)$, introducing artificially a second instationary equation. An according manipulation of the flow is detailed in the following.

Starting from the flow of the O(N) model (5.7), we obtain the flow of the pion mass $u = \partial_\rho V_k(\rho) = m_\pi^2$ by taking a $\rho$ derivative

$$\partial_t u = \partial_\rho\left(f_{N-1}(u) + f_1(u+2\rho v)\right), \tag{B.23a}$$

where the bosonic flux is given by $f_i(x) = A_d\frac{i}{1+\frac{x}{k^2}}$ and the prefactor $A_d = \frac{v_d k^d}{2(2\pi)^d}$. The diffusive contribution is captured in $v = \partial_\rho^2 V_k(\rho)$, which appears in (B.23a) in a non-linear way. We can solve this issue by deriving a flow equation for $v$ explicitly. Taking an additional $\rho$ derivative of (B.23a) yields

$$\begin{aligned}\partial_t v &= \partial_\rho\partial_t u = \partial_\rho\big(\partial_\rho(f_{N-1}(u) + f_1(u+2\rho v))\\ &= \partial_\rho\big(v\;\partial_u f_{N-1}(u) + \partial_\rho s\,\partial_s f_1(s)|_{s=u+2\rho v}\big).\end{aligned} \tag{B.23b}$$

The last line now contains a simple convective flux and a second term which suits the LDG scheme presented in Section 5.2.2. Furthermore, the correct diffusive behaviour, i.e. a flattening and not a steepening of slopes, is ensured by the requirement $0 > 2\rho\partial_s f_1(s)$. For a more throughout discussion see [387] and in a fRG context [4]. In our case, the fulfilment of this requirement is always given since

$$\partial_s f_1(s) = -\frac{A_d k^2}{(k^2+s)^2}\,. \tag{B.24}$$

We continue by computing the flux of the stationary equation in (5.20), where the integral can be computed analytically

$$j(u+2\rho v) = \int_0^{u+2\rho v} ds \frac{A_d^{1/2} k}{(k^2+s)} = A_d^{1/2} k \log(k^2+(u+2\rho v)) - \text{const}. \tag{B.25}$$

The constant drops out, since $j$ is a flux. Hence only the derivative, or differences of $j$ are evaluated in the computation. The argument of the logarithm in (B.25) is always positive, due to the convexity restoring properties of the equation and therefore $k^2+(u+2\rho v) > 0$ at all times during the flow [292].

## B.4. Formulae: Applications to general RG-flows

*The following section gives technical details for Chapter 7 and are taken from [7, 8].*

### B.4.1. Diagrammatics of the modified flow equation

In this section we outline the derivation of the modified flow of the wave function. The full flow of the two-point function reads with $R_{k,ij} = R\,\delta_{ij}$,

$$\begin{aligned}\partial_t \Gamma_{ij} = \partial_t \Gamma_{ij}|_{\dot\phi=0} + \Big[ G_{nm,ij}\dot\phi_{n,m} + G_{nm,i}\dot\phi_{m,nj} + G_{nm,j}\dot\phi_{m,ni} + G_{nm}\dot\phi_{m,rij}\Big] R \\ - \left(\dot\phi_n \Gamma_{nij} + \dot\phi_{n,i}\Gamma_{nj} + \dot\phi_{n,j}\Gamma_{ni} + \dot\phi_{n,ij}\Gamma_n\right),\end{aligned} \tag{B.26}$$

where we used the short-hand notation introduced for the propagator derivatives in (7.13) and below as well as

$$\dot\phi^{(m)}_{i,\phi_{n_1}\cdots\phi_{n_m}} = \frac{\delta \dot\phi_i}{\delta\phi_{n_1}\cdots\delta\phi_{n_m}}, \tag{B.27}$$

as well as the short hand notation $\dot\phi_{i,n_1\cdots n_m}$. In (B.27) we have dropped the momentum arguments. Note also that all quantities in (B.26) depend on $k$.

The first contribution is the standard 1PI Wetterich flow of the two-point function. The next line can also be thought of in terms of diagrams: the terms correspond to the 2-, 1- point-function and potential flows respectively, but the regulator term is replaced by $\partial_t R_k \to \dot\phi^{(m)} R_k$, where the superscript denoted the derivative and $m = 1,2,3$. $\dot\phi^{(2)}$ has one outer leg, $\dot\phi^{(3)}$ two. We can use this picture to drop some of the terms. Since the reparametrisation $\dot\phi$ has no external momentum dependence, the diagram containing $\dot\phi^{(3)}$ drops after taking the momentum derivative.

Furthermore, all $\dot\phi_{,\phi\pi_i}$ contributions drop when evaluated at the expansion point $\phi_0 = (\sqrt{\rho}, \mathbf{0})$. We can see this by a symmetry argument: The left hand side of (B.26) is a function of the invariant $\rho$. Thus the right hand side is necessarily too, which implies that $\dot\phi^{(1)}$ is a function of $\rho$, whereas $\dot\phi$ and $\dot\phi^{(2)}$ are odd in $\phi$. Using the relation

$$\partial_{\phi_i} f(\rho) = \phi_i\, \partial_\rho f(\rho), \tag{B.28}$$

for an arbitrary function $f(\rho)$, we find that

$$\dot\phi_{\phi\pi_i}|_{\phi=\phi_0} = \pi_i\, \partial_\rho \frac{\delta\dot\phi}{\delta\phi}|_{\phi=\phi_0} = 0. \tag{B.29}$$

### B.4.2. Evaluation of the RG-adapted flow $\dot{\phi}$

The $\rho-$dependent anomalous dimension is obtained from (7.23) by integration. However, in order to highlight the sole occurrence of $\rho\,\eta_\phi(\rho)$, we rewrite (7.23) accordingly,

$$(\rho\,\eta_\phi)' = \left(\rho + \frac{(\rho\,\eta_\phi)}{d+1}\right)\mathscr{T}_{\eta_\phi}(\bar{V}', \bar{V}''; \rho, T)\,, \tag{B.30}$$

where $\mathscr{T}_{\eta_\phi}(\bar{V}', \bar{V}''; \rho, T)$ is the resummed threshold function

$$\mathscr{T}_{\eta_\phi}(\bar{V}', \bar{V}'', \rho) = \frac{4A_d\,(\bar{V}'')^2 BB_{(2,2)}}{1 + 8A_d\,\bar{\rho}(\bar{V}'')^2 BB_{(2,2)}}\,, \tag{B.31}$$

with the threshold function $BB_{(2,2)}(\bar{m}_\sigma^2, \bar{m}_\pi^2; T)$ defined in Appendix B.7.2 and

$$\bar{m}_\pi^2 = \bar{V}'(\bar{\rho})\,, \qquad \bar{m}_\sigma^2 = \bar{m}_\pi^2 + 2\bar{\rho}\bar{V}''\bar{\rho})\,, \tag{B.32}$$

the dimensionless versions of the masses (5.6), with the dimensionless fields $\bar{\rho} = k^{d-2}\rho$ and potential $\bar{V} = k^d\,V$. Solving (B.30) for $\rho\,\eta_\phi$ instead of solving (7.23) for $\eta_\phi$ also reduces the error on the numerical integration. Both equations can be solved by using the variation of constants method as (7.23) and (B.30) have the form,

$$\partial_{\bar{\rho}}\,y(\bar{\rho}) = c(\bar{\rho})\,y(\bar{\rho}) + d(\bar{\rho})\,. \tag{B.33}$$

The solutions of (B.33) are given by

$$y(\bar{\rho}) = \mathscr{C}(\bar{\rho})\,[c_0 + \mathscr{D}(\bar{\rho})]\,, \tag{B.34a}$$

with the integrated 'constants'

$$\mathscr{C}(\bar{\rho}) = \exp\left\{\int_0^{\bar{\rho}} \mathrm{d}\bar{\rho}'\,c(\bar{\rho}')\right\}\,, \quad \mathscr{D}(\bar{\rho}) = \int_0^{\bar{\rho}} \mathrm{d}\bar{\rho}'\,\frac{d(\bar{\rho}')}{\mathscr{C}(\bar{\rho}')}\,. \tag{B.34b}$$

and the integration constant $c_0$. The constant $c_0$ can be used to tune boundary conditions for $\eta_\phi(\rho)$, for example for $\rho = 0$ or for $\rho = \infty$.

For the solution of (B.30) we read off the three functions $y(\bar{\rho}), c(\bar{\rho}), d(\bar{\rho})$ with

$$y(\bar{\rho}) = \bar{\rho}\,\eta_\phi(\bar{\rho})\,, \quad c(\bar{\rho}) = \frac{1}{d+1}\,\mathscr{T}_{\eta_\phi}\,, \quad d(\bar{\rho}) = \bar{\rho}\,\mathscr{T}_{\eta_\phi}\,, \tag{B.35}$$

with the resummed threshold function $\mathscr{T}_{\eta_\phi}(\bar{V}', \bar{V}'', \rho)$ defined in (B.31). Then, (B.35) is inserted in (B.34b), leads to the solution (B.34a) for $\bar{\rho}\,\eta_\phi(\bar{\rho})$.

The boundary condition $c_0$ in (B.34a) can now be used for different purposes. Below we discuss some prominent choices.

#### LPA′ from flowing fields

Firstly, we could use the equation to obtain LPA′ within the current approximation with $\eta_\phi(\rho)$: in LPA′ the wave function or rather the anomalous dimension is taken to be constant and is evaluated at the flowing expansion point, the solution of the equation of motion $\rho_{0,k}$. Now we chose $c_{0,k}$ such that

$$\eta_\phi'(\rho_{0,k}) = 0\,, \tag{B.36}$$

which implies that corrections to a constant $Z_\phi$ are of order $(\rho - \rho_{0,k})^2$. With the choice (B.36), the flows (7.23) and (B.30) reduce to the flow of the standard LPA′ scheme at $\rho = \rho_{k,0}$.

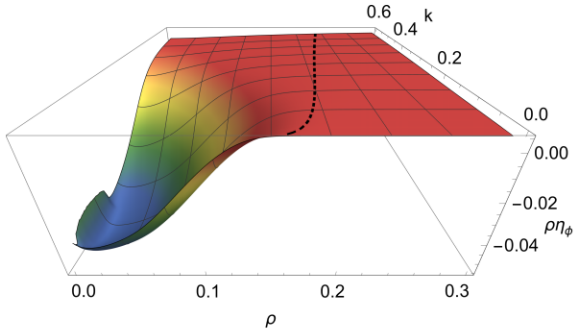


Figure B.1.: Anomalous dimension (multiplied by $\rho$) in $d = 1+2$ deep in the broken phase ($T = 0.05$). We can infer from $\rho\eta_\phi|_{\rho=0} \neq 0$ that the anomalous dimension $\eta_\phi$ diverges as $\rho \to 0$, necessitating the numerical correction Appendix B.4.3. Since the numerical simulation uses the cut-off solution, the reconstruction of the anomalous dimension at small $\rho$ displays some numerical artefacts.

### Regular flowing fields

The implicit choice of $c_0$ leading to (B.36) or similar conditions is beneficial for approximations that use expansion about a given $\rho$. For global $\rho$-dependent solutions it is more important to take care of potential reparametrisation singularities. These singularities occur in a similar fashion as coordinate singularities in a stereographic projection, and hence they do not imply or even indicate the failure of the field reparametrisation. Still, they make a numerical solution more intricate. To see the latter fact we consider two different singularities, one for $\rho \to 0$ and one for $\rho > \rho_0$ and $k \to 0$.

The generic occurrence of a singularity for $\rho \to 0$ is easily explained in terms of a solution for $y(\rho) = \rho\,\eta_\phi(\rho)$. Evidently, for $y(0) \neq 0$, the anomalous dimension diverges for $\rho \to 0$. This singularity is avoided by choosing $c_0$ such that

$$|\eta_\phi(\rho \to 0)| < \infty\,, \quad \longrightarrow \quad c_0 = 0\,, \tag{B.37}$$

The unique solution $c_0 = 0$ in (B.37) follows from $\mathscr{C}(0) = 1$ and $\mathscr{D}(0) = 0$ as long as $(\bar{V}'')^2 B B_{(2,2)}$ does not diverge for $\rho \to 0$. However, with $c_0 = 0$, the flow of the field coordinate $\eta_\phi(\rho)$ stays finite and positive within the regime $\rho < \rho_0$, i.e. in the broken phase, even as $k \to 0$. Then the definition of the anomalous dimension, (7.8), directly manifests how the weight of the coordinate range is pushed onto zero. This emergent coordinate singularity for $k \to 0$ cannot be avoided for (B.37), but is well-controlled.

To avoid such an emergent coordinate singularity for $k \to 0$ in the regime with $\rho > 0$ we have to ensure that $|\eta_\phi|$ decays at least linearly with the cutoff scale $k$. However, for $\rho > \rho_0$, both masses $m_\sigma$ and $m_\pi$ are larger than zero and stay finite in the limit $k \to 0$. Hence, $\bar{m}_\sigma, \bar{m}_\pi \to \infty$ and $\eta_\phi(\rho > \rho_0)/k^2$ stays finite for $k \to 0$.

## B.4.3. A numerical cut-off

In our discussion of possible solutions to the anomalous dimension, we have seen a family of solutions with $|\eta_\phi| \to \infty$ as $\rho \to 0$. In this section, we argue that these solutions can nevertheless be used in the flow.

We have seen in (B.30) that the RG-flow of the anomalous dimension is best solved in terms of $y = \rho\eta_\phi$. Hence, we expect the second family of solutions (compare Appendix B.4.2) to

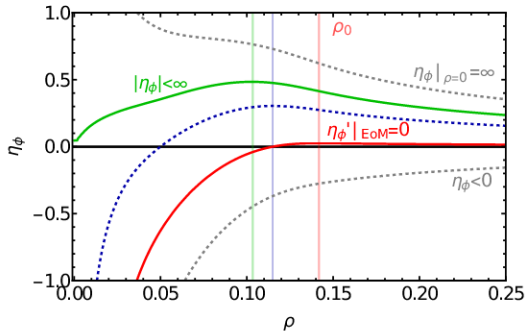


Figure B.2.: Different solutions to the RG-adapted flow (7.23) in the $d = 1+2$ calculation at $k = 0.001$. All units are given in terms of the UV-cutoff $\Lambda = 1$. We depict the regular solution $\eta_{\phi,1}$ *(green)*, specified in Appendix B.4.2, as well as the LPA′-like solution $\eta_{\phi,2}$ *(red)*, which is used in the computation, from Appendix B.4.2. The solution to the equations of motion $\rho_0$ is indicated for reference, as well as the respective focus points of the other $\eta_\phi$ . Irregularities in $\eta_{\phi,1}$ at small $\rho$ are caused by the numerical cut-off Appendix B.4.3. The other solutions are for illustrative purposes, the dashed solutions are unusable for our application: *(grey)* zoom into a numerically unstable coordinate range ($\eta_\phi < 0$) or produce non-monotonous fields $\phi_k$ ($\eta_\phi|_{\rho\to 0} = \infty$), *(blue)* can be numerically implemented but has all of the drawbacks of $\eta_{\phi,1}$ and $\eta_{\phi,2}$ and none of the benefits.

diverge with at least $|\eta_\phi| \propto \frac{1}{\rho}$. To circumvent this issue numerically we cut off $\eta_\phi$ at some point. This is implemented by choosing $\rho_{\min} < \rho_0$, where $\rho_0$ is the solution to the equations of motion (6.36b), and multiplying $y$ with

$$f(\rho) = \frac{\rho}{\rho_{\min}}\left(2 - \frac{\rho}{\rho_{\min}}\right)\Theta(\rho_{\min} - \rho). \tag{B.38}$$

Thereby we obtain a finite maximal value for our numerical anomalous dimension $\tilde{\eta}$, to wit

$$\tilde{\eta}_\phi(0) = \eta_\phi(\rho) f(\rho)|_{\rho\to 0} = 2\frac{y(0)}{\rho_{\min}}, \tag{B.39}$$

and a smooth transition to the real solution at $\rho_{\min}$, since $f(\rho_{\min}) = 1$ and $f'(\rho_{\min}) = 0$.

We find that for small enough cut-off $2\rho_{\min} < \rho_0$, the solution of the potential on the equations of motion is not influenced (within the numerical accuracy of the DG-scheme) if the cut-off is varied between $\rho_{\min} \in \left[\frac{\rho_0}{4}, \frac{\rho_0}{2}\right]$. We depict the cut-off solution in terms of $y = \rho\eta_\phi$ in Figure B.1. We emphasise that the plotted full result in Figure B.1 is computed using the numerical cut-off and is hence faulty for $\rho < \rho_{\min}$, but does not affect the equations of motion in the broken phase.

### B.4.4. Coordinate resolution and magnification points

Since the RG-adapted flow of the field basis (7.23) is described by an ODE, we can find a set of coordinate transformations $\{\eta_\phi\}$ which implement $Z_k(\rho) = 1$. Every solution corresponds to different boundary conditions, see also Appendix B.4.2. In (B.30) we have seen, that $(\eta_\phi\rho)'$ is proportional to the (resummed) threshold-function (B.31), and hence is vanishing for large $\rho$. An integration of $(\eta_\phi\rho)' \approx 0$ implies $\eta_\phi \propto \rho^{-1}$, i.e. $\eta_\phi \to 0$ for $\rho \to \infty$ is build into the structure of the flow. A depiction of possible solutions is shown in Figure B.2. We immediately exclude solutions of type $\eta_\phi \to \infty$ for $\rho \to 0$, since they produce non-monotonous field bases

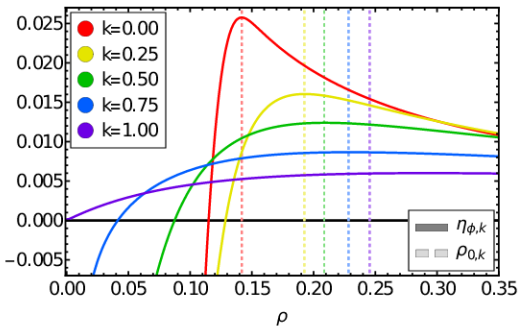


Figure B.3.: RG-time dependence of the anomalous dimension in $d = 2+1$ at $T = 0.05$. The *(purple)* solution is regular and of type $\eta_{\phi,1}$ (see Appendix B.4.2), the others are of type $\eta_{\phi,2}$ (see Appendix B.4.2) and diverge as $\rho \to 0$. The dashed lines indicate the solution to the equations of motion $\rho_0$, which corresponds to the magnification point in solutions of type $\eta_{\phi,2}$.

$\phi_k$. In the following we have a closer look at the remaining solutions $\{\eta_\phi\}$, so that we can identify which boundary conditions are easiest to implement numerically.

With our definition (7.8), the anomalous dimension $\eta_{\phi,k}(\rho)$ corresponds to a non-linear reparametrisation of the field basis $\phi_k$ at every RG-time step $\Delta k$. One can think of it as effectively zooming in (out) of specific regions of the field basis and increasing (decreasing) the resolution of the potential $V_k(\rho)$. The resolution of a region, in terms of the initial field basis $\phi_\Lambda \in [a, b]$, is

- *increased (zoomed in)* by the RG-step $\Delta k$ if $\eta_{\phi,k} > 0$ for $\phi_\Lambda \in [a, b]$, that is

$$|\phi_k(b) - \phi_k(a)| < |\phi_{k-\Delta k}(b) - \phi_{k-\Delta k}(a)|\,. \tag{B.40}$$

  This is apparent in Figure 7.2b for the interval $\phi_\Lambda \in [0.55, 0.8]$.

- *decreased (zoomed out)* by the RG-step $\Delta k$ if $\eta_{\phi,k} < 0$ for $\phi_\Lambda \in [a, b]$, that is

$$|\phi_k(b) - \phi_k(a)| > |\phi_{k-\Delta k}(b) - \phi_{k-\Delta k}(a)|\,. \tag{B.41}$$

  As an extreme example, we indicate the interval $\phi_\Lambda \in [0., 0.5]$ in Figure 7.2b, which is projected onto a single point as $k \to 0$.

To ensure numerical stability and precision, we require an increasing of the resolution for physical field values $\rho \geq \rho_0$, where $\rho_0$ is the solution to the equations of motion (EoM) (6.36b). Choosing a zooming out solution, in an evaluation with a fixed numerical interval $|\phi_{k-\Delta k}(b) - \phi_{k-\Delta k}(a)|$, would require non-trivial information about the solution, that is not contained in $|\phi_k(b) - \phi_k(a)|$. Numerically, this translates to unstable boundary conditions. This excludes completely negative solutions $\eta_{\phi,k} < 0$ in the numerical evaluation.

To get an intuition for the remaining solutions $\eta_\phi$, we introduce the concept of a scale-dependent *focus point*. This point is given by the maximum of $\eta_{\phi,k}(\rho)$, and we denote it as $\rho_{\max}$ in the following. By its definition as maximum, the resolution of its immediate vicinity, $(\rho_{\max} - \epsilon, \rho_{\max} + \epsilon)$ for some $\epsilon > 0$, is increased maximally in comparison to all other intervals of the same length $(2\epsilon)$. The location of the focus point decides which regions of the field basis are zoomed into and which ones are pushed out of the computational interval $(0, \rho_{\mathrm{UV}}]$.

The discussion in Appendix B.4.2 points out two specific solutions which are of interest to the numerical implementation,

1. $\eta_{\phi,1}$ is the only solution which remains finite at $\rho = 0$ (*(green)* in Figure B.2). Its focus point $\rho_{\max,1}$ is dependent on $k$ and decreases monotonously during the integration after starting at very high field values at $k = \Lambda$. Most importantly, $\rho_{\max,1}$ enters the flat regime of the potential, i.e. the unphysical field values $\rho$, where $\partial_\rho V_{k>0} < 0$, for computations in the broken phase. Here, the flow remains finite as $k \to 0$ and the flat region around $\rho_{\max,1}$ is infinitely zoomed in.

2. $\eta_{\phi,2}$ is the solution which focusses the region around the equations of motion, i.e. $\rho_{\max,2} = \rho_0$ in (6.36b) (*(red)* in Figure B.2). By focussing on the equations of motion we smooth out the well known non-analyticity of the potential at $V(\rho_0)$ as $k \to 0$. This comes at the cost of $\eta_{\phi,2} \to -\infty$ as $\rho \to 0$, which can be understood as a coordinate singularity, see Appendix B.4.2.

Neither $\eta_{\phi,1}$ nor $\eta_{\phi,2}$ are optimal for every computation: $\eta_{\phi,1}$ has an infinite magnification of the unphysical region in the broken phase, whereas $\eta_{\phi,2}$ is difficult to implement numerically and cannot resolve $\rho = 0$ due to a diverging flow. The *(blue)* solution in Figure B.2 combines both of these issues. In practice we use a hybrid of both $\eta_{\phi,1}$ and $\eta_{\phi,2}$: $\eta_{\phi,1}$ is used whenever $\rho_{\max,1} > \rho_0$, this comprises the entirety of computations which result in the symmetric phase at $k \to 0$, see Figure 7.1b. A continuous transition to $\eta_{\phi,2}$ is implemented once $\rho_{\max,1} \leq \rho_0$, i.e. once the focus point $\rho_{\max,1}$ of $\eta_{\phi,1}$ slips into the flat regime, we switch to $\eta_{\phi,2}$ and continue to zoom in on the equations of motion $\rho_{\max,2} = \rho_0$. This switch occurs in the broken phase and shows up as a kink in the $k$ dependence of $\eta_\phi$, compare Figure 7.1a. For a numerical implementation of $\eta_{\phi,2}$ we cut off the diverging flow around $\rho = 0$, this procedure is described in Appendix B.4.3. The RG-time dependence of the anomalous dimension, together with its magnification point on the equations of motion is $\rho_0$ is visualised in Figure B.3.

### B.4.5. Flowing with the minimum

In general, the CS-flow equation (7.45a) can be evaluated for arbitrary values of the external field $\phi$, which requires the computation of the full effective potential. Here, we simply evaluate the flow on the solution $\phi_0$ of the equation of motion. This is a commonly used truncation and gives access to the physical correlation functions. In the broken phase, the minimum of the full effective potential depends on $k$, and the total mass flow of the two-point function is given by the flow diagrams originating from the CS equation, $\partial_t \Gamma^{(2)}[\phi_0](p)$ and a term proportional to the mass flow of $\phi_0$,

$$\frac{d}{dt}\Gamma^{(2)}[\phi_0](p) = \partial_t \Gamma^{(2)}[\phi_0](p) + \left(\partial_t \phi_0 \, \Gamma^{(3)}[\phi_0]\right)(p) \,. \tag{B.42}$$

The novel ingredient in the present setup originates in the tree-level $k$-dependence of $\phi_0 \approx \sqrt{6k^2/\lambda_\phi} + \mathcal{O}(\lambda_\phi k)$, where the second term comprises the loop contributions. This tree-level dependence is usually absent in the flow of the minimum of standard momentum-shell flows. There, $\partial_t \phi_0$ only comprises the effects of the momentum shell integration and is inherently one-loop and beyond. The tree-level $k$-dependence of $\phi_0$ in the present case triggers a tree-level $k$-dependence of $\partial_t \phi_0 \Gamma^{(3)}(p)$ and the tree-level flow of the physical two-point function considered here reads

$$\frac{d}{dt}\Gamma^{(2)}\Big|_{\text{tree-level}} = -2k^2 + \partial_t \phi_0 S^{(3)}[\phi_0] = 4k^2 \,, \tag{B.43}$$

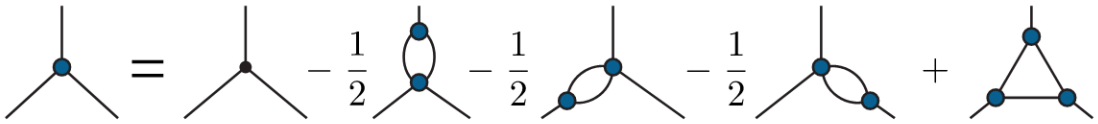

Figure B.4.: Truncated DSE for the three-point function in the skeleton expansion. Lines indicate full propagators, small black dots classical vertices, and larger blue dots full vertices.

where the classical three-point function is given by $S^{(3)}[\phi] = \lambda_\phi \phi$. Note that only the combination of both terms leads to the expected positive flow of the physical mass, while the flow of the mass parameter $-k^2$ has a negative sign.

To obtain the full momentum structure of the second term in of (B.42), we first note that the additional leg of the three-point function is always augmented with an incoming momentum of zero, as it is contracted with the scale derivative of a constant field. The full momentum dependence can then be incorporated via the DSE of the three-point function, which allows for an exact diagrammatic flow of the two-point function on the physical minimum. In the presence of approximations, a fully self-consistent treatment would require us to use the integrated flow of $\Gamma^{(3)}[\phi_0](p,0)$. However, also the flow of $\Gamma^{(3)}[\phi_0]$ includes a similar additional term as in (B.43), which is proportional to the four-point function. To avoid solving the flow of the three- and four-point function, we resort to the DSE to include the leading momentum dependence of the (contracted) three-point function. To ensure the correct RG-scaling of the flow equation, we further employ the skeleton expansion in the DSE, where every vertex is dressed. Approximating $\Gamma^{(n>4)} \approx 0$ and dropping the remaining two-loop diagrams, we arrive at the simple diagrammatic structure of the three-point function depicted in Figure B.4.

Additionally, using the DSE for $\Gamma^{(3)}$ in (B.42) demonstrates the structure of the flow as a total derivative. To make this explicit, we choose the vertical leg in Figure B.4 to be contracted with $\partial_t \phi_0$. Then, the three-point functions connected to this leg carry only internal momenta, and we approximate them as constant. With that, the first fish- and the triangle diagram in Figure B.4 are proportional to the tadpole and polarisation diagram respectively, and the second term on the RHS of the flow (B.42) reads

$$\left(\partial_t \phi_0 \, \Gamma^{(3)}[\phi_0]\right)(p) = \partial_t \phi_0 \left( S^{(3)}[\phi_0] - \frac{1}{2}\Gamma^{(3)}[\phi_0] D_{\text{tad}}(p) - D_{\text{fish}}(p) + \Gamma^{(3)}[\phi_0] D_{\text{pol}}(p) \right). \tag{B.44}$$

Note that the explicit three-point functions on the right-hand side are now momentum independent. We discuss our approximations for the remaining vertices in Appendix B.4.6.

Substituting (7.46) and (B.44) into (B.42), we arrive at the full flow equation of the two-point function. The full equation reads

$$\frac{d}{dt}\Gamma^{(2)}[\phi_0](p) = (\partial_t \phi_0) S^{(3)}[\phi_0] - \left(2 - \eta_\phi\right) Z_\phi k^2 + \dot{\mathscr{R}} \left[ -\frac{1}{2} D_{\text{tad}} + D_{\text{pol}} \right] - \partial_t \phi_0 D_{\text{fish}} - \partial_t S_{\text{ct}}[\phi_0], \tag{B.45a}$$

where

$$\dot{\mathscr{R}} = \left( \partial_t \phi_0 \Gamma^{(3)}[\phi_0] - \left(2 - \eta_\phi\right) Z_\phi k^2 \right). \tag{B.45b}$$

Note the appearance of a relative minus sign in front of the mass derivative contribution (second term) to (B.45b) due to $\mu = -k^2$ in the broken phase. The first line in (B.45a) carries the

trivial, tree-level running of inverse propagator. It consists of the running of the mass parameter and the classical part of the three-point function, connected to the flow of the minimum. Its mean-field value cannot be altered by the renormalisation condition and is, analogue to the respective term in $\dot{\mathscr{R}}$, crucial to recover the correct sign of the flow, see (B.43). A detailed evaluation of (B.45a) can be found in Appendix B of [7].

### B.4.6. Approximations and real-time flows in the symmetric and broken phase

In the following section, we discuss the approximations used for the higher correlation functions, which lead to non-trivial spectral flow-equations in both phases. This enables us to write down the renormalised flow equations for the two-point function and evaluate them on the real frequency axes.

In the $\phi^4$-theory, correlation functions of an odd number of fields, $\Gamma^{(2n+1)}[\phi]$, are proportional to the mean field $\phi$. In the present approximation we only consider three- and four-point functions, setting all the higher correlation functions to zero:

$$\Gamma^{(n>4)} \approx 0\,. \tag{B.46}$$

Then, the three-point function is proportional to a product of the four-point function and $\phi_0$. This closes our approximation.

For constant vertices, the tadpole diagram only provides a constant contribution to the flow of the two-point function. This contribution is absorbed completely in the on-shell renormalisation condition (7.51) and (7.50), for the broken and symmetric phase respectively. In the symmetric phase of the theory with $\phi_0 = 0$, the tadpole is the only contribution to the flow of the two-point function. Hence, the scattering tail originates only from the non-trivial momentum dependence of the four-point function. In a first but important step towards the full momentum dependence of $\Gamma^{(4)}(p_1,...,p_4)$ we use an $s$-channel resummation of the full four-point function,

$$\Gamma^{(4)}(p^2) = \frac{\lambda_\phi}{1 + \frac{\lambda_\phi}{2}\int_q G(p+q)G(q)}\,. \tag{B.47}$$

In (B.47), $p^2 = s = (p_1+p_2)^2$ is the $s$-channel momentum, and we choose vanishing t and u channels to perform the resummation: $(p_3-p_1)^2 = (p_1-p_4)^2 = 0$. This approximation admits the simple spectral representation (7.38) of the four-point function, see also [168].

We emphasise that (B.47) only holds true in the symmetric phase. In contrast, in the broken phase the flow or BSE for the four-point function contains additional diagrams with two or four three-point vertices. Their combined contributions are readily estimated and are suppressed by a factor $1/8$. Hence, they are dropped in the following computation. Accordingly, we use (B.47) in both phases.

Note also, that the four-point function exhibits a bound state pole below $2m_{\text{pole}}$ close to the phase transition. This is discussed for example in [388] in terms of a Bethe-Salpeter equation, and indeed seen in lattice and fRG calculations, see [389–391]. The present $s$-channel resummation for the four-vertex does not include the resonant channel. A full bound state analysis and the systematic inclusion of other channels will be considered elsewhere.

It is left to specify the three-point function $\Gamma^{(3)}(p_1,p_2,p_3)$ in (B.45a). In contrast to the pivotal importance of the momentum dependence of the four-point function, that of the three-point function is averaged out in the vacuum polarisation and the fish diagram. For the sake of

simplicity, we therefore approximate the full vertex by its value at vanishing momenta, $p_i = 0$ for $i = 1,2,3$. There, the three-point function is given by the third derivative of the effective potential on the equations of motion, $V_{\text{eff}}^{(3)}(\phi_0)$. The effective potential $V_{\text{eff}}(\phi)$ is the quantum analogue of the classical potential, and is nothing but the effective action $\Gamma[\phi]$, evaluated for constant fields $\phi_c$,

$$V_{\text{eff}}(\phi_c) = \frac{1}{\mathcal{V}}\Gamma[\phi_c], \qquad \mathcal{V} = \int d^3x\,. \tag{B.48}$$

Due to the $Z_2$-symmetry of the $\phi^4$-theory under $\phi \to -\phi$, the effective potential is symmetric, $V_{\text{eff}}(-\phi) = V_{\text{eff}}(\phi)$. Moreover, it admits an expansion about the solution to the equation of motion, $\phi^2 = \phi_0^2$, which is valid for $\phi^2 \geq \phi_0^2$. The latter constraint on the modulus of $(\phi^2 - \phi_0^2)$ originates from the fact that the classical effective potential is the double Legendre transform of the classical potential. In the case of a non-convex potential it is simply the convex hull. We shall consider the expansion up to $(\phi^2 - \phi_0^2)^2$, dropping higher order terms in accordance with (B.46), and discuss the symmetric and broken phase separately in Appendix B.4.6 and Appendix B.4.6 below.

### Symmetric phase

In the symmetric phase with $\phi_0 = 0$ in (7.47), we use a Taylor expansion about $\phi^2 = 0$ for the effective potential,

$$V_{\text{eff}}(\phi) = \sum_{n=1}^{\infty} \frac{\lambda_n}{2n!}\phi^{2n}\,. \tag{B.49}$$

The first two couplings, $\lambda_1$ and $\lambda_2$ are related to the correlation functions $\Gamma^{(2)}$ and $\Gamma^{(4)}$ considered here. Hence, the coupling $\lambda_1$ agrees with the curvature mass squared in the symmetric phase, where the curvature mass is defined as

$$m_{\text{curv}}^2 = V_{\text{eff}}^{(2)}(\phi_0) = \Gamma^{(2)}[\phi_0](p=0), \tag{B.50}$$

in both phases. Moreover, the coupling $\lambda_2$ is nothing but the full four-point function, evaluated at vanishing momentum. In summary we have

$$\lambda_1 = m_{\text{curv}}^2, \qquad \lambda_2 = \Gamma^{(4)}(p=0)\,. \tag{B.51}$$

For the initial UV pole mass $m_{\text{pole}} = \Lambda$, the curvature mass and the pole mass agree, $\lambda_1 = \Lambda^2$, and the initial coupling is the classical one, $\lambda_2 = \lambda_\phi$. Hence, the initial effective potential $V_{\text{UV}}(\phi)$ at $k = \Lambda$ reads

$$V_{\text{UV}}(\phi) = \frac{1}{2}\Lambda^2\phi^2 + \frac{1}{4!}\lambda_\phi\,\phi^4\,. \tag{B.52}$$

With the above approximations, all higher correlation functions are fixed and the flow equation of the two-point function on the real frequency axes reads

$$\partial_t\Gamma^{(2)}(\omega_+) = -\frac{Z_\phi\left(2-\eta_\phi\right)k^2}{2}D_{\text{tad}}^{\text{dyn}}(\omega_+) + 2k^2 - \partial_t\hat{S}_{\text{ct}}^{(2)}, \tag{B.53}$$

where the retarded limit is given by $\omega_+ = -\mathrm{i}(w + \mathrm{i}0^+)$. $\hat{S}^{(2)}_{\mathrm{ct}}$ is given schematically by

$$\hat{S}^{(2)}_{\mathrm{ct}} = \text{diagramms}\left(p^2 = -k^2\right). \tag{B.54}$$

We denoted the counterterm action with a tilde since we already dropped constant terms in the flow of order $\lambda_\phi k$. Hence, only the dynamic part of the tadpole $D^{\mathrm{dyn}}_{\mathrm{tad}}$ contributes. It arises from the scattering tail of $\Gamma^{(4)}(p)$ and carries the spectral structure of the polarisation diagram.

### Broken phase

In the broken phase with $\phi_0 \neq 0$ we use a Taylor expansion about $\phi^2 = \phi_0^2$ for the effective potential,

$$V_{\mathrm{eff}}(\phi) = \sum_{n=2}^{\infty} \frac{\lambda_n}{2n!} \left(\phi^2 - \phi_0^2\right)^n . \tag{B.55}$$

At vanishing momentum and constant fields, the correlation functions derived from the effective action $\Gamma[\phi_0]$ coincide with the moments of the effective potential. We consider $n$-point functions for $n \leq 4$ with

$$\begin{aligned}
\Gamma^{(2)}[\phi_0](p=0) &= \frac{1}{3}\lambda_2 \phi_0^2 , \\
\Gamma^{(3)}[\phi_0](p=0) &= \lambda_2 \, \phi_0 + \frac{\lambda_3}{15} \, \phi_0^3 , \\
\Gamma^{(4)}[\phi_0](p=0) &= \lambda_2 + \frac{2}{5}\lambda_3 \, \phi_0^2 + \frac{1}{105}\lambda_4 \, \phi_0^4 ,
\end{aligned} \tag{B.56}$$

In contrast to the symmetric phase discussed in Appendix B.4.6, also higher order terms up to order $n$ with couplings $\lambda_n$ contribute due to $\phi_0 \neq 0$. For this reason we have indicated the $\phi_0$-dependence of $\Gamma^{(n)}$ in (B.56). We generically drop the $\phi_0$-dependence for the sake of readability, it is implicitly assumed that all expressions are evaluated at $\phi_0$.

As a consequence of (B.46), all expansion coefficients $\lambda_n$ with $n \geq 3$ vanish. The three and four-point couplings are then given by

$$\Gamma^{(3)}(0) = \Gamma^{(4)}(0)\phi_0 , \qquad \lambda_2 = \Gamma^{(4)}(0) . \tag{B.57}$$

With (B.50) we can express the minimum of the effective potential in terms of the curvature mass and $\lambda_2$, yielding

$$\phi_0^2 = \frac{3 m^2_{\mathrm{curv}}}{\Gamma^{(4)}(0)} , \tag{B.58}$$

Using (B.58), the three-point function is expressed in terms of the full two- and four-point functions at vanishing momentum,

$$\Gamma^{(3)}(0) = \sqrt{3\,\Gamma^{(4)}(0)}\, m_{\mathrm{curv}} . \tag{B.59}$$

Evidently, in the classical limit with $Z_\phi = 1$ and $\tilde{\rho}_k = 0$, the curvature mass agrees with the pole mass. This limit is approached for asymptotically large pole masses, where the effective coupling $\lambda_\phi / m_{\mathrm{pole}}$ tends towards zero. Hence, the ultraviolet effective potential $V_{\mathrm{UV}}(\phi)$ with

$k = \Lambda \to \infty$ is augmented with a classical dispersion with $\mu = -\Lambda^2$ and the initial (classical) coupling $\lambda_2 = \lambda_\phi$,

$$V_{\mathrm{UV}}(\phi) = \frac{1}{4!}\lambda_\phi \left(\phi^2 - \phi_0^2\right)^2 , \qquad \phi_0^2 = \frac{6\Lambda^2}{\lambda_\phi} , \tag{B.60}$$

for $\phi^2 \geq \phi_0^2$. The initial curvature and pole mass are given by

$$m^2_{\mathrm{pole}} = m^2_{\mathrm{curv}} = 2\Lambda^2 . \tag{B.61}$$

With these approximations, the real-time flow of the two-point function in the broken phase reads.

$$\partial_t \Gamma^{(2)}(\omega_+^2) = \dot{\mathscr{R}} \left( D_{\mathrm{pol}}(\omega_+^2) - \frac{1}{2} D^{\mathrm{dyn}}_{\mathrm{tad}}(\omega_+^2) \right) + A D_{\mathrm{fish}}(\omega_+^2) + 4k^2 - \partial_t \hat{S}^{(2)}_{\mathrm{ct}} , \tag{B.62}$$

The prefactors are given in Appendix B of [7] and $\hat{S}^{(2)}_{\mathrm{ct}}$ is given by

$$\hat{S}^{(2)}_{\mathrm{ct}} = \mathrm{diagramms}\left(p^2 = -2k^2\right) . \tag{B.63}$$

Additionally to the polarisation topology, we note that flow equation in the broken phase differs from that in the symmetric phase. The constant part of (B.62) carries an additional factor of 2. This resembles the additional factor 2 of the squared pole-mass in the broken phase compared to its symmetric phase counterpart. Also the prefactor of the tadpole diagram deviates from the symmetric case, since it includes the implicit $k$-dependence of the internal lines via the flowing physical minimum.

### Resumé

In both phases, we have a positive curvature mass $m_{\mathrm{curv}} > 0$ on the equation of motion $\phi_0$. Its value is related to the pole mass $m_{\mathrm{pole}} = k$ in the symmetric, and $m_{\mathrm{pole}} = 2k$ in the broken phase. The difference between the flows is the existence of vertices $\Gamma^{(2n+1)}$ in the broken phase. They are proportional to sums of powers of $\phi_0$, see (B.56), and hence vanish in the symmetric phase. Specifically, the flow of the two-point function in the broken phase contains the diagrammatic topology of a vacuum polarisation.

This leads us to the following structure: the CS flows are initiated deep in the symmetric and deep in the broken phase for large pole masses and a given classical coupling $\lambda_\phi$, see (B.52) and (B.60) respectively. For the broken phase this entails, that also the field expectation value at the initial scale is large as it scales with $\Lambda$, see (B.58) and (B.60). Then, the pole mass is successively lowered and for $k = 0$ one reaches the phase transition point from both sides. In particular, the flows do not leave the broken or symmetric phase. This is in seeming contradiction to the standard fRG picture in a scalar theory, where flows in the broken phase may end up in the symmetric phase, and those in the symmetric phase end up deeper in the symmetric phase. This apparent contradiction is resolved by the fact, that $\phi_0$ in the standard fRG is defined from the subtracted EoM. There, the trivial cutoff flow, which is $\propto k^2\phi$, is subtracted from the effective potential, and one recovers physics only in the limit $k \to 0$.

## B.5. Formulae: Functional flows for complex effective actions

*This section is taken from [4] and provides additional technical details which compliment the main text.*

### B.5.1. The Polchinski flow

In this Appendix we briefly recapitulate the derivation of the Polchinski equation [68] for a scalar theory. All correlation functions in Euclidean field theory can be obtained from the generating functional. The generating functional is defined by its derivatives, see Equation (3.1). It can, however, also be linked to an explicit path integral representation;

$$Z_k[J] = \int d\varphi \, e^{-S[\varphi]-\frac{1}{2}\int_x \varphi R_k \varphi + \int_x J(x)\varphi(x)}, \tag{B.64}$$

for a given theory of the real scalar field, $\varphi \in \mathbb{R}$. In accordance with the general procedure of the functional renormalisation group, we have already introduced the (infrared) cutoff term in (B.64). The cutoff term $R_k$ suppresses all contributions with $p^2 < k^2$ to the generating functional. The correlation functions, derived from the generating functional $Z[J]$, are the full ones including their disconnected parts. The connected parts are derived from the Schwinger functional

$$W_k[J] = \log Z[J]. \tag{B.65}$$

Important examples are given by the mean field in a given background current,

$$\phi[J] = \frac{\delta W_k[J]}{\delta J}, \tag{B.66}$$

and the propagator,

$$G_k = \langle \varphi(x)\varphi(y)\rangle_c = W_k^{(2)}[J], \tag{B.67}$$

where the subscript $_c$ stands for *connected*. The flow of $W_k[J]$ is given by

$$\partial_t W_k[J] = -\frac{1}{2}\,\mathrm{Tr}\,\partial_t R_k \left[W^{(2)}[J] + \left(W^{(1)}[J]\right)^2\right]. \tag{B.68}$$

Equation (B.68) and its generalisations are the master equations for the derivation of flow equations for the Wilsonian effective action (generating functional of *amputated connected* correlation functions), the 1PI effective action (generating functional of *one particle irreducible* correlation functions), functional symmetry identities, and further generating functions.

The derivation of the Wilsonian effective action continues, by using the inverse classical propagator in the current. This removes (amputates) the external legs from the Schwinger functional $W_k[J]$,

$$J = S_k^{(2)}\phi, \quad \text{with} \quad S_k^{(2)} = S^{(2)}[\phi_0] + R_k, \tag{B.69}$$

with a given background $\phi_0$, which can be chosen conveniently. The respective generating functional,

$$S_{\mathrm{eff},k}[\phi] = -W_k[S_k^{(2)}\phi], \tag{B.70}$$

is the generating functional of *amputated connected* correlation functions. This amputation is elucidated at the example of the one- and two-point functions,

$$S_k^{(2)} \frac{\delta W_k[J]}{\delta J} = -\frac{\delta S_{\text{eff},k}[\phi]}{\delta \phi},$$
$$S_k^{(2)} \frac{\delta^2 W_k[J]}{\delta J^2} S_k^{(2)} = -\frac{\delta^2 S_{\text{eff},k}[\phi]}{\delta \phi^2}. \tag{B.71}$$

The flow equation for the Wilsonian effective action $S_{\text{eff},k}[\phi]$ can be obtained by inserting (B.70) or rather (B.71) into the master-equation (B.68). It is given by

$$\left(\partial_t + \int_x \phi\, S_k^{(2)}\, \partial_t G_k^{(0)} \frac{\delta}{\delta \phi}\right) S_{\text{eff},k}[\phi] = \frac{1}{2} \operatorname{Tr}\, \partial_t G_k^{(0)} \left[S^{(2)}_{\text{eff},k}[\phi] - \left(S^{(1)}_{\text{eff},k}[\phi]\right)^2\right], \tag{B.72}$$

with the classical propagator

$$G_k^{(0)} = \frac{1}{S_k^{(2)}} = \frac{1}{S^{(2)}[\phi_0] + R_k}. \tag{B.73}$$

This is Wegner's flow (3.20) with the kernel (3.25) and the anomalous dimension (3.28) as discussed in Section 3.3.1.

Note that for cutoff-dependent (evolving) backgrounds $\phi_0$ the $t$-derivative in $\partial_t S_k^{(2)}$ also hits the field. When expanding the Wilsonian effective action about its classical (or rather UV) counter part $S_k[\phi]$, the trivial flow for the cutoff term is apparent. Already in the case of real external fields, we find some inconveniences with this formulation. For example in the investigation of chiral symmetry breaking, $G_k^{(0)}$ runs into a singularity at some $k > 0$, thus necessitating a formulation in evolving backgrounds. This observation motivates the choice of an expansion about an RG-adapted propagator (see Section 6.1.1), already in a real setting.

Continuing with the derivation of the classical expansion of the Polchinski flow, we separate the full two-point function from the effective action,

$$S_{\text{eff},k}[\phi] = S_{\text{int},k}[\phi, \phi_0] - \frac{1}{2} \int_x \phi\, S_k^{(2)}[\phi_0]\, \phi\,, \tag{B.74}$$

This split eliminates the trivial running of $S^{(2)}[\phi_0]$ from the flow and makes numerical computations more convenient. Inserting (B.74) into the Polchinski flow (B.72) leads us to the flow of the interaction part $S_{\text{int},k}[\phi]$

$$\partial_t S_{\text{int},k}[\phi] = \frac{1}{2} \operatorname{Tr}\, \partial_t G_k^{(0)} \left[S^{(2)}_{\text{int},k}[\phi] - \left(S^{(1)}_{\text{int},k}[\phi]\right)^2\right] + \frac{1}{2} G_k^{(0)}\, \partial_t S_k^{(2)}, \tag{B.75}$$

where the second line is $\phi$-independent, but $\phi_0$-dependent.

### B.5.2. Field expansion and flows of $n$-point functions of the RG-adapted flow

This Appendix contains some technical details of the derivation of the RG-adapted flow derived in Section 6.1.2. With (6.6), the one-point function is simply

$$\bar{\phi} = -G_k[\phi_0] S^{(1)}_{\text{ad},k}[0], \quad \text{with} \quad \bar{\phi} = \langle \varphi \rangle_{J=0}. \tag{B.76}$$

This entails that the one-point function encodes the information about the expectation value $\bar{\phi}$ of the field (up to the propagator). The latter is given by the two-point function,

$$S^{(2)}_{\mathrm{ad}}[0,\phi_0] = -G_k^{-1}[\phi_0] = -\left(\Gamma_k^{(2}[\phi_0] + R_k\right), \tag{B.77}$$

with the 1PI effective action $\Gamma_k[\phi]$. We emphasise that (B.77) entails that the argument $\phi$ of $S^{(2)}_{\mathrm{ad},k}$ is the difference field to $\phi_0$, the possibly $k$-dependent expansion point. We have

$$S_{\mathrm{ad}}[\phi] = -\frac{1}{2}\int (\phi+\bar{\phi})G_k^{-1}[\phi_0](\phi+\bar{\phi}) + \Delta S_{\mathrm{eff}}[\phi,\bar{\phi}]\,. \tag{B.78}$$

Finally, the higher $n$-point functions $S^{(n>2)}_{\mathrm{eff},k}$ encode the interactions. We now disentangle the flow of the latter from that of the propagator $G_k[\phi_0]$ or rather $\Gamma^{(2)}_k[\phi_0]$. This is the crucial ingredient of the RG-adapted flow for $S_{\mathrm{dyn}}$, (6.13a) in Section 6.1.2, and reads

$$\partial_t \Gamma^{(2)}_k[\phi_0] = \frac{1}{2}\,\mathrm{Tr}\;\mathscr{C}_k\left[S^{(4)}_{\mathrm{dyn},k}[0] - 2S^{(1)}_{\mathrm{dyn},k}[0]S^{(3)}_{\mathrm{dyn},k}[0]\right]. \tag{B.79}$$

In (B.79) the vertices $S^{(3,4)}_{\mathrm{dyn},k}[0]$ enter as well as the one-point function. The latter is given by (B.76) with the flow

$$\left(\partial_t + \gamma_{\mathrm{dyn},k}\right)S^{(1)}_{\mathrm{dyn},k}[0] = \frac{1}{2}\,\mathrm{Tr}\;\mathscr{C}_k\,S^{(3)}_{\mathrm{dyn},k}[0]\,. \tag{B.80}$$

Finally, the flow of the interaction part,

$$S_{\mathrm{int},k}[\phi] = S_{\mathrm{dyn},k}[\phi] - S^{(1)}_{\mathrm{dyn},k}[0]\phi\,, \tag{B.81}$$

is given by

$$\left(\partial_t + \int_x\left[\phi\,\gamma_{\mathrm{dyn},k} + \mathscr{D}_k\right]\frac{\delta}{\delta\phi}\right)S_{\mathrm{int},k}[\phi] = \frac{1}{2}\,\mathrm{Tr}\;\mathscr{C}_k\left[\hat{S}^{(2)}_{\mathrm{int},k}[\phi] - \left(S^{(1)}_{\mathrm{int},k}[\phi]\right)^2\right], \tag{B.82}$$

with

$$\begin{aligned}\mathscr{D}_k &= \mathscr{C}_k S^{(1)}_{\mathrm{dyn},k}[0]\,,\\ \hat{S}^{(2)}_{\mathrm{int},k}[\phi] &= S^{(2)}_{\mathrm{int},k}[\phi] - S^{(3)}_{\mathrm{int},k}[0]\cdot\phi - \frac{1}{2}S^{(4)}_{\mathrm{int},k}[0]\cdot\phi^2\,.\end{aligned} \tag{B.83}$$

The definition of the Schwinger functional in the complex plane suggests an ambiguity in the definition of the complex part of (B.82) due to the complex logarithm.

### B.5.3. Large cutoff limit

To begin with, one can easily convince oneself that for $R_k \to \infty$ in the limit $k \to \infty$, where the path integral gets approximately Gaußian, to wit

$$S_{\mathrm{eff},k}[\phi] \overset{k\to\infty}{\longrightarrow} -\frac{1}{2}\int_x \phi\left(S^{(2)}_k + R_k\right)\phi + O(\phi^3)\,. \tag{B.84}$$

The Wilsonian effective action tends towards the classical Wilsonian action, including the cutoff term, in the UV. This property is essential in deriving the initial conditions. Strictly speaking it tends towards the UV-relevant part of the Wilsonian effective action. This holds true for sufficiently small fields.

The case of general fields is resolved in a indirect way. We utilise that the flow of the effective action $\Gamma_k$ decays for large fields and only the primitively divergent terms in the action flow. This leaves us with the limit

$$\Gamma_{k\to\infty}[\bar{\phi}] \to S_{\rm cl}[\bar{\phi}]\,. \tag{B.85}$$

This implies that the relation between the current and the (mean 1PI) field $\bar{\phi}$ is given by

$$J = \frac{\delta\Gamma_k}{\delta\bar{\phi}} + R_k\bar{\phi}\,. \tag{B.86}$$

For the classical action

$$S_{\rm cl}[\bar{\phi}] = \frac{1}{2}\int \bar{\phi}S^{(2)}\bar{\phi} + \frac{\lambda}{4!}\bar{\phi}^4\,, \tag{B.87}$$

we arrive at

$$J = \left(S^{(2)} + R_k\right)\bar{\phi} + \frac{\lambda}{6}\bar{\phi}^3\,, \tag{B.88}$$

which entails that the 1PI mean field $\bar{\phi}$ and the Wilsonian field $\phi$ in (B.69) agree up to the interaction piece. We have

$$\phi = \bar{\phi} + \frac{\lambda}{6}G_k^{(0)}\bar{\phi}^3\,. \tag{B.89}$$

Evidently, for sufficiently small field we have $\phi \approx \bar{\phi}$ and the Wilsonian action tends (B.84). In turn, for large fields $\phi \to \infty$ we have

$$\phi \approx \frac{\lambda}{6}G_k^{(0)}\bar{\phi}^3 \quad\longrightarrow\quad \bar{\phi} \approx \left(\frac{6}{\lambda}S_k^{(2)}\phi\right)^{\frac{1}{3}}\,. \tag{B.90}$$

In any case we have for $k \to \infty$,

$$W_k[J] \to \frac{1}{2}\int \bar{\phi}S_k^{(2)}\bar{\phi} + \frac{\lambda}{8}\int \bar{\phi}^4\,, \tag{B.91}$$

and hence

$$S_{{\rm eff},k}[\phi] \to -\frac{1}{2}\int \bar{\phi}S_k^{(2)}\bar{\phi} - \frac{\lambda}{8}\int \bar{\phi}^4\,, \tag{B.92}$$

where $\bar{\phi}[\phi]$ solves (B.89).

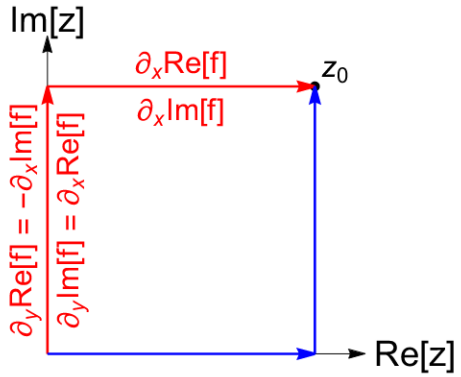


Figure B.5.: Path choices for an integration of the holomorphic function $f$ at some coordinate $z_0$ in the complex plane. Both the red and blue lines are convenient choices, since the computation gives $\partial_x \mathrm{Re}[f]$ and $\partial_x \mathrm{Im}[f]$ as an output.

### B.5.4. Analytic relations for the susceptibility

The susceptibility indicates the response of the magnetisation $M$ to the application of an external field $H$ and is given by

$$\chi(\phi_y, H=0) = \frac{\partial M}{\partial H}(\phi_y, H)|_{H=0}\,. \tag{B.93}$$

The magnetisation is expected to diverge at the phase transition following (6.41). Hence, a direct, numerical evaluation of this expression is impractical. Therefore, we make use of the following analytic relation. We start from the definition of the magnetisation, via the equation of motion (6.36b), by taking a derivative with respect to the external field $H$.

$$1 = \partial_H \frac{\partial w[J(\phi)]}{\partial \phi}\bigg|_{\phi=\phi_{\mathrm{EoM}}} = \frac{\partial \phi_{\mathrm{EoM}}}{\partial H}\,\frac{\partial^2 w[J(\phi)]}{\partial \phi^2}\bigg|_{\phi=\phi_{\mathrm{EoM}}}, \tag{B.94}$$

where $\phi_{\mathrm{EoM}} = M$ is simply the magnetisation, see (6.36b). Furthermore, $\partial_\phi^2 V_{\mathrm{dyn}}$ is directly evaluated in the LDG-scheme (see Section 6.2.4) and relates to the effective potential of the Schwinger functional via (6.34). Putting everything together, the susceptibility can be evaluated via

$$\chi(\phi_y, H=0) = \frac{1}{\left(m^2_{k=0} - \partial_\phi^2 V_{\mathrm{dyn}}(\phi)\right)}\bigg|_{\phi=\phi_{\mathrm{EoM}}}, \tag{B.95}$$

where $m^2_{k=0}$ is the RG-time dependent mass at $k=0$, depicted in Figure 6.5. Equation (B.95) forgoes taking a difficult numerical derivative with respect to $H$. An additional benefit is easy access to the divergence, via the zeroes of the enumerator.

### B.5.5. Complex integration and holomorphicity

In this section we discuss how we obtain the full potential from the numerical data. For an explicit complex integration a convenient path in the complex plane can, and should, be chosen due to holomorphicity, which we implemented in Section 6.2.3. Possible path choices are indicated in Figure B.5.

First, we check if our results are holomorphic: to this aim we integrate along the red and blue path in Figure B.5 and compute their relative error given by

$$\Delta I = \frac{I_{\text{red}} - I_{\text{blue}}}{I_{\text{red}}} \,. \tag{B.96}$$

The Cauchy-Riemann equations are used to obtain the respective $y$ derivatives. The relative error remains below $10^{-3}$ for all schemes up until $\phi = 2$. From there on, a small numerical error is generated, which stems from the interpolation of steep structures in post-processing.

Generally, all integrated results are obtained by integration along the red path. Although ideally both paths should yield the same result, the numerical precision along the red path is superior: The numerical grid, and thus the high numerical precision, follows the real direction. Therefore, the biggest contribution to the path should follow from a horizontal line, whereas the vertical contribution should, preferably, be small. The red path is now favoured by two observations:

- Symmetry dictates, that either the real or imaginary part of the function $f$ is zero on the imaginary axis, i.e. the vertical red path.
- The imaginary part on the real axis is zero, i.e the horizontal, imaginary blue path does not contribute at all.

## B.6. Formulae: The quark-meson model

*This section is taken from [1] and provides additional technical details which compliment the main text.*

### B.6.1. The large-$N_f$ limit

Some of the numerical results in Chapter 8 are obtained in the large-$N_f$ limit of the flows, as it simplifies the numerical treatment significantly: it eliminates the second derivative terms in the sigma meson mass term. We are left with only the pion loops as well as the quark loop. The pion loops constitute the flow of a pure O(N)-theory in the large-$N_f$ limit as considered in [65] with discontinuous Galerkin methods. Such a non-linear first order system is solved using approximate Riemann solvers. These solvers rely on the assumption that the solution is dominated by one strong wave, for more details see Appendix A. This assumption holds if the flow is dominated by contributions of the pion and quark loops, which is always ensured in the large-$N_f$ limit.

This simplification is also helpful when considering systems of multiple differential equations. However, it will also be instructive to make a comparison between both the finite $N_f$ case and the large-$N_f$ limit in the case with constant Yukawa coupling. Moreover, we can simulate the physics case, $N_f = 2$ and $N_c = 3$, with a suitable chosen large-$N_f$ limit:

To begin with we keep the ratio of color and flavour fixed to that of the $N_f = 2$ quark-meson model in QCD,

$$\frac{N_c}{N_f} = \frac{3}{2} \,. \tag{B.97a}$$

With (B.97a) we keep the flavour-colour balance of QCD intact. This ensures that the contributions of the quark-loop are not suppressed by $1/N_f$. Moreover, the flavour-colour ratio is

certainly of crucial importance for e.g. the question of the existence and size of a quarkyonic phase. Finally, we consider the following generic rescaling of $\rho$, $V_k(\rho)$ and $h_k(\rho)$,

$$\rho \to \frac{N_f^2-1}{N_\pi}\rho\,, \qquad V_k(\rho) \to \frac{N_f^2-1}{N_\pi} V_k(\rho)\,, \qquad h_k(\rho) \to \sqrt{\frac{N_\pi}{N_f^2-1}}\, h_k(\rho)\,. \tag{B.97b}$$

The factor $N_\pi$ in (B.97b) is introduced to simulate the flows of a quark-meson model with $N_\pi$ pions instead of one sigma meson and three pions. Both cases are relevant for the physics of two-flavor QCD or the two-flavour QM-model.

In the chirally symmetric phase for large temperatures and cutoff scales, the pions and the sigma are degenerate on-shell at $\rho = 0$. The second derivative term vanishes $2\rho V''(\rho)\big|_{\rho=0} = 0$, and the on-shell $\sigma$-propagator agrees with the pion one, and the (on-shell) flow equation resembles that with four pions.

In turn, in the broken phase, the $\sigma$-mode develops a mass and quickly decouples from the dynamics of the system. Then, the (on-shell) dynamics of the theory is driven by the three (massless or light) pions. From previous fRG investigations of the quark-meson model as well as QCD we know that the mesonic dynamics in the broken phase is of sub-dominant importance for not too large chemical potential. This suggests that the $N = 4$ case should mimic the two-flavour case best. A full discussion of the comparison is provided in Section 8.2.1 and Section 8.2.2.

With the limit $N_f \to \infty$ and (B.97) we derive the flow equations for large-$N_f$ Yukawa coupling, $h_k^{\mathrm{lN}}(\rho)$, and effective potential, $V_k^{\mathrm{lN}}(\rho)$,

$$\partial_t V_k^{\mathrm{lN}}(\rho) = \frac{k^5}{12\pi^2}\Big\{\frac{N_\pi}{\epsilon_k^\pi}(1+2n_B(\epsilon_k^\pi)) - \frac{4\times 2\times 3}{\epsilon_k^q}(1-n_f(\epsilon_k^q+\mu)-n_f(\epsilon_k^q-\mu))\Big\}\,, \tag{B.98}$$

and

$$\partial_t h_k^{\mathrm{lN}}(\rho) = -4N_\pi v_3 (h_k^{\mathrm{lN}}(\rho))^3 L^{(4)}_{(1,1)}(m_{q,k}^2, m_{\pi,k}^2; T,\mu) - 2N_\pi v_3 k^2 (h_k^{\mathrm{lN}}(\rho))' l_1^{(B,4)}(m_{\pi,k}^2; T)\,. \tag{B.99}$$

This concludes our derivation of the set of flow equations in LPA. Numerical results for finite $N_f$ and the large-$N_f$ limit are presented in Section 8.2.

### Flows in the large-$N_f$ limit

In this section the quark-meson model flows in the large-$N_f$ limit are reformulated to simplify their numerical treatment. Equation (8.3) and (B.98) are rearranged following the idea of Section 5.1.2. Here, the dependency on the first derivative can be eliminated by introducing it as a new variable, which coincides with the pion mass squared,

$$u_k(\rho) = \partial_\rho V_k(\rho) = m_{\pi,k}^2\,. \tag{B.100}$$

The flow of the Yukawa coupling at finite N is given by a highly non-linear equation of second order. Since it can not be made to fit the form given in (A.1), it is not solved within the direct DG framework. However, the expression simplifies significantly in the large-$N_f$ limit and (B.99) can be written to suit the formalism. Equation (B.99) is rewritten in terms of the quark mass

squared $m_q^2(\rho)$, as we are primarily interested in physical observables. Thus, a new variable is introduced,

$$w_k(\rho) = 2h_k(\rho)^2\rho = m_{q,k}^2 \,. \tag{B.101}$$

Appendix B.6.1 explains how the ambiguity in splitting the conservative and non-conservative contributions to the flux are used to accommodate boundary conditions. For completeness the final form of the equations is stated,

$$\begin{aligned} \partial_t u_k &= \partial_\rho f_u(u_k, w_k)\,, \\ \partial_t w_k &= \partial_\rho(a(u_k)w_k) - (w_k \partial_u a(u_k))\partial_\rho u_k + s(u_k, w_k)\,. \end{aligned} \tag{B.102}$$

This version of the equation has the advantage that the non-conservative product is rather small in comparison to the conservative part.

### Explicit equations

The flow equation of the pion mass is obtained by taking a $\rho$ derivative of the effective potential. In case of the large-$N_f$ model this is given by,

$$\partial_t u_k^{\mathrm{lN}}(\rho) = \partial_\rho \left[ \frac{k^5}{12\pi^2} \left\{ \frac{N_\pi}{\epsilon_k^\pi} \left[1 + 2n_B(\epsilon_k^\pi)\right] - \frac{4\times 2\times 3}{\epsilon_k^q} \left[1 - n_f(\epsilon_k^q + \mu) - n_f(\epsilon_k^q - \mu)\right] \right\} \right]. \tag{B.103}$$

The flow equation of the Yukawa coupling in (B.99) is rewritten in terms of the quark mass squared $m_q^2(\rho)$. To this aim, we multiply the original flow equation by $4h(\rho)\rho$, which gives

$$\begin{aligned} \partial_t w_k =& 4h_k\rho A(u_k)\partial_\rho h_k + 4\rho h_k^4 B(w_k, u_k) = 2\rho A(u_k)\partial_\rho h_k^2 + 4\rho h_k^4 B(w_k, u_k) \\ =& A(u_k)\partial_\rho w_k - 2h_k^2 A(u_k) + 4\rho h_k^4 B(w_k, u_k) \\ =& A(u_k)\partial_\rho w_k + \frac{w_k}{\rho}\Big[w_k B(w_k, u_k) - A(u_k)\Big], \end{aligned} \tag{B.104}$$

where

$$A(m_{\pi,k}^2; T, \mu) = -2N_\pi v_3 k^2 l_1^{(B,4)}(m_{\pi,k}^2; T)\,, \tag{B.105}$$

corresponds to the contribution of the pion tadpole diagram and

$$B(m_{q,k}^2, m_{\pi,k}^2; T, \mu) = -4N_\pi v_3 L_{(1,1)}^{(4)}(m_{q,k}^2, m_{\pi,k}^2; T, \mu)\,, \tag{B.106}$$

to the mixed contribution in Figure 8.1. The explicit form of the threshold functions is given in Appendix B.7.2.

### Calculation of the non-conservative numerical Flux

The flow equation for the Yukawa coupling (B.99) was reformulated in Appendix B.6.1 to suit the general form of the partial differential equations given in (A.1) and contains a non-conservative flux term and a source term $s$,

$$\partial_t w_k = A(u_k)\partial_\rho w_k + s(u_k, w_k)\,. \tag{B.107}$$

The exact definition and derivation of the appearing terms is given in (B.104).

The formulation requires the computation of a non-conservative flux, using the integral derived by the jump condition in Appendix A in (A.5). We chose a straight path across an interface,

$$w(s) = w^- + s(w^+ - w^-)\,,$$
$$u(s) = u^- + s(u^+ - u^-)\,.$$

We note again that this is a path along the solutions $u$ and $w$ and not a path in the 'spatial' coordinate $\rho$. The straight path was chosen because it is often the simplest choice for the evaluation of the integral. In our case the expression simplifies so much that it can be evaluated analytically, due to the explicit form of the equations, where the non-conservative flux is given by

$$A(u(s)) = \partial_u g\,(u(s)) = \frac{1}{u^+ - u^-}\partial_s g\,(u(s))\,. \tag{B.108}$$

This gives

$$\begin{aligned}\boldsymbol{D}(u^+, u^-, w^+, w^-, \hat{\boldsymbol{n}}) &= \frac{1}{2(u^+ - u^-)}\int_0^1 \hat{\boldsymbol{n}}\frac{\partial g(u(s))}{\partial s}\frac{\partial w(s)}{\partial s}\,ds + C[[\boldsymbol{w}]] \\ &= \frac{\hat{\boldsymbol{n}}}{2}\frac{g(u^+) - g(u^-)}{u^+ - u^-}\,(w^+ - w^-) + C[[\boldsymbol{w}]]\,,\end{aligned} \tag{B.109}$$

where we used in the last equality that $\partial_s w$ is a constant expression. Instead, the constant $C$ is simply the absolute value of the jacobian matrix.

$$C = \int_0^1 |A(u(s))\hat{\boldsymbol{n}}|\,ds\,. \tag{B.110}$$

Often, it can be approximated as the maximal characteristic speed of the non conservative product. Note that for constant $u$ across the interface $\frac{g(u^+)-g(u^-)}{u^+-u^-} = A(u)$, such that we recover a conservative flux for constant $u$. There is a large set of paths across the interface that lead to the same value in the integral, due to the fact that $A$ can be written as a derivative of $u$. This hints at the possibility that there might be a conservative formulation for the system of equations.

Since this formulation only allows flux boundary conditions for conservative fluxes a partial integration is performed,

$$A(u_k)\partial_\rho w_k = \partial_\rho(A(u_k)w_k) - w_k\partial_\rho A(u_k)\,. \tag{B.111}$$

We now have a conservative flux $A(u_k)w_k$ the proper in-/out-flow boundary conditions for $w_k$ and a very small non-conservative flux contribution $\boldsymbol{D'}$ accounting for jumps in $u_k$,

$$\boldsymbol{D'} = \boldsymbol{D} - [A(u_k^+)w_k^+ - A(u_k^-)w_k^-]\,. \tag{B.112}$$

This contribution is very small when $u_k$ is smooth and only contains small jumps across interfaces. It obviously vanishes at the outer boundary since there we have $u_k^+ = u_k^-$. Thanks to this formulation of the equation the maximal wave speed of the non conservative product is rather small and can be neglected in practice. In the general case however the inclusion of this term is important especially if the non conservative product are the only convective term in the equation, since it introduce the necessary numerical dissipation to make the numerical scheme stable.

## B.7. Expressions for the flat regulator

*This section is taken in parts from [1] and [9].*

Many of the current applications use a 3d or 4d flat cutoff, since it is the optimal choice in the commonly used local potential approximation. In the following, we summarise the expressions for the regulator Appendix B.7.1 and give the explicit expressions for the momentum integrated loop-diagrams in Appendix B.7.2 for this explicit regulator.

### B.7.1. Regulators

In the present work we often use the flat or Litim regulator, see [308]. The flat bosonic regulator is given by,

$$R_B(p) = Z_{B,k} p^2 \, r_B(x), \quad r_B(x) = \left(\frac{1}{x} - 1\right)\theta(1-x), \tag{B.113}$$

with $x = p^2/k^2$, and the fermionic one reads

$$R_F = Z_{F,k} \not{p} \, r_F(x), \qquad r_F(x) = \left(\frac{1}{\sqrt{x}} - 1\right)\theta(1-x). \tag{B.114}$$

$Z_{B,k}$ and $Z_{F,k}$ indicate the wave functions evaluated on some background, for the corresponding particles. The specific choice is indicated with the application. For example in LPA we set $Z = 1$. Furthermore the gluon regulator is given by

$$\left(R_k^A\right)_{\mu\nu}(q_0, \boldsymbol{q}) = Z_{A,k}(\rho_0)\boldsymbol{q}^2 \, r_B\left(\boldsymbol{q}^2/k^2\right)\left(\delta_{\mu\nu} - \frac{q_\mu\nu}{q^2}\right) \quad + \frac{\boldsymbol{q}^2}{\xi} r_B\left(\boldsymbol{q}^2/k^2\right)\left(\frac{q_\mu\nu}{q^2}\right), \tag{B.115}$$

in the Landau gauge with $\xi \to 0$.

At finite temperatures, we resort to a spatial cutoff (usually three-dimensional), where we replace the $p = (p_0, \boldsymbol{p})$ dependence in the regulator with a purely spatial momentum dependence $\boldsymbol{p}$ and accordingly $x = p^2/k^2 \to \boldsymbol{p}^2/k^2$.

The flat cutoff is optimised for the 0th order in the derivative expansion, which is used throughout this work, [127, 129, 130].

### B.7.2. Common threshold functions

This section is a compilation of threshold functions. First we perform the Matsubara summation and secondly we perform the momentum integration. Since we are surrently considering a flat regulator, the momentum dependence drops from the denominator and both steps can be neatly separated. This is different when smooth regulators are used.

#### Matsubara summation

The threshold functions are computed in terms of the scalar parts of the propagators with the flat cutoff, see Appendix B.7.1. The bosonic and fermionic ones are given by,

$$G_b(q, \bar{m}^2) = \frac{1}{(q_0/k)^2 + 1 + \bar{m}^2}, \tag{B.116}$$

$$G_f(q, \bar{m}^2) = \frac{1}{\left((\tilde{q}_0 + i\mu_q)/k\right)^2 + 1 + \bar{m}^2}, \tag{B.117}$$

respectively. The Matsubara frequencies read $q_0 = 2j\pi T$, with $j \in \mathbb{Z}$ for the Bosons and $\tilde{q}_0 = (2j+1)\pi T$, with $j \in \mathbb{Z}$ for the Fermions. With renormalised dimensionless masses $\bar{m} = m/k$.

The threshold functions, in which we perform the Matsubara summation, are defined in the standard way. Firstly, we consider fermionic and bosonic loops that contain $n_1, n_2, \ldots$ fermionic and bosonic particles, that is

$$\begin{aligned} B_{(n)}(\bar{m}^2; T) &= \frac{T}{k} \sum_j \left(G_b(q, \bar{m}^2)\right)^n , \\ F_{(n)}(\bar{m}^2; T, \mu_q) &= \frac{T}{k} \sum_j \left(G_f(q, \bar{m}^2)\right)^n , \end{aligned} \tag{B.118}$$

for loops with a single particle. For multiple particle loops they follow the scheme

$$\begin{aligned} FB_{(n_1,n_2)}(\bar{m}_f^2, \bar{m}_b^2; T, \mu_q) &= \frac{T}{k} \sum_j \left(G_f(q, \bar{m}_f^2)\right)^{n_1} \left(G_b(q, \bar{m}_b^2)\right)^{n_2} , \\ BB_{(n_1,n_2)}(\bar{m}_{b1}^2, \bar{m}_{b2}^2; T) &= \frac{T}{k} \sum_j \left(G_b(q, \bar{m}_{b1}^2)\right)^{n_1} \left(G_b(q, \bar{m}_{b2}^2)\right)^{n_2} . \end{aligned} \tag{B.119}$$

The $n+1$-th function can be inferred from the $n$-th by taking a derivative with respect to $\bar{m}^2$

$$P_{(n+1)}(\bar{m}^2) = -\frac{1}{n} \partial_{\bar{m}^2} P_{(n)}(\bar{m}^2), \tag{B.120}$$

where $P \in \{B, F\}$. Naturally, (B.120) generalises to multiple particle loops, i.e. $FB(n_1, n_2)$ are obtained in a similar fashion. This follows simply by taking the structure of the scalar part of the propagator (B.116) into account. Therefore it suffices to compute the lowest threshold function with $n = 1$ for which the Matsubara summation reads

$$\begin{aligned} B_{(1)}(\bar{m}^2; T) &= \frac{\coth\left(\frac{E\,k}{2T}\right)}{2E}, \\ F_{(1)}(\bar{m}^2; T, \mu_q) &= \frac{\tanh\left(\frac{(E-\mu_q)\,k}{2T}\right) + \tanh\left(\frac{(E+\mu_q)\,k}{2T}\right)}{4E}, \end{aligned} \tag{B.121}$$

where the dispersion relation is given by $E_x = \sqrt{1+\bar{m}_x^2}$. We note, that we chose to indicate the threshold functions in terms of hyperbolic functions instead of the conventional choice of thermodynamic distributions. The definitions are equivalent to the expressions used in [51,58]. The notation is changed to accommodate the need for higher numerical precision in a field dependent formulation. The loops containing a fermionic and a bosonic species each are evaluated to

$$\begin{aligned} &FB_{(1,1)}(\bar{m}_f^2, \bar{m}_b^2; T, \mu_q) = k^2/4 \\ &\left( \frac{\tanh\left(\frac{E_f\,k-\mu_q}{2T}\right)/E_f}{k^2(m_b^2-m_f^2)+(\pi T+i\mu_q)^2-2kiE_f(\pi T+i\mu_q)} + \frac{\tanh\left(\frac{E_f\,k+\mu_q}{2T}\right)/E_f}{k^2(m_b^2-m_f^2)+(\pi T+i\mu_q)^2+2kiE_f(\pi T+i\mu_q)} \right. \\ &\left. + \frac{\coth\left(\frac{E_b\,k}{2T}\right)/E_b}{-k^2(m_b^2-m_f^2)+(\pi T+i\mu_q)^2+2kiE_b(\pi T+i\mu_q)} + \frac{\coth\left(\frac{E_b\,k}{2T}\right)/E_b}{-k^2(m_b^2-m_f^2)+(\pi T+i\mu_q)^2-2kiE_b(\pi T+i\mu_q)} \right). \end{aligned} \tag{B.122}$$

Furthermore, we have loops with two boson species, with masses $\bar{m}^2_{b1}$ and $\bar{m}^2_{b2}$, and one fermion given by,

$$
\begin{aligned}
&FBB_{(1,1,1)}(\bar{m}^2_f,\bar{m}^2_{b1},\bar{m}^2_{b2};T,\mu_q) = k^2/4 \\
&+\Bigg(\frac{k^2\tanh\left(\frac{E_f\,k-\mu_q}{2T}\right)/E_f}{\left[(i(\pi T+i\mu_q)+kE_f)^2-k^2E^2_{b1}\right]\left[(i(\pi T+i\mu_q)+kE_f)^2-k^2E^2_{b2}\right]} \\
&+\frac{k^2\tanh\left(\frac{E_f\,k+\mu_q}{2T}\right)/E_f}{\left[(i(\pi T+i\mu_q)-kE_f)^2-k^2E^2_{b1})\right]\left[(i(\pi T+i\mu_q)-kE_f)^2-k^2E^2_{b2})\right]} \\
&+\frac{\coth\left(\frac{E_{b1}\,k}{2T}\right)/E_{b1}}{m^2_{b1}-m^2_{b2}}\left[\frac{1}{(-i(\pi T+i\mu_q)+kE_{b1})^2-k^2E^2_f}+\frac{1}{(-i(\pi T+i\mu_q)-kE_{b1})^2-k^2E^2_f}\right] \\
&+\frac{\coth\left(\frac{E_{b2}\,k}{2T}\right)/E_{b2}}{m^2_{b2}-m^2_{b1}}\left[\frac{1}{(-i(\pi T+i\mu_q)+kE_{b2})^2-k^2E^2_f}+\frac{1}{(-i(\pi T+i\mu_q)-kE_{b2})^2-k^2E^2_f}\right]\Bigg).
\end{aligned}
\tag{B.123}
$$

Loops containing only bosons from different species are evaluated to

$$
BB_{(1,1)}(\bar{m}^2_{b1},\bar{m}^2_{b2};T) = -\frac{1}{2(m^2_{b1}-m^2_{b2})}\left[\frac{\coth\left(\frac{kE_{b1}}{2T}\right)}{E_{b1}}-\frac{\coth\left(\frac{kE_{b2}}{2T}\right)}{E_{b2}}\right]. \tag{B.124}
$$

### Momentum integration

With the flat regulator function the momentum integrations ia somewhat trivial, since the denominator of the propagators is completely momentum independent. In the presence of an anomalous dimension however, we obtain differing prefactors. To this aim we define the threshold functions $l_0^{(B/F,d)}$ in $d$ space-time dimensions. They are related to bosonic/fermionic loops and are defined as follows

$$
l_0^{(B,d)}(\bar{m}^2_{\phi,k},\eta_{\phi,k};T) = \frac{2}{d-1}\left(1-\frac{\eta_{\phi,k}}{d+1}\right)B_{(1)}(\bar{m}^2_{\phi,k};T), \tag{B.125}
$$

and

$$
l_0^{(F,d)}(\bar{m}^2_{\psi,k},\eta_{\psi,k};T,\mu) = \frac{1}{d-1}\left(1-\frac{\eta_{\psi,k}}{d}\right)F_{(1)}(\bar{m}^2_{\psi,k};T,\mu), \tag{B.126}
$$

where the Matsubara sums $B_{(1)},F_{(1)}$ are given in (B.121). Higher threshold functions $l_n^{(B/F,d)}$ are again obtained by the respective derivatives (B.120).

Similarly, the momentum integration over mixed fermionic/bosonic loops yields

$$
L^{(d)}_{(1,1)}\left(\bar{m}^2_{\psi,k},\bar{m}^2_{\phi,k},\eta_{\psi,k},\eta_{\phi,k};T,\mu\right) = \frac{2}{d-1}\left[\left(1-\frac{\eta_{\phi,k}}{d+1}\right)FB_{(1,2)}+\left(1-\frac{\eta_{\psi,k}}{d}\right)FB_{(2,1)}\right]. \tag{B.127}
$$

# APPENDIX C

## Side notes

## C.1. Additional material: Gluon condensate

### C.1.1. UV Asymptotics of the effective potential and regulator independence

The present work utilises the ghost and gluon propagators from [47]; which has been obtained within a quantitative approximation to the full Yang-Mills system. There, and in respective works in QCD, [44,48,125] it has been checked that the choice of the regulator is of subleading importance for the propagators at vanishing cutoff scale, which is one of the self-consistency checks that goes into an estimate of the systematic error.

As mentioned at the end of Appendix B.2.3, the relatively sharp regulator here delays the onset of UV asymptotics and hence the onset cutoff scale $k \gtrsim k_{\text{on}}$ of the regime in which the effective potential reduces to the classical form (4.56). For the sake of convenience we recall it,

$$\mathscr{W}_k(F^a) \overset{k\gtrsim k_{\text{on}}}{\longrightarrow} \frac{F^2}{16\pi\alpha_s(k)}\,, \qquad \alpha_s(k) = \frac{1}{4\pi}\frac{g_s^2}{Z_A(k)}\,. \tag{C.1}$$

In this regime the flow is simply a linear function in $F^2$ with the slope $\partial_t 1/(16\pi\alpha_s)$. Hence, for large cutoff scales we have,

$$\partial_t \mathscr{W}_k(F^a) \to -\frac{\partial_t\alpha_s(k)}{\alpha_s(k)}\frac{1}{16\pi\alpha_s(k)}F^2\,. \tag{C.2}$$

The coupling $\alpha_s$ in (C.1) is the background coupling which has the same (two-loop) universal $\beta$-function as the fluctuation coupling $\alpha_{s,\text{fluc}} = g_s^2/(4\pi Z_a Z_c^2)$ computed in [47]. However, the equivalence of the perturbative $\beta$-functions still allows for a global rescaling $\alpha_s = \bar{\gamma}\,\alpha_{s,\text{fluc}}$ whose value is checked by comparing the two flows for $k \to k_{\text{UV}}$,

$$\bar{\gamma} = \lim_{F^2\to 0}\frac{16\pi\alpha_{s,\text{fluc}}^2}{\partial_t\alpha_{s,\text{fluc}}}\frac{\partial_t\mathscr{W}_k}{F^2} \approx 1\,. \tag{C.3}$$

This fixes our initial condition, and in Figure C.1b we show both, the respective integrated flow, Figure C.1a, and the full cutoff dependent effective potential that also involves the initial

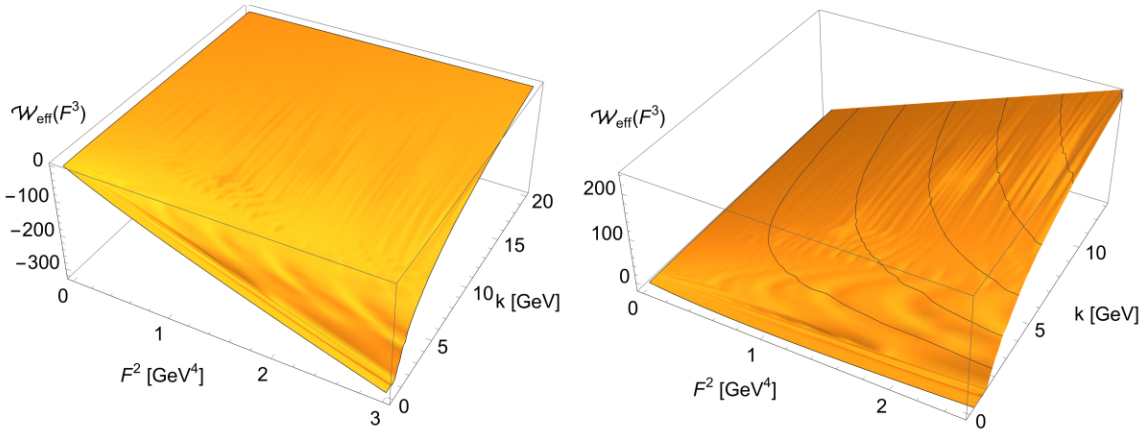


(a) Integrated UV Flow of the effective potential, $\mathcal{W}_k(F^a) - \mathcal{W}_{k_{\rm UV}}(F^a)$, defined in (C.4), for $F^a = F\delta^{a3}$ as a function of $F^2$. Here, $k_{\rm UV} = 20$ GeV. The substructure for $k_{\rm on} \gtrsim k \gtrsim 1$ GeV resolves the shape of the regulator (B.18).

(b) Effective Potential $\mathcal{W}_k(F^a)$, defined in (4.55), for $F^a = F\delta^{a3}$ as a function of $F^2$ in the regime $0 \leq k \leq k_{\rm UV} = 20$ GeV. The substructure for $k_{\rm on} \gtrsim k \gtrsim 1$ GeV resolves the shape of the regulator (B.18). For $k = 0$ see also Figure 4.1.

Figure C.1.: Cutoff dependence of the effective potential.

condition, Figure C.1b. The integrated flow from the UV scale $k_{\rm UV} = 20$ GeV to a general cutoff scale $k$ is given by

$$\mathcal{W}_k(F^a) - \mathcal{W}_{k_{\rm UV}}(F^a) = -\int_k^{k_{\rm UV}} \frac{\mathrm{d}k}{k}\, \partial_t \mathcal{W}_k(F^a)\,. \tag{C.4}$$

One clearly sees the linear dependence on $F^2$ for $k \to k_{\rm UV}$. At lower scales $k \to k_{\rm on}$ with $k_{\rm on} \approx 14$ GeV the transition regime sets in, in which the integrated flow resolves the shape function. Finally, for physical cutoff scales $k \lesssim 1$ GeV, the form of the shape function gets irrelevant and the integrated flow is getting smooth again. This shows very impressively that the information about the shape function is integrated out and disappears in the physical limit $k \to 0$.

We have also checked that the effective potential $\mathcal{W}_{\rm eff}(F^a)$ is RG-consistent [61, 127]. This is the simple requirement that $\mathcal{W}_{\rm eff}(F^a)$ does not vary if the flow is initiated at another cutoff scale

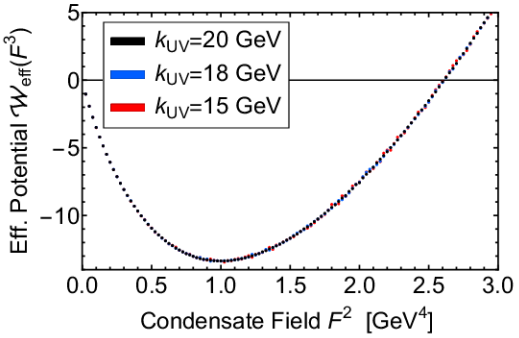


Figure C.2.: RG-consistency of the effective potential $\mathcal{W}_{\rm eff}(F^a)$: It is shown for integrating the initial effective potential (C.1) at different initial cutoff-scales $k_{\rm UV} = 20, 18, 15$ GeV to $k = 0$. The result is independent of the initial scale (RG-consistency).

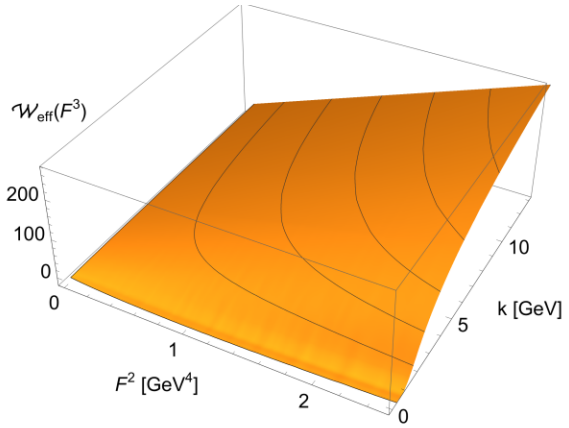


Figure C.3.: Effective Potential $\mathcal{W}_k(F^a)$, defined in (4.55), for $F^a = F\delta^{a3}$ as a function of $F^2$ obtained from integrating the flow with the regulator (C.5). In comparison to Figure C.1b the regulator is much smoother, which translates to the smoothness in $k_{\rm on} \gtrsim k \gtrsim 1\,$GeV.

$k_{\rm UV}$. Accordingly, it is a consistency check on the initial effective potential $\mathcal{W}_{k_{\rm UV}}$. Figure C.2 depicts the physical effective potential $\mathcal{W}_{\rm eff}(F^a)$, obtained from computations with $k_{\rm UV} = 15, 18, 20\,$GeV. The initial effective potentials are given by (C.1), where the scale dependency of the coupling $\alpha_s$ is obtained from the 1-loop beta function of the background coupling. These computations confirm the quantitative validity of the one-loop estimate for $\mathcal{W}_{k_{\rm UV}}$ for these large initial cutoff scales. In turn, for lower cutoff scales, the one-loop form is gradually lost which can be easily seen by the substructure (in $F^2$) of the flow.

Finally, we also report on results for the effective potential obtained by integrating the flow with a smoother regulator

$$R_k(p) = k^2\, e^{-p^2/k^2}\,. \tag{C.5}$$

Such a regulator decreases the numerical effort considerably. Note that this is not a self-consistent computation as it also requires cutoff-dependent propagators computed with the same regulator (C.5). However, we use this as a stability test of our results, and hence a further systematic error control. The respective result for the cutoff dependent effective potential is shown in Figure C.3, and one clearly sees that the use of a smoother regulator removes the substructures in the flow. The minimum value of $F^2$ at $k = 0$ is given by

$$\langle F^2\rangle_{\lambda_3} = 0.93(14)\,\text{GeV}^4\,, \tag{C.6}$$

to be compared with (4.61). These values compare well, which informs our estimate of the systematic error.

## C.1.2. Fitting procedure

Formally, the coefficient $Z_{\rm cond}$ in (4.47) is defined via an operator product expansion of the gluon propagator, and stems from the local operator (4.17). The present computation of the effective potential $\mathcal{W}_{\rm eff}$ is detailed in Appendix C.1.1, Appendix B.2.4, Appendix B.2.3 and uses the scaling propagator from [47]. The latter is obtained within a quantitative approximation of the coupled set of functional equations for Yang-Mills correlation functions, for respective DSE results see [225]. In [47], also decoupling solutions have been computed including a lattice-type solution, for respective lattice propagators see [192, 234].

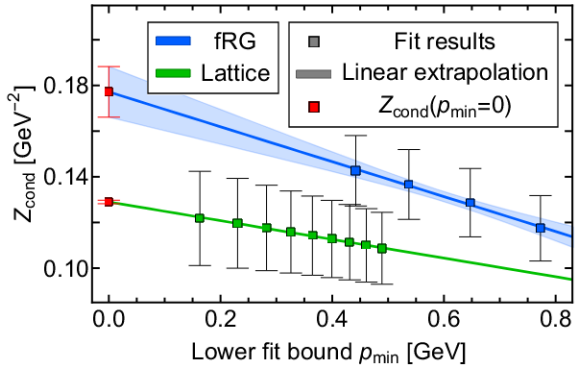


Figure C.4.: Linear extrapolation of $Z_{\text{cond}}$ to the lower fit interval bound $p_{\text{min}} = 0$, yielding $Z_{\text{cond}} = 0.149(19)$. The explicit fit results for $Z_{\text{cond}}$ are obtained via a fit of (C.7) to the scaling fRG data of [47] (blue squares), and to the lattice data of [194, 234] (green squares). $Z_{\text{cond}}$, being defined as the operator product expansion coefficient should be extracted at $p = 0$: we extract this information from an extrapolation of the fit results towards $p = 0$ (red squares), and use as a minimal $p_{\text{min}} \approx 0.8\,\text{GeV}$, below which the details of the implementation of the IR dynamics begin to matter. The triangular data points mark fit results for $p_{\text{min}}$ below the fit regime for the interpolation. The final estimate for $Z_{\text{cond}}$ ((C.11) and (4.65)) is obtained as the mean of the lattice and scaling fRG results for $Z_{\text{cond}}$, whose numerical values can be found in Table C.1.

The extraction of the $p^4$-coefficient stemming from (4.17) requires the distinction of the infrared dynamics in the propagator, which in the present approach relates to the emergence of the color condensates, from the coefficients of the local operators. This mixing for small momenta makes it impossible to extract the $p^4$-coefficient in an expansion about $p = 0$ without further information on the momentum dependence of the condensate. Instead we shall evaluate the propagator for sufficiently large momentum scales, for which the condensate vanishes, $\langle F \rangle \to 0$. The cutoff scale resembles the momentum scale $p$, indeed it is introduced in the two-point function itself as a momentum cutoff. Hence, we deduce from the flow of the minimum of $\mathcal{W}_{\text{eff}}$ depicted in Figure 4.3, that the condensate vanishes for $p \gtrsim 1/2$ GeV. Accordingly we determine $Z_{\text{cond}}$ from fits

$$Z_a^{\text{fit}}(p^2) = \frac{Z_m}{p^2} + Z_{p^2} + Z_{\text{cond}}\, p^2 \tag{C.7}$$

| | $Z_{\text{cond}}$ [GeV$^{-2}$] |
|---|---|
| scaling (fRG) | 0.168(31) |
| decoupling (lattice) | 0.129(19) |
| decoupling (fRG) | 0.1147(22) |
| Estimate | 0.149(19) |

Table C.1.: Extrapolation results for the wave function renormalisation $Z_{\text{cond}}$ at $p = 0$ based on the fit results for $Z_{\text{cond}}(p_{\text{min}})$ as a function of the lower fit interval bound $p_{\text{min}}$, see Figure C.4. The final estimate is obtained as the average of the scaling fRG and decoupling lattice data. In order to conservatively estimate possible systematic uncertainties (see text), we use the separate scaling fRG and lattice results as error bars.

to the gluon wave function $Z_a(p^2)$ in the momentum regime

$$p \in [p_{\min}, p_{\max}], \tag{C.8}$$

with

$$p_{\min} \in [0.77, 1.27]\,\mathrm{GeV}, \quad p_{\max} \in [1.95, 2.23]\,\mathrm{GeV}, \tag{C.9}$$

where the range of values for $p_{\min}$ is adapted to the data points of the sparse fRG data.

The upper bound $p_{\max}$ is chosen such, that the interval sustains a Taylor expansion while containing a sufficient amount of data points for fitting, also adapted to the fRG data points. Its maximum value is further constrained by the UV boundary of the lattice data from [234], which are used for comparison as well as the error estimate, together with the lattice data from [194].

The constants $Z_m$, $Z_{p^2}$ and $Z_{\mathrm{cond}}$ in (C.7) are fit parameters. Here $Z_m$ takes care of the infrared gapping dynamics, and $Z_{p^2}$ related to a standard (infrared) wave function renormalisation. Both parts carry the details of the IR behaviour of the propagator and may vary largely for different solutions. In turn, the coefficient $Z_{\mathrm{cond}}$ should not.

We perform the fits for different values of the lower fitting interval bound $p_{\min}$. For every fit, $p_{\max}$ is varied between the points in the $p_{\max}$ interval, comp. (C.9). In addition, we transform the lattice and fRG data sets into the respective (inverse) dressing function and inverse propagator, and fit those with the respective fit functions corresponding to (C.7). This provides us with a $Z_{\mathrm{cond}}(p_{\min})$ given as the average over the single fit results for the different values of $p_{\max}$ and representations of the data set, with uncertainty given by the standard deviation.

Eventually, we extract the wave function renormalisation $Z_{\mathrm{cond}}$ at $p = 0$ via a limiting procedure as

$$Z_{\mathrm{cond}} = \lim_{p_{\min}\to 0} Z_{\mathrm{cond}}(p_{\min})\,. \tag{C.10}$$

The limit is obtained within an extrapolation of the $Z_{\mathrm{cond}}(p_{\min})$ discussed below. We extract $Z_{\mathrm{cond}}$ from both the scaling fRG data of [47] as well as the lattice solution [234], see Figure C.4 and Table C.1 for the numerical values. We also provide $Z_{\mathrm{cond}}$ from a lattice-type fRG decoupling solution for comparison in Table C.1. When lowering the lower fit interval bound $p_{\min}$, the results for $Z_{\mathrm{cond}}$ differ more and more. This can be attributed to the different infrared behaviour of the two data sets. Accordingly, we exclude as many incompatible data points as possible from the extrapolation fit regime while keeping enough data for a meaningful prediction of $Z_{\mathrm{cond}}(p = 0)$.

As the data from [47] are relatively sparse and hence the respective $Z_{\mathrm{cond}}(p_{\min})$ and the extrapolation show large error bars, we support this extrapolation with one obtained from dense fRG data provided in [392]. While the approximation used in the latter computations is not as sophisticated as that used in [47], it allows for a relatively quick production of dense data. The scaling solution yields $Z_{\mathrm{cond}} = 0.166(33)$, which agrees extremely well with the scaling solution estimate of [47], comp. Table C.1.

Our final estimate for $Z_{\mathrm{cond}}$ is obtained by averaging the scaling fRG and lattice result, yielding

$$Z_{\mathrm{cond}} = 0.149(19)\,. \tag{C.11}$$

The error bars are given by the separate extrapolation results for scaling fRG and lattice data in order to incorporate systematic uncertainties such as the influence of the different infrared behaviours.

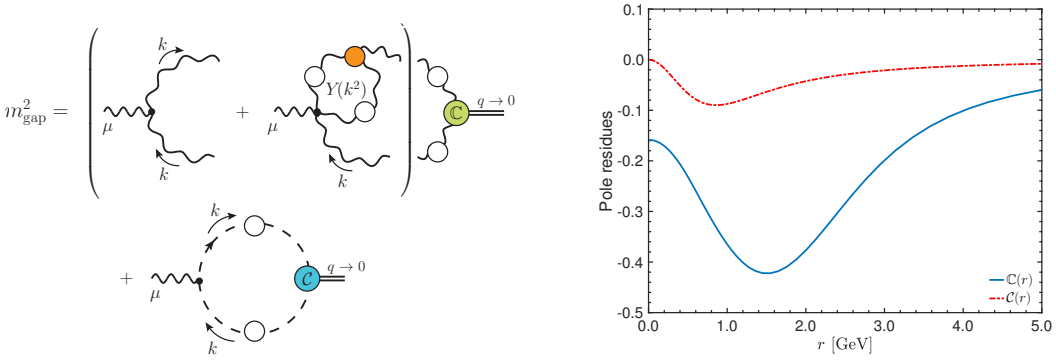


Figure C.5.: Left panel: Diagrammatic representation of (C.15). Right panel: the momentum dependence of $\mathbb{C}(q^2)$ and $\mathscr{C}(q^2)$.

### C.1.3. Schwinger mechanism

In order to facilitate the comparison with the literature, in this Appendix we modify the notation employed in the main body of the article, denoting by $\Delta(q^2)$ and $D(q^2)$ the gluon and ghost propagators, respectively, and by $\mathscr{Z}(q^2)$ and $F(q^2)$ their dressing functions: $\mathscr{Z}(q^2) := q^2\Delta(q^2)$ and $F(q^2) := q^2 D(q^2)$.

According to one of the main approaches put forth in a number of works [246, 393–396], the generation of an effective gluon mass proceeds through the non-Abelian implementation of the well-known Schwinger mechanism [397–400]. Within this scenario, the fundamental vertices that enter in the DSE of the gluon propagator, $\Delta(q^2)$, contain longitudinally coupled massless poles, which eventually trigger the result $\Delta^{-1}(0) := m^2_{\rm gap}$.

In particular, the three-gluon vertex, $I\!\Gamma_{\mu\alpha\beta}(q,r,p)$, and the ghost-gluon vertex, $I\!\Gamma_{\mu}(q,r,p)$ , are composed by two distinct types of terms, namely

$$
\begin{aligned}
I\!\Gamma_{\mu\alpha\beta}(q,r,p) &= \Gamma_{\mu\alpha\beta}(q,r,p) + \frac{q_\mu}{q^2} g_{\alpha\beta} C_1(q,r,p) + \cdots , \\
I\!\Gamma_{\mu}(q,r,p) &= \Gamma_{\mu}(r,p,q) + \frac{q_\mu}{q^2} C(q,r,p) ,
\end{aligned}
\tag{C.12}
$$

where the terms $\Gamma_{\mu\alpha\beta}(q,r,p)$ and $\Gamma_{\mu}(q,r,p)$ contain all pole-free contributions, which may diverge at most logarithmically as $q \to 0$ [401]. The ellipses in the first relation of (C.12) denote terms proportional to $r_\alpha/r^2$ or $p_\beta/p^2$, which are annihilated when contracted with the transverse (Landau gauge) gluon propagators inside the relevant diagrams of the DSEs, or tensorial structures that are subleading in the limit $q \to 0$.

A detailed analysis [402] based on the Slavnov-Taylor identities satisfied by the above vertices reveals that

$$
C_1(0,r,-r) = C(0,r,-r) = 0 . \tag{C.13}
$$

Therefore, the Taylor expansion of $C_1(q,r,p)$ and $C(q,r,p)$ around $q=0$ yields

$$\lim_{q\to 0} C_1(q,r,p) = 2(q\cdot r)\underbrace{\left[\frac{\partial C_1(q,r,p)}{\partial p^2}\right]_{q=0}}_{\mathbb{C}(r^2)} + \mathcal{O}(q^2)\,, \tag{C.14}$$

$$\lim_{q\to 0} C(q,r,p) = 2(q\cdot r)\underbrace{\left[\frac{\partial C(q,r,p)}{\partial p^2}\right]_{q=0}}_{\mathscr{C}(r^2)} + \mathcal{O}(q^2)\,.$$

Thus, inserting the vertices of (C.12) into the DSE of the gluon propagator and taking the limit $q\to 0$, one arrives at (see Appendix C.1.2) [395]

$$m_{\rm gap}^2 = \frac{3C_{\rm A}\alpha_s}{8\pi}\int_0^\infty dy\, \mathscr{Z}^2(y)[6\pi\alpha_s C_{\rm A} Y(y)-1]\mathbb{C}(y) + \frac{C_{\rm A}\alpha_s}{8\pi}\int_0^\infty dy\, F^2(y)\mathscr{C}(y)\,. \tag{C.15}$$

In the above formula, $\alpha_s = g_s^2/4\pi$, defined at the renormalisation point $\mu$ where the ingredients of (C.15) have been renormalised, within the momentum subtraction (MOM) scheme; the renormalisation point has been chosen at $\mu = 4.3$ GeV. Moreover, $C_{\rm A}$ is the Casimir eigenvalue of the adjoint representation with $C_A = N_c$ for $SU(N)$. Finally, $\mathscr{Z}(y)$ and $F(y)$ denote the dressing functions of the gluon and ghost, respectively, and $Y(k^2)$ is an appropriately projected contribution of the sub-diagram shown in Appendix C.1.2.

The functional form of the pole residues $\mathbb{C}(k^2)$ and $\mathscr{C}(k^2)$ is determined from the linear homogeneous system of coupled Bethe-Salpeter equations that they satisfy. This system is derived from the corresponding DSEs governing the dynamics of $I\!\Gamma_{\mu\alpha\beta}(q,r,p)$ and $I\!\Gamma_{\mu}(q,r,p)$, in the limit $q\to 0$; for further details, see [395].

The resulting eigenvalue problem yields non-trivial solutions for $\mathbb{C}(k^2)$ and $\mathscr{C}(k^2)$, for a specific value of the coupling $\alpha_s$, which depends on the details of the ingredients that enter in the kernels of the Bethe-Salpeter system. It is important to emphasise that the homogeneity and linearity of the equations leaves the overall scale of the corresponding solutions undetermined. The scale setting is implemented by solving the vertex DSEs for *general kinematics*, using as input the particular $\alpha_s$ that was singled out by the eigenvalue condition. Then, from the general 3-D solution the particular slice that corresponds to $\mathbb{C}(k^2)$ and $\mathscr{C}(k^2)$ is identified, furnishing precisely the correctly rescaled version of the solutions obtained from the system. The final form of the scale-fixed pole residues is shown in Appendix C.1.2.

The next step consists in substituting into (C.15) the scale-fixed $\mathbb{C}(k^2)$ and $\mathscr{C}(k^2)$, and use refined lattice data [234] for the gluon and ghost dressing functions, $\mathscr{Z}(k^2)$ and $F(k^2)$. The lattice propagators have been normalised at the point $\mu = 4.3$ GeV, namely the highest momentum scale available in this simulation. For the purpose of the comparison with the results computed in the present work we match the scales of the lattice data in [234] with that in [47], which leads us to

$$m_{\rm gap}^{\rm (Schwinger)} = 0.320(35)\,{\rm GeV}\,. \tag{C.16}$$

Equation (C.16) is in excellent agreement with the estimate $m_{\rm gap} = 0.322(34)\,{\rm GeV}$ obtained in the present work, see (4.66). Both compare rather favourably to the central lattice value $\Delta^{-1/2}(0) = 0.354\,{\rm GeV}$. The predominant source of error in the calculation using the Schwinger mechanism originates from the uncertainties in the non-perturbative structure of the pole-free vertex $\Gamma_{\mu\alpha\beta}(q,r,p)$, which affects both the determination of the function $Y(k^2)$ in (C.15), as well as the kernels of the Bethe-Salpeter equations that determine the functions $\mathbb{C}(k^2)$ and $\mathscr{C}(k^2)$.

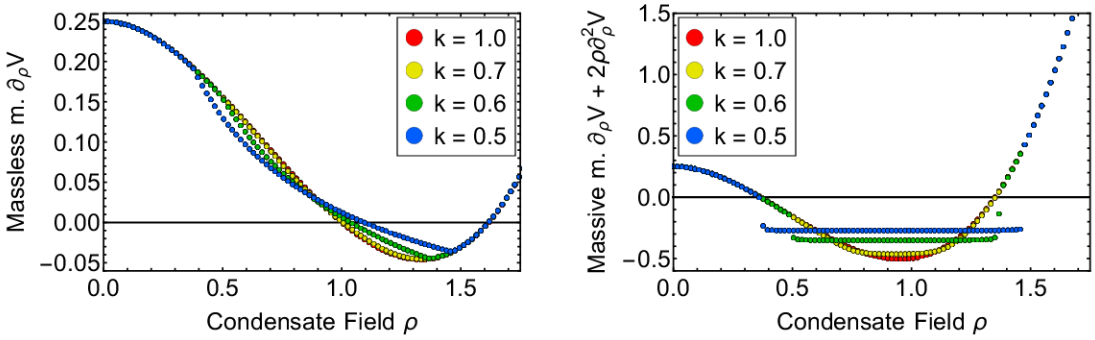


(a) RG-time dependence of the massless modes $\pi$.

(b) RG-time dependence of the massive mode $\sigma$.

Figure C.6.: Shock development in the O(N) model at finite $N$. Shocks can appear in the massive mode $\sigma$ and translate to kinks in the massless mode $\pi$. The initial conditions for this computation are given in (C.17) with an initial cutoff $\Lambda = 1$. The equation is terminated at $k = 0.5$ due to a very small step-size.

## C.2. Additional material: On shock development

We investigate the possibility of shock development in the O(N) model at finite $N$, in particular the physical scenario $N = 4$. Shock development can be found in the large-$N$ limit of the O(N) model for specific sets of initial conditions [65]. Furthermore the high density region of the quark-meson model in the large-$N$ limit also holds the potential for shock development [1]. Shock development in the quark-meson model is linked to competing order effects at high densities. Its occurrence is decided by the dynamics and respective strengths of the quark and bosonic fluxes. In the O(N) model it is much easier to tune the initial conditions such that shocks develop. The general idea is to create a non trivial minimum in the non-convex initial potential $V_{t=0}(\rho)$, which is given by

$$V_{t=0}(\rho) = \lambda_2\rho + \lambda_4\frac{\rho^2}{2} + \lambda_6\frac{\rho^3}{3} + \lambda_8\frac{\rho^4}{4}\,. \tag{C.17a}$$

We now discuss the requirements of shock formation for different couplings $\lambda_i$. The convective dynamics of the bosonic/scalar field are such that waves always propagate to the IR, i.e. to lower field values $\rho$. In the absence of diffusion, i.e the large-$N$ limit, a shock builds up in the massless mode/pion at some position $\rho_0 \neq 0$ if the flow towards the IR is sufficiently 'jammed' at some value $\rho < \rho_0$. This translates into the requirement $F(\rho) \ll F(\rho_0)$ for some $\rho < \rho_0$, where $F$ refers to the pion flux. In the large-$N$ limit of the O(N) model, it is possible to create shocks in a $\phi^6$ potential, i.e only using the couplings $\lambda_2$, $\lambda_4$ and $\lambda_6$, while $\lambda_8 = 0$ in (C.17a), see [65]. At finite $N$, shock development becomes harder to grasp. The dynamics shift towards the massive mode/sigma. The sigma mass $m_\sigma^2 = \partial_\rho V + 2\rho\partial_\rho^2 V$ contains a second derivative term (5.6), which acts as a non-linear diffusion term in the pion-flow $F$. With this additional diffusive contribution the $\phi^6$ initial conditions are no longer able to produce shocks in the current setting. This scenario changes, if we include higher orders. Using the initial conditions

$$\lambda_2 = 0.25\,,\ \lambda_4 = 0\,,\ \lambda_6 = -0.5 \text{ and } \lambda_8 = 0.25\,, \tag{C.17b}$$

at $\Lambda = 1$ we discover the formation of shocks in the massive mode, compare Figure C.6. Interestingly, the non-linear diffusion term in the pion-flow $F$ allows for the formation of a kink, but not of a shock in the pion mass $m_\pi^2 = \partial_\rho V$. Figure C.8 demonstrates nicely, how a

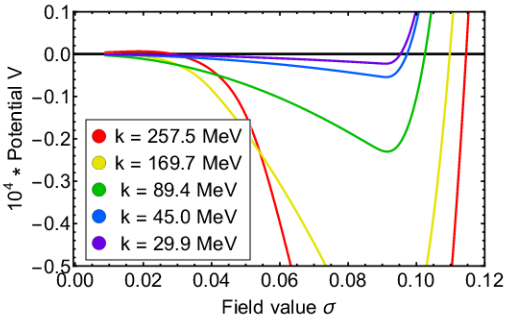


(a) Potential in the broken phase.

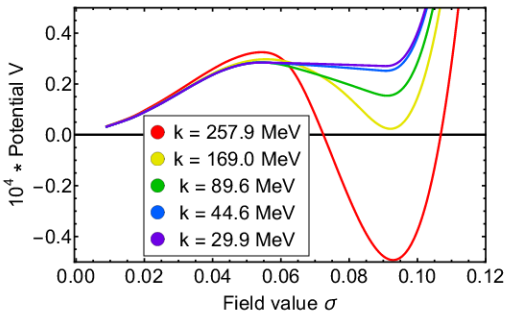


(b) Potential in the symmetric phase.

Figure C.7.: The effective potential $V_k(\rho)$ in the vicinity of the phase transition at $\mu = 0.30$ GeV (Figure C.7a) and $\mu = 0.32$ GeV (Figure C.7b) in the large $N_f$ limit with $N_\pi = 3$.

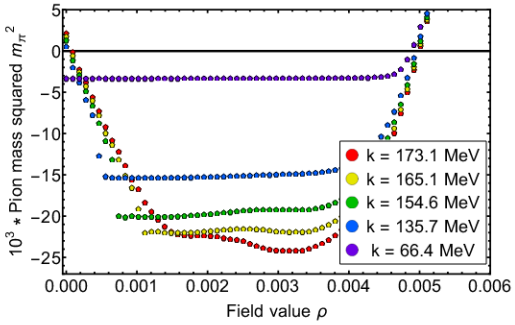


(a) Derivative of the potential in the broken phase. The developing shock travels to unphysical values of the field value $\rho$ and the potential is flattened out.

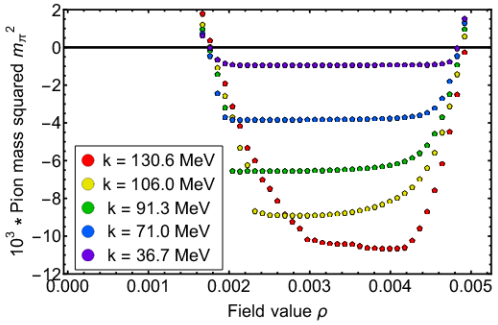


(b) Derivative of the potential in the symmetric phase. The developing shock freezes in at finite $\rho$, creating a global mimumum at $\rho = 0$.

Figure C.8.: Shock development at high densities. The potential derivative $\partial_\rho V_k(\rho)$ is plotted in the vicinity of the phase transition at $\mu = 0.30$ GeV (Figure C.8a) and $\mu = 0.32$ GeV (Figure C.8b) in the large $N_f$ limit with $N_\pi = 3$. The numerical oscillations around the shock were flattened out by a minmod slope limiter. The figure depicts the grid points on which the computation was carried out.

kink in the massless mode $\pi$ translates to a shock in the massive mode $\sigma$. Due to the high numerical cost in the precise evaluation of shock development in convexity restoring flows, we terminate the computation in Figure C.6 at $k = 0.5$ with a RG-time step-size $\leq 10^{-10}$. Further investigations in this direction are deferred to further work and require technical improvements, such as the correct limiting procedures or improved time stepping schemes.

In summary, we can report on the appearance of shocks and non-analyticities in the O(N) model. The development of a shock is tightly linked to the form of the potential and requires the formation of a non-trivial minimum at finite RG-scale $k$, as well as higher order scattering processes at the UV cutoff. These conditions cannot be excluded in more elaborate models, for example low energy effective models of QCD at high densities. Hence, we hope to present an in depth analysis of shock development at finite $N$ in connection to first order phase transitions in future work. A similar studies have been done in [1, 65] for the large-$N$ limit.

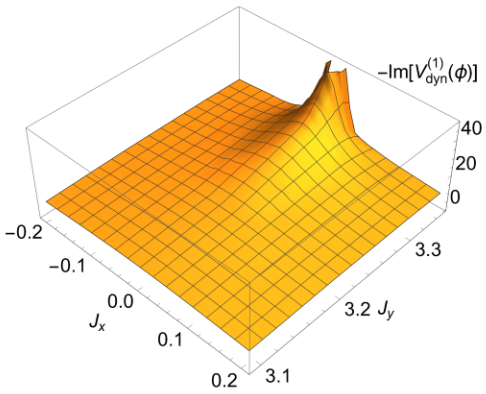


(a) Raw data: Negative imaginary part of the first derivative of the effective interaction potential $-\mathrm{Im}[\partial_{\phi_x} V_{\mathrm{dyn,k}}(\phi)]$. Computations converged up to $J_y = 3.35$.

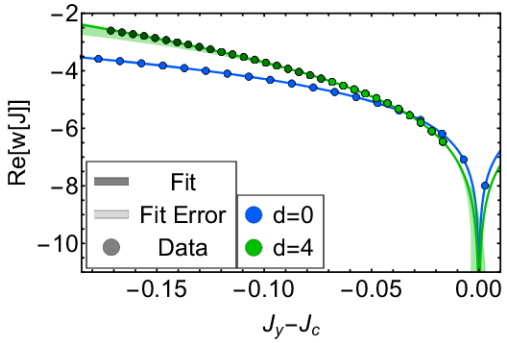


(b) Fit of the position of the Lee-Yang singularity on data points of the density $\mathrm{Re}[w(J)]$. The singularity in the $d = 0$ case is fitted as a consistency check of the fit function. The fit error band is obtained by adding/removing 10 data points from the fitted dataset. The data points in question are shaded darker. The original fit is performed on the two lighter shades.

Figure C.9.: Plots for the computations on the position of the numerical blow-up. The blow-ups are located at $J_c = 3.3659(42)\mathrm{i}$ (and $J_c = 3.002(1)\mathrm{i}$ in $d = 4$ ( and $d = 0$). We show the raw data in $d = 4$, which is directly obtained from the RG-adapted flow (6.29). From this we compute the full potential (6.34) and fit the exact position of the singularity. The fit-function is indicated in (C.18) and the fitted parameters are given in Table C.2. All units are given in terms of the UV mass $m = 1$ with an initial cutoff $\Lambda = 5$.

### C.2.1. Shock development at large-$N_f$

In this section we illustrate the dynamics of shock development in the large-$N_f$ model. In Section 8.2 we distinguished two scenarios of shock development which are both illustrated in Figure C.8. Figure C.8a shows the pion mass/the potential derivative in the broken symmetry phase, where the shock eventually proceeds to move to unphysical values for $\rho$. This leads to the creation of a temporary maximum in the potential, depicted in Figure C.7a, which flattens out again for $k \to 0$. Figure C.7a shows the typical form of a potential in the broken symmetry phase with a degenerate global minimum at $k = 0$. In Figure C.8b the shock freezes at some positive finite value. The temporary maximum still vanishes due to convexity restoration, however it remains at a positive value such that the potential in the symmetric phase has a unique global minimum at $\sigma_0 = 0\,\mathrm{GeV}$. The shock-position and the position of the temporary maximum coincide in the deep infrared.

## C.3. Additional material: Functional flows for complex effective actions

*These appendices are taken from [4]. We provide additional material on the parabolic blow up of the RG-adapted flow. Furthermore we give results and the flow equations of different generating functionals.*

### C.3.1. The parabolic blow-up

In Section 6.3.2 and Section 6.4 we compute the dynamical potential $V_{\mathrm{dyn,k}}(\phi)$, and thus the Schwinger functional $W[J]$, in the complex plane. Convergence is achieved until some critical value of the current $J_c$. For $|J_y| > J_c$ the numerical solution displays a *blow-up*, i.e. it develops a singularity at some finite $k > 0$. This possibility was discussed in Section 6.2.1. The existence of complex poles in the potential of the Schwinger functional follows from the analytic structure of the equation, see [264, 403]. In $d = 0$ the blow up can directly be associated with the zero of the generating functional. In any case, the numerical blow-up is the final slice, for which the expansion around $\phi_0$ in the RG-adapted scheme still applies. The last converging computation in $d = 4$ is at $\phi_y = 3.25$ ($J \approx 3.35$). Although we are not at the pole position yet, there is a premature blow up in the equations due to the numerical approximation scheme. The occurrence of oscillations around discontinuities is expected in numerical schemes using polynomials and is generally accounted for in the numerical fluxes. In the close proximity of a blow up, the arising oscillations create negative diffusion, which causes an instant failure of the computation, or prematurely triggers a blow-up. These issues can be dealt with using positivity preserving LDG-schemes, see [317], but is not within the scope of this work.

The converged slices are interpolated in $\phi_y$ direction. To resolve the real direction we use a grid from $\phi_x \in [-3, 3]$ with a polynomial order $N = 2$ and a cell number $K = 200$, to further reduce the occurrence of oscillatory behaviour. In Figure C.9 we show the raw data from the evaluation of the RG-adapted flow (6.29). The build up of the singularity is clearly visible, all other structures of the potential vanish in comparison.

We are now interested in obtaining the exact position of the divergence from the derivative of the effective interaction potential. We make use of the Cauchy-Riemann equations to obtain the expression for the real part of the dynamical potential,

$$\mathrm{Re}[V_{\mathrm{dyn}}(0,\phi_y)] = \int_0^{\phi_y} d\phi_y' \, \frac{\partial \mathrm{Re}[V_{\mathrm{dyn}}]}{\partial \phi_y'}(0,\phi_y') = -\int_0^{\phi_y} d\phi_y' \, \frac{\partial \mathrm{Im}[V_{\mathrm{dyn}}]}{\partial \phi_x'}(0,\phi_y') \,.$$

Furthermore, we obtain the full potential of the Schwinger functional from (6.34). Since we are investigating a zero of the generating functional, we use a logarithm as a fit function. To accommodate the overall structure of the potential, we add a mass parameter $c$, which significantly improves the stability of the fit. This choice is further supported by previous

| Fit param. | $a$ | $b$ | $J_c$ | $c$ |
|---|---|---|---|---|
| $d = 0$ | 0.388(90) | 1.0008(55) | 3.002104(65) | −0.281(12) |
| $d = 4$ | 9.7(88) | 1.24(41) | 3.3659(42) | −0.99(91) |

Table C.2.: Fit parameters to the fit in (C.18) and plotted with the data-set in Figure C.9. The error to the fit parameters in $d = 4$ is given by removing/adding the last 10 data-points from/to the fit. The $d = 0$ fit only uses the data-points left of the singularity. Here, errors were obtained by adding 25 data-points to the fit interval (generated from the numerical integral). Surprisingly, we find that the fit allows for big deviations in the parameters $a, b$ and $c$. The position of the singularity, however, is barely affected by adding/removing data points from the fit.

analyses [403], which suggest a simple, purely imaginary pole in the first derivative of the potential. The fit-function is given by,

$$\mathrm{Re}[w(0,J_y)] = c\,J_y^2 + a + b\log(J_c - J_y)\,, \tag{C.18}$$

where $J_c$ is the position of the singularity. To check if this function is able to fit the position correctly, we perform a benchmark check in $d=0$, additionally to the $d=4$ data. In $d=0$ we evaluate the integral (3.2) directly, as discussed in Section 6.3.3. The fit parameters are given in Table C.2. The fit error is determined by adding/removing data points from the fit-interval, as indicated in Figure C.9. The blow-up is located at $J_c = 3.3659(42)\mathrm{i}$ and contains only a very small error from the fit.

### C.3.2. Polchinski flow

Additionally to the RG-adapted scheme, we explore the approach using a classical propagator in Appendix B.5.1, which is simply the Polchinski flow. In this scheme, the effective interaction potential also carries the change to the classical mass term $V_{\mathrm{int,k}}(\phi) = V_{\mathrm{dyn,k}}(\phi) + \frac{m^2-m_k^2}{2!}\phi^2$. Following the derivation we define the current via the classical propagator at the expansion point $\phi_0 = 0$, to wit

$$J = \left(G_k^{(0)}[\phi_0]\right)^{-1}\phi = \left(m^2 + p^2 + R_k(p^2)\right)\phi\,. \tag{C.19}$$

The insertion in (B.75) yields:

$$\begin{aligned}\partial_t V_{\mathrm{int,k}}(\phi) &= \frac{1}{2}\int_p \left\{ \frac{\left(\left(V^{(1)}_{\mathrm{int,k}}(\phi)\right)^2 - V^{(2)}_{\mathrm{int,k}}(\phi)\right)\partial_t R_k(p^2)}{\left(m^2+p^2+R_k\left(p^2\right)\right)^2} \right\} \\ &= v(d)\frac{k^{2+d}}{\left(m^2+k^2\right)^2}\left[\left(V^{(1)}_{\mathrm{int,k}}(\phi)\right)^2 - V^{(2)}_{\mathrm{int,k}}(\phi)\right], \end{aligned} \tag{C.20}$$

where the trace is evaluated over momentum space. Additionally, a flat cutoff is used, for details see Appendix B.7.1.

The choice $\phi_0 = 0$ ensures the prefactor $\frac{k^2}{(m^2+k^2)^2}$ is real and positive, which is not trivial for arbitrary complex fields $\phi_0$. Since it is the simplest numerical scenario, we present results for the $\phi_0 = 0$ case. For the sake of comparison we use the same initial conditions as given in Section 6.3.1. With the classical mass $m^2 = 1$, we have $J_k = (1+k^2)\phi$, i.e. $J_0 = \phi$ at $k = 0$.

Computations are performed on slices of constant $\phi_y$. To this aim we use:

- Values of $\phi_y$ spaced by 0.1.
- A 1d-numerical grid, ranging from $\phi_x \in [-3,3]$ containing $K = 60$ cells and a polynomial of order $N = 2$ in each cell.

Figure 6.1 shows the comparison to the analytic result. The current cell density allows to resolve the potential up to $\phi_y = 2.4$, the pole is situated at $\phi_y = 3$. Numerical computations break down due to the pole building up in the numerical expressions for (6.23). This can be improved slightly by increasing the cell density of the grid, but not infinitely.

Naively, we could try to improve the numerical scheme by chose a different expansion point, closer to the pole position. However, in Section 6.2 we discussed the necessity of real, positive

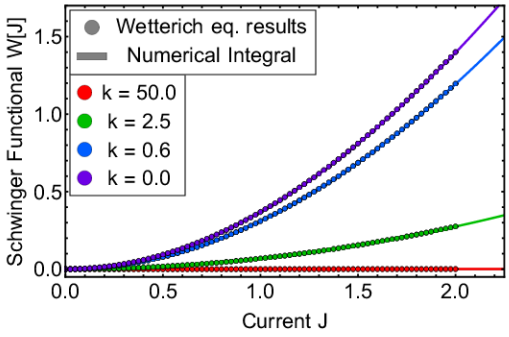


Figure C.10.: RG-time dependence of the Schwinger functional computed from the 1PI flow and by a direct numerical evaluation in $d = 0$. All units are given in terms of the UV mass $m = 1$ with an initial cutoff $\Lambda = 5$.

diffusion $a(t)$ in (6.18) to ensure numerical stability and convergence. For arbitrary $\phi_0$ this is no longer ensured. By reading off of (6.1) we obtain,

$$0 \overset{!}{\leq} a(k) = \frac{k^2}{\left[S_k^{(2)}\right]^2} = \frac{k^2}{\left(m^2 + k^2 + \frac{\lambda}{2}\phi_0^2\right)^2}\,. \tag{C.21}$$

It follows that $\left(S_k^{(2)}\right)^2 \in \mathbb{R}_{>0}$ restricts the choice of $\phi_0$ to the coordinate axes. This is additionally enforced by the assumption made in Section 6.2.3, which explicitly prohibits introducing a dependency on an additional complex variable. Choosing an expansion point along the imaginary axis $\phi_0 = i\,|\phi_0|$ with $|\phi_0^2| > 2\frac{m^2}{\lambda}$ eventually introduces a pole to the flow and is therefore also impractical for numerical computations.

### C.3.3. 1PI flow

In this section we discuss the 1PI flow in a complex setting. This is illustrated by the example of the numerical test case $d = 0$, which is also used as a benchmark for numerical convergence of the Wilsonian effective action flows in Section 6.3.2. We make use of LPA 1PI effective action in (6.16). The full propagator is then given by

$$G_k[\phi] = p^2 + V_{\text{eff},k}^{(2)}(\phi) + R_k(p^2)\,. \tag{C.22}$$

This expression is inserted into the 1PI flow (3.35) using a flat Regulator, see Appendix B.7.1. Evaluating the momentum trace yields the known flow of the effective potential $V_{\text{eff},k}$ in an $O(1)$ theory [65, 255],

$$\partial_t V_{\text{eff},k}(\phi) = v(d)\frac{k^{d+2}}{k^2 + \partial_\phi^2 V_{\text{eff},k}(\phi)}\,. \tag{C.23}$$

Equation (C.23) is rewritten in terms of the second derivative of the potential $u(\phi) = \partial_\phi^2 V_{\text{eff},k}(\phi)$, to suit the numerical framework presented in Section 6.2.2 and more thoroughly in [5]

$$\begin{aligned}\partial_t u &= -\partial_\phi\Big(\frac{v(d)k^{d+2}}{(k^2+u)^2}\partial_\phi u\Big) = -\partial_\phi\Big(\frac{v(d)k^{d+2}}{k^2+u}p\Big)\\ p &= \partial_\phi\Big(\log(1+u/k^2)\Big),\end{aligned} \tag{C.24}$$

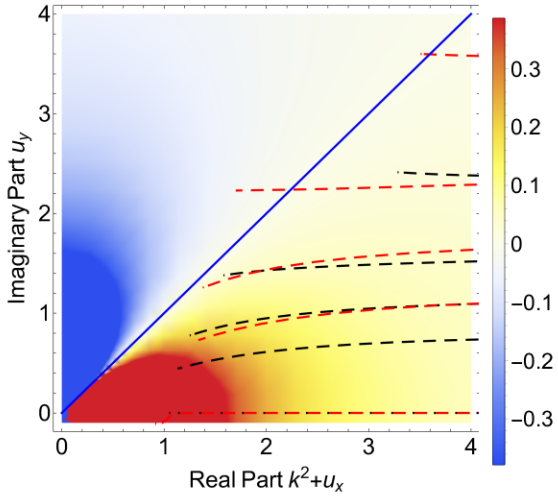


Figure C.11.: Real part of the diffusion $\mathrm{Re}[f\,] = f_x$ in a complex setting. The blue line indicates $\mathrm{Re}[f\,] = 0$. The dotted lines follow the diffusion flux for different $q_x = 0,\ 0.8,\ 1.2,\ 1.6,\ 1.8$ at $q_y = 1.0$ (black) and $q_y = 1.5$ (red). The trajectories start at the right side of the plot and move to the left as the RG-scale $k$ decreases. Whilst the diffusion is positive to the right of the blue line, trajectories crossing this line become unstable. The black lines are therefore stable. The computation of the red lines is numerically unstable and breaks off at $k \approx 0.85$, when the blue line is crossed for a specific $q_x$ and the diffusion is no longer positive. All units are given in terms of the UV mass $m = 1$ with an initial cutoff $\Lambda = 5$.

where $p_k(\phi)$ is solved in a separate, stationary equation. For an in depth discussion of the numerical framework in the context of 1PI flows see [5], in this work we only focus on the extension to the complex plane. The positivity condition for the real diffusion term follows from the square in the denominator. Since the equation is exact in $d = 0$ we can recover the RG-running of the Schwinger functional by performing the (modified) Legendre transformation (3.7), see Figure C.10 in the case $d = 0$.

### The complex 1PI flow

Following the arguments in Section 6.2.3, the 1PI flow is now extended to the complex plane. For complex values, (C.24) is a system of four equations. The substitution $\partial_z \to \partial_x$, where $z = x + \mathrm{i}\,y$ is performed, to wit

$$\partial_t u_x + \partial_x \left( f_x \partial_x u_x - f_y \partial_x u_y \right) = 0 \tag{C.25}$$

$$\partial_t u_y + \partial_x \left( f_x \partial_x u_y + f_y \partial_x u_x \right) = 0\,, \tag{C.26}$$

and the flux $f = v(d) k^{d+2}/(k^2+u)^2$, compare (C.24). The direct comparison to (6.22) and (6.23) shows the increased complexity of the equations. Most importantly, the flux $f$ is no longer necessarily strictly positive in a complex setting.

Before attempting to naively solve this system with the given framework, its stability within the presented numerical scheme needs to be investigated. General requirements for stability of complex partial differential equations are known and have been studied in the context of Schrœdinger-type equations, or the image-denoising process [404, 405]. In fact, stability of numerical schemes can be proven for certain classes of non-linear complex diffusion equations. The most central elements of this proof are the positivity of $f_x$ and finiteness of the flux. The

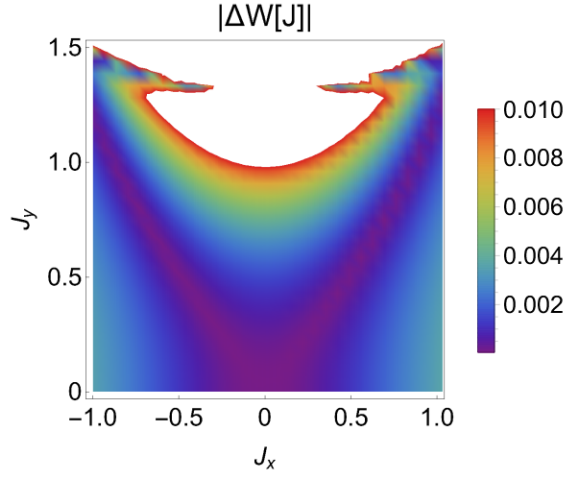


Figure C.12.: Absolute, relative error on the Legendre transformed of the 1 PI effective Potential $V_{\text{eff}}$ in $d = 0$. The numerical evaluation of the integral in (3.2) is used as a reference. All units are given in terms of the UV mass $m = 1$ with an initial cutoff $\Lambda = 5$.

second requirement is quite straight-forward, and we briefly explain the former by the example of a Gaußian: While convection movements will move the mean of the Gaußian, positive diffusion is known for smoothing out the structure, i.e. increasing the width of the Gaußian as (RG-)time progresses, see Figure C.13a. Negative diffusion can be thought of as simply switching the sign in the time evolution: Instead of increasing the width, it is decreased. As the (RG-)time evolution progresses, an uncontrollably growing Gaußian develops, which is highly numerically instable. Nevertheless, systems containing two-way diffusion, i.e. diffusion of varying sign, have been studied in literature [406, 407]. Numerical solutions to purely diffusive systems containing two-way diffusion rely on iterative procedures. Such algorithms require previous knowledge of the solution at the end $t_1$ and beginning $t_0$ of the time-integration [408].

In case of the 1PI flow, the finiteness of the diffusive flux is ensured by the convexity restoring properties of the 1PI flow. The pole in the flow (C.24) is never reached [292]. However, $f_x + \mathrm{i} f_y = \frac{k}{(k^2+u_x+\mathrm{i}u_y)^2}$ does not ensure positive diffusion as it does on the real axis, in fact, it is spoiled by it. To illustrate this we perform a computation at different field values and track the real diffusion throughout our calculation Figure C.11. This plot shows the numerical limitations when trying to solve the complex 1PI flow. We find that with increasing external imaginary field, also the trajectories with negative diffusion increase and calculations become unstable. We have yet to determine if this is caused by a numerical fine-tuning problem or is a property of the flow itself. Diffusive contributions remain positive until $\phi_y = 1$, which coincides with the initial UV-mass.

Finally, the full expression for the 1PI effective potential is obtained by the integration procedure outlined in Appendix B.5.5.

### The complex Legendre transform

In this section we discuss the complex Legendre transformation of a holomorphic function. The difficulty in defining a general complex Legendre transformation is within the definition of the derivative. For a holomorphic function this issue is resolved, since derivatives are well defined. In the present case, we make use of the mapping $\partial_z \to \partial_x$ for a derivative with respect

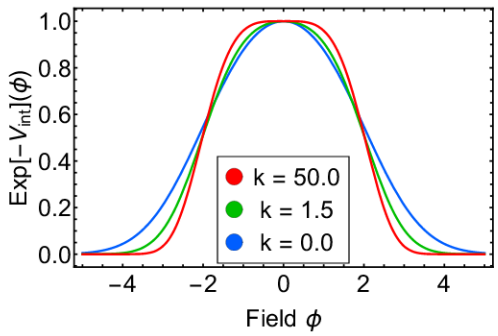


(a) RG-time dependence of $e^{-V_{\text{int}}}(\phi)$.

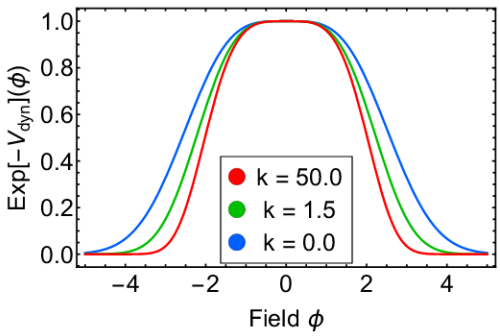


(b) RG-time dependence of $e^{-V_{\text{dyn}}}(\phi)$.

Figure C.13.: Comparison of the exponential formulations of the Polchinski flow (C.30) and the RG-adapted scheme (C.32) in $d = 0$. One can clearly see the development of a $\phi^2$ contribution to the exponential in (a) and the lack thereof in (b), due to the RG-adapted scheme. All units are given in terms of the UV mass $m = 1$ with an initial cutoff $\Lambda = 5$.

to the complex number $z = x + \mathrm{i}\, y$, which was discussed in Section 6.2.3. Then, the coordinate transformation can be inferred from the first derivative, using

$$J = \frac{\partial V_{\text{eff}}}{\partial \phi_x}[\phi_x, \phi_y] \quad \Rightarrow \quad \phi(J_x, J_y) = \left(\frac{\partial V_{\text{eff}}}{\partial \phi_x}\right)^{-1}[J_x, J_y]\,. \tag{C.27}$$

Now, the Legendre transformation is naturally extended to the complex plane by

$$W[J_x, J_y] = \left(J_x + \mathrm{i} J_y\right)\phi(J_x, J_y) - \Gamma\left[\phi(J_x, J_y)\right]\,. \tag{C.28}$$

The error on the Legendre transformation is computed by a comparison with the direct numerical evaluation of the integral in (3.2). We compute the absolute relative error from,

$$|\Delta W[J]| = \left|\frac{W_{\text{1PI}} - W_{\text{int}}}{W_{\text{1PI}}}\right|[J]\,. \tag{C.29}$$

The result is shown in Figure C.12. Furthermore, we obtain $V_{\text{dyn}}$ from the 1PI Schwinger functional $W_{\text{1PI}}$ using (6.15). It convergence, in comparison to the RG-adapted scheme and the Polchinski flow is shown in Figure 6.1. We conclude, that the current numerical evaluation of the 1PI flow needs further improvement for evaluations in the complex plane.

### C.3.4. Alternative formulations

The Polchinski equation is very challenging to resolve numerically. One specific challenge is the determination of boundary conditions, since the flow of the Wilsonian effective action increases at higher field values. This is due to many remaining redundancies which are removed in the 1PI effective action.

To circumvent this problem and to quantify the numerical error at the boundaries, we make use of an alternative formulation in terms of exponentials. Structurally, these new equations resemble Wegner's flow (3.20), whose numerical properties are discussed in Section 6.2.1. This has the additional advantage that we can directly solve for the exponentials of $S_{\text{int},k}[\phi]$, (B.74), and $S_{\text{dyn},k}[\phi]$, (6.9), instead of using the first derivative. However, using this formulation is increasingly challenging at higher imaginary field values. A bigger imaginary part of $\phi$ ia

accompanied by increasingly strong oscillations. Resolving the initial conditions already requires a very high cell density. So whilst this formulation is not tailored to perform computations at big imaginary fields, we find that it makes for a useful check of convergence close to the real axis.

First we focus on reformulating the Polchinski flow (B.75) in terms of $\exp(-S_{\mathrm{int},k}[\phi])$. Multiplying the equation with $-\exp(-S_{\mathrm{int},k}[\phi])$ yields

$$\partial_t \mathrm{e}^{-S_{\mathrm{int},k}[\phi]} = \frac{1}{2}\,\mathrm{Tr}\;\partial_t G_k^{(0)}\left[\frac{\delta^2}{\delta\phi\delta\phi}\mathrm{e}^{-S_{\mathrm{int},k}[\phi]}\right] - \frac{1}{2}\,G_k^{(0)}\,\partial_t S_k^{(2)}\mathrm{e}^{-S_{\mathrm{int},k}[\phi]}. \tag{C.30}$$

To simplify the equation further we replace $\mathrm{e}^{-S_{\mathrm{int},k}[\phi]} \to N_k \mathrm{e}^{-S_{\mathrm{int},k}[\phi]}$, where $N_k$ is an RG-time dependent constant in $\phi$. Introducing $N_k$ does not affect physics, since the physical correlation functions are normalised by definition. This results in

$$\partial_t \mathrm{e}^{-S_{\mathrm{int},k}[\phi]} = A(k)\left[\frac{\delta^2}{\delta\phi\delta\phi}\mathrm{e}^{-S_{\mathrm{int},k}[\phi]}\right] - B(k)\;\mathrm{e}^{-S_{\mathrm{int},k}[\phi]} - \partial_t(\ln(N_k))\mathrm{e}^{-S_{\mathrm{int},k}[\phi]}, \tag{C.31}$$

after dividing by $N_k$ and $A, B$ can be read off of (C.30). Now we discuss possible options to determine $N_k$: the obvious choice would be fixing some normalisation, i.e. $\int \mathrm{d}\phi\; N_k \mathrm{e}^{-S_{\mathrm{int},k}[\phi]} = 1$. Another, numerically much more convenient choice would be to impose $\partial_t(\ln(N_k)) = -B(k)$, and thereby dropping the last line of (B.75). We chose the normalisation $N_k$ such that $S_{\mathrm{int}}[0] = 0$.

Let us now consider the RG-adapted flow (6.13a). Multiplying by $\mathrm{e}^{-S_{\mathrm{dyn},k}[\phi]}$ yields

$$\left(\partial_t + \int_x \phi\,\gamma_{\mathrm{dyn},k}\,\frac{\delta}{\delta\phi}\right)\mathrm{e}^{-S_{\mathrm{dyn},k}[\phi]} - \frac{1}{2}\int_x \phi\;\partial_t\Gamma_k^{(2)}[\phi_0]\,\phi\;\mathrm{e}^{-S_{\mathrm{dyn},k}[\phi]}$$
$$= \frac{1}{2}\,\mathrm{Tr}\;\mathscr{C}_k\left[\frac{\delta^2}{\delta\phi\delta\phi}\mathrm{e}^{-S_{\mathrm{dyn},k}[\phi]}\right]. \tag{C.32}$$

Again, all terms $\propto \mathrm{e}^{-S_{\mathrm{dyn},k}[\phi]}$ can be dropped by introducing an appropriate normalising condition. The RG kernel $\mathscr{C}$ is given by the RG-adapted kernel (6.4b).

The flows are now solved in terms of the potentials $V_{\mathrm{int}}$ and $V_{\mathrm{dyn}}$. Their relation to the interaction part $S_{\mathrm{int}}$ and the dynamical part $S_{\mathrm{dyn}}$ of the effective action follows immediately from their respective definitions (6.15) and (6.14), to wit

$$V_{(\mathrm{int/dyn})} = S_{(\mathrm{int/dyn})}/\mathscr{V}_d \quad \text{and} \quad \mathscr{V}_d = \int \mathrm{d}^d x\,. \tag{C.33}$$

| Dimension | 0 | 1 | 2 |
|---|---|---|---|
| Classical Prop. | $2.5\;10^{-4}$ | $3.1\;10^{-4}$ | $4.4\;10^{-4}$ |
| RG-adapted Prop. | $5.9\;10^{-5}$ | $5.9\;10^{-5}$ | $6.0\;10^{-5}$ |

Table C.3.: Absolute value of the difference in solutions $\Delta\mathrm{e}^{-V_x}$, computed by the exponential formulation and the formulation in $V_{\mathrm{dyn/int}}$, see Section 6.3 and Appendix C.3.2. The error is computed using (C.34). We take this as an estimate of the error generated by the flux-boundary conditions.

In our approximation, the volume $\mathcal{V}_d$ drops out of the equations. Finally, (C.30) and (C.32) are solved for varying dimensions $d = 0$, to $d = 2$ on the real axis. The results in $d = 0$ are depicted in Figure C.13. Figure C.13a clearly shows the development of a $\phi^2$ contribution to $V_{\text{int}}$ in the Polchinski flow. In contrast, Figure C.13b demonstrates the lack of a $\phi^2$ contribution to $V_{\text{dyn}}$ in the RG-adapted scheme. This is in accordance with (6.11) and beautifully emphasises the reduced degree of redundancy of the scheme. Table C.3 gives the error $\Delta \mathrm{e}^{-V_x}$ between solutions computed by the exponential formulation and the formulation in $V_{(\text{int/dyn})}$ at $\phi = 2$, to wit

$$\Delta \mathrm{e}^{-V_x} = \mathrm{e}_h^{-V_x}(\phi) - \mathrm{e}^{-V_{x,h}(\phi)}|_{\phi=2}\,, \tag{C.34}$$

where $x = \text{int/dyn}$. The index $h$ indicates the numerically computed object. The field value $\phi = 2$ is chosen, because it displays the most dynamics in the RG-time evolution and also generates the biggest overall error. The error values in Table C.3 are satisfyingly small, with a slight superiority of the RG-adapted scheme.

# Acknowledgments

Firstly, I would like to thank Jan M. Pawlowski for supervising the process of creating this thesis, his advice and collaboration on the featured projects and the valuable scientific and professional insights given in the past years. Countless discussions and guidance in compiling and promoting my work have always been very helpful. I have always highly appreciated and benefited of the amount of time, effort and joy he has put into creating this fruitful research environment.

Secondly I would like to thank Manfred Salmhofer for his interest in my research and agreeing to be my second referee.

Many thanks go to my collaborators whom I have enjoyed working with. Their insights, ideas and contributions have been invaluable to this work and to me.

I would also like to thank my colleagues at the Institute for Theoretical Physics in Heidelberg. I am very grateful for the wonderful time we have spent and for being companions during a time of not only scientific learning, but also a global pandemic. Here I would like to mention those whom I have spent the most time with: Jan Horak, Viktoria Noel, Franz R. Sattler, Julian Urban, Jonas Wessely and Nicolas Wink.

My research during the compilation of this thesis has been funded by the *Studienstiftung des deutschen Volkes*. I am very thankful for the financial support, as well as the ample opportunities and programs for academic exchange and personal growth. Furthermore, I would like to mention the *HGS-HIRe* for allowing me the funds to attend conferences and their helpful non-scientific program.

Lastly, I would like to thank my friends and family for their support and encouragement.

# Bibliography


[1] Eduardo Grossi, Friederike J. Ihssen, Jan M. Pawlowski, and Nicolas Wink. Shocks and quark-meson scatterings at large density. *Phys. Rev. D*, 104(1):016028, 2021.

[2] Jan Horak, Friederike Ihssen, Joannis Papavassiliou, Jan M. Pawlowski, Axel Weber, and Christof Wetterich. Gluon condensates and effective gluon mass. *SciPost Phys.*, 13:042, 2022.

[3] Jens Braun et al. Renormalised spectral flows. 6 2022.

[4] Friederike Ihssen and Jan M. Pawlowski. Functional flows for complex effective actions. 7 2022.

[5] Friederike Ihssen, Jan M. Pawlowski, Franz R. Sattler, and Nicolas Wink. Local Discontinuous Galerkin for the Functional Renormalisation Group. 7 2022.

[6] Friederike Ihssen, Franz R. Sattler, and Nicolas Wink. Numerical RG-time integration of the effective potential: Analysis and Benchmark. 2 2023.

[7] Jan Horak, Friederike Ihssen, Jan M. Pawlowski, Jonas Wessely, and Nicolas Wink. Scalar spectral functions from the spectral fRG. 3 2023.

[8] Friederike Ihssen and Jan M. Pawlowski. Preliminary: Flowing fields and optimal RG-flows. In preparation.

[9] Friederike Ihssen, Jan M. Pawlowski, Franz Sattler, and Nicolas Wink. Preliminary: Towards quantitative precision in functional qcd. In preparation.

[10] Friederike Ihssen, Jan M. Pawlowski, Franz Sattler, and Nicolas Wink. Preliminary: Local Discontinuous Galerkin for higher quark-mesonic scattering orders. In preparation.

[11] Friederike Ihssen, Wladimir Krinitsin, and Jan M. Pawlowski. Preliminary: Towards the chiral phase structure at large densities. In preparation.

[12] Friederike Ihssen and Franz R. Sattler. dune-FRGDG. `https://github.com/satfra/dune-FRGDG`, 2022.

[13] Jens Braun, Yong-rui Chen, Wei-jie Fu, Fei Gao, Andreas Geissel, Jan Horak, Chuang Huang, Friederike Ihssen, Yi Lu, Jan M. Pawlowski, Fabian Rennecke, Franz Sattler, Benedikt Schallmo, Jonas Stoll, Yang-yang Tan, Sebastian Töpfel, Jonas Turnwald, Rui Wen, Jonas Wessely, Nicolas Wink, Shi Yin, and Niklas Zorbach. fQCD collaboration. 2023.

[14] Wolfram Research, Inc. Mathematica, Version 13.2. Champaign, IL, 2022.

[15] Guido Van Rossum and Fred L. Drake. *Python 3 Reference Manual*. CreateSpace, Scotts Valley, CA, 2009.

[16] Jeff Bezanson, Alan Edelman, Stefan Karpinski, and Viral B Shah. Julia: A fresh approach to numerical computing. *SIAM Review*, 59(1):65–98, 2017.

[17] Xiaofeng Luo and Nu Xu. Search for the QCD Critical Point with Fluctuations of Conserved Quantities in Relativistic Heavy-Ion Collisions at RHIC : An Overview. *Nucl. Sci. Tech.*, 28(8):112, 2017.

[18] L. Adamczyk et al. Bulk Properties of the Medium Produced in Relativistic Heavy-Ion Collisions from the Beam Energy Scan Program. *Phys. Rev.*, C96(4):044904, 2017.

[19] Christian S. Fischer. QCD at finite temperature and chemical potential from Dyson-Schwinger equations. *Prog. Part. Nucl. Phys.*, 105:1–60, 2019.

[20] Yi Yin. The QCD critical point hunt: emergent new ideas and new dynamics. 2018.

[21] Anton Andronic, Peter Braun-Munzinger, Krzysztof Redlich, and Johanna Stachel. Decoding the phase structure of QCD via particle production at high energy. *Nature*, 561(7723):321–330, 2018.

[22] M. A. Stephanov. QCD phase diagram: An Overview. *PoS*, LAT2006:024, 2006.

[23] Jens O. Andersen, William R. Naylor, and Anders Tranberg. Phase diagram of QCD in a magnetic field: A review. *Rev. Mod. Phys.*, 88:025001, 2016.

[24] Edward Shuryak. Strongly coupled quark-gluon plasma in heavy ion collisions. *Rev. Mod. Phys.*, 89:035001, 2017.

[25] Jan M. Pawlowski. Equation of state and phase diagram of strongly interacting matter. *Nucl. Phys.*, A931:113–124, 2014.

[26] Craig D. Roberts and Sebastian M. Schmidt. Dyson-Schwinger equations: Density, temperature and continuum strong QCD. *Prog. Part. Nucl. Phys.*, 45:S1–S103, 2000.

[27] Mark G. Alford, Andreas Schmitt, Krishna Rajagopal, and Thomas Schäfer. Color superconductivity in dense quark matter. *Rev. Mod. Phys.*, 80:1455–1515, 2008.

[28] A. Bazavov et al. Freeze-out Conditions in Heavy Ion Collisions from QCD Thermodynamics. *Phys. Rev. Lett.*, 109:192302, 2012.

[29] S. Borsanyi, Z. Fodor, S. D. Katz, S. Krieg, C. Ratti, and K. K. Szabo. Freeze-out parameters: lattice meets experiment. *Phys. Rev. Lett.*, 111:062005, 2013.

[30] S. Borsanyi, Z. Fodor, S. D. Katz, S. Krieg, C. Ratti, and K. K. Szabo. Freeze-out parameters from electric charge and baryon number fluctuations: is there consistency? *Phys. Rev. Lett.*, 113:052301, 2014.

[31] R. Bellwied, S. Borsanyi, Z. Fodor, J. Guenther, S. D. Katz, C. Ratti, and K. K. Szabo. The QCD phase diagram from analytic continuation. *Phys. Lett.*, B751:559–564, 2015.

[32] A. Bazavov et al. The QCD Equation of State to $\mathcal{O}(\mu_B^6)$ from Lattice QCD. *Phys. Rev.*, D95(5):054504, 2017.

[33] A. Bazavov et al. Skewness and kurtosis of net baryon-number distributions at small values of the baryon chemical potential. *Phys. Rev.*, D96(7):074510, 2017.

[34] A. Bazavov et al. Chiral crossover in QCD at zero and non-zero chemical potentials. *Phys. Lett.*, B795:15–21, 2019.

[35] H.T. Ding et al. Chiral Phase Transition Temperature in ( 2+1 )-Flavor QCD. *Phys. Rev. Lett.*, 123(6):062002, 2019.

[36] A. Bazavov et al. Skewness, kurtosis, and the fifth and sixth order cumulants of net baryon-number distributions from lattice QCD confront high-statistics STAR data. *Phys. Rev. D*, 101(7):074502, 2020.

[37] Szabolcs Borsanyi, Zoltan Fodor, Jana N. Guenther, Ruben Kara, Sandor D. Katz, Paolo Parotto, Attila Pasztor, Claudia Ratti, and Kalman K. Szabo. The QCD crossover at finite chemical potential from lattice simulations. *Phys. Rev. Lett.*, 125(5):052001, 2020.

[38] Frithjof Karsch. Critical behavior and net-charge fluctuations from lattice QCD. *PoS*, CORFU2018:163, 2019.

[39] Adam Bzdak and Volker Koch. Acceptance corrections to net baryon and net charge cumulants. *Phys. Rev.*, C86:044904, 2012.

[40] Fabian Rennecke. Review of Critical Point Searches and Beam-Energy Studies. *MDPI Proc.*, 10(1):8, 2019.

[41] A. Steidl at CRC-TR-211 GSI Helmholtzzentrum für Schwerionenforschung GmbH. *https://www.gsi.de/work/forschung/theorie/theory-new/hot-and-dense-qcd*, Accessed February 28, 2022.

[42] Jens Braun. The QCD Phase Boundary from Quark-Gluon Dynamics. *Eur. Phys. J.*, C64:459–482, 2009.

[43] Jens Braun, Lisa M. Haas, Florian Marhauser, and Jan M. Pawlowski. Phase Structure of Two-Flavor QCD at Finite Chemical Potential. *Phys. Rev. Lett.*, 106:022002, 2011.

[44] Mario Mitter, Jan M. Pawlowski, and Nils Strodthoff. Chiral symmetry breaking in continuum QCD. *Phys. Rev. D*, 91:054035, 2015.

[45] Jens Braun, Leonard Fister, Jan M. Pawlowski, and Fabian Rennecke. From Quarks and Gluons to Hadrons: Chiral Symmetry Breaking in Dynamical QCD. *Phys. Rev. D*, 94(3):034016, 2016.

[46] Wei-jie Fu, Jan M. Pawlowski, Fabian Rennecke, and Bernd-Jochen Schaefer. Baryon number fluctuations at finite temperature and density. *Phys. Rev.*, D94(11):116020, 2016.

[47] Anton K. Cyrol, Leonard Fister, Mario Mitter, Jan M. Pawlowski, and Nils Strodthoff. Landau gauge Yang-Mills correlation functions. *Phys. Rev. D*, 94(5):054005, 2016.

[48] Anton K. Cyrol, Mario Mitter, Jan M. Pawlowski, and Nils Strodthoff. Nonperturbative quark, gluon, and meson correlators of unquenched QCD. *Phys. Rev. D*, 97(5):054006, 2018.

[49] Anton K. Cyrol, Mario Mitter, Jan M. Pawlowski, and Nils Strodthoff. Nonperturbative finite-temperature Yang-Mills theory. *Phys. Rev. D*, 97(5):054015, 2018.

[50] Wei-jie Fu, Jan M. Pawlowski, and Fabian Rennecke. Strangeness Neutrality and QCD Thermodynamics. *SciPost Phys. Core*, 2:002, 2020.

[51] Wei-jie Fu, Jan M. Pawlowski, and Fabian Rennecke. QCD phase structure at finite temperature and density. *Phys. Rev. D*, 101(5):054032, 2020.

[52] Christian S. Fischer, Jan Luecker, and Jens A. Mueller. Chiral and deconfinement phase transitions of two-flavour QCD at finite temperature and chemical potential. *Phys. Lett.*, B702:438–441, 2011.

[53] Christian S. Fischer, Jan Luecker, and Christian A. Welzbacher. Phase structure of three and four flavor QCD. *Phys. Rev.*, D90(3):034022, 2014.

[54] Chao Shi, Yong-Long Wang, Yu Jiang, Zhu-Fang Cui, and Hong-Shi Zong. Locate QCD Critical End Point in a Continuum Model Study. *JHEP*, 07:014, 2014.

[55] Fei Gao and Yu-xin Liu. QCD phase transitions via a refined truncation of Dyson-Schwinger equations. *Phys. Rev.*, D94(7):076009, 2016.

[56] Fei Gao and Jan M. Pawlowski. Chiral phase structure and critical end point in QCD. *Phys. Lett. B*, 820:136584, 2021.

[57] Fei Gao and Jan M. Pawlowski. Phase structure of (2+1)-flavor QCD and the magnetic equation of state. *Phys. Rev. D*, 105(9):094020, 2022.

[58] Jan M. Pawlowski and Fabian Rennecke. Higher order quark-mesonic scattering processes and the phase structure of QCD. *Phys. Rev. D*, 90(7):076002, 2014.

[59] Fabian Rennecke. Vacuum structure of vector mesons in QCD. *Phys. Rev. D*, 92(7):076012, 2015.

[60] Kenji Fukushima, Jan M. Pawlowski, and Nils Strodthoff. Emergent hadrons and diquarks. *Annals Phys.*, 446:169106, 3 2022.

[61] Jens Braun, Marc Leonhardt, and Jan M. Pawlowski. Renormalization group consistency and low-energy effective theories. *SciPost Phys.*, 6(5):056, 2019.

[62] Jens Braun, Marc Leonhardt, and Martin Pospiech. Fierz-complete NJL model study: Fixed points and phase structure at finite temperature and density. *Phys. Rev. D*, 96(7):076003, 2017.

[63] Jens Braun, Marc Leonhardt, and Martin Pospiech. Fierz-complete NJL model study. II. Toward the fixed-point and phase structure of hot and dense two-flavor QCD. *Phys. Rev.*, D97(7):076010, 2018.

[64] Jens Braun, Marc Leonhardt, and Martin Pospiech. Fierz-complete NJL model study III: Emergence from quark-gluon dynamics. *Phys. Rev. D*, 101(3):036004, 2020.

[65] Eduardo Grossi and Nicolas Wink. Resolving phase transitions with Discontinuous Galerkin methods. 3 2019.

[66] Franz J. Wegner and Anthony Houghton. Renormalization group equation for critical phenomena. *Phys. Rev.*, A8:401–412, 1973.

[67] Christof Wetterich. Exact evolution equation for the effective potential. *Phys. Lett. B*, 301:90–94, 1993.

[68] Joseph Polchinski. Renormalization and Effective Lagrangians. *Nucl. Phys.*, B231:269–295, 1984.

[69] V. N. Gribov. Quantization of non-Abelian gauge theories. *Nucl. Phys.*, B139:1, 1978.

[70] J. C. Taylor. Ward Identities and Charge Renormalization of the Yang-Mills Field. *Nucl. Phys. B*, 33:436–444, 1971.

[71] A. A. Slavnov. Ward Identities in Gauge Theories. *Theor. Math. Phys.*, 10:99–107, 1972.

[72] C. Becchi, A. Rouet, and R. Stora. Renormalization of Gauge Theories. *Annals Phys.*, 98:287–321, 1976.

[73] I. V. Tyutin. Gauge Invariance in Field Theory and Statistical Physics in Operator Formalism. 1975.

[74] Arthur M. Jaffe and Edward Witten. Quantum Yang-Mills theory. 2000.

[75] Raymond F. Streater and Arthur S. Wightman. *PCT, Spin and Statistics, and All That*. Princeton University Press, 1989.

[76] Konrad Osterwalder and Robert Schrader. AXIOMS FOR EUCLIDEAN GREEN'S FUNCTIONS. *Commun. Math. Phys.*, 31:83–112, 1973.

[77] Konrad Osterwalder and Robert Schrader. Axioms for Euclidean Green's Functions. 2. *Commun. Math. Phys.*, 42:281, 1975.

[78] C. Patrignani et al. Review of Particle Physics. *Chin. Phys. C*, 40(10):100001, 2016.

[79] Alexandre Deur, Stanley J. Brodsky, and Guy F. de Teramond. The QCD Running Coupling. *Nucl. Phys.*, 90:1, 2016.

[80] A. Deur, V. Burkert, Jian-Ping Chen, and W. Korsch. Experimental determination of the effective strong coupling constant. *Phys. Lett. B*, 650:244–248, 2007.

[81] A. Airapetian et al. Precise determination of the spin structure function g(1) of the proton, deuteron and neutron. *Phys. Rev. D*, 75:012007, 2007.

[82] V. Yu. Alexakhin et al. The Deuteron Spin-dependent Structure Function g1(d) and its First Moment. *Phys. Lett. B*, 647:8–17, 2007.

[83] J. H. Kim et al. A Measurement of alpha(s)(Q**2) from the Gross-Llewellyn Smith sum rule. *Phys. Rev. Lett.*, 81:3595–3598, 1998.

[84] P. L. Anthony et al. Deep inelastic scattering of polarized electrons by polarized He-3 and the study of the neutron spin structure. *Phys. Rev. D*, 54:6620–6650, 1996.

[85] K. Abe et al. Measurements of the proton and deuteron spin structure functions g(1) and g(2). *Phys. Rev. D*, 58:112003, 1998.

[86] D. Adams et al. Spin structure of the proton from polarized inclusive deep inelastic muon - proton scattering. *Phys. Rev. D*, 56:5330–5358, 1997.

[87] Reinhard Alkofer and J. Greensite. Quark Confinement: The Hard Problem of Hadron Physics. *J. Phys.*, G34:S3, 2007.

[88] Jens Braun, Holger Gies, and Jan M. Pawlowski. Quark Confinement from Color Confinement. *Phys.Lett.*, B684:262–267, 2010.

[89] Leonard Fister and Jan M. Pawlowski. Confinement from Correlation Functions. *Phys. Rev. D*, 88:045010, 2013.

[90] Taichiro Kugo and Izumi Ojima. Local Covariant Operator Formalism of Nonabelian Gauge Theories and Quark Confinement Problem. *Prog. Theor. Phys. Suppl.*, 66:1–130, 1979.

[91] Daniel Zwanziger. Fundamental modular region, Boltzmann factor and area law in lattice gauge theory. *Nucl. Phys. B*, 412:657–730, 1994.

[92] Christian S. Fischer, Axel Maas, and Jan M. Pawlowski. On the infrared behavior of Landau gauge Yang-Mills theory. *Annals Phys.*, 324:2408–2437, 2009.

[93] Christian S. Fischer and Jan M. Pawlowski. Uniqueness of infrared asymptotics in Landau gauge Yang- Mills theory. *Phys. Rev.*, D75:025012, 2007.

[94] Christian S. Fischer and Jan M. Pawlowski. Uniqueness of infrared asymptotics in Landau gauge Yang- Mills theory II. *Phys. Rev.*, D80:025023, 2009.

[95] Jan M. Pawlowski, Daniel F. Litim, Sergei Nedelko, and Lorenz von Smekal. Infrared behavior and fixed points in Landau gauge QCD. *Phys.Rev.Lett.*, 93:152002, 2004.

[96] John M. Cornwall. Dynamical Mass Generation in Continuum QCD. *Phys. Rev. D*, 26:1453, 1982. Decoupling.

[97] Gerard 't Hooft. Symmetry Breaking Through Bell-Jackiw Anomalies. *Phys. Rev. Lett.*, 37:8–11, 1976.

[98] Gerard 't Hooft. Computation of the Quantum Effects Due to a Four-Dimensional Pseudoparticle. *Phys. Rev. D*, 14:3432–3450, 1976. [Erratum: Phys.Rev.D 18, 2199 (1978)].

[99] M. Kobayashi and T. Maskawa. Chiral symmetry and eta-x mixing. *Prog. Theor. Phys.*, 44:1422–1424, 1970.

[100] Fei Gao and Jan M. Pawlowski. QCD phase structure from functional methods. *Phys. Rev. D*, 102(3):034027, 2020.

[101] Pascal J. Gunkel and Christian S. Fischer. Locating the critical endpoint of QCD: Mesonic backcoupling effects. *Phys. Rev. D*, 104(5):054022, 2021.

[102] Holger Gies and Christof Wetterich. Universality of spontaneous chiral symmetry breaking in gauge theories. *Phys. Rev. D*, 69:025001, 2004.

[103] Reinhard Alkofer, Axel Maas, Walid Ahmed Mian, Mario Mitter, Jordi París-López, Jan M. Pawlowski, and Nicolas Wink. Bound state properties from the functional renormalization group. *Phys. Rev. D*, 99(5):054029, 2019.

[104] N. Dupuis, L. Canet, A. Eichhorn, W. Metzner, J. M. Pawlowski, M. Tissier, and N. Wschebor. The nonperturbative functional renormalization group and its applications. *Phys. Rept.*, 910:1–114, 6 2021.

[105] J. Hubbard. Calculation of partition functions. *Phys. Rev. Lett.*, 3:77–80, 1959.

[106] R. L. Stratonovich. On a Method of Calculating Quantum Distribution Functions. *Soviet Physics Doklady*, 2:416, Jul 1957.

[107] Philippe de Forcrand. Simulating QCD at finite density. *PoS*, LAT2009:010, 2009.

[108] F. Karsch. Lattice QCD at high temperature and density. *Lect. Notes Phys.*, 583:209–249, 2002.

[109] Owe Philipsen. Lattice QCD at finite temperature and density. *Eur. Phys. J. ST*, 152:29–60, 2007.

[110] Christof Gattringer and Kurt Langfeld. Approaches to the sign problem in lattice field theory. *International Journal of Modern Physics A*, 31(22):1643007, Aug 2016.

[111] Philippe de Forcrand and Owe Philipsen. The QCD phase diagram for small densities from imaginary chemical potential. *Nucl. Phys.*, B642:290–306, 2002.

[112] Claudio Bonati, Massimo D'Elia, Francesco Negro, Francesco Sanfilippo, and Kevin Zambello. Curvature of the pseudocritical line in QCD: Taylor expansion matches analytic continuation. *Phys. Rev.*, D98(5):054510, 2018.

[113] Szabolcs Borsanyi, Zoltan Fodor, Jana N. Guenther, Sandor K. Katz, Kalman K. Szabo, Attila Pasztor, Israel Portillo, and Claudia Ratti. Higher order fluctuations and correlations of conserved charges from lattice QCD. *JHEP*, 10:205, 2018.

[114] Jana N. Guenther, Szabolcs Borsanyi, Zoltan Fodor, Sandor K. Katz, K. K. Szab, Attila Pasztor, Israel Portillo, and Claudia Ratti. Lattice thermodynamics at finite chemical potential from analytical Continuation. *J. Phys. Conf. Ser.*, 1070(1):012002, 2018.

[115] Philipp Isserstedt, Michael Buballa, Christian S. Fischer, and Pascal J. Gunkel. Baryon number fluctuations in the QCD phase diagram from Dyson-Schwinger equations. *Phys. Rev.*, D100(7):074011, 2019.

[116] M. Leonhardt, M. Pospiech, B. Schallmo, J. Braun, C. Drischler, K. Hebeler, and A. Schwenk. Symmetric nuclear matter from the strong interaction. *Phys. Rev. Lett.*, 125(14):142502, 2020.

[117] Jens Braun, Wei-jie Fu, Jan M. Pawlowski, Fabian Rennecke, Daniel Rosenblüh, and Shi Yin. Chiral susceptibility in ( 2+1 )-flavor QCD. *Phys. Rev. D*, 102(5):056010, 2020.

[118] Konstantin Otto, Micaela Oertel, and Bernd-Jochen Schaefer. Nonperturbative quark matter equations of state with vector interactions. *Eur. Phys. J. ST*, 229(22-23):3629–3649, 2020.

[119] Wei-jie Fu, Xiaofeng Luo, Jan M. Pawlowski, Fabian Rennecke, Rui Wen, and Shi Yin. Hyper-order baryon number fluctuations at finite temperature and density. *Phys. Rev. D*, 104(9):094047, 2021.

[120] Yong-rui Chen, Rui Wen, and Wei-jie Fu. Critical behaviors of the O(4) and Z(2) symmetries in the QCD phase diagram. *Phys. Rev. D*, 104(5):054009, 2021.

[121] Leo P. Kadanoff. Scaling laws for ising models near $T_c$. *Physics Physique Fizika*, 2:263–272, Jun 1966.

[122] Kenneth G. Wilson. Renormalization group and critical phenomena. 1. Renormalization group and the Kadanoff scaling picture. *Phys. Rev. B*, 4:3174–3183, 1971.

[123] Holger Gies and Christof Wetterich. Renormalization flow of bound states. *Phys. Rev. D*, 65:065001, 2002.

[124] Jens Braun. The QCD Phase Boundary from Quark-Gluon Dynamics. *Eur. Phys. J. C*, 64:459–482, 2009.

[125] Lukas Corell, Anton K. Cyrol, Mario Mitter, Jan M. Pawlowski, and Nils Strodthoff. Correlation functions of three-dimensional Yang-Mills theory from the FRG. *SciPost Phys.*, 5(6):066, 2018.

[126] Wei-jie Fu. QCD at finite temperature and density within the fRG approach: an overview. *Commun. Theor. Phys.*, 74(9):097304, 2022.

[127] Jan M. Pawlowski. Aspects of the functional renormalisation group. *Annals Phys.*, 322:2831–2915, 2007.

[128] Jan M. Pawlowski, Michael M. Scherer, Richard Schmidt, and Sebastian J. Wetzel. Physics and the choice of regulators in functional renormalisation group flows. *Annals Phys.*, 384:165–197, 2017.

[129] Daniel F. Litim. Optimization of the exact renormalization group. *Phys. Lett. B*, 486:92–99, 2000.

[130] Daniel F. Litim. Optimized renormalization group flows. *Phys. Rev. D*, 64:105007, 2001.

[131] F J Wegner. Some invariance properties of the renormalization group. *Journal of Physics C: Solid State Physics*, 7(12):2098, jun 1974.

[132] Tim R. Morris. A Gauge invariant exact renormalization group. 1. *Nucl. Phys. B*, 573:97–126, 2000.

[133] Hidenori Sonoda and Hiroshi Suzuki. Gradient flow exact renormalization group. *PTEP*, 2021(2):023B05, 2021.

[134] Oliver J. Rosten. Fundamentals of the Exact Renormalization Group. *Phys. Rept.*, 511:177–272, 2012.

[135] Christof Wetterich. Integrating out gluons in flow equations. *Z. Phys. C*, 72:139–162, 1996.

[136] Alessio Baldazzi, Riccardo Ben Alì Zinati, and Kevin Falls. Essential renormalisation group. *SciPost Phys.*, 13(4):085, 2022.

[137] Ulrich Ellwanger. FLow equations for N point functions and bound states. *Z. Phys.*, C62:503–510, 1994. [,206(1993)].

[138] Tim R. Morris. The Exact renormalization group and approximate solutions. *Int. J. Mod. Phys.*, A9:2411–2450, 1994.

[139] Florian Lamprecht. Diploma thesis Heidelberg University, 2007.

[140] Manfred Salmhofer. Dynamical Adjustment of Propagators in Renormalization Group Flows. *Annalen Phys.*, 16:171–206, 2007.

[141] Jordan Cotler and Semon Rezchikov. Renormalization Group Flow as Optimal Transport. 2 2022.

[142] Felipe Isaule, Michael C. Birse, and Niels R. Walet. Thermodynamics of Bose gases from functional renormalization with a hydrodynamic low-energy effective action. *Annals Phys.*, 412:168006, 2020.

[143] Alessio Baldazzi and Kevin Falls. Essential Quantum Einstein Gravity. *Universe*, 7(8):294, 2021.

[144] Fabian Rennecke. *The Chiral Phase Transition of QCD*. PhD thesis, Heidelberg U., 2015.

[145] S. Floerchinger, M. M. Scherer, and C. Wetterich. Modified Fermi-sphere, pairing gap and critical temperature for the BCS-BEC crossover. *Phys. Rev. A*, 81:063619, 2010.

[146] Aleksandr N. Mikheev, Christian-Marcel Schmied, and Thomas Gasenzer. Low-energy effective theory of nonthermal fixed points in a multicomponent Bose gas. *Phys. Rev. A*, 99(6):063622, 2019.

[147] Thomas Gasenzer and Jan M. Pawlowski. Towards far-from-equilibrium quantum field dynamics: A functional renormalisation-group approach. *Phys. Lett. B*, 670:135–140, 2008.

[148] Thomas Gasenzer, Stefan Kessler, and Jan M. Pawlowski. Far-from-equilibrium quantum many-body dynamics. *Eur.Phys.J.*, C70:423–443, 2010.

[149] Stefan Floerchinger. Analytic Continuation of Functional Renormalization Group Equations. *JHEP*, 05:021, 2012.

[150] Kazuhiko Kamikado, Nils Strodthoff, Lorenz von Smekal, and Jochen Wambach. Real-time correlation functions in the $O(N)$ model from the functional renormalization group. *Eur. Phys. J. C*, 74(3):2806, 2014.

[151] Ralf-Arno Tripolt, Nils Strodthoff, Lorenz von Smekal, and Jochen Wambach. Spectral Functions for the Quark-Meson Model Phase Diagram from the Functional Renormalization Group. *Phys. Rev.*, D89(3):034010, 2014.

[152] Jan M. Pawlowski and Nils Strodthoff. Real time correlation functions and the functional renormalization group. *Phys. Rev. D*, 92(9):094009, 2015.

[153] Takeru Yokota, Teiji Kunihiro, and Kenji Morita. Functional renormalization group analysis of the soft mode at the QCD critical point. *PTEP*, 2016(7):073D01, 2016.

[154] Kazuhiko Kamikado, Takuya Kanazawa, and Shun Uchino. Mobile impurity in a Fermi sea from the functional renormalization group analytically continued to real time. *Phys. Rev.*, A95(1):013612, 2017.

[155] Christopher Jung, Fabian Rennecke, Ralf-Arno Tripolt, Lorenz von Smekal, and Jochen Wambach. In-Medium Spectral Functions of Vector- and Axial-Vector Mesons from the Functional Renormalization Group. *Phys. Rev.*, D95(3):036020, 2017.

[156] Jan M. Pawlowski, Nils Strodthoff, and Nicolas Wink. Finite temperature spectral functions in the O(N)-model. *Phys. Rev.*, D98(7):074008, 2018.

[157] Takeru Yokota, Teiji Kunihiro, and Kenji Morita. Tachyonic instability of the scalar mode prior to the QCD critical point based on the functional renormalization-group method in the two-flavor case. *Phys. Rev.*, D96(7):074028, 2017.

[158] Ziyue Wang and Pengfei Zhuang. Meson spectral functions at finite temperature and isospin density with the functional renormalization group. *Phys. Rev. D*, 96(1):014006, 2017.

[159] Ralf-Arno Tripolt, Christopher Jung, Naoto Tanji, Lorenz von Smekal, and Jochen Wambach. In-medium spectral functions and dilepton rates with the Functional Renormalization Group. *Nucl. Phys.*, A982:775–778, 2019.

[160] Ralf-Arno Tripolt, Johannes Weyrich, Lorenz von Smekal, and Jochen Wambach. Fermionic spectral functions with the Functional Renormalization Group. *Phys. Rev.*, D98(9):094002, 2018.

[161] Lukas Corell, Anton K. Cyrol, Markus Heller, and Jan M. Pawlowski. Flowing with the temporal renormalization group. *Phys. Rev. D*, 104(2):025005, 2021.

[162] Sven Huelsmann, Soeren Schlichting, and Philipp Scior. Spectral functions from the real-time functional renormalization group. *Phys. Rev. D*, 102(9):096004, 2020.

[163] Christopher Jung, Jan-Hendrik Otto, Ralf-Arno Tripolt, and Lorenz von Smekal. Self-consistent O(4) model spectral functions from analytically continued functional renormalization group flows. *Phys. Rev. D*, 104(9):094011, 2021.

[164] Yang-yang Tan, Yong-rui Chen, and Wei-jie Fu. Real-time dynamics of the $O(4)$ scalar theory within the fRG approach. *SciPost Phys.*, 12:026, 2022.

[165] Markus Heller and Jan M. Pawlowski. Causal Temporal Renormalisation Group Flow of the Energy-Momentum Tensor. 12 2021.

[166] Jannik Fehre, Daniel F. Litim, Jan M. Pawlowski, and Manuel Reichert. Lorentzian Quantum Gravity and the Graviton Spectral Function. *Phys. Rev. Lett.*, 130(8):081501, 2023.

[167] Johannes V. Roth, Dominik Schweitzer, Leon J. Sieke, and Lorenz von Smekal. Real-time methods for spectral functions. *Phys. Rev. D*, 105(11):116017, 2022.

[168] Jan Horak, Jan M. Pawlowski, and Nicolas Wink. Spectral functions in the $\phi^4$-theory from the spectral DSE. *Phys. Rev. D*, 102:125016, 2020.

[169] Jan Horak, Joannis Papavassiliou, Jan M. Pawlowski, and Nicolas Wink. Ghost spectral function from the spectral dyson-schwinger equation. *Phys. Rev. D*, 104:074017, Oct 2021.

[170] Ralf-Arno Tripolt, Lorenz von Smekal, and Jochen Wambach. Flow equations for spectral functions at finite external momenta. *Phys. Rev. D*, 90(7):074031, 2014.

[171] K. Symanzik. Small distance behavior in field theory and power counting. *Commun. Math. Phys.*, 18:227–246, 1970.

[172] Markus Q. Huber, Jan M. Pawlowski, and Nicolas Wink. Finite Dyson-Schwinger Equations. 2022. in preparation.

[173] Harald Fritzsch and Murray Gell-Mann. Current algebra: Quarks and what else? *eConf*, C720906V2:135–165, 1972.

[174] Harald Fritzsch and Peter Minkowski. Psi Resonances, Gluons and the Zweig Rule. *Nuovo Cim. A*, 30:393, 1975.

[175] Christopher Michael and M. Teper. The Glueball Spectrum in SU(3). *Nucl. Phys. B*, 314:347–362, 1989.

[176] G. S. Bali, K. Schilling, A. Hulsebos, A. C. Irving, Christopher Michael, and P. W. Stephenson. A Comprehensive lattice study of SU(3) glueballs. *Phys. Lett. B*, 309:378–384, 1993.

[177] Colin J. Morningstar and Mike J. Peardon. The Glueball spectrum from an anisotropic lattice study. *Phys. Rev. D*, 60:034509, 1999.

[178] E. Gregory, A. Irving, B. Lucini, C. McNeile, A. Rago, C. Richards, and E. Rinaldi. Towards the glueball spectrum from unquenched lattice QCD. *JHEP*, 10:170, 2012.

[179] Andreas Athenodorou and Michael Teper. The glueball spectrum of SU(3) gauge theory in 3 + 1 dimensions. *JHEP*, 11:172, 2020.

[180] Adam Szczepaniak, Eric S. Swanson, Chueng-Ryong Ji, and Stephen R. Cotanch. Glueball spectroscopy in a relativistic many body approach to hadron structure. *Phys. Rev. Lett.*, 76:2011–2014, 1996.

[181] Adam P. Szczepaniak and Eric S. Swanson. The Low lying glueball spectrum. *Phys. Lett. B*, 577:61–66, 2003.

[182] Vincent Mathieu, Nikolai Kochelev, and Vicente Vento. The Physics of Glueballs. *Int. J. Mod. Phys. E*, 18:1–49, 2009.

[183] D. Dudal, M.S. Guimaraes, and S.P. Sorella. Glueball masses from an infrared moment problem and nonperturbative Landau gauge. *Phys.Rev.Lett.*, 106:062003, 2011.

[184] Joseph Meyers and Eric S. Swanson. Spin Zero Glueballs in the Bethe-Salpeter Formalism. *Phys. Rev. D*, 87(3):036009, 2013.

[185] Ian C. Cloet and Craig D. Roberts. Explanation and Prediction of Observables using Continuum Strong QCD. *Prog. Part. Nucl. Phys.*, 77:1–69, 2014.

[186] Helios Sanchis-Alepuz, Christian S. Fischer, Christian Kellermann, and Lorenz von Smekal. Glueballs from the Bethe-Salpeter equation. *Phys. Rev. D*, 92:034001, 2015.

[187] Emanuel V Souza, Mauricio Narciso Ferreira, Arlene Cristina Aguilar, Joãnnis Papavassiliou, Craig D Roberts, and Shu-Sheng Xu. Pseudoscalar glueball mass: a window on three-gluon interactions. *Eur. Phys. J. A*, 56(1):25, 2020.

[188] Markus Q. Huber, Christian S. Fischer, and Hèlios Sanchis-Alepuz. Spectrum of scalar and pseudoscalar glueballs from functional methods. *Eur. Phys. J. C*, 80(11):1077, 2020.

[189] Attilio Cucchieri and Tereza Mendes. What's up with IR gluon and ghost propagators in Landau gauge? A puzzling answer from huge lattices. *PoS*, LATTICE2007:297, 2007.

[190] A. Cucchieri and T. Mendes. Constraints on the IR behavior of the gluon propagator in Yang-Mills theories. *Phys. Rev. Lett.*, 100:241601, 2008.

[191] Attilio Cucchieri and Tereza Mendes. Landau-gauge propagators in Yang-Mills theories at beta = 0: Massive solution versus conformal scaling. *Phys. Rev. D*, 81:016005, 2010.

[192] A. Sternbeck, E. M. Ilgenfritz, M. Muller-Preussker, A. Schiller, and I. L. Bogolubsky. Lattice study of the infrared behavior of QCD Green's functions in Landau gauge. *PoS*, LAT2006:076, 2006.

[193] I. L. Bogolubsky, E. M. Ilgenfritz, M. Muller-Preussker, and A. Sternbeck. The Landau gauge gluon and ghost propagators in 4D SU(3) gluodynamics in large lattice volumes. *PoS*, LATTICE2007:290, 2007.

[194] I. L. Bogolubsky, E. M. Ilgenfritz, M. Muller-Preussker, and A. Sternbeck. Lattice gluodynamics computation of Landau gauge Green's functions in the deep infrared. *Phys. Lett. B*, 676:69–73, 2009.

[195] O. Oliveira and P. J. Silva. The Lattice infrared Landau gauge gluon propagator: The Infinite volume limit. *PoS*, LAT2009:226, 2009.

[196] O. Oliveira and P. Bicudo. Running Gluon Mass from Landau Gauge Lattice QCD Propagator. *J. Phys. G*, 38:045003, 2011.

[197] Axel Maas. Describing gauge bosons at zero and finite temperature. *Phys. Rept.*, 524:203–300, 2013.

[198] A. C. Aguilar, D. Binosi, and J. Papavassiliou. Gluon and ghost propagators in the Landau gauge: Deriving lattice results from Schwinger-Dyson equations. *Phys. Rev. D*, 78:025010, 2008.

[199] Philippe Boucaud, J-P. Leroy, A. Le Yaouanc, J. Micheli, O. Pene, and J. Rodriguez-Quintero. IR finiteness of the ghost dressing function from numerical resolution of the ghost SD equation. *JHEP*, 06:012, 2008.

[200] D. Binosi and J. Papavassiliou. Pinch Technique: Theory and Applications. *Phys.Rept.*, 479:1–152, 2009.

[201] Markus Q. Huber. Nonperturbative properties of Yang–Mills theories. *Phys. Rept.*, 879:1–92, 2020.

[202] Holger Gies. Introduction to the functional RG and applications to gauge theories. *Lect. Notes Phys.*, 852:287–348, 2012.

[203] Jens Braun. Fermion Interactions and Universal Behavior in Strongly Interacting Theories. *J. Phys. G*, 39:033001, 2012.

[204] E. Farhi and R. Jackiw, editors. *Dyanamical gauge symmetry breaking. A collection of reprints*. 1982.

[205] Ian J. R. Aitchison and Anthony J. G. Hey. *Gauge Theories in Particle Physics: A Practical Introduction, Volume 2: Non-Abelian Gauge Theories : QCD and The Electroweak Theory, Fourth Edition*. Taylor & Francis, 2013.

[206] M. J. Lavelle and M. Schaden. Propagators and Condensates in QCD. *Phys. Lett. B*, 208:297–302, 1988.

[207] Martin Lavelle. Gauge invariant effective gluon mass from the operator product expansion. *Phys. Rev. D*, 44:26–28, 1991.

[208] Christof Wetterich. Phase transition between three and two flavor QCD? 2 2001.

[209] Christof Wetterich. Spontaneously broken color. *Phys. Rev. D*, 64:036003, 2001.

[210] C. Wetterich. Higgs picture of the QCD-vacuum. *AIP Conf. Proc.*, 739(1):123–159, 2004.

[211] Astrid Eichhorn, Holger Gies, and Jan M. Pawlowski. Gluon condensation and scaling exponents for the propagators in Yang-Mills theory. *Phys. Rev. D*, 83:045014, 2011. [Erratum: Phys.Rev.D 83, 069903 (2011)].

[212] Christof Wetterich. Gluon meson duality. *Phys. Lett. B*, 462:164–168, 1999.

[213] Christof Wetterich. Gluon meson duality in the mean field approximation. *Eur. Phys. J. C*, 18:577–582, 2001.

[214] Holger Gies, Joerg Jaeckel, Jan M. Pawlowski, and Christof Wetterich. Do instantons like a colorful background? *Eur.Phys.J.*, C49:997–1010, 2007.

[215] Christopher T. Hill. Are There Significant Gravitational Corrections to the Unification Scale? *Phys. Lett. B*, 135:47–51, 1984.

[216] Q. Shafi and C. Wetterich. Modification of GUT Predictions in the Presence of Spontaneous Compactification. *Phys. Rev. Lett.*, 52:875, 1984.

[217] U. Ellwanger and C. Wetterich. Evolution equations for the quark - meson transition. *Nucl. Phys. B*, 423:137–170, 1994.

[218] Florian Lamprecht. Confinement in Polyakov gauge and flow equation of dynamical degrees of freedom. 2007. Diploma thesis Heidelberg.

[219] S. Floerchinger and C. Wetterich. Exact flow equation for composite operators. *Phys. Lett. B*, 680:371–376, 2009.

[220] Felipe Isaule, Michael C. Birse, and Niels R. Walet. Application of the functional renormalization group to Bose gases: from linear to hydrodynamic fluctuations. *Phys. Rev. B*, 98(14):144502, 2018.

[221] Romain Daviet and Nicolas Dupuis. Flowing bosonization in the nonperturbative functional renormalization-group approach. *SciPost Phys.*, 12(3):110, 2022.

[222] M. Reuter and C. Wetterich. Indications for gluon condensation for nonperturbative flow equations. 11 1994.

[223] M. Reuter and C. Wetterich. Gluon condensation in nonperturbative flow equations. *Phys. Rev. D*, 56:7893–7916, 1997.

[224] L. F. Abbott. The Background Field Method Beyond One Loop. *Nucl. Phys. B*, 185:189–203, 1981.

[225] Markus Q. Huber. Correlation functions of Landau gauge Yang-Mills theory. *Phys. Rev. D*, 101:114009, 2020.

[226] Daniele Binosi and Joannis Papavassiliou. Pinch technique and the Batalin-Vilkovisky formalism. *Phys. Rev. D*, 66:025024, 2002.

[227] Fei Gao, Joannis Papavassiliou, and Jan M. Pawlowski. Fully coupled functional equations for the quark sector of QCD. *Phys. Rev. D*, 103(9):094013, 2021.

[228] Daniel F. Litim and Jan M. Pawlowski. On gauge invariant Wilsonian flows. In *Workshop on the Exact Renormalization Group*, pages 168–185, 9 1998.

[229] Juergen Berges, Nikolaos Tetradis, and Christof Wetterich. Nonperturbative renormalization flow in quantum field theory and statistical physics. *Phys. Rept.*, 363:223–386, 2002.

[230] Pierre van Baal. QCD in a finite volume. 8 2000.

[231] Tina K. Herbst, Jan Luecker, and Jan M. Pawlowski. Confinement order parameters and fluctuations. 10 2015.

[232] Stephan Narison. Power corrections to alpha(s)(M(tau)),|V(us)| and anti-m(s). *Phys. Lett. B*, 673:30–36, 2009.

[233] Gunnar S. Bali and Antonio Pineda. Phenomenology of renormalons and the OPE from lattice regularization: the gluon condensate and the heavy quark pole mass. *AIP Conf. Proc.*, 1701(1):030010, 2016.

[234] A. C. Aguilar, C. O. Ambrósio, F. De Soto, M. N. Ferreira, B. M. Oliveira, J. Papavassiliou, and J. Rodríguez-Quintero. Ghost dynamics in the soft gluon limit. *Phys. Rev. D*, 104(5):054028, 2021.

[235] G. Parisi and R. Petronzio. On Low-Energy Tests of QCD. *Phys. Lett. B*, 94:51–53, 1980.

[236] Claude W. Bernard. Monte Carlo Evaluation of the Effective Gluon Mass. *Phys. Lett. B*, 108:431–434, 1982.

[237] Claude W. Bernard. Adjoint Wilson Lines and the Effective Gluon Mass. *Nucl. Phys. B*, 219:341–357, 1983.

[238] John F. Donoghue. The Gluon 'Mass' in the Bag Model. *Phys. Rev. D*, 29:2559, 1984.

[239] J. E. Mandula and M. Ogilvie. The Gluon Is Massive: A Lattice Calculation of the Gluon Propagator in the Landau Gauge. *Phys. Lett.*, B185:127–132, 1987.

[240] Chueng-Ryong Ji and F. Amiri. Perturbative QCD Analysis of the Pion Form-factor Using a Frozen Coupling Constant. *Phys. Rev. D*, 42:3764–3769, 1990.

[241] F. Halzen, G. I. Krein, and A. A. Natale. Relating the QCD pomeron to an effective gluon mass. *Phys. Rev. D*, 47:295–298, 1993.

[242] F. J. Yndurain. Limits on the mass of the gluon. *Phys. Lett. B*, 345:524–526, 1995.

[243] J. H. Field. A Phenomenological analysis of gluon mass effects in inclusive radiative decays of the J / psi and Upsilon. *Phys. Rev. D*, 66:013013, 2002.

[244] Owe Philipsen. On the nonperturbative gluon mass and heavy quark physics. *Nucl. Phys. B*, 628:167–192, 2002.

[245] E. G. S. Luna, A. F. Martini, M. J. Menon, A. Mihara, and A. A. Natale. Influence of a dynamical gluon mass in the pp and p anti-p forward scattering. *Phys. Rev. D*, 72:034019, 2005.

[246] A. C. Aguilar, M. N. Ferreira, and J. Papavassiliou. Exploring smoking-gun signals of the Schwinger mechanism in QCD. *Phys. Rev. D*, 105(1):014030, 2022.

[247] Ken-Ichi Aoki, Shin-Ichiro Kumamoto, and Masatoshi Yamada. Phase structure of NJL model with weak renormalization group. *Nucl. Phys.*, B931:105–131, 2018.

[248] Adrian Koenigstein, Martin J. Steil, Nicolas Wink, Eduardo Grossi, Jens Braun, Michael Buballa, and Dirk H. Rischke. Numerical fluid dynamics for FRG flow equations: Zero-dimensional QFTs as numerical test cases. I. The O(N) model. *Phys. Rev. D*, 106(6):065012, 2022.

[249] Adrian Koenigstein, Martin J. Steil, Nicolas Wink, Eduardo Grossi, and Jens Braun. Numerical fluid dynamics for FRG flow equations: Zero-dimensional QFTs as numerical test cases. II. Entropy production and irreversibility of RG flows. *Phys. Rev. D*, 106(6):065013, 2022.

[250] Martin J. Steil and Adrian Koenigstein. Numerical fluid dynamics for FRG flow equations: Zero-dimensional QFTs as numerical test cases. III. Shock and rarefaction waves in RG flows reveal limitations of the N$\to\infty$ limit in O(N)-type models. *Phys. Rev. D*, 106(6):065014, 2022.

[251] Bernardo Cockburn and Chi-Wang Shu. The local discontinuous galerkin method for time-dependent convection-diffusion systems. *SIAM Journal on Numerical Analysis*, 35(6):2440–2463, 1998.

[252] M. Blatt, A. Burchardt, A. Dedner, Ch. Engwer, J. Fahlke, B. Flemisch, Ch. Gersbacher, C. Gräser, F. Gruber, Ch. Grüninger, D. Kempf, R. Klöfkorn, T. Malkmus, S. Müthing, M. Nolte, M. Piatkowski, and O. Sander. The Distributed and Unified Numerics Environment, Version 2.4. *Archive of Numerical Software*, 4(100):13–29, 2016.

[253] J. Berges, N. Tetradis, and C. Wetterich. Coarse graining and first order phase transitions. *Phys. Lett. B*, 393:387–394, 1997.

[254] G. Papp, B.-J. Schaefer, H.J. Pirner, and J. Wambach. On the convergence of the expansion of renormalization group flow equation. *Phys.Rev.*, D61:096002, 2000.

[255] Daniel F. Litim. Derivative expansion and renormalization group flows. *JHEP*, 0111:059, 2001.

[256] Daniel F. Litim and Lautaro Vergara. Subleading critical exponents from the renormalization group. *Phys.Lett.*, B581:263–269, 2004.

[257] J. P. Blaizot, Ramon Mendez Galain, and Nicolas Wschebor. A New method to solve the non perturbative renormalization group equations. *Phys. Lett. B*, 632:571–578, 2006.

[258] Daniel F. Litim. Universality and the renormalisation group. *JHEP*, 0507:005, 2005.

[259] Bernd-Jochen Schaefer and Jochen Wambach. Susceptibilities near the QCD (tri)critical point. *Phys. Rev.*, D75:085015, 2007.

[260] Marcela Peláez and Nicolás Wschebor. Ordered phase of the $O(N)$ model within the nonperturbative renormalization group. *Phys. Rev. E*, 94(4):042136, 2016.

[261] Julia Borchardt and Benjamin Knorr. Global solutions of functional fixed point equations via pseudospectral methods. *Phys. Rev. D*, 91(10):105011, 2015. [Erratum: Phys.Rev.D 93, 089904 (2016)].

[262] Julia Borchardt and Benjamin Knorr. Solving functional flow equations with pseudospectral methods. *Phys. Rev. D*, 94:025027, 2016.

[263] Daniel F. Litim and Edouard Marchais. Critical $O(N)$ models in the complex field plane. *Phys. Rev.*, D95(2):025026, 2017.

[264] Andreas Juttner, Daniel F. Litim, and Edouard Marchais. Global Wilson Fisher fixed points. *Nucl. Phys.*, B921:769–795, 2017.

[265] Daniel F. Litim, Edouard Marchais, and Péter Mati. Fixed points and the spontaneous breaking of scale invariance. *Phys. Rev. D*, 95(12):125006, 2017.

[266] Daniel F. Litim and Matthew J. Trott. Asymptotic safety of scalar field theories. *Phys. Rev. D*, 98(12):125006, 2018.

[267] Ivan Balog, Hugues Chaté, Bertrand Delamotte, Maroje Marohnic, and Nicolás Wschebor. Convergence of Nonperturbative Approximations to the Renormalization Group. *Phys. Rev. Lett.*, 123(24):240604, 2019.

[268] Gonzalo De Polsi, Ivan Balog, Matthieu Tissier, and Nicolás Wschebor. Precision calculation of critical exponents in the $O(N)$ universality classes with the nonperturbative renormalization group. *Phys. Rev. E*, 101(4):042113, 2020.

[269] Gonzalo De Polsi, Guzmán Hernández-Chifflet, and Nicolás Wschebor. Precision calculation of universal amplitude ratios in O(N) universality classes: Derivative expansion results at order O($\partial 4$). *Phys. Rev. E*, 104(6):064101, 2021.

[270] Gonzalo De Polsi and Nicolás Wschebor. Regulator dependence in the functional renormalization group: A quantitative explanation. *Phys. Rev. E*, 106(2):024111, 2022.

[271] Discontinuous galerkin finite element methods for hyperbolic nonconservative partial differential equations. *Journal of computational physics*, 227(3):1887–1922, January 2008.

[272] Zheng Sun, José A. Carrillo, and Chi-Wang Shu. A discontinuous galerkin method for nonlinear parabolic equations and gradient flow problems with interaction potentials. *Journal of Computational Physics*, 352:76–104, 2018.

[273] Douglas N. Arnold, Franco Brezzi, Bernardo Cockburn, and Donatella Marini. Discontinuous galerkin methods for elliptic problems. In Bernardo Cockburn, George E. Karniadakis, and Chi-Wang Shu, editors, *Discontinuous Galerkin Methods*, pages 89–101, Berlin, Heidelberg, 2000. Springer Berlin Heidelberg.

[274] Jan S. Hesthaven and Tim Warburton. *Nodal Discontinuous Galerkin Methods: Algorithms, Analysis, and Applications*. Springer Publishing Company, Incorporated, 1st edition, 2007.

[275] Benjamin Knorr. Ising and Gross-Neveu model in next-to-leading order. *Phys. Rev. B*, 94(24):245102, 2016.

[276] Benjamin Knorr. Critical chiral Heisenberg model with the functional renormalization group. *Phys. Rev. B*, 97(7):075129, 2018.

[277] Lennart Dabelow, Holger Gies, and Benjamin Knorr. Momentum dependence of quantum critical Dirac systems. *Phys. Rev. D*, 99(12):125019, 2019.

[278] Benjamin Knorr. Exact solutions and residual regulator dependence in functional renormalisation group flows. *J. Phys. A*, 54(27):275401, 2021.

[279] Simon Resch, Fabian Rennecke, and Bernd-Jochen Schaefer. Mass sensitivity of the three-flavor chiral phase transition. *Phys. Rev.*, D99(7):076005, 2019.

[280] Mario Mitter and Bernd-Jochen Schaefer. Fluctuations and the axial anomaly with three quark flavors. *Phys. Rev.*, D89(5):054027, 2014.

[281] Jennifer A. Adams, J. Berges, S. Bornholdt, F. Freire, N. Tetradis, and C. Wetterich. Solving nonperturbative flow equations. *Mod. Phys. Lett.*, A10:2367–2380, 1995.

[282] O. Bohr, B. J. Schaefer, and J. Wambach. Renormalization group flow equations and the phase transition in O(N) models. *Int. J. Mod. Phys. A*, 16:3823–3852, 2001.

[283] Konstantin Otto, Christopher Busch, and Bernd-Jochen Schaefer. Regulator scheme dependence of the chiral phase transition at high densities. *Phys. Rev. D*, 106(9):094018, 6 2022.

[284] P. Bastian, M. Blatt, A. Dedner, Ch. Engwer, R. Klöfkorn, S.P. Kuttanikkad, M. Ohlberger, and O. Sander. The Distributed and Unified Numerics Environment (DUNE). In *Proc. of the 19th Symposium on Simulation Technique in Hannover, Sep. 12 - 14*, 2006.

[285] A. Dedner, B. Flemisch, and R. Klöfkorn. *Advances in DUNE*. Springer, 2012.

[286] P. Bastian, F. Heimann, and S. Marnach. Generic implementation of finite element methods in the Distributed and Unified Numerics Environment (DUNE). *Kybernetika*, 46:294–315, 2010.

[287] M. Blatt and P. Bastian. The iterative solver template library. In B. Kagström, E. Elmroth, J. Dongarra, and J. Wasniewski, editors, *Applied Parallel Computing – State of the Art in Scientific Computing*, pages 666–675, Berlin/Heidelberg, 2007. Springer.

[288] P. Bastian, M. Blatt, A. Dedner, C. Engwer, R. Klöfkorn, M. Ohlberger, and O. Sander. A Generic Grid Interface for Parallel and Adaptive Scientific Computing. Part I: Abstract Framework. *Computing*, 82(2–3):103–119, 2008.

[289] P. Bastian, M. Blatt, A. Dedner, C. Engwer, R. Klöfkorn, R. Kornhuber, M. Ohlberger, and O. Sander. A Generic Grid Interface for Parallel and Adaptive Scientific Computing. Part II: Implementation and Tests in DUNE. *Computing*, 82(2–3):121–138, 2008.

[290] Mengping Zhang and Chi-Wang Shu. An analysis of three different formulations of the discontinuous galerkin method for diffusion equations. *Mathematical Models and Methods in Applied Sciences*, 13, 11 2011.

[291] Chi-Wang Shu. Discontinuous galerkin methods: General approach and stability. *Numerical Solutions of Partial Differential Equations*, 01 2009.

[292] Daniel F. Litim, Jan M. Pawlowski, and Lautaro Vergara. Convexity of the effective action from functional flows. 2 2006.

[293] Shunsuke Yabunaka and Bertrand Delamotte. Surprises in $O(N)$ Models: Nonperturbative Fixed Points, Large $N$ Limits, and Multicriticality. *Phys. Rev. Lett.*, 119(19):191602, 2017.

[294] Shunsuke Yabunaka and Bertrand Delamotte. Why Might the Standard Large $N$ Analysis Fail in the O($N$) Model: The Role of Cusps in the Fixed Point Potentials. *Phys. Rev. Lett.*, 121(23):231601, 2018.

[295] Shunsuke Yabunaka, Claude Fleming, and Bertrand Delamotte. Incompleteness of the large-N analysis of the O(N) models: Nonperturbative cuspy fixed points and their nontrivial homotopy at finite N. *Phys. Rev. E*, 106(5):054105, 2022.

[296] Xiaobing Feng and Thomas Lewis. Local discontinuous galerkin methods for one-dimensional second order fully nonlinear elliptic and parabolic equations, 2012.

[297] Chen-Ning Yang and T. D. Lee. Statistical theory of equations of state and phase transitions. 1. Theory of condensation. *Phys. Rev.*, 87:404–409, 1952.

[298] T. D. Lee and Chen-Ning Yang. Statistical theory of equations of state and phase transitions. 2. Lattice gas and Ising model. *Phys. Rev.*, 87:410–419, 1952.

[299] Felipe Attanasio, Marc Bauer, Lukas Kades, and Jan M. Pawlowski. Searching for Yang-Lee zeros in O($N$) models. In *38th International Symposium on Lattice Field Theory*, 11 2021.

[300] P. Dimopoulos, L. Dini, F. Di Renzo, J. Goswami, G. Nicotra, C. Schmidt, S. Singh, K. Zambello, and F. Ziesché. Contribution to understanding the phase structure of strong interaction matter: Lee-Yang edge singularities from lattice QCD. *Phys. Rev. D*, 105(3):034513, 2022.

[301] Guido Nicotra, Petros Dimopoulos, Lorenzo Dini, Francesco Di Renzo, Jishnu Goswami, Christian Schmidt, Simran Singh, Kevin Zambello, and Felix Ziesche. Lee-Yang edge singularities in 2+1 flavor QCD with imaginary chemical potential. In *38th International Symposium on Lattice Field Theory*, 11 2021.

[302] Simran Singh, Petros Dimopoulos, Lorenzo Dini, Francesco Di Renzo, Jishnu Goswami, Guido Nicotra, Christian Schmidt, Kevin Zambello, and Felix Ziesche. Lee-Yang edge singularities in lattice QCD : A systematic study of singularities in the complex $\mu_B$ plane using rational approximations. In *38th International Symposium on Lattice Field Theory*, 11 2021.

[303] Jan M. Pawlowski and Julian M. Urban. Flow-based density of states for complex actions. 3 2022.

[304] Luca Zambelli and Omar Zanusso. Lee-Yang model from the functional renormalization group. *Phys. Rev. D*, 95(8):085001, 2017.

[305] Xin An, David Mesterházy, and Mikhail A. Stephanov. Functional renormalization group approach to the Yang-Lee edge singularity. *JHEP*, 07:041, 2016.

[306] Andrew Connelly, Gregory Johnson, Fabian Rennecke, and Vladimir Skokov. Universal Location of the Yang-Lee Edge Singularity in $O(N)$ Theories. *Phys. Rev. Lett.*, 125(19):191602, 2020.

[307] Fabian Rennecke and Vladimir V. Skokov. Universal location of Yang–Lee edge singularity for a one-component field theory in 1≤d≤4. *Annals Phys.*, 444:169010, 2022.

[308] Daniel F. Litim. Critical exponents from optimized renormalization group flows. *Nucl. Phys. B*, 631:128–158, 2002.

[309] Alessio Baldazzi, Kevin Falls, and Renata Ferrero. Relational observables in asymptotically safe gravity. *Annals Phys.*, 440:168822, 2022.

[310] Benjamin Knorr. Safe essential scalar-tensor theories. 4 2022.

[311] Catherine Bandle and Hermann Brunner. Blowup in diffusion equations: A survey. *Journal of Computational and Applied Mathematics*, 97(1):3–22, 1998.

[312] Edja Kouame Beranger, Kidjegbo Toure, and Brou Koua. Numerical blow-up for a heat equation with nonlinear boundary conditions. *Journal of Mathematics Research*, 10:119, 09 2018.

[313] R. S. Hamilton. The formation of singularities in the ricci flow.

[314] Siegfried Roth. Mathematics and biology: a kantian view on the history of pattern formation theory. *Development Genes and Evolution*, 221(5):255–279, Dec 2011.

[315] Alan M. Turing. The chemical basis of morphogenesis. *Trans. R. Soc. Lond.*, page B23737–72, 1952.

[316] Alfred Gierer and Hans Meinhardt. Gierer, a. meinhardt, h. a theory of biological pattern formation. kybernetik 12, 30- 39. *Biological Cybernetics*, 12:30–39, 01 1972.

[317] Li Guo and Yang Yang. Positivity preserving high-order local discontinuous galerkin method for parabolic equations with blow-up solutions. *Journal of Computational Physics*, 289:181–195, 2015.

[318] Robert D. Pisarski and Fabian Rennecke. Signatures of Moat Regimes in Heavy-Ion Collisions. *Phys. Rev. Lett.*, 127(15):152302, 2021.

[319] Fabian Rennecke, Robert D. Pisarski, and Dirk H. Rischke. Particle Interferometry in a Moat Regime. 1 2023.

[320] Jan Horak, Jan M. Pawlowski, and Nicolas Wink. On the complex structure of Yang-Mills theory. 2 2022.

[321] Jan Horak, Jan M. Pawlowski, and Nicolas Wink. On the quark spectral function in QCD. 10 2022.

[322] Gunnar Kallen. On the definition of the Renormalization Constants in Quantum Electrodynamics. *Helv. Phys. Acta*, 25(4):417, 1952.

[323] H. Lehmann. On the Properties of propagation functions and renormalization contants of quantized fields. *Nuovo Cim.*, 11:342–357, 1954.

[324] Johannes V. Roth and Lorenz von Smekal. Critical dynamics in a real-time formulation of the functional renormalization group. 3 2023.

[325] V. Skokov, B. Stokic, B. Friman, and K. Redlich. Meson fluctuations and thermodynamics of the Polyakov loop extended quark-meson model. *Phys. Rev.*, C82:015206, 2010.

[326] Tina Katharina Herbst, Jan M. Pawlowski, and Bernd-Jochen Schaefer. The phase structure of the Polyakovquarkmeson model beyond mean field. *Phys. Lett.*, B696:58–67, 2011.

[327] Kazuhiko Kamikado, Teiji Kunihiro, Kenji Morita, and Akira Ohnishi. Functional Renormalization Group Study of Phonon Mode Effects on Chiral Critical Point. *PTEP*, 2013:053D01, 2013.

[328] Jens Braun and Tina K. Herbst. On the Relation of the Deconfinement and the Chiral Phase Transition in Gauge Theories with Fundamental and Adjoint Matter. 2012.

[329] Ralf-Arno Tripolt, Jens Braun, Bertram Klein, and Bernd-Jochen Schaefer. Effect of fluctuations on the QCD critical point in a finite volume. *Phys. Rev.*, D90(5):054012, 2014.

[330] Tina K. Herbst, Jan M. Pawlowski, and Bernd-Jochen Schaefer. Phase structure and thermodynamics of QCD. *Phys. Rev.*, D88(1):014007, 2013.

[331] Tina Katharina Herbst, Mario Mitter, Jan M. Pawlowski, Bernd-Jochen Schaefer, and Rainer Stiele. Thermodynamics of QCD at vanishing density. *Phys. Lett.*, B731:248–256, 2014.

[332] Matthias Drews, Thomas Hell, Bertram Klein, and Wolfram Weise. Thermodynamic phases and mesonic fluctuations in a chiral nucleon-meson model. *Phys. Rev. D*, 88(9):096011, 2013.

[333] Alexander J. Helmboldt, Jan M. Pawlowski, and Nils Strodthoff. Towards quantitative precision in the chiral crossover: masses and fluctuation scales. *Phys. Rev. D*, 91(5):054010, 2015.

[334] Wei-jie Fu and Jan M. Pawlowski. Relevance of matter and glue dynamics for baryon number fluctuations. *Phys. Rev.*, D92(11):116006, 2015.

[335] Yin Jiang, Tao Xia, and Pengfei Zhuang. Topological Susceptibility in Three-Flavor Quark Meson Model at Finite Temperature. *Phys. Rev.*, D93(7):074006, 2016.

[336] Fabian Rennecke and Bernd-Jochen Schaefer. Fluctuation-induced modifications of the phase structure in (2+1)-flavor QCD. *Phys. Rev.*, D96(1):016009, 2017.

[337] Hui Zhang, Defu Hou, Toru Kojo, and Bin Qin. Functional renormalization group study of the quark-meson model with $\omega$ meson. *Phys. Rev.*, D96(11):114029, 2017.

[338] Ralf-Arno Tripolt, Bernd-Jochen Schaefer, Lorenz von Smekal, and Jochen Wambach. Low-temperature behavior of the quark-meson model. *Phys. Rev. D*, 97(3):034022, 2018.

[339] Wei-Jie Fu. Chiral criticality and glue dynamics. *Chin. Phys. C*, 43(7):074101, 2019.

[340] Wei-jie Fu, Jan M. Pawlowski, and Fabian Rennecke. Strangeness neutrality and baryon-strangeness correlations. *Phys. Rev.*, D100(11):111501, 2019.

[341] Shi Yin, Rui Wen, and Wei-jie Fu. Mesonic dynamics and the QCD phase transition. *Phys. Rev. D*, 100(9):094029, 2019.

[342] Rui Wen and Wei-jie Fu. Correlations of conserved charges and QCD phase structure. *Chin. Phys. C*, 45(4):044112, 2021.

[343] Renan Câmara Pereira, Rainer Stiele, and Pedro Costa. Functional renormalization group study of the critical region of the quark-meson model with vector interactions. *Eur. Phys. J. C*, 80(8):712, 2020.

[344] Jens Braun, Timon Dörnfeld, Benedikt Schallmo, and Sebastian Töpfel. Renormalization Group Studies of Dense Relativistic Systems. *Phys. Rev. D*, 104(9):096002, 8 2020.

[345] Fabian Rennecke. *The Chiral Phase Transition of QCD*. PhD thesis, U. Heidelberg (main), 2015.

[346] Bernd-Jochen Schaefer and Jochen Wambach. Renormalization group approach towards the QCD phase diagram. *Phys. Part. Nucl.*, 39:1025–1032, 2008.

[347] Bernd-Jochen Schaefer and Jochen Wambach. The Phase diagram of the quark meson model. *Nucl. Phys. A*, 757:479–492, 2005.

[348] Gian Paolo Vacca and Luca Zambelli. Multimeson Yukawa interactions at criticality. *Phys. Rev. D*, 91(12):125003, 2015.

[349] A. Jakovac, I. Kaposvari, and A. Patkos. Scalar mass stability bound in a simple Yukawa-theory from renormalization group equations. *Mod. Phys. Lett. A*, 32(02):1750011, 2016.

[350] Holger Gies, René Sondenheimer, and Matthias Warschinke. Impact of generalized Yukawa interactions on the lower Higgs mass bound. *Eur. Phys. J. C*, 77(11):743, 2017.

[351] G. Fejős and A. Patkós. Field dependence of the Yukawa coupling in the three flavor quark-meson model. *Phys. Rev. D*, 103(5):056015, 2021.

[352] Gernot Eichmann, Christian S. Fischer, and Christian A. Welzbacher. Baryon effects on the location of QCD's critical end point. *Phys. Rev.*, D93(3):034013, 2016.

[353] Thomas D . Cohen. Functional integrals for QCD at nonzero chemical potential and zero density. *Phys. Rev. Lett.*, 91:222001, 2003.

[354] Naseemuddin Khan, Jan M. Pawlowski, Fabian Rennecke, and Michael M. Scherer. The Phase Diagram of QC2D from Functional Methods. 2015.

[355] Wei-jie Fu and Jan M. Pawlowski. Correlating the skewness and kurtosis of baryon number distributions. *Phys. Rev.*, D93(9):091501, 2016.

[356] Daniel F. Litim and Jan M. Pawlowski. Completeness and consistency of renormalisation group flows. *Phys. Rev. D*, 66:025030, 2002.

[357] Daniel F. Litim and Jan M. Pawlowski. Wilsonian flows and background fields. *Phys. Lett. B*, 546:279–286, 2002.

[358] Jens Braun, Bertram Klein, and Piotr Piasecki. On the scaling behavior of the chiral phase transition in QCD in finite and infinite volume. *Eur.Phys.J.*, C71:1576, 2011.

[359] Richard Williams, Christian S. Fischer, and Walter Heupel. Light mesons in QCD and unquenching effects from the 3PI effective action. *Phys. Rev.*, D93(3):034026, 2016.

[360] Leonard Fister and Jan M. Pawlowski. Yang-Mills correlation functions at finite temperature. 2011.

[361] Carlos Parés. Numerical methods for nonconservative hyperbolic systems: a theoretical framework. *SIAM Journal on Numerical Analysis*, 44(1):300–321, 2006.

[362] Manuel Castro, José Gallardo, and Carlos Parés. High order finite volume schemes based on reconstruction of states for solving hyperbolic systems with nonconservative products. applications to shallow-water systems. *Mathematics of computation*, 75(255):1103–1134, 2006.

[363] Thomas Y Hou and Philippe G LeFloch. Why nonconservative schemes converge to wrong solutions: error analysis. *Mathematics of computation*, 62(206):497–530, 1994.

[364] Manuel J. Castro, José M. Gallardo, and Antonio Marquina. Approximate osher–solomon schemes for hyperbolic systems. *Applied Mathematics and Computation*, 272:347–368, 2016. Recent Advances in Numerical Methods for Hyperbolic Partial Differential Equations.

[365] Michael Dumbser, Arturo Hidalgo, Manuel Castro, Carlos Parés, and Eleuterio F Toro. Force schemes on unstructured meshes ii: Non-conservative hyperbolic systems. *Computer Methods in Applied Mechanics and Engineering*, 199(9-12):625–647, 2010.

[366] Michael Dumbser, Manuel Castro, Carlos Parés, and Eleuterio F Toro. Ader schemes on unstructured meshes for nonconservative hyperbolic systems: Applications to geophysical flows. *Computers & Fluids*, 38(9):1731–1748, 2009.

[367] Manuel Castro, Alberto Pardo, Carlos Parés, and E Toro. On some fast well-balanced first order solvers for nonconservative systems. *Mathematics of computation*, 79(271):1427–1472, 2010.

[368] Manuel J Castro, Philippe G LeFloch, María Luz Muñoz-Ruiz, and Carlos Parés. Why many theories of shock waves are necessary: Convergence error in formally path-consistent schemes. *Journal of Computational Physics*, 227(17):8107–8129, 2008.

[369] Michael Dumbser and Eleuterio F. Toro. A simple extension of the osher riemann solver to non-conservative hyperbolic systems. *Journal of Scientific Computing*, 48(1):70–88, 2011.

[370] Michael Dumbser, Federico Guercilena, Sven Köppel, Luciano Rezzolla, and Olindo Zanotti. Conformal and covariant z4 formulation of the einstein equations: Strongly hyperbolic first-order reduction and solution with discontinuous galerkin schemes. *Phys. Rev. D*, 97:084053, Apr 2018.

[371] Xiaobing Feng, Thomas Lewis, and Michael Neilan. Discontinuous galerkin finite element differential calculus and applications to numerical solutions of linear and nonlinear partial differential equations. *Journal of Computational and Applied Mathematics*, 299:68–91, 2016. Recent Advances in Numerical Methods for Systems of Partial Differential Equations.

[372] Jue Yan and Chi-Wang Shu. Local discontinuous galerkin methods for partial differential equations with higher order derivatives. 17(1):27–47.

[373] Xiaobing Feng and M. Neilan. The vanishing moment method for fully nonlinear second order partial differential equations: Formulation, theory, and numerical analysis. *arXiv: Numerical Analysis*, 2011.

[374] Kathryn Eleda Brenan, Stephen L Campbell, and Linda Ruth Petzold. *Numerical solution of initial-value problems in differential-algebraic equations*. SIAM, 1995.

[375] Kendall Atkinson, Weimin Han, and David E Stewart. *Numerical solution of ordinary differential equations*. John Wiley & Sons, 2011.

[376] Alan C Hindmarsh, Peter N Brown, Keith E Grant, Steven L Lee, Radu Serban, Dan E Shumaker, and Carol S Woodward. SUNDIALS: Suite of nonlinear and differential/algebraic equation solvers. *ACM Transactions on Mathematical Software (TOMS)*, 31(3):363–396, 2005.

[377] David J Gardner, Daniel R Reynolds, Carol S Woodward, and Cody J Balos. Enabling new flexibility in the SUNDIALS suite of nonlinear and differential/algebraic equation solvers. *ACM Transactions on Mathematical Software (TOMS)*, 2022.

[378] Alan C Hindmarsh. Odepack: A systemized collection of ode solvers. *Scientific computing*, pages 55–64, 1983.

[379] Christopher Rackauckas and Qing Nie. Differentialequations.jl–a performant and feature-rich ecosystem for solving differential equations in julia. *Journal of Open Research Software*, 5(1), 2017.

[380] R. Courant, K. Friedrichs, and H. Lewy. On the Partial Difference Equations of Mathematical Physics. *IBM Journal of Research and Development*, 11:215–234, March 1967.

[381] Duifje Maria van Egmond, Urko Reinosa, Julien Serreau, and Matthieu Tissier. A novel background field approach to the confinement-deconfinement transition. *SciPost Phys.*, 12(3):087, 2022.

[382] Biagio Lucini and Marco Panero. Introductory lectures to large-$N$ QCD phenomenology and lattice results. *Prog. Part. Nucl. Phys.*, 75:1–40, 2014.

[383] Leonard Fister and Jan Martin Pawlowski. Functional renormalization group in a finite volume. *Phys. Rev. D*, 92(7):076009, 2015.

[384] M. Reuter and C. Wetterich. Effective average action for gauge theories and exact evolution equations. *Nucl. Phys. B*, 417:181–214, 1994.

[385] Holger Gies. Running coupling in Yang-Mills theory: A flow equation study. *Phys. Rev. D*, 66:025006, 2002.

[386] Gerald V. Dunne and Christian Schubert. Two loop selfdual Euler-Heisenberg Lagrangians. 1. Real part and helicity amplitudes. *JHEP*, 08:053, 2002.

[387] Bernardo Cockburn and Chi-Wang Shu. The local discontinuous galerkin method for time-dependent convection-diffusion systems. *SIAM Journal on Numerical Analysis*, 35(6):2440–2463, 1998.

[388] M. Caselle, M. Hasenbusch, P. Provero, and K. Zarembo. Bound states and glueballs in three-dimensional Ising systems. *Nucl. Phys. B*, 623:474–492, 2002.

[389] V. Agostini, G. Carlino, M. Caselle, and M. Hasenbusch. The Spectrum of the (2+1)-dimensional gauge Ising model. *Nucl. Phys. B*, 484:331–352, 1997.

[390] M. Caselle, M. Hasenbusch, and P. Provero. Nonperturbative states in the 3-D phi**4 theory. *Nucl. Phys. B*, 556:575–600, 1999.

[391] F. Rose, F. Benitez, F. Léonard, and B. Delamotte. Bound states of the $\phi^4$ model via the nonperturbative renormalization group. *Phys. Rev. D*, 93(12):125018, 2016.

[392] Jan M. Pawlowski, Coralie S. Schneider, and Nicolas Wink. QMeS-Derivation: Mathematica package for the symbolic derivation of functional equations. *Comput. Phys. Commun.*, 287:108711, 2023.

[393] A. C. Aguilar, D. Ibanez, V. Mathieu, and J. Papavassiliou. Massless bound-state excitations and the Schwinger mechanism in QCD. *Phys. Rev. D*, 85:014018, 2012.

[394] D. Binosi, D. Ibanez, and J. Papavassiliou. The all-order equation of the effective gluon mass. *Phys. Rev. D*, 86:085033, 2012.

[395] A. C. Aguilar, D. Binosi, C. T. Figueiredo, and J. Papavassiliou. Evidence of ghost suppression in gluon mass scale dynamics. *Eur. Phys. J. C*, 78(3):181, 2018.

[396] Gernot Eichmann, Jan M. Pawlowski, and João M. Silva. Mass generation in Landau-gauge Yang-Mills theory. *Phys. Rev. D*, 104(11):114016, 2021.

[397] Julian S. Schwinger. Gauge Invariance and Mass. *Phys. Rev.*, 125:397–398, 1962.

[398] Julian S. Schwinger. Gauge Invariance and Mass. 2. *Phys. Rev.*, 128:2425–2429, 1962.

[399] R. Jackiw and K. Johnson. Dynamical Model of Spontaneously Broken Gauge Symmetries. *Phys. Rev. D*, 8:2386–2398, 1973.

[400] E. Eichten and F. Feinberg. Dynamical Symmetry Breaking of Nonabelian Gauge Symmetries. *Phys. Rev. D*, 10:3254–3279, 1974.

[401] A.C. Aguilar, D. Binosi, D. Ibáñez, and J. Papavassiliou. Effects of divergent ghost loops on the Green's functions of QCD. *Phys.Rev.*, D89:085008, 2014.

[402] A. C. Aguilar, D. Binosi, C. T. Figueiredo, and J. Papavassiliou. Unified description of seagull cancellations and infrared finiteness of gluon propagators. *Phys. Rev. D*, 94(4):045002, 2016.

[403] H. Osborn and D. E. Twigg. Reparameterisation Invariance and RG equations: Extension of the Local Potential Approximation. *J. Phys. A*, 42:195401, 2009.

[404] Tony F. Chan and Longjun Shen. Stability analysis of difference schemes for variable coefficient schrödinger type equations. *SIAM Journal on Numerical Analysis*, 24(2):336–349, 1987.

[405] Adérito Araújo, Sílvia Barbeiro, and Pedro Serranho. Stability of finite difference schemes for complex diffusion processes. *SIAM Journal on Numerical Analysis*, 50(3):1284–1296, 2012.

[406] Nathaniel J. Fisch and Martin D. Kruskal. Separating variables in two-way diffusion equations. *Journal of Mathematical Physics*, 21(4):740–750, 1980.

[407] Richard Beals. Partial-range completeness and existence of solutions to two-way diffusion equations. *Journal of Mathematical Physics*, 22(5):954–960, 1981.

[408] V. Vanaja. Numerical solution of a two-way diffusion equation. *AIP Conference Proceedings*, 1562(1):191–193, 2013.